# Additively Manufactured Lattice-Based Enhanced Heat Transfer Concepts for Superior Particle-to-Supercritical Carbon Dioxide Heat Exchanger for CSP Applications

A Dissertation Presented for the

Doctor of Philosophy

Degree

The University of Tennessee, Knoxville

Youssef Aider

December 2024

Copyright © 2024 by Youssef Aider.
All rights reserved.

## DEDICATION

I dedicate this work to my parents.

## ACKNOWLEDGEMENTS

I would like to express my sincere appreciation to my advisor, Dr. Prashant Singh, for his invaluable guidance and support throughout my doctoral studies. His expertise and commitment to academic excellence have been instrumental in shaping this research.

I am grateful to my committee members Dr. HeeJin Cho, Dr. Wei Wang, Dr. Andy Sarles, Dr. Tony Schmitz, and Dr. Kivanc Ekici for their insightful feedback and encouragement have greatly enhanced the quality of this work. Special thanks to Dr. Jeffrey Reinbolt, the graduate coordinator of the Mechanical Engineering department, who has patiently answered all my queries regarding requirements to fulfill this degree.

I would also like to acknowledge my colleagues, Inderjot Kaur and Junaid Khan, for their collaboration and the productive discussions we shared.

I extend my gratitude to the staff at Mississippi State University's Institute for Clean Energy Technology (ICET) Kristian Gonzalez, Devin Starkey, Michael Sullivan, who provided crucial assistance in fabricating some of my experimental tools.

Finally, I would like to thank my family for their continued support throughout this process.

## ABSTRACT

This research investigates the enhancement of heat transfer in packed bed heat exchangers using additively manufactured novel lattice structures, with applications in concentrated solar power (CSP) plants. The study encompasses multiple stages, examining various lattice topologies and their impact on heat transfer and fluid flow characteristics.

Initially, four lattice topologies (Octet, FD-Cube, Tetrakaidecahedron, and Cube) were investigated using air as the working fluid. The research revealed that lattices provided 10-20 times higher heat transfer augmentation compared to smooth channels. A unified correlation for Nusselt numbers as a function of Reynolds numbers was developed, applicable across all studied configurations. Utilizing additively manufactured lattices in 420 Stainless Steel, the study evaluated conjugate heat transfer capabilities, effective thermal conductivity, and forced convective heat transfer performance. The Octet lattice demonstrated the highest heat transfer coefficient; however, due to its highest pressure drop, its overall hydraulic performance was low. Results indicated that the Cube topology provided the best overall thermal hydraulic performance. Further research explored a novel moving packed bed heat exchanger with Octet lattice structures for CSP applications. The Octet lattice was chosen because, despite having high pressure drop with air, it demonstrated the highest heat transfer performance compared to other lattice structures studied. This made it ideal for particle heat transfer performance, as particles are driven by gravity and pumping power is not a cost to be accounted for, as long as particles flow through the lattice. Granular flow analysis, conducted through experiments and DEM-based simulations, revealed complex flow phenomena within the lattice structures.

The final stage characterized heat transfer in additively manufactured Octet-shaped lattice frame materials using particles and air as working fluids. The presence of lattices enhanced effective thermal conductivity by 2-4 times compared to particle-only packed beds, achieving high convective heat transfer coefficients ranging from 200-400 $W/m^2K$.

This comprehensive study demonstrates the potential of additively manufactured lattice structures in significantly improving heat transfer performance in packed bed heat exchangers, with promising applications in CSP plants.

## TABLE OF CONTENTS

CHAPTER ONE : GENERAL INTRODUCTION & LITERATURE REVIEW ..... 1
Lattice structures' interaction with moving packed bed of particles ..... 12
References ..... 17
CHAPTER TWO : PERIODIC HEAT TRANSFER CHARACTERISTICS OF ADDITIVELY MANUFACTURED LATTICES ..... 27
Abstract ..... 28
Introduction ..... 29
Geometric details of the test samples ..... 33
Experimental setup ..... 37
Experimental method and data reduction ..... 39
Forced convection experimental procedure ..... 39
Heat loss measurements ..... 40
Data reduction for heat transfer coefficient ..... 41
Results and discussion ..... 43
Benchmarking heat transfer data ..... 43
Mean heat transfer characteristics ..... 48
Heat transfer augmentation ..... 58
Pressure drop characteristics ..... 59
Pumping power requirements ..... 61
Thermal-hydraulic performance (THP) ..... 63
Conclusions ..... 64
Nomenclature ..... 65
Greek symbols ..... 67
Subscripts ..... 67
References ..... 68
CHAPTER THREE : EXPERIMENTAL STUDY ON FLOW AND THERMAL TRANSPORT IN ADDITIVELY MANUFACTURED LATTICES BASED ON CUBE-SHAPED UNIT CELL ..... 72
Abstract ..... 73

Introduction ..... 73
Lattice structures for forced convection ..... 75
Lattice structures for buoyancy-induced convection ..... 78
Experimental setups ..... 80
Effective thermal conductivity experimental setup ..... 80
Buoyancy-driven convection experimental setup ..... 82
Forced convection experimental setup ..... 85
Data reduction procedures ..... 87
Effective thermal conductivity ..... 87
Buoyancy-driven convection experiment ..... 88
Forced convection experiment ..... 88
Results and discussion ..... 89
Effective thermal conductivity ..... 89
Buoyancy-induced convection ..... 91
Forced convection ..... 94
Conclusions ..... 100
Nomenclature ..... 101
Greek symbols ..... 101
References ..... 102
CHAPTER FOUR : EXPERIMENTAL STUDY ON FLOW AND THERMAL TRANSPORT CHARACTERISTICS OF MOVING PACKED BED THROUGH A CHANNEL FEATURING SINGLE COLUMN OF INLINE CYLINDRICAL PINS .. 106
Abstract ..... 107
Introduction ..... 107
Test section details ..... 108
Effective thermal conductivity experiments ..... 108
Convective heat transfer and optical flow experiments ..... 111
Experimental procedures and measurement techniques ..... 116
Effective thermal conductivity experiments ..... 116
Convective heat transfer experiments ..... 117

Optical flow experiments ..... 119
Uncertainty analysis ..... 121
Results and discussion ..... 122
Heat transfer and flow dynamics of MPB [baseline configuration] ..... 124
Heat transfer and flow dynamics of MPB [pin-fin configuration] ..... 130
Conclusions ..... 135
References ..... 137
CHAPTER FIVE : GRANULAR FLOW IN NOVEL OCTET SHAPE-BASED LATTICE FRAME MATERIAL ..... 138
Abstract ..... 139
Introduction ..... 139
Experimental setup and computational domain ..... 145
Particle characteristics ..... 148
Discrete element method (dem) procedure ..... 150
Numerical setup ..... 154
Results and discussion ..... 156
Calibration of sliding friction coefficient for DEM simulations ..... 156
Rolling friction models ..... 158
Instantaneous flow characteristics ..... 159
Effect of porosity on the mass flow rate ..... 162
Effect of particle diameter on the mass flow rate ..... 165
Conclusions ..... 167
Acknowledgments ..... 168
Nomenclature ..... 168
Greek symbols ..... 169
Abbreviations ..... 169
Superscript ..... 170
References ..... 171

CHAPTER SIX : HEAT TRANSFER CHARACTERISTICS OF PARTICLE AND AIR FLOW THROUGH ADDITIVELY MANUFACTURED LATTICE FRAME MATERIAL BASED ON OCTET-SHAPE TOPOLOGY ..... 178
Abstract ..... 179
Introduction ..... 179
Experimental setups and measurement techniques ..... 183
Effective thermal conductivity test samples, experimental setup and $k_{eff}$ measurement procedure ..... 183
Forced convection setup with air as working fluid, and heat transfer coefficient calculation procedure ..... 187
Particle heat transfer test facility and heat transfer coefficient calculation procedure ..... 190
Particle size distribution and particle packing in AM lattice parts ..... 193
Uncertainty analysis ..... 194
Results and discussion ..... 194
Effective thermal conductivity ($k_{eff}$) ..... 194
Forced convection with air as working fluid ..... 196
Forced convection with particle as working fluid ..... 197
Conclusions ..... 202
Nomenclature ..... 203
Greek letters ..... 204
Abbreviations ..... 204
Acknowledgments ..... 204
References ..... 205
CHAPTER SEVEN : CONCLUSIONS AND RECOMMENDATIONS FOR FUTURE WORK ..... 209
VITA ..... 212

## LIST OF TABLES

Table 2.1 Measured porosity and designed fiber diameter of the RUC ..... 36

Table 2.2 Correlation $cRe_{dh}^{m}$ for Octet, FD-Cube, and TKD under different heating conditions ..... 51

Table 2.3 Correlation $cRe_{dh}^{m}$ for Cube under different heating conditions ..... 51

Table 2.4 Pore diameter of different RUC topologies ..... 54

Table 2.5 Correlation $cRe_{dp}^{m}$ for all investigated topologies under different heating conditions ..... 56

Table 2.6 Correlation $cRe_{df}^{m}$ for all investigated topologies under different heating conditions ..... 57

Table 2.7 Values of coefficients in correlation $Nu = cRe^{m}$ for different characteristic length scales ..... 57

Table 5.1 Mean diameter values of three different particle types experimentally investigated ..... 148

## LIST OF FIGURES

Figure 2.1 Four representative unit cell (RUC) topologies of the investigated samples .. 35
Figure 2.2 Dimensions of the printed samples..... 35
Figure 2.3 Schematic of the experimental setup (not drawn to scale)..... 38
Figure 2.4 Schematic of the lattice sample and test-section assembly (not drawn to scale) ..... 38
Figure 2.5 Streamwise distribution of Nusselt number in the smooth channel ..... 44
Figure 2.6 Streamwise distribution of Nusselt number in the smooth channel ..... 45
Figure 2.7 Mean total and forced heat transfer coefficient under both wall and only bottom wall heated conditions ..... 47
Figure 2.8 Mean total and forced heat transfer coefficient under both wall and only bottom wall heated conditions ..... 49
Figure 2.9 Nusselt number as a function of Reynolds number based on channel hydraulic diameter..... 51
Figure 2.10 Pore diameters ($dp$) corresponding to the largest sphere that could pass through the voids of (a) Octet, (b FD-Cube, (c) Tetrakaidecahedron, and (d) Cube.53
Figure 2.11 Pore diameter based Nusselt number as a function of Reynolds number ..... 54
Figure 2.12 Fiber diameter based Nusselt number as a function of Reynolds number .... 56
Figure 2.13 Comparison of values predicted from correlations with the values obtained from experiments ..... 57
Figure 2.14 Nusselt number enhancement with respect to smooth channel Dittus-Boelter correlation ..... 58
Figure 2.15 Conjugate heat transfer coefficient as a function of pumping power requirement ..... 60
Figure 2.16 Conjugate heat transfer coefficient as a function of pumping power requirement ..... 62
Figure 2.17 Thermal-hydraulic performance based on conjugate Nusselt number in reference to the Reynolds number ..... 63
Figure 3.1 Thermal conductivity test setup, and additively manufactured sample ..... 80

Figure 3.2 Schematic representation of test setup for buoyancy-driven convection experiments, sample cubic lattice, and three different heating orientations ..... 83
Figure 3.3Three different aspect ratios (width-to-height ratio) for buoyancy-driven convection experiments (sample images are not representative of their true size, the scale shown at the bottom of each sample's image should be used for the intercomparisons of the size of samples) ..... 84
Figure 3.4 Schematic of the forced convection experimental setup, test sample and its placement in the duct as seen by the flow entering the test section..... 85
Figure 3.5 Normalized results for effective thermal conductivity in the form $k_{eff}/k_s$ with respect to different levels of heat flux (left), comparison of the $k_{eff}/k_s$ results with correlations prescribed by Kaur et al. [3.24] and Wang et al. [3.23], along with the extension of obtained $k_{eff}$ results to lattice porosity of 0.87..... 90
Figure 3.6 A qualitative description of convection over a flat plate (small) with hot surface facing upwards, based on [3.26]..... 92
Figure 3.7 Convective heat transfer coefficient versus wall to fluid temperature difference ..... 92
Figure 3.8 Nusselt number versus Rayleigh number based on characteristic length scale of length or width of heated plate, also shown Al-Arabi & El-Riedy [3.26] correlation for flat heated plate facing upwards ($Nu_L = 0.7Ra_L^{1/4}$)..... 93
Figure 3.9 Streamwise variation of local convective heat transfer coefficient determined at the top and bottom walls, also shown is the averaged heat transfer coefficient ($h$) by taking the local mean of the top and bottom plate $h$. ..... 94
Figure 3.10 Convective heat transfer coefficient in the periodic regime versus average inlet flow velocity ..... 96
Figure 3.11 Variation of pressure gradient with flow velocity, dependence of determined values of $K, C_f$ on the choice of $\langle u \rangle_{max}$ for regression analysis ..... 98
Figure 3.12 Variation of $Nu$ and $Nu/Nu_0$ with Reynolds number (left), variation of THP and $f/f_0$ with Reynolds number (right) ..... 98

Figure 4.1 (a) single-pin test coupon for $k_{eff}$ characterization, (b) heater assembly and thermocouple slot arrangement, (c) test section for $k_{eff}$ experiments ..... 110
Figure 4.2 (a) exploded view of the convective heat transfer test section, (b) assembled view of the same test section. ..... 112
Figure 4.3 Details of nomenclature used for convective heat transfer experiments ..... 113
Figure 4.4(a) CAD model of the optical flow test setup including the particle elevator and heat exchanger test facility, (b) zoomed-in view of optical flow experimental test setup, (c) details of the test section employed for optical flow experiments ..... 115
Figure 4.5 Image enhancement to facilitate post-processing of images acquired in optical flow experiments ..... 120
Figure 4.6 Effective thermal conductivity versus conduction heat flux for three configurations ..... 123
Figure 4.7 Variation of local convective heat transfer coefficient with streamwise distance for different plate spacings of baseline configuration (parallel plates with no pin fins). $h_1$ is the convective heat transfer coefficient obtained from the wall temperature measurement at $T_{cw,1}$ (Fig. 4.3) ..... 125
Figure 4.8 Periodic regime convective heat transfer coefficient variation with MPB mass flux and flow rate ..... 127
Figure 4.9 Near-wall time-averaged flow velocity magnitude of MPB in cm/s, total mass flow rate of particles for each configuration: ~ 9.95 g/s. ..... 129
Figure 4.10 Variation of convective heat transfer coefficient with mass flow rate and mass flux, for pin-fin and plane channel configurations. The pin-fin *h* data is taken for the 7$^{th}$ pin from the entrance (periodic heat transfer regime). The corresponding location for plane channel (also periodic heat transfer regime) is plotted for direct comparison. ..... 131
Figure 4.11 Time-averaged near-wall moving packed bed velocity magnitude for 3-, 5-, 7-mm pin fin heights. The contours are shown for domain corresponding to periodic heat transfer. Total mass flow rate of particles for each configuration: ~ 9.95 g/s. The packed bed movement is vertically downwards. ..... 132

Figure 4.12 The nomenclature used for azimuthal and streamwise variation of flow velocities, azimuthal variation of u (cm/s) for the three pin configurations ..... 134
Figure 4.13 Streamwise variation of u (cm/s) for three pin configurations. x=0 corresponds to pin fin center (Fig. 4.13). ..... 134
Figure 5.1 Schematic of the falling-particle receiver system coupled with power cycle [5.2] ..... 140
Figure 5.2 (a) Schematic of experimental set-up used for granular flow visualization (not drawn to scale), (b) additively manufactured Octet lattice packed between enclosure of acrylic glass ..... 146
Figure 5.3 Geometrical dimensions of the hopper and lattice section in the computational domain ..... 146
Figure 5.4 Particles settled in the hopper before being discharged through the Octet lattice ..... 149
Figure 5.5 Particle-size distribution profiles ..... 149
Figure 5.6 Spring-dashpot model for interaction in the normal and tangential directions ..... 151
Figure 5.7 Comparison of mass flow rates obtained from DEM simulations for three different particle-wall sliding friction coefficients against the experimental data . 157
Figure 5.8 Comparison of mass flow rates obtained from DEM simulations for two different rolling friction models ..... 158
Figure 5.9 Instantaneous images of the free-fall of particles in three different lattices taken during experiments ..... 160
Figure 5.10 (a) Instantaneous image of the free-fall of particles from DEM simulations with particles colored with their local flow velocities, (b) zoomed-in view of the front side of the channel, and (c) zoomed-in side view of the channel ..... 161
Figure 5.11 Image of the particles taken after the completion of the DEM simulation showing accumulation in the junction regions ..... 163
Figure 5.12 Temporal evolution of mass flow rate profiles for three lattice porosities obtained from DEM simulations ..... 164

Figure 5.13 (a) Experimentally obtained mass flow rates for three different particle batches as a function of lattice porosity, (b) comparison of mean mass flow rates obtained from the experiments and DEM simulations for CP 30/60 particles as a function of lattice porosity ..... 164
Figure 5.14 Experimentally obtained mass flow rates for three different lattice porosities as a function of particle diameter ..... 166
Figure 6.1 Concentrating solar power plant [6.2] and representation of particle-to-sCO2 heat exchanger; present study focused on particle-side heat transfer enhancement 182
Figure 6.2 Three samples of different porosities tested for effective thermal conductivity (dimensions in top figure in mm, scale in sample images in inches) ..... 184
Figure 6.3 (a) Experimental setup for keff determination, (b) unidirectional heat flow obtained via patch heater and cold sink (bottom) ..... 186
Figure 6.4 (a) Schematic of the experimental setup (not drawn to scale), (b) zoom-in view of heat transfer section, (c) additively manufactured sandwich-type Octet panel in SS316L ..... 188
Figure 6.5 Particle heat transfer test facility ..... 191
Figure 6.6 Particle Size Distribution (PSD) measured using laser diffraction method .. 193
Figure 6.7 Effective thermal conductivity of Octet lattice (void space occupied by air) ..... 195
Figure 6.8 Effective thermal conductivity of Octet lattice (void space occupied by particles) and $k_{\text{eff}}$ enhancement factor ($\eta$) with respect to packed bed of particles. 196
Figure 6.9 Heat transfer coefficient in the periodic regime, variation presented with respect to average air flow velocity (measured at the inlet of the porous section) [channel diameter-based Reynolds numbers varied between 3,000 and 13,000 for SS316L and SS420 samples] ..... 197
Figure 6.10 Transient convective heat transfer coefficient at five different locations in the streamwise direction for three particle types (Octet panel porosity of 0.88, SS316L), (a) CP 40/100, (b) CP 30/60, (c) HSP 20/40 ..... 199
Figure 6.11 Time-averaged heat transfer coefficient in the periodic heat transfer regime, variation presented with respect to particle diameter ..... 200

Figure 6.12 (a) Time-averaged convective heat transfer coefficient variation with streamwise location, (b) enhancement factor of heat transfer coefficient with respect to streamwise location..... 201

# CHAPTER ONE :
# GENERAL INTRODUCTION & LITERATURE REVIEW

The renewable energy sources, including wind, solar, hydro, and geothermal, have been extensively investigated in many geographical areas worldwide. According to International Energy Agency (IEA), the contribution of renewable energy sources to worldwide electricity generation is rapidly increasing with 38% share recorded in 2022 [1.1]. Solar energy has become the predominant form of clean energy due to its widespread availability throughout the year. According to the IEA, solar energy accounted for 10.3% of worldwide electricity output in 2022. It is expected that solar energy would have the most substantial growth in the foreseeable future, mostly attributed to the ongoing reduction in the cost of solar energy-based power generation. According to IEA, there is a projected increase in global solar capacity from 843 gigawatts (GW) in 2022 to 2,800 GW by 2030 [1.2]. It is projected that the solar market in the United States would experience a threefold increase in size by the year 2028, resulting in the installation of approximately 375 GW of solar power [1.3,1.4]. As of now, solar photovoltaic (PV) stands as the most economically viable technology and is a prevalent method for harnessing solar energy. CSP is anticipated to have a substantial impact, particularly in large-scale solar initiatives. Concentrating Solar Power (CSP) plants have the capability to offer dependable and dispatchable electricity, which is of utmost importance in ensuring the stability of the power grid. Furthermore, CSP technology exhibits an advantage over PV due to its ability to facilitate thermal energy storage (TES), whereas PV technology involves the use of costly batteries.

The predominant form of TES technology employed in CSP facilities is based on molten salts. This system effectively stores thermal energy by utilizing a mixture of sodium nitrate and potassium nitrate in a molten state. Molten salts have the capability to attain elevated temperatures, reaching up to 565°C. This characteristic enables molten salt TES systems to store large amounts of energy and generate electricity over prolonged durations, including during the absence of solar radiation. Some examples of current CSP power storage projects include the Andasol Solar Power Facility in Spain, the Crescent Dunes Solar Power Plant in Nevada USA, and the Noor Energy Complex in Morocco, which have molten salt TES systems capable of storing enough energy to generate electricity for 7.5, 10, and 7 hours without sunlight, respectively [1.5]. Despite being

extensively utilized in modern CSP facilities, the implementation of molten salt encounters various obstacles, including its high cost [1.6], corrosive effects on CSP components [1.7], and the possibility of system malfunctions arising from salt solidification [1.8]. Furthermore, the existing molten salt technique is based on a binary composition including 60% sodium nitrate ($NaNO_3$) and 40% potassium nitrate ($KNO_3$), which exhibits a tendency to deteriorate when subjected to temperatures over 565°C [1.9]. These issues inhibit the employment of molten salt-based solutions in operational environments with temperatures exceeding 700°C- a critical need to advance the levelized cost of electricity targets for solar-based power generation. Higher operating temperatures augment power generation efficiency by improving the thermodynamic efficiency of the power cycle.

The ongoing development of next generation CSP facilities, also referred to as Gen3 CSP plants in the U.S., aims to enhance the efficiency, cost-effectiveness, and reliability of CSP technology. Gen3 CSP plants in the U.S. aim to operate at elevated temperatures [1.10], have alternative heat transfer fluids such as more thermally stable molten salts [1.11] and utilize supercritical fluids (SCFs), advanced solar collectors, and innovative thermal energy storage devices [1.12]. Gen3 CSP was launched by the U.S. Department of Energy (DOE) in 2017 with the primary objective to achieve a significant reduction in the cost of energy generated by CSP below $0.05 per kilowatt-hour (kWh) by 2030 [1.13]. The Gen3-CSP plants will be required to operate at temperatures over 700°C [1.14], leading to enhanced efficiency in electricity generation. The operation at elevated temperatures enables the exploitation of power cycles that are considerably more efficient, employing alternative working fluid, i.e., supercritical carbon dioxide ($sCO_2$) as opposed to traditional steam. $sCO_2$-based power cycles have the potential to exhibit superior thermal efficiencies compared to the traditional steam-based cycles. $sCO_2$ exhibits non-flammability and chemical stability at elevated temperatures. The process of $CO_2$ condensation during heat rejection facilitates seamless integration with heating and cooling systems, hence enabling the combined, generation of power and heating/cooling functionalities.

The integration of $sCO_2$-based power cycles into the CSP technology shows promising outcomes towards the DOE's goals of levelized cost of electricity (LCoE) of \$0.05/kWh [1.13]. The heat transfer media (HTM) research is divided in three categories/ pathways: (1) liquid pathway (molten salts), (2) particle pathway, and (3) gas phase pathway, among which, the particle pathway is considered the most promising. Further technology maturation in the particle pathway is subjected to some challenges, which includes the difficulty in efficiently heating the particles at the solar receiver, efficiently extracting the thermal energy from the particles and its transfer to the cold side of the heat exchanger, erosion, attrition, conveyance, and parasitic loss. In addition to that, ceramic particles that are known for their high solar absorptivity and thermal stability, tend to have low intrinsic thermal conductivity [1.15,1.16]. Due to the low thermal conductivity, significant improvements in heat transfer at the particle side of the heat exchanger are required to maximize the performance of the particle-to-$sCO_2$ heat exchanger and hence boost the power plant's efficiency. One of the configurations for particle-to-$sCO_2$ heat exchanger, is shell-and-plate, where particles move between adjacent parallel plates under the influence of gravity in a packed bed manner and is commonly known as moving packed bed heat exchanger (MPBHE) [1.17]. Note that MPBHEs can also be found in shell-and-tube configurations, however, the shell-and-plate configuration is considered more suitable than the former, in terms of factors such as, cost, heat transfer, structural reliability, manufacturability, parasitic losses, scalability, erosion etc. [1.18].

The MPBHEs are widely utilized in a variety of applications including heat recovery, solid drying, filtration, and thermochemical conversion [1.19]. In context with particle-to-$sCO_2$ heat exchangers, the heat exchanged between the moving packed bed with the parallel plates is poor, due to low inherent thermal conductivity of the packed bed of particles in motion, improper contact between particles and walls, and void space between the particles even in moving packed bed configuration. Fang et al. [1.20] explored a parallel shell-and-plate design, and found that the distance between the heat transfer plates (channel width) significantly influences the heat transfer between the particles and the fluid. The authors observed that narrow channels lead to a higher local heat transfer coefficient. Isaza et al. [1.21,1.22] presented analytical solutions for the heat

transfer in parallel plate heat exchanger in both co-current [1.21] and counter-current configurations [1.22], under simplified conditions where the moving solid bed was considered as a homogeneous medium under local thermal equilibrium. The results underscored the impact of the Biot number on the temperature gradient near the walls, highlighting the importance of particles' effective thermal conductivity on the heat exchanger's performance. The study also affirmed that a smaller width between the plates enhances the heat transfer coefficient. However, flow visualization revealed that extremely narrow distances between the plates could lead to temporary particle bridging, impeding the flow which leads to poor heat transfer performance. Besides the plate width, the particle thermal conductivity and void fraction were found to significantly affect the thermal performance of a parallel plate heat exchanger.

Yin et al. [1.23] demonstrated that an increase in particle diameter resulted in increased effective thermal conductivity of the packed bed, albeit at the expense of a reduced overall heat transfer coefficient. Conversely, a higher particle void fraction led to a decrease in both the effective thermal conductivity and the overall heat transfer coefficient. An experimental study by Maskalunas et al. [1.24] showed that a heat transfer coefficient of 350 $W/m^2K$ can be achieved. The experiments were conducted with silica sand particles of varying diameters moving between heated parallel plates, simplified the measurement of the heat transfer coefficient as it obviated the need for heating the particles. Despite the promising findings, most research on parallel plate heat exchangers has primarily focused on the effects of particle properties and the distance between the plates, leaving room for further exploration. The simplicity of the parallel plate heat exchanger design makes it a promising candidate for their implementation in CSP power plants' particle-to-s$CO_2$ heat exchangers. However, as mentioned above, the convective heat transfer between the MPB and parallel plates is generally low. Further, a long parallel plate channel leads to the development of thermal boundary layer, which increases in size, resulting in inferior heat transfer. One way to address this issue was proposed in [1.17] through incorporation of smaller banks, however, this design feature comes at a significant upfront cost, as well as higher accumulated operational and maintenance costs.

Literature review suggests that low heat transfer coefficient on the particle side is considered a *bottleneck* in the employment of shell-and-plate configuration with MPB for particle-to-s$CO_2$ heat exchanger. The particle side thermal transport can be increased by modifying the parallel plate configuration for a fixed channel width. The first design consideration is channel width since particle heat transfer significantly depends on this factor. This parameter also affects the reliability in the particles' flowability, if reduced below a certain level for a given particle size distribution. To this end, particle channel widths between 4-10 mm have potential, as currently, the most explored particle diameter varies between 100-500 microns. Now, for a certain channel width, the parallel plate domain needs to be modified, to achieve higher thermal transport. One way to enhance heat transfer between the moving packed and the parallel plates, is to install obstacles/bluff bodies such that particles interact with them and move around them, which causes local velocity enhancement and increases the conjugate heat transfer capabilities. Although there have been some limited computational studies on understanding the MPB flow around obstructions, they are mostly inspired by the shell-and-tube arrangement, where particles move in the shell and the tubes carry a suitable working fluid. In a shell-and-plate configuration, particles moving between two parallel plates and secondary fluid to which heat is to be transferred moves in minichannels bonded on the parallel plates. The fundamental studies on MPB around obstructions can be leveraged to develop advanced concepts for shell-and-plate particle-to-s$CO_2$ heat exchanger, with a focus on enhancing the particle-side heat transfer coefficient.

Deng et al. [1.25] carried out experimental and numerical study on MPB of particles through staggered arrangement of circular tubes. Through discrete element modeling (DEM), the high and low velocity zones of particles were identified, where typically, the zones above the pins had low particle flow velocities, while particles moved faster in between two adjacent pins. An experimental study was conducted by Dai et al. [1.26], where the authors studied the movement of three types of particles, with one of them being glass beads, around circular obstruction. A similar trend on high and low velocity zones as observed in [1.25] was observed by the authors in [1.26]. In [1.26], the void zones were also identified around the circular obstruction, where particles were not

present. Such zones are detrimental to heat exchange between particles and circular walls. A combined particle image velocimetry (PIV) and DEM study was carried out by Bartsch and Zunft [1.27], where this void region just downstream of the cylindrical pin was studied in detail for a staggered arrangement of cylindrical obstructions. It was shown that particle velocity increased around the sides of the cylinders, while two distinct low heat transfer zones were also identified. These zones correspond to the area right above the cylinders where particle motion is effectively non-existent, and the other zones is the region right downstream of the cylinders which does not even feature particles. These zones can be called 'dead/stagnant' and 'void' zones, respectively. One approach to address the so called 'dead' and 'void' zones is to modify the circular profile of the obstruction. Tian et al. [1.28] studied circular, elliptical and hexagonal tubes through DEM, to characterize the MPB flow and heat transfer around these obstructions. The elliptical shape alleviated some of the stagnation concerns, while significantly improving the void zone, particularly when the ellipse was elongated in the direction of MPB. In a follow-up study, the authors in [1.28] carried out a DEM study [1.29] on a trapezoidal obstruction with smoothened corners and reported a 14% increase in heat transfer compared to parallel plate.

Literature review on the methods to enhance heat transfer between moving packed bed through obstruction suggests that very limited studies have been carried out, with most studies on shell-and-tube configuration which involves long tubes resulting in two-dimensional flow around the tubes. The studies carried out on the obstructions in context with the shell-and-plate heat exchangers, where a solid pin joins the two parallel plates, are also sparse, and largely limited to computations. Furthermore, the effect of spacing of two parallel plates on heat transfer is profound, and this aspect is not studied in reference to obstructions' employment in closely spaced parallel plates. To this end, we have carried out a comprehensive experimental study to understand the fundamental flow and thermal transport of MPB of particles through an inline arrangement of cylindrical obstructions, where the plate spacing was varied between 3 to 7 mm, which represents the state-of-the-art shell-and-plate heat exchangers. The particles' flow-field near the wall is captured through a novel optical flow method, and the local heat transfer coefficient is

determined by carrying out quasi steady state experiments. Following sections provide details on the different experimental setups employed for the study of flow and thermal transport of MPB of particles, test section details, flow, and heat transfer measurement technique, followed by uncertainty analysis, results and their discussion, and concluding remarks.

Lattice structures have emerged as a promising alternative to open-cell metal foams for enhancing heat transfer in various engineering applications. The periodic and well-defined geometry of lattice structures offers distinct advantages over the random organization of fibers/struts in metal foams. The regular arrangement of struts in lattice structures results in desired flow distribution in the passages and controlled flow mixing. Additionally, the interconnected network of struts provides a high specific surface area, which is crucial for effective heat exchange between the solid and fluid phases. Numerous experimental and numerical studies have been conducted to investigate the hydraulic and thermal properties of lattice structures. Truss-based lattice structure is a class of cellular materials that is characterized by an organized arrangement of interconnected struts or walls, delineating a network of voids. These structures, which are composed of interconnected struts or plates, exhibit high strength-to-weight ratios and high surface area-to-volume ratios, making them attractive for lightweight and multi-functional designs [1.30]. The lattice struts are connected to form a stable three-dimensional structure that can withstand large mechanical loads. These types of structures are also used in the construction of bridges, towers, and other large structures. Lattice structures have garnered significant attention in various engineering applications due to their unique properties and the advantages they offer over conventional structures. Lattice structures can be tailored to achieve specific mechanical properties, such as high compressive strength, excellent elastic isotropy, and high specific energy absorption, by optimizing their geometrical parameters [1.31]. These structures often present higher porosities leading to improved fluid flow and heat transfer for air and particles [1.32,1.33]. It is known that truss-based lattice structures offer a better buckling resistance compared to other types of lattice structures such as reinforced grid-like and bio-inspired lattices due to their unique design achieved through inverse methods [1.34].

Truss-based lattices such as octet truss and plate-hybrid lattices, offer superior elastic isotropy and energy absorption compared to other lattice structures due to their unique design and material alignment [1.31]. In addition, these types of the structures have an important advantage of being self-supporting during additive manufacturing which is helpful in building complex shaped lattice-based heat exchangers. Due to their superior structural strength and lightweight nature, lattice structures can be designed with topology optimization technique to reduce the weight and material usage, thereby reducing the unit cost of production and manufacturing time [1.35,1.36]. Additive Manufacturing (AM) techniques, particularly Electron Beam Melting (EBM), are widely used due to their ability to directly manufacture complex 3D models, including lattice structures with intricate geometries [1.37–1.39]. This process is well-suited for creating lightweight structures with superior mechanical properties, such as the octet-truss lattice structure [1.40]. To overcome the limitations of traditional AM processes and enhance the energy absorption capabilities of truss-based lattices, hybrid manufacturing approaches have also been developed. For example, a combination of AM and metal casting has been used to produce aluminum alloy lattice structures, which were then experimentally evaluated for their performance under different compressive loads [1.41]. This hybrid approach combines the design freedom of AM with the material properties of cast metals to optimize the specific internal energy absorption of the structures [1.42].

The performance of truss-based lattice structures is greatly influenced by critical design parameters, such as the topology of the unit cell, the overall porosity of unit cell, physical size of the unit cell which determines the strut diameter, and their arrangement in three dimensions [1.37,1.43,1.44]. The effective properties of lattice trusses are significantly determined by structural factors, including the Maxwell stability parameter, the coordination number, and the truss thickness [1.45]. Moreover, the porosity level in lattice structures plays a vital role in the osseointegration and load-bearing capacity of implants [1.34]. By optimizing these variables, it is possible to enhance the specific internal energy and overall performance of lattice structures, thereby increasing their efficiency in various applications, such as energy absorption and medical implants. In addition, recent advancements in computational technologies have facilitated the

refinement of lattice structure designs to address specific requirements, further improving their performance and functionality.

Truss-based lattice structures are also known for their effective heat dissipation capabilities. The enhancement in heat transfer can be attributed to their unique design and structure. The lattice structure helps in increasing the surface area for heat exchange with the surrounding fluid, resulting in improved thermal performance [1.46,1.47]. The use of these structures in heat exchangers has the potential for developing more efficient and effective thermal systems [1.48]. The high effective thermal conductivity achieved with the addition of lattice structure is also an important aspect of enhancing the overall heat transfer. The effective thermal conductivity is inversely proportional to the unit cell porosity. Further, for forced convection applications which involves pumping of fluid, the pressure drop is also inversely proportional to the lattice porosity. Hence, there exists a trade-off between achieving high effective thermal conductivity and low pressure drop – both cannot be achieved simultaneously. AM-based fabrication provides the design freedom to explore moderate porosity levels to strike a balance between gain in heat transfer with the penalty on pressure drop. Further, the truss-based lattice structures can be strong and lightweight, which means they can support a lot of weight without being heavy while having high stiffness, meaning they don't bend easily [1.43], which is useful for manufacturing high pressure/high temperature heat exchangers.

From the multifunctional property perspective, the commonly explored unit cell topologies include cubic, octet, BCC, Octahedron, among others [1.49]. Each topology has its own distinct characteristics, such as mechanical strength, stiffness, and heat transfer performance. The choice of unit cell topology depends on the specific requirements of the application, such as load-bearing capacity, effective thermal conductivity, interstitial heat transfer coefficient, permeability, and inertial coefficient. Our previous experimental work on the thermal and flow transport characteristics of additively manufactured lattice structures involved the study of four-unit cell topologies: Octet, FD-Cube, Tetrakaidecahedron (TKD), and Cube. It was found that Octet provided the highest heat transfer performance, while Cube yielded the lowest values. These studies contribute to understanding the influence of topology, porosity, and

manufacturing methods on the thermal-hydraulic characteristics of lattice structures for heat transfer applications. Numerical study on the conjugate heat transfer performance and pressure drop of TKD, Octet, and Dodecahedron at a fixed lattice porosity of 0.9 showed that the TKD lattice exhibited the highest overall wall heat transfer coefficient and the lowest pressure drop, while octet lattice had the highest flow resistance. The conjugate heat transfer coefficient was found to be dependent on the thickness of struts in contact with the endwall, unit cell topology, and flow velocities/Reynolds number [1.50]. A study by Narkhede et al. [1.51] showed that when comparing the heat transfer performance of tetrahedral and pyramid lattices at a unit cell length-to-lattice truss diameter ratio (L/D) of 5, the tetrahedral topology offered less pressure drop compared to the pyramidal lattice topology due to fewer lattice members per unit cell. In addition to unit cell topology, the diameter and length of the struts within the lattice structure play a crucial role in determining its properties. For instance, strut diameter and length can influence the temperature field and cooling rate by affecting the heat transfer paths and induce localized temperature variations [1.52]. The struts' diameter and length also affect the porosity. In general, it is known that high porosity allows easier fluid flow or low pressure drop. The impact of lattice porosity on heat transfer is both significant and multifaceted as some authors have delved into the role of porosity in enhancing or reducing heat transfer within porous media [1.53]. The permeability of various structures are greatly influenced by their porosity, with ordered structures exhibiting higher permeability compared to their randomized counterparts [1.54]. Furthermore, the geometry of the pores also play a crucial role in natural convection, as certain shapes have been shown to lead to increased Nusselt numbers [1.55].

In addition to topology, strut diameter and length, the choice of material for the truss-based lattice structure significantly affects its thermal and mechanical properties. Common materials include metals (e.g., aluminum, copper, steel), polymers, and ceramics. The material's thermal conductivity, specific heat capacity, and mechanical strength should be considered when selecting the appropriate material for the application. In our previous study on lattice heat transfer [1.32], we have tested the effective thermal conductivity and heat transfer coefficient of both air and particle flow through Octet

lattice structure. The results showed that lattice structure manufactured from Stainless Steel 420 (SS420) resulted in superior heat transfer coefficient measurement and effective thermal conductivity for both air and particles as working fluid or convective agents. The octet-truss lattice offers a promising framework for optimizing mechanical properties and porosity in various applications. Such control over structural characteristics is a testament to the adaptability of lattice designs when facing diverse functional demands. This adaptability is equally crucial when considering thermal applications, where heat transfer mechanisms play a defining role in the performance and efficiency of a system [1.56]. Furthermore, the octet-truss lattice can be combined with other structural elements, such as plates, to create hybrid lattice structures that exhibit excellent elastic isotropy, high compressive strength, and high specific energy absorption [1.31].

**Lattice structures' interaction with moving packed bed of particles**

Transitioning from the macro design elements of lattice structures to the microscopic interactions within particle heat transfer, we encounter a multifaceted arena of thermal dynamics. The fundamental mechanism of particle heat transfer is complex since it involves conduction between interacting particles, conduction between particle and wall, convection between particle and fluid, as well as radiation between the particles. Additional factors can influence the heat transfer in each of these fundamental mechanisms such as dispersed phase heat transfer which becomes more important in fluidized beds, packed bed density, and gas layer induced between particle MPB and heat transfer walls [1.57–1.59]. Here, the understanding of heat conduction through solids, a process governed by temperature gradients and the thermal conductivity of the materials, is imperative, along with the lattice's ability to influence flow and thermal pathways [1.57–1.59]. The subsequent section delves into these intricacies, detailing the fundamental mechanisms of particle heat transfer and the consequential effects of lattice integration.

Multiple factors influence the heat transfer of particles in packed beds, such as particle thermal conductivity, specific heat capacity, particle diameter, heat transfer surface material, and the distance between heat transfer plates in parallel plate moving packed

bed (MPB) heat exchangers. An analytical solution to heat transfer in packed bed was provided by Isaza et al. [1.60] for a counter current parallel plate heat exchanger. It was shown that that the heat transfer is influenced by the Biot number, the heat capacity ratio, and the number of transfer units (NTU). The thermal conductivity of particle, mean particle diameter and particle size distribution affects the conduction heat transfer [1.61]. Zhang et al. used the discrete element method (DEM) for simulating individual particle flow, coupled with a heat transfer model to study the effect of particle size distribution (PSD) on heat transfer in moving packed bed heat exchangers. The authors found that wider PSD enhances particle size segregation and flow instability around a circular tube, which positively affects particle renewal in the stagnation zone and reduces local heat transfer resistance, resulting in up to ~10% increase in the total heat transfer coefficient between particle flow and the tube wall. Furthermore, a binary distribution PSD showed a ~30% increase in heat transfer compared to mono-sized PSD. Overall, it was shown that smaller particle size provide higher heat transfer coefficient [1.62]. On the other hand, an increase in particle diameter showed an increase in the effective thermal conductivity of the packed bed [1.63]. Common methods for modeling and simulating particle heat transfer include Discrete Element Method (DEM) and continuum modeling [1.64,1.65]. DEM is widely used to study particle flow and heat transfer in various geometries, such as tubes and plates. Continuum modeling is employed to investigate heat transfer in moving packed-bed heat exchangers. The contact resistance between particles and the wall affects the overall heat transfer coefficient [1.59,1.66]. In addition to that, particle flow around circular surfaces is affected by stagnation and void zones which decreases the effective heat transfer area between the particles and the tube.

Particle heat transfer has numerous applications in various industrial processes and systems. In moving packed beds, such as those used in iron ore sintering, cement production, and waste heat recovery, particle heat transfer is crucial for the design and optimization of heat exchangers, prediction of temperature distribution, and analysis of cooling rate [1.48]. Packed beds are widely used in the chemical industry, and particle heat transfer plays a significant role in enhancing heat transfer between gas and solid states inside these beds [1.33,1.48,1.49]. In concentrating solar power (CSP) systems,

particles are being employed as thermal energy storage (TES) medium due to their high thermal stability and natural abundance, as well as heat transfer fluid (HTF). Unlike molten salt, which is the state-of-the-art solar thermal energy storage medium that can only withstand temperatures up to 565°C, particles such as silica sand and aluminum oxide can be heated to temperatures exceeding 1,000°C without significant thermal degradation [1.67,1.68]. However, particles having low thermal conductivity impose a challenge for their implementation in CSP-TES applications. Significant research activities are ongoing to address this limitation by improving the heat transfer at the particle level of MPB heat exchanger. Techniques such as fluidization of the packed bed are proposed and have shown to be effective in enhancing heat transfer at the particle level, however at the cost of parasitic power drawn by the air fluidization and the added complexity to the heat exchanger design [1.69]. One other technique of improving the heat transfer in particle packed beds is to increase the surface area of the heat transfer. Different heat enhancement geometries have been studied [1.70]. Increasing the specific surface area leads to an increase in heat transfer by packing the maximum heat transfer surface into a relatively small volume of the heat exchanger. The increased specific surface can also act as a mechanism to agitate particles, which also contributes to the heat transfer enhancement. The studies on MPB heat exchangers have been primarily focused on shell-and-tube with tube bundles carrying the secondary fluid, and shell-and-plate with plate minichannels carrying the working fluid. The flow around the tube bundles is hindered by stagnation and void zones occurring at the top and bottom of the tubes, respectively. Measurement of particle flow around the tubes showed that maximum particle flow velocity occurs around the horizontal sides of the tube [1.71,1.72]. In addition to that, flow patterns such as funnel- and arch-shaped flow patterns are observed in MPB flow in presence of tube bundles. These flow patterns are influenced by the arrangement of the tubes [1.73]. Various methods have been proposed to enhance heat transfer in tube bundle moving packed bed heat exchangers, primarily by minimizing the stagnation and void zones. Niegsch et al. [1.74] showed that the local heat transfer coefficient is lower at the upper and lower parts of the tube due to stagnation and void regions, respectively. Zhoutuo et al. [1.75] found that helically shaped tubes eliminate

these regions, and hence, improving heat transfer. Staggered tube arrangements [1.61] and increased horizontal tube density [1.76] also enhance heat transfer by increasing particle-wall contact and velocity. Agitators [1.77] and tube vibration [1.78] have reduced void regions, resulting in overall improved heat transfer. However, vibration may increase tube wear. Shell-and-plate HEs are superior compared to the shell-and-tube counterparts in the particle-to-supercritical carbon dioxide ($CO_2$) heat exchanger configurations. Despite the potential for parallel plate MPB HEs to enhance heat transfer, there is a paucity of research focusing on particle-level improvements in thermal transport. The few existing studies have primarily investigated the impact of reducing the distance between parallel plates [1.65]. However, the utilization of lattice structures to augment heat transfer in parallel plate heat exchangers remains unexplored.

Previous work by our research group focused on the heat transfer characteristics of octet lattice structures for air/particles as convective heat transfer agents. The current study aims to expand this knowledge by exploring a broader range of lattice topologies. The novelty of the present work lies in the comprehensive investigation of heat transfer performance for particles with four different lattice topologies, providing valuable insights into the effectiveness of these structures in enhancing particle-based convective heat transfer. In addition to the heat transfer characterization of moving packed bed of particle flow through the lattice structure, this study also employs an optical flow algorithm to determine the MPB velocity magnitude and direction, a technique that has not been previously used for particle flow characterization in the context of lattice structures. The main motivation behind this research is twofold:

(I) It aims to develop a deeper understanding of the heat transfer behavior of these lattice structures with both particles and air. Air-based experiments were conducted in the present study due to two reasons: (a) the particle-based channels can be further improved by counter fluidization by air, for which, the understanding of the heat transfer characteristics of airflow through series of lattice structures is imperative, (b) a wide range of applications require air-based cooling, for which the quantified convection results will be useful.

(II) This work is motivated by the increasing demand for efficient particle-based heat exchangers, particularly in the context of next generation concentrated solar power (CSP) applications. In these applications, effective heat transfer between particles and $sCO_2$ is crucial for optimizing system performance and efficiency.

By addressing the identified research gap and presenting novel findings on the heat transfer performance of various lattice topologies with particles, this study contributes to the advancement of particle-based enhanced heat transfer technologies. The insights gained from this work have the potential to guide the design and development of high-performance heat exchangers for particles, ultimately supporting the implementation of more efficient and sustainable CSP systems.

## References

[1.1] 2022, “Renewables 2022 – Analysis,” IEA. [Online]. Available: https://www.iea.org/reports/renewables-2022. [Accessed: 28-Mar-2024].

[1.2] “Solar,” IEA. [Online]. Available: https://www.iea.org/energy-system/renewables/solar-pv. [Accessed: 28-Mar-2024].

[1.3] “U.S. Solar Market Insight | SEIA.” [Online]. Available: https://www.seia.org/us-solar-market-insight. [Accessed: 28-Mar-2024].

[1.4] 2022, “World Energy Outlook 2022 – Analysis,” IEA. [Online]. Available: https://www.iea.org/reports/world-energy-outlook-2022. [Accessed: 28-Mar-2024].

[1.5] “Concentrating Solar Power Projects by Country | Concentrating Solar Power Projects | NREL.” [Online]. Available: https://solarpaces.nrel.gov/by-country. [Accessed: 28-Mar-2024].

[1.6] Zhao, B., Cheng, M., Liu, C., and Dai, Z., 2018, “System-Level Performance Optimization of Molten-Salt Packed-Bed Thermal Energy Storage for Concentrating Solar Power,” Appl. Energy, **226**, pp. 225–239. https://doi.org/10.1016/j.apenergy.2018.05.081.

[1.7] Wei, X., Yang, C., Lu, J., Wang, W., and Ding, J., 2017, “The Mechanism of NO*x* Emissions from Binary Molten Nitrate Salts Contacting Nickel Base Alloy in Thermal Energy Storage Process,” Appl. Energy, **207**, pp. 265–273. https://doi.org/10.1016/j.apenergy.2017.06.109.

[1.8] Guccione, S., and Guedez, R., 2023, “Techno-Economic Optimization of Molten Salt Based CSP Plants through Integration of Supercritical CO2 Cycles and Hybridization with PV and Electric Heaters,” Energy, **283**, p. 128528. https://doi.org/10.1016/j.energy.2023.128528.

[1.9] Gong, Q., Hanke, A., Kessel, F., Bonk, A., Bauer, T., and Ding, W., 2023, “Molten Chloride Salt Technology for Next-Generation CSP Plants: Selection of Cold Tank Structural Material Utilizing Corrosion Control at 500 °C,” Sol. Energy Mater. Sol. Cells, **253**, p. 112233. https://doi.org/10.1016/j.solmat.2023.112233.

[1.10] Turchi, C. S., Gage, S., Martinek, J., Jape, S., Armijo, K., Coventry, J., Pye, J., Asselineau, C.-A., Venn, F., Logie, W., Fontalvo, A., Wang, S., McNaughton, R., Potter,

D., Steinberg, T., and Will, G., 2021, *CSP Gen3: Liquid-Phase Pathway to SunShot*, NREL/TP-5700-79323, National Renewable Energy Lab. (NREL), Golden, CO (United States); Sandia National Lab. (SNL-NM), Albuquerque, NM (United States); Australian National Univ., Canberra, ACT (Australia); Commonwealth Scientific and Industrial Research Organization (CSIRO), Newcastle, NSW (Australia); Queensland Univ. of Technology, Brisbane (Australia). https://doi.org/10.2172/1807668.

[1.11] Ding, W., and Bauer, T., 2021, "Progress in Research and Development of Molten Chloride Salt Technology for Next Generation Concentrated Solar Power Plants," Engineering, **7**(3), pp. 334–347. https://doi.org/10.1016/j.eng.2020.06.027.

[1.12] Mehos, M., Turchi, C., Vidal, J., Wagner, M., Ma, Z., Ho, C., Kolb, W., Andraka, C., and Kruizenga, A., 2017, *Concentrating Solar Power Gen3 Demonstration Roadmap*, NREL/TP--5500-67464, 1338899. https://doi.org/10.2172/1338899.

[1.13] Murphy, C., Cole, W., Sun, Y., Mehos, M., Turchi, C., and Maclaurin, G., 2019, "The Potential Role of Concentrating Solar Power within the Context of DOE's 2030 Solar Cost Targets." [Online]. Available: https://research-hub.nrel.gov/en/publications/the-potential-role-of-concentrating-solar-power-within-the-contex. [Accessed: 28-Mar-2024].

[1.14] Mancini, T. R., Gary, J. A., Kolb, G. J., and Ho, C. K., 2011, *Power Tower Technology Roadmap and Cost Reduction Plan.*, SAND2011-2419, Sandia National Laboratories (SNL), Albuquerque, NM, and Livermore, CA (United States). https://doi.org/10.2172/1011644.

[1.15] Farchado, M., San Vicente, G., Barandica, N., Sutter, F., Alkan, G., Sánchez-Señorán, D., and Ángel Morales, 2024, "Performance Improvement of CSP Particle Receivers by Depositing Spinel Absorber Coatings," Sol. Energy Mater. Sol. Cells, **266**, p. 112681. https://doi.org/10.1016/j.solmat.2023.112681.

[1.16] Chung, K. M., Zeng, J., Adapa, S. R., Feng, T., Bagepalli, M. V., Loutzenhiser, P. G., Albrecht, K. J., Ho, C. K., and Chen, R., 2021, "Measurement and Analysis of Thermal Conductivity of Ceramic Particle Beds for Solar Thermal Energy Storage," Sol. Energy Mater. Sol. Cells, **230**, p. 111271. https://doi.org/10.1016/j.solmat.2021.111271.

[1.17] Albrecht, K. J., and Ho, C. K., 2019, “Design and Operating Considerations for a Shell-and-Plate, Moving Packed-Bed, Particle-to-sCO2 Heat Exchanger,” Sol. Energy, **178**, pp. 331–340. https://doi.org/10.1016/j.solener.2018.11.065.

[1.18] Ho, C. K., Carlson, M., Albrecht, K. J., Ma, Z., Jeter, S., and Nguyen, C. M., 2019, “Evaluation of Alternative Designs for a High Temperature Particle-to-sCO2 Heat Exchanger,” J. Sol. Energy Eng., **141**(021001). https://doi.org/10.1115/1.4042225.

[1.19] Almendros-Ibáñez, J. A., Soria-Verdugo, A., Ruiz-Rivas, U., and Santana, D., 2011, “Solid Conduction Effects and Design Criteria in Moving Bed Heat Exchangers,” Appl. Therm. Eng., **31**(6), pp. 1200–1207. https://doi.org/10.1016/j.applthermaleng.2010.12.021.

[1.20] Fang, W., Chen, S., Xu, J., and Zeng, K., 2021, “Predicting Heat Transfer Coefficient of a Shell-and-Plate, Moving Packed-Bed Particle-to-sCO2 Heat Exchanger for Concentrating Solar Power,” Energy, **217**, p. 119389. https://doi.org/10.1016/j.energy.2020.119389.

[1.21] Isaza, P. A., Warnica, W. D., and Bussmann, M., 2015, “Co-Current Parallel-Plate Moving Bed Heat Exchanger: An Analytical Solution,” Int. J. Heat Mass Transf., **87**, pp. 616–624. https://doi.org/10.1016/j.ijheatmasstransfer.2015.02.079.

[1.22] Isaza, P. A., Warnica, W. D., and Bussmann, M., 2015, “Counter-Current Parallel-Plate Moving Bed Heat Exchanger: An Analytical Solution,” Int. J. Heat Mass Transf., **87**, pp. 625–635. https://doi.org/10.1016/j.ijheatmasstransfer.2015.02.056.

[1.23] Yin, J.-M., Zheng, Q.-Y., and Zhang, X.-R., 2020, “Heat Transfer Model of a Particle Energy Storage-Based Moving Packed Bed Heat Exchanger,” Energy Storage, **2**(1), p. e113. https://doi.org/10.1002/est2.113.

[1.24] Maskalunas, J., Nellis, G., and Anderson, M., 2022, “The Heat Transfer Coefficient Associated with a Moving Packed Bed of Silica Particles Flowing through Parallel Plates,” Sol. Energy, **234**, pp. 294–303. https://doi.org/10.1016/j.solener.2022.01.052.

[1.25] Deng, S., Wen, Z., Lou, G., Zhang, D., Su, F., Liu, X., and Dou, R., 2020, “Process of Particles Flow across Staggered Tubes in Moving Bed,” Chem. Eng. Sci., **217**, p. 115507. https://doi.org/10.1016/j.ces.2020.115507.

[1.26] Dai, Y. L., Liu, X. J., and Xia, D., 2020, “Flow Characteristics of Three Typical Granular Materials in near 2D Moving Beds,” Powder Technol., **373**, pp. 220–231. https://doi.org/10.1016/j.powtec.2020.06.057.

[1.27] Bartsch, P., and Zunft, S., 2019, “Granular Flow around the Horizontal Tubes of a Particle Heat Exchanger: DEM-Simulation and Experimental Validation,” Sol. Energy, **182**, pp. 48–56. https://doi.org/10.1016/j.solener.2019.01.086.

[1.28] Tian, X., Yang, J., Guo, Z., Wang, Q., and Sunden, B., 2020, “Numerical Study of Heat Transfer in Gravity-Driven Dense Particle Flow around a Hexagonal Tube,” Powder Technol., **367**, pp. 285–295. https://doi.org/10.1016/j.powtec.2020.04.001.

[1.29] Tian, X., Zhu, F., Guo, Z., Zhang, J., Yang, J., and Wang, Q., 2022, “Numerical Investigation of Gravity-Driven Particle Flow along the Trapezoidal Corrugated Plate for a Moving Packed Bed Heat Exchanger,” Powder Technol., **405**, p. 117526. https://doi.org/10.1016/j.powtec.2022.117526.

[1.30] Jost, E. W., Moore, D. G., and Saldana, C., 2021, “Evolution of Global and Local Deformation in Additively Manufactured Octet Truss Lattice Structures,” Addit. Manuf. Lett., **1**, p. 100010. https://doi.org/10.1016/j.addlet.2021.100010.

[1.31] Yu, T., Li, X., Zhao, M., Guo, X., Ding, J., Qu, S., Kwok, T. W. J., Li, T., Song, X., and Chua, B. W., 2023, “Truss and Plate Hybrid Lattice Structures: Simulation and Experimental Investigations of Isotropy, Large-Strain Deformation, and Mechanisms,” Mater. Today Commun., **35**, p. 106344. https://doi.org/10.1016/j.mtcomm.2023.106344.

[1.32] Youssef Aider, Inderjot Kaur, Ashreet Mishra, Like Li, Hee-Min Cho, Janna Martinek, Zhiwen Ma, and Prashant Singh, 2023, “Heat Transfer Characteristics of Particle and Air Flow Through Additively Manufactured Lattice Frame Material Based on Octet-Shape Topology,” J. Sol. Energy Eng.-Trans. Asme, **145**(6). https://doi.org/10.1115/1.4062196.

[1.33] Kaur, I., Aider, Y., Cho, H., and Singh, P., 2024, “Granular Flow in Novel Octet Shape–Based Lattice Frame Material,” J. Sol. Energy Eng., **146**(3).

[1.34] Maurizi, M., Gao, C., and Berto, F., 2022, “Inverse Design of Truss Lattice Materials with Superior Buckling Resistance,” Npj Comput. Mater., **8**(1), p. 247. https://doi.org/10.1038/s41524-022-00938-w.

[1.35] Flores, I., Kretzschmar, N., Azman, A. H., Chekurov, S., Pedersen, D. B., and Chaudhuri, A., 2020, “Implications of Lattice Structures on Economics and Productivity of Metal Powder Bed Fusion,” Addit. Manuf., **31**, p. 100947. https://doi.org/10.1016/j.addma.2019.100947.

[1.36] Zhu, J., Zhou, H., Wang, C., Zhou, L., Yuan, S., and Zhang, W., 2021, “A Review of Topology Optimization for Additive Manufacturing: Status and Challenges,” Chin. J. Aeronaut., **34**(1), pp. 91–110. https://doi.org/10.1016/j.cja.2020.09.020.

[1.37] Manuel Umanzor, Romesh C. Batra, Christopher B. Williams, and Alan Druschitz, 2023, “Parametric Study on the Performance of Cast Lattice Structures Loaded at Low Strain-Rates,” JOM, **75**(6), pp. 1–13. https://doi.org/10.1007/s11837-023-05812-8.

[1.38] Boris van Sosin, Daniil Rodin, H. O. Sliusarenko, Michael Bartoň, Michael Bartoň, and Gershon Elber, 2021, “The Construction of Conforming-to-Shape Truss Lattice Structures via 3D Sphere Packing,” Comput.-Aided Des., **132**, p. 102962. https://doi.org/10.1016/J.CAD.2020.102962.

[1.39] Neils, A., Dong, L., and Wadley, H., 2022, “The Small-Scale Limits of Electron Beam Melt Additive Manufactured Ti–6Al–4V Octet-Truss Lattices,” AIP Adv., **12**(9), p. 095021. https://doi.org/10.1063/5.0094155.

[1.40] Pierre-Thomas Doutre, Christelle Grandvallet, L. Gobet, Frédéric Vignat, and Rémy Dendievel, 2023, “Influence of Fillets onto Mechanical Properties of Octet-Truss Lattice Structures.”

[1.41] Zhuangzhuang Wang, Xiaofei Cao, Haoming Yang, Xiao Du, Binlin Ma, Qiu-Ju Zheng, Zhishuai Wan, and Ying Li, 2023, “Additively-Manufactured 3D Truss-Lattice Materials for Enhanced Mechanical Performance and Tunable Anisotropy: Simulations & Experiments,” Thin-Walled Struct., **183**, pp. 110439–110439. https://doi.org/10.1016/j.tws.2022.110439.

[1.42] Alexander Marutyan, 2022, “Optimization of Truss Lattices from Profile Pipes (Bent-Welded Profiles),” Stroit. Meh. Rasč Sooruž., **302**(3), pp. 71–78. https://doi.org/10.37538/0039-2383.2022.3.71.78.

[1.43] Jiyeon Kim, Dong Hwan Jung, and Yongwoo Kwon, 2022, “Numerical Study on the Quantitative Structure-Property Relation of Lattice Truss Metals,” Mater. Trans., **63**(10), pp. 1317–1322. https://doi.org/10.2320/matertrans.mt-mb2022015.

[44] Mohammad Zahid Khan, Jitendra Bhaskar, and Anand Kumar, 2023, “Design and Analysis of Strut-Based Lattice Structure Cranial Implant,” J. Mech. Eng. Sci., pp. 9307–9314. https://doi.org/10.15282/jmes.17.1.2023.1.0735.

[1.45] Tohid Dastan, Reza Jafari Nedoushan, Mohammad Sheikhzadeh, and Woong-Ryeol Yu, 2023, “Designs of Lattice Truss Core Sandwich Structures with Improved Compressive Strength and Stiffness,” J. Compos. Mater., **57**(15), pp. 2367–2387. https://doi.org/10.1177/00219983231160277.

[1.46] Lotfi, B., and Sunden, B. A., 2023, “A Novel Trussed Fin-and-Elliptical Tube Heat Exchanger with Periodic Cellular Lattice Structures,” Int. J. Numer. Methods Heat Fluid Flow, **33**(3), pp. 1076–1115. https://doi.org/10.1108/HFF-04-2022-0206.

[1.47] Daynes, S., and Feih, S., 2022, “Bio-Inspired Lattice Structure Optimisation with Strain Trajectory Aligned Trusses,” Mater. Des., **213**, p. 110320. https://doi.org/10.1016/j.matdes.2021.110320.

[1.48] Babak Lotfi and Bengt Sundén, 2022, “A Novel Trussed Fin-and-Elliptical Tube Heat Exchanger with Periodic Cellular Lattice Structures,” **33**(3), pp. 1076–1115. https://doi.org/10.1108/hff-04-2022-0206.

[1.49] Yin, H., Zhang, W., Zhu, L., Meng, F., Liu, J., and Wen, G., 2023, “Review on Lattice Structures for Energy Absorption Properties,” Compos. Struct., **304**, p. 116397. https://doi.org/10.1016/j.compstruct.2022.116397.

[1.50] Inderjot Kaur and Prashant Singh, 2022, “Conjugate Heat Transfer in Lattice Frame Materials Based on Novel Unit Cell Topologies,” Numer. Heat Transf. Part - Appl., **82**(12), pp. 788–801. https://doi.org/10.1080/10407782.2022.2083874.

[1.51] Swapnil Narkhede, Anirban Sur, and Ratnesh Tiwari, 2023, “The Effects of Topological Configuration and Geometric Parameters on Heat Transfer and Fluid Flow

Characteristics of Lattice-Based Heat Sinks," Numer. Heat Transf. Part -Appl., pp. 1–20. https://doi.org/10.1080/10407782.2023.2205182.

[1.52] David Downing, Martin Leary, Matthew McMillan, Ahmad Al-Ghamdi, and Milan Brandt, 2020, "Heat Transfer in Lattice Structures during Metal Additive Manufacturing: Numerical Exploration of Temperature Field Evolution," Rapid Prototyp. J., **26**(5), pp. 911–928. https://doi.org/10.1108/RPJ-11-2018-0288.

[1.53] Shuang Liu, Linfeng Jiang, Kai Leong Chong, Xiaojue Zhu, Zhen-Hua Wan, Roberto Verzicco, Richard J. A. M. Stevens, Detlef Lohse, and Chao Sun, 2020, "From Rayleigh─Bénard Convection to Porous-Media Convection: How Porosity Affects Heat Transfer and Flow Structure," J. Fluid Mech., **895**. https://doi.org/10.1017/JFM.2020.309.

[1.54] Fu Jiale, Zhang Tiechen, Li Menghan, Li Su, Xianglin Zhong, and Xiaori Liu, 2019, "Study on Flow and Heat Transfer Characteristics of Porous Media in Engine Particulate Filters Based on Lattice Boltzmann Method," Energies, **12**(17), p. 3319. https://doi.org/10.3390/EN12173319.

[1.55] Yousef Kazemian, Mohammad Javad Sayyari, and Javad Abolfazli Esfahani, 2021, "Effects of Pore Geometry on the Natural Convective Heat Transmission in a Porous Cavity: A Lattice Boltzmann Simulation," J. Therm. Anal. Calorim., **143**(3), pp. 2557–2575. https://doi.org/10.1007/S10973-020-10342-5.

[1.56] Feng, J., Liu, B., Lin, Z., and Fu, J., 2021, "Isotropic Octet-Truss Lattice Structure Design and Anisotropy Control Strategies for Implant Application," Mater. Des., **203**, p. 109595. https://doi.org/10.1016/j.matdes.2021.109595.

[1.57] Wang, S., Xu, C., Liu, W., and Liu, Z., 2019, "Numerical Study on Heat Transfer Performance in Packed Bed," Energies, **12**(3), p. 414. https://doi.org/10.3390/en12030414.

[1.58] Oschmann, T., and Kruggel-Emden, H., 2017, "Numerical and Experimental Investigation of the Heat Transfer of Spherical Particles in a Packed Bed with an Implicit 3D Finite Difference Approach," Granul. Matter, **19**(3), p. 47. https://doi.org/10.1007/s10035-017-0711-z.

[1.59] Zhang, R., Yang, H., Lu, J., and Wu, Y., 2013, “Theoretical and Experimental Analysis of Bed-to-Wall Heat Transfer in Heat Recovery Processing,” Powder Technol., **249**, pp. 186–195. https://doi.org/10.1016/j.powtec.2013.08.017.

[1.60] Isaza, P. A., Warnica, W. D., and Bussmann, M., 2015, “Counter-Current Parallel-Plate Moving Bed Heat Exchanger: An Analytical Solution,” Int. J. Heat Mass Transf., **87**, pp. 625–635. https://doi.org/10.1016/j.ijheatmasstransfer.2015.02.056.

[1.61] Qiu, L., Sang, D., Feng, Y., Huang, H., and Zhang, X., 2020, “Study on Heat Transfer of Process Intensification in Moving Bed Reactor Based on the Discrete Element Method,” Chem. Eng. Process. - Process Intensif., **151**, p. 107915. https://doi.org/10.1016/j.cep.2020.107915.

[1.62] Zheng, Y., Dong, H., Cai, J., Feng, J., Zhao, L., Liu, J., and Zhang, S., 2019, “Experimental Investigation of Volumetric Heat Transfer Coefficient in Vertical Moving-Bed for Sinter Waste Heat Recovery,” Appl. Therm. Eng., **151**, pp. 335–343. https://doi.org/10.1016/j.applthermaleng.2019.01.055.

[1.63] Gao, H., Liu, Y., Zheng, B., Sun, P., Lu, M., and Tian, G., 2020, “Fractal Heat Conduction Model of Semi-Coke Bed in Waste Heat Recovery Heat Exchanger,” J. Clean. Prod., **258**, p. 120663. https://doi.org/10.1016/j.jclepro.2020.120663.

[1.64] Bartsch, P., and Zunft, S., 2019, “Numerical Investigation of Dense Granular Flow around Horizontal Tubes: Qualification of CFD Model with Validated DEM Model,” Sol. Energy, **182**, pp. 298–303. https://doi.org/10.1016/j.solener.2019.01.087.

[1.65] Fang, W., Chen, S., Xu, J., and Zeng, K., 2021, “Predicting Heat Transfer Coefficient of a Shell-and-Plate, Moving Packed-Bed Particle-to-sCO2 Heat Exchanger for Concentrating Solar Power,” Energy, **217**, p. 119389. https://doi.org/10.1016/j.energy.2020.119389.

[1.66] Guo, Z., Tian, X., Tan, Z., Yang, J., Zhang, S., and Wang, Q., 2021, “Numerical Investigation of Heat Resistances in Uniform Dense Granular Flows along a Vertical Plate,” Powder Technol., **385**, pp. 396–408. https://doi.org/10.1016/j.powtec.2021.02.051.

[1.67] Wilson, G., Sahoo, S., Sabharwal, P., and Bindra, H., 2019, “Chapter Seven - Packed Bed Thermal Storage for LWRs,” *Storage and Hybridization of Nuclear Energy*,

H. Bindra, and S. Revankar, eds., Academic Press, pp. 229–248. https://doi.org/10.1016/B978-0-12-813975-2.00007-7.

[1.68] Díaz-Heras, M., Calderón, A., Navarro, M., Almendros-Ibáñez, J. A., Fernández, A. I., and Barreneche, C., 2021, "Characterization and Testing of Solid Particles to Be Used in CSP Plants: Aging and Fluidization Tests," Sol. Energy Mater. Sol. Cells, **219**, p. 110793. https://doi.org/10.1016/j.solmat.2020.110793.

[1.69] Ma, Z., and Martinek, J., 2017, "Fluidized-Bed Heat Transfer Modeling for the Development of Particle/Supercritical-CO2 Heat Exchanger," American Society of Mechanical Engineers Digital Collection. https://doi.org/10.1115/ES2017-3098.

[1.70] Jiang, B., Xia, D., Guo, H., Xiao, L., Qu, H., and Liu, X., 2019, "Efficient Waste Heat Recovery System for High-Temperature Solid Particles Based on Heat Transfer Enhancement," Appl. Therm. Eng., **155**, pp. 166–174. https://doi.org/10.1016/j.applthermaleng.2019.03.101.

[1.71] Dai, Y. L., Liu, X. J., and Xia, D., 2020, "Flow Characteristics of Three Typical Granular Materials in near 2D Moving Beds," Powder Technol., **373**, pp. 220–231. https://doi.org/10.1016/j.powtec.2020.06.057.

[1.72] Bartsch, P., and Zunft, S., 2019, "Granular Flow around the Horizontal Tubes of a Particle Heat Exchanger: DEM-Simulation and Experimental Validation," Sol. Energy, **182**, pp. 48–56. https://doi.org/10.1016/j.solener.2019.01.086.

[1.73] Qiu, L., Sang, D., Feng, Y., and Zhang, X., 2020, "Experimental Study on Particle Flow Characteristics of Three-Dimensional Moving Bed," Powder Technol., **374**, pp. 399–408. https://doi.org/10.1016/j.powtec.2020.07.061.

[1.74] Niegsch, J., Köneke, D., and Weinspach, P.-M., 1994, "Heat Transfer and Flow of Bulk Solids in a Moving Bed," Chem. Eng. Process. Process Intensif., **33**(2), pp. 73–89. https://doi.org/10.1016/0255-2701(94)85006-2.

[1.75] Tan, Z., Guo, Z., Yang, J., and Wang, Q., 2019, "Numerical Investigation of Heat Transfer for Elliptical Tube in Granular Flow Using DEM," Energy Procedia, **158**, pp. 5504–5509. https://doi.org/10.1016/j.egypro.2019.01.595.

[1.76] Baumann, T., and Zunft, S., 2015, “Development and Performance Assessment of a Moving Bed Heat Exchanger for Solar Central Receiver Power Plants,” Energy Procedia, **69**, pp. 748–757. https://doi.org/10.1016/j.egypro.2015.03.085.

[1.77] Jiang, B., Xia, D., Zhang, H., Pei, H., and Liu, X., 2020, “Effective Waste Heat Recovery from Industrial High-Temperature Granules: A Moving Bed Indirect Heat Exchanger with Embedded Agitation,” Energy, **208**, p. 118346. https://doi.org/10.1016/j.energy.2020.118346.

[1.78] Guo, Z., Zhang, S., Tian, X., Yang, J., and Wang, Q., 2020, “Numerical Investigation of Tube Oscillation in Gravity-Driven Granular Flow with Heat Transfer by Discrete Element Method,” Energy, **207**, p. 118203. https://doi.org/10.1016/j.energy.2020.118203.

# CHAPTER TWO : PERIODIC HEAT TRANSFER CHARACTERISTICS OF ADDITIVELY MANUFACTURED LATTICES

**Abstract**

In the present study, the flow and heat transfer characteristics of lattices with four different unit cell topologies, namely, (a) Octet, (b) FD-Cube, (c) Tetrakaidecahedron (TKD), and (d) Cube were investigated with air as the working fluid. All the samples had the designed porosity of ~ 0.88 and unit cell size of 10 mm. The distribution of local heat transfer coefficient revealed that depending on the unit cell topology, the flow became thermally developed after travelling over five or six rows of unit cells in streamwise direction. The heat transfer coefficient values in thermally developed zones were similar for Octet, FD-Cube and TKD. Overall heat transfer coefficient provided by Octet, FD-Cube, and TKD was in the range of ~216 $W/m^2K$ to 415 $W/m^2K$ and Cube yielded the lowest heat transfer coefficient values between 167 $W/m^2K$ and 290 $W/m^2K$. Three different characteristic length scales, viz. (a) channel hydraulic diameter, (b) pore-diameter, and (c) fiber-diameter were used to define the Nusselt number. The usage of pore-scale dimensions such as pore-diameter and fiber-diameter provided a very coherent data set for Nusselt number of all the topologies which helped in deriving a single correlation for predicting the thermal performance. The lattices provided heat transfer augmentation of 10-20 times higher than the smooth channel counterparts. Amongst all the investigated topologies, FD-Cube incurred the highest and Cube yielded the lowest pressure drop. It was also observed that convective heat transfer coefficients obtained for different lattices can be conveniently reported in Nusselt number forms with pore diameter and/or fiber diameters as reference length scales, where such Nusselt numbers for different lattice configurations converges to a single trendline when plotted against Reynolds numbers (also based on same reference length scales). We have provided a single correlation for Nusselt numbers as a function of Reynolds numbers which fits all the lattice configurations studied here. Finally, the thermal-hydraulic performance of lattices is reported which had similar magnitude levels for all the investigated topologies and a single correlation has been proposed for THP covering all the configurations of present study. The investigated topologies provided THP of ~ 3 at the lowest investigated Reynolds number.

## Introduction

Open-cell metal foams are an effective medium to augment the dissipation of high heat fluxes in several engineering applications. Tortuous flow path enabled enhanced flow mixing combined with flow stagnation with randomly organized fibers yield in superior thermal transport. The resultant high interfacial heat transfer coefficient in combination with high effective thermal conductivity and specific surface area makes the open-cell metal foams promising candidates for modern-day heat exchangers. Various experimental studies have characterized the hydraulic and thermal properties of metal foams. The superior thermal performance of the metal foams is because of conjugate thermal exchange between the metal and fluid at pore-scale. The numerical prediction of this conjugate performance requires *a priori* knowledge of the interfacial heat transfer coefficient for the closure of the governing equations dictated by local-thermal non equilibrium (LTNE) boundary condition. Estimation of interfacial heat transfer coefficient through numerical simulations by imposing either constant heat flux or constant temperature thermal condition on the fiber walls is convenient, but few experimental procedures such as single-blow transient technique and fin-efficiency methods have been adopted by several authors to evaluate the same [2.1–2.3].The mechanical and shock-absorbing capabilities of the metal-foams are also well known [2.4] which further extends their viability in applications demanding superior mechanical strength. Numerous studies in the past have been dedicated to understanding the thermal exchange processes in metal foams and quantifying the associated parameters. Comprehensive reviews on these investigations have been provided by several authors [2.5,2.6].

The performance of metal foams made through traditional *'foaming'* process is limited by several factors such as limited user control over unit cell topology, pore and fiber diameters, the inherent need for bonding agent at the fiber-endwall interface, etc. On the other hand, well-defined geometry, and periodic three-dimensional arrangement of a known Representative Unit Cell (RUC) are emerging as an alternative. Sandwich-type truss panels composed of Tetrahedral, Pyramidal, and Kagome shaped RUCs became very popular for their mechanical load bearing capabilities. The hydraulic and thermal

characteristics of these structures were later reported by several researchers. A comprehensive review of these investigations can be found in [2.7]. Recently, flow losses and heat transfer properties of X-lattice core sandwich configuration were investigated by Yan et al. [2.8,2.9]. These lattices can be manufactured via wire-weaving, stamping, investment-casting, and sheet-folding techniques. Although these traditional techniques are capable of producing regular patterns of RUCs, the reticulation in three-dimensional block configuration becomes challenging with increasing complexity of the RUC architecture. Also, one has to still resort to brazing, welding, or some bonding agent to ensure perfect thermal contact of these traditionally manufactured regular lattices with the endwall.

Recent progress in metal additive manufacturing (AM) processes such as Binder Jetting, Direct Metal Laser Sintering (DMLS), and Selective Laser Melting (SLM) provides not only an opportunity to fabricate a monolithic structure of the lattice and endwall but also allows the construction of architecturally more complex and advanced RUCs. The increased user control due to CAD software and program-based working interface with the 3D printing machines makes the AM an attractive alternative to conventional metal foam fabrication technologies. Several topologies such as Octet, Rhombic-dodecahedron, Rhombi-octet, Face-centered cube (FCC), etc. are being investigated actively under the scenarios of forced convection, pool boiling, and buoyancy-driven flows. These lattices exhibit superior mechanical properties, for e.g., Octet demonstrates stretch-dominated deformation as opposed to the wall-bending failure mode of the stochastic metal foams under uniaxial loading conditions [2.10]. A detailed analysis of the thermal-hydraulic performance of these structures has been reported by Kaur and Singh in prior investigations [2.7,2.11]. Critical review presented by the authors in [2.7,2.11] articulated the limitations of AM technologies from the perspective of lattice construction for heat exchange applications. One of the challenges of these technologies is the inferior surface quality that is rendered to the lattices. The surface roughness profiles can significantly influence the heat transfer at the smaller realizable dimensional scales. The hydraulic and heat transfer results reported for an RUC lattice block built in a particular material with a selected AM process can vary from the exact same RUC lattice

manufactured in same material but with a different AM process. Despite various limitations imposed by state-of-the-art AM technologies on fabrication of lattices with complex topologies, this topic should still be explored from the heat transfer perspective and efforts should be made towards quantifying the effects of roughness on local heat transfer. While AM field is witnessing rapid advancements, it is expected in near future that complex and smaller length scale unit cell topologies could be fabricated in alloys suitable for high temperature applications [2.12,2.13]

The experimental investigations on the metal foams and additively manufactured lattices typically report the mean flow and heat transfer properties. The common characteristics that are reported include pressure gradient, permeability, inertial coefficient, effective thermal conductivity, and endwall heat transfer coefficient. Correlations for predicting these variables and interfacial heat transfer coefficient [2.14] have been proposed by several authors. The volume-averaged and pore-scale direct simulations have been extensively conducted to analyze the local flow and heat transfer phenomenon in metal foams. In volume-averaged simulations, the mean geometrical and thermo-physical properties of metal foam/fluid are used to solve for the temperature and velocity fields whereas in direct simulations, the actual pore-scale geometry is simulated. For periodic lattices, the pore-scale numerical investigations are convenient for well-defined RUCs. These numerical simulations are the primary source for analyzing the development of local flow and thermal features in metal foams and lattices. Very few experimental studies have discussed the thermal development of the flows in metal foams, and, to the best of author's knowledge such studies are not present for the additively manufactured lattices.

Dukhan et al. [2.15] conducted steady-state heat transfer experiments on an aluminum foam (porosity $\varepsilon$~ 0.876, 20 ppi) cylinder subjected to constant heat flux boundary condition with water as the working fluid. A wide range of mass flow rates was tested which spanned from Darcy to non-Darcy regime. In Darcy regime, the pressure gradient shows linear dependence on the mean flow velocity whereas in non-Darcy regime, the relationship becomes quadratic in nature due to inertial effects. The cylinder in [2.15] had sufficient length in the mean flow direction to achieve thermally and hydrodynamically

developed flow. Thermal entry length for Darcy flow was about two tube diameters irrespective of the mass flow rate. The Nusselt number in the fully developed region for Darcy flow was a constant value of ~124 and in non-Darcy regime the Nusselt number scaled with Reynolds number as Nu ~ $Re^{0.53}$. In a different study, Arbak et al. [2.16] showed that 10- and 40- ppi samples ($\varepsilon$~ 0.885) in a cylinder had thermal entry length of 2.9 pipe diameters and 2.4 diameters, respectively, with water as the working fluid. Noh et al. [2.17] used water as the working fluid and investigated an annulus filled with aluminum foam ($\varepsilon$~0.90, 10 ppi) within non-Darcy regime. The Nusselt number showed decreasing trend for the entire length of the sample indicating that the flow was in developing state. Finally, the authors proposed a correlation for the Nusselt number as a function of Reynolds number, Prandtl number, and Darcy number. Hooman et al. [2.18] and Haji-Sheikh et al. [2.19] performed numerical investigations on the thermal development phenomenon in porous media. Iasiello et al. [2.20] analyzed thermally developing flows in metal foams by conducting direct pore-scale simulations on an array of Kelvin structure ($\varepsilon$~0.87). Non-conjugate simulations were performed where constant heat flux boundary condition was imposed on the fiber walls of the Kelvin cells. Kelvin structure used in this investigation is a commonly employed representative topology for the stochastic metal foams. The authors [2.20] proposed correlation for the Nusselt number in the thermally developed region as a function of Reynolds number and porosity as Nu ~ $Re^{0.454}\varepsilon^{0.1644}$. Similar computational modelling procedure was followed by Wu et al. [2.21] to determine the thermal development effects in an array of Tetrakaidecahedron (similar to Kelvin cell with slight variations in fiber curvature) cell with isothermal boundary conditions. The authors proposed correlations for the local heat transfer coefficient as $Nu_l \sim Re^{0.438}\varepsilon^{0.38}$. Suleiman and Dukhan [2.22] also used idealized cell similar to Kelvin structure ($\varepsilon$~0.949, 20 ppi) arranged in a two-dimensional array to analyze the thermal entrance region effects in the Darcy regime. Conjugate simulations with the constant heat flux boundary condition on the base wall attached to the array were performed. The authors concluded that thermally developing region extended up to ~ 30 cells in the streamwise direction from the entrance.

Several studies related to porous media exist and few significant studies assess the effects of thermally developing flows at the entrance of the test samples. In many scenarios, such as in electronic components where the space constraints strictly allow very compact-sized lattice heat exchangers, the flow might stay in the thermally developing state over the entire length of the lattice domain. The mean wall heat transfer coefficient calculated from the experiments is very useful for estimating the performance of such configurations. However, many engineering applications require active cooling over a significantly large heated surface area where the length of the lattice heat exchanger is sufficiently long for flows to become thermally developed and hence, heat transfer becomes periodic. Assessing the periodic nature of heat transfer is crucial for such configurations to quantify the relative benefits of different types of RUC topologies. In this study, the authors report findings from an experimental investigation on lattices composed of four different RUCs, namely, (a) Octet, (b) FD-Cube, (c) Tetrakaidecahedron (TKD), and (d) Cube, each having designed porosity of ~0.88 and unit cell size of ~10mm. The candidacy of these RUC topologies for thermal exchange applications to augment heat transfer has already been established by the authors in prior investigations [2.23,2.24]. The lattice samples considered in the current analysis were sandwiched between two substrate endwalls. Steady-state experiments were performed on the samples with constant heat flux boundary condition maintained on the endwalls during the test runs with air as the working fluid. The streamwise length of the samples was long enough to ensure that the periodicity in the heat transfer coefficient was achieved at some distance downstream of the entrance of the samples. The local distribution of the wall heat transfer coefficient, mean wall heat transfer coefficient, pressure gradient, Nusselt number based on different characteristic length scales, heat transfer and friction factor augmentation relative to smooth channel, and thermal-hydraulic performance of all the lattices is thoroughly discussed. Correlations for predicting the heat transfer performance of the investigated samples are also proposed.

**Geometric details of the test samples**

The four test samples were additively manufactured via *Binder jetting* in 420 Stainless Steel infiltrated with Bronze and the surface finish was achieved through the bead-

blasting process. The metal powder size for 420 Stainless Steel was ~30 microns and layer thickness resolution was ~ 100 microns. The samples were printed on M-FX-0000 binder jetting machine which had total build volume of 400 mm × 250 mm × 250 mm. After printing the samples, the parts were cured in oven and later infiltrated with Bronze at high temperature. The matrix material was composed of 60% Stainless Steel and 40% Bronze providing the final solid thermal conductivity of ~20.8 $W/mK$ (the measurement details are provided elsewhere [2.25]). The four RUCs of the manufactured lattices: (a) Octet, (b) FD-Cube, (c) TKD, and (d) Cube are presented in **Fig.2.1**. The fibers of all the topologies were cylindrical (circular cross-section) in shape.

Two distinct types of lattice structures can be obtained through the reticulation of the FD-Cube cell in three-dimensional space. The first method involves performing a translational linear pattern of the single Representative Unit Cell (RUC), where the cell is simply repeated in a uniform arrangement along specified vectors in 3D space. In the second method, one can generate the lattice by mirroring the RUC about the face of the cell, creating a reflected pattern that produces subtle variations in the overall structure. For the present investigation, the FD-Cube lattice was generated through the implementation of the former procedure, specifically by linearly patterning the unit cell in a systematic arrangement.

The final lattice section had the dimensions of 50 mm X 50 mm X 100 mm, the details of which are shown in **Fig. 2.2** along with thermocouple slot locations. Each thermocouple slot reached to the center of the heated substrate walls (3.175 mm thick). The designed unit cell size and porosity of all the samples was 10 mm and ~0.88, respectively. There were five unit cells in the spanwise and normal directions whereas ten unit cells were organized in the direction of the mean flow (streamwise). Porosity (ε) and pore density (ppi) are two fundamental parameters that are required to characterize the metal foams morphologically, however, the definition and values of both these parameters have shown significant discrepancies across the metal foam literature. Cell density is measured in cells per inch (cpi) for additively manufactured lattices due to ambiguous pore characteristics, while unit cell size remains definite for periodic lattices regardless of topology.

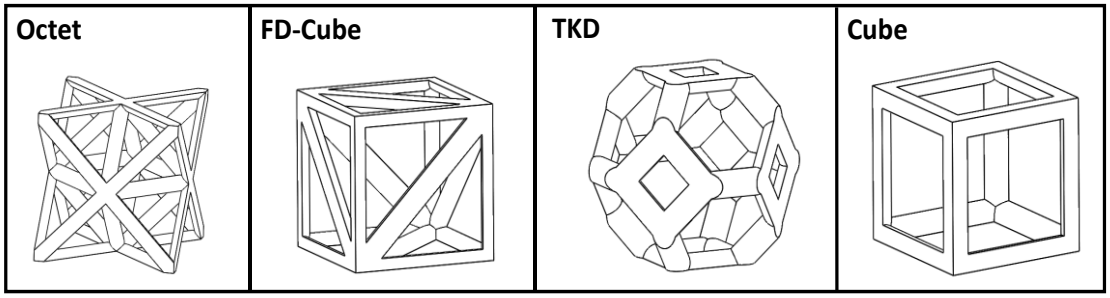



**Figure 2.1 Four representative unit cell (RUC) topologies of the investigated samples**

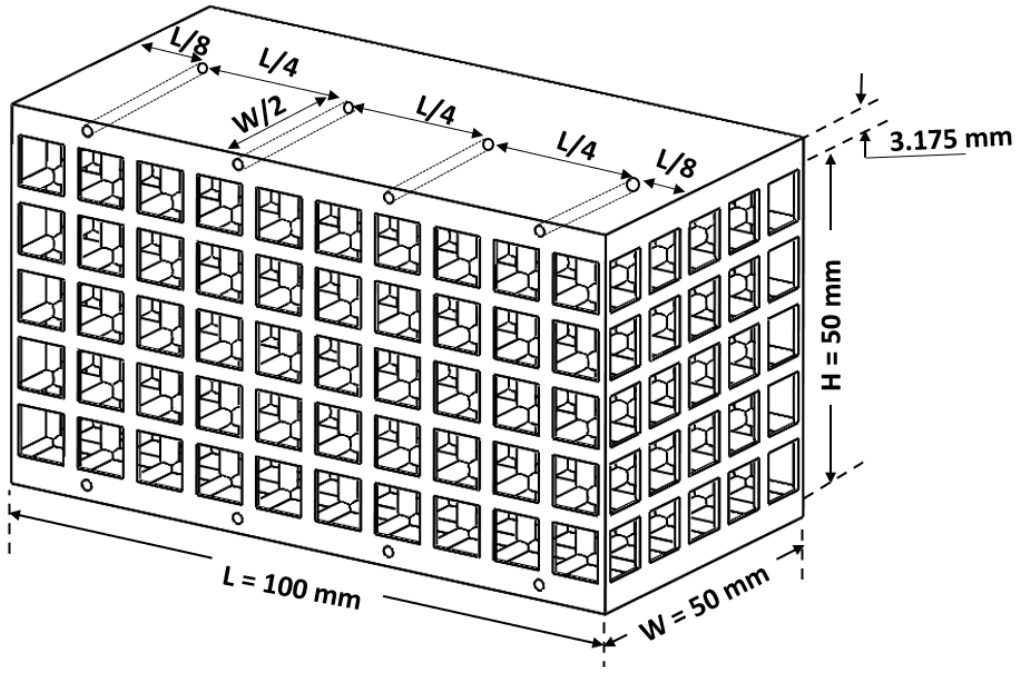



**Figure 2.2 Dimensions of the printed samples**

The lattices in the present investigation had cell density of ~ 2.5 cpi. The in-house measured bulk porosities of the manufactured samples were slightly different from the designed porosity of ~ 0.88 (**Table 2.1**). About 1.15% to 2.32% deviation was observed in the porosities of the fabricated samples relative to the intended CAD design porosity. The values of designed fiber diameters correspond to ach RUC are also shown in **Table 2.1**. Additive manufacturing processes inherently produce surface roughness on lattice structures, with these roughness profiles exhibiting spatial variations that depend on multiple factors: the orientation of the sample relative to the build direction, the specific process parameters employed during fabrication, and any post-manufacturing surface treatments applied to the final product. This inherent surface roughness typically leads to enhanced heat transfer characteristics and increased pressure drop across the lattice structure. The significance of surface roughness in determining the relative performance ranking of different lattice topologies becomes particularly crucial when the length scales of the surface roughness features are comparable to the fundamental morphological dimensions of the lattices themselves. This relationship between roughness and structural dimensions plays a critical role in the overall thermal-hydraulic behavior of the system. In the present investigation, the lattice structures were characterized by unit cell sizes of approximately 10 millimeters, with fiber diameters equal to or exceeding 1 millimeter. Due to the inherent surface roughness present in the manufactured lattices, the experimentally measured values of both heat transfer coefficients and pressure drops across these structures may exhibit marginally higher magnitudes compared to what would be theoretically expected in idealized configurations featuring geometrically perfect, smooth surfaces.

**Table 2.1 Measured porosity and designed fiber diameter of the RUC**

| RUC topology | Measured bulk porosity | % Deviation from the designed porosity | Designed fiber diameter |
|---|---|---|---|
| **Octet** | 0.86 | 2.32 | 1.00 mm |
| **FD-Cube** | 0.86 | 2.32 | 1.54 mm |
| **TKD** | 0.87 | 1.15 | 1.43 mm |
| **Cube** | 0.87 | 1.15 | 2.37 mm |

However, given the relative scale of the surface roughness features compared to the primary lattice dimensions, it can be reasonably concluded that the observed relative trends and comparative rankings of the investigated lattice structures remain valid and independent of these surface roughness effects. The consistency of these findings was further validated through multiple experimental trials.

## Experimental setup

**Figure 2.3** shows the components of the experimental facility used in the present study. Air was the working fluid in this investigation and was drawn from a compressed air tank maintained at ~ 1MPa. A pressure regulator was placed downstream of the compressor to adjust the mass flow rate to a desired value. The air was directed to an ASME orifice plate for flow metering. Differential pressure across the orifice meter, static air pressure upstream of the orifice plate and air temperature were measured using Dwyer 477AV-2
(0-10 kPa) [accuracy: $\pm 0.5\%$ Full Scale (F.S.)], Dwyer DPG-002 (0-100 kPa) [accuracy: $\pm 0.25\%$ F.S.] and fast response T-type thermocouple [accuracy: $\pm 0.5℃$], respectively, which were then fed into an in-house MATLAB code to determine the mass flow rate. The metered flow was then passed through a control valve regulating the flow into the test section. The transition of the flow from circular pipe to square duct was executed with the help of a diffuser.

**Figure 2.4** shows the schematic of the sample and test section assembly. The test section was made from plexiglass and had a square cross-section of 50.8 mm x 50.8 mm, resulting in hydraulic diameter ($d_h = 4A_c/P$) of 50.8 mm. The test section was ~16 $d_h$ long and the samples were placed ~10 $d_h$ downstream the test-section inlet. The entry length was long enough to ensure that the flow reaching the test sample was hydrodynamically fully developed. After passing through the lattice sample, which was 100 mm (nearly 2 $d_h$) in streamwise direction, the air travelled through ~ 4 $d_h$ test section exit length before it was vented out to the ambient. The static pressure was measured using pressure tap flushed against the inner plexiglass surface and positioned upstream of the lattice sample. The pressure drop measurements were conducted for a wide range of mass flow rates.

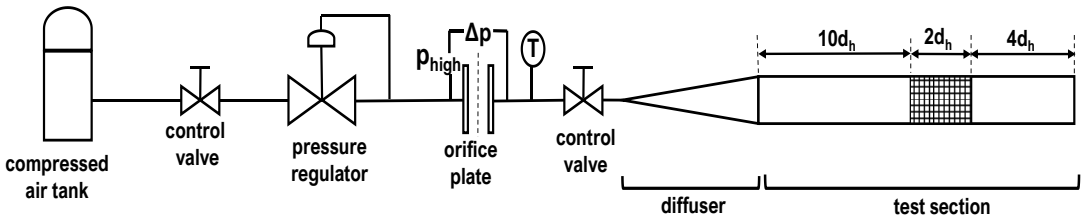



**Figure 2.3 Schematic of the experimental setup (not drawn to scale)**

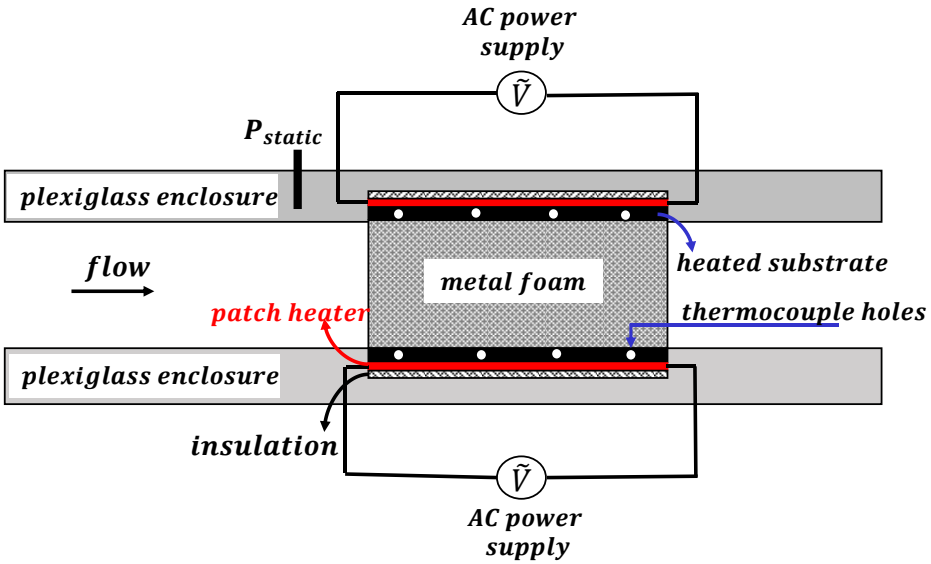



**Figure 2.4 Schematic of the lattice sample and test-section assembly (not drawn to scale)**

Therefore, the pressure values at smaller flow rates were measured through sensitive manometer Dwyer 477AV-000 (0 – 0.2 kPa) [accuracy: $\pm 0.5\%$ Full Scale (F.S.)] and higher-pressure drops were recorded using Dwyer 477AV-00 (0 – 1 kPa) [accuracy: $\pm 0.5\%$ Full Scale (F.S.)]. The pressure measurements were obtained directly from a digital display readout of the pressure transducer, eliminating parallax error and other human observation bias that typically occur with analog instruments.

Patch heaters were glued to the top and bottom substrates of the sample and were connected to variable transformer (range of 0-130 V) to adjust the power output by varying the voltage. The backside of the heaters was covered by insulation to minimize the heat losses. The wall temperature measurements were conducted by T-type thermocouples at four slots provided on each substrate walls, whereas thin thermocouples were placed on the inner and outer surface of the insulation cover to evaluate the conduction heat losses through insulation. The mainstream inlet temperature was also measured by thin thermocouples placed into the flow path upstream of the lattices. The lattice, heater and insulation ensemble were carefully fitted into a socket type slot of the test section while conducting experiments.

## Experimental method and data reduction

This section provides details of the steady-state experimental procedure and heat transfer coefficient calculation methodology.

### *Forced convection experimental procedure*

The voltage of the variable transformers connected to the heaters was preset and the mass flow rates through the test section was adjusted to a known value. The current investigation covered the air mass flow rate range of about ~ 4.8 g/s to 21 g/s and the corresponding Reynolds number based on the channel hydraulic diameter was between 5,000 < $Re_{d_h}$ < 22, 500. The mean flow velocity corresponding to this investigated Reynolds number range varied between 1.54 m/s and 6.95 m/s. The mass flow rate was constantly monitored to ensure that it remained uniform during the test runs. Each unique run was allowed sufficient time to reach the steady-state. Once the steady-state condition was achieved, the temperatures and the corresponding voltage readings were recorded.

The total heat output from the heaters was calculated using the applied voltage and the known heater resistance as following:

**Equation 2-1**

$$Q_t = \frac{V^2}{R_{htr}}$$

Local heat transfer coefficient was defined as:

**Equation 2-2**

$$h_l = \frac{Q_{net}}{A_w(T_{w,l} - T_{b,l})}$$

where, $Q_{net} = (Q_t - Q_{loss})$ was the net heat input from a substrate wall, $A_w$ was the substrate wall area, $T_{w,l}$ and $T_{b,l}$ were the local wall temperature and bulk fluid temperature, respectively. The local bulk fluid temperature ($T_{b,l}$) was calculated using the energy balance method and two methods were adopted in the present study to evaluate the $Q_{loss}$, which are explained in detail the following subsection. After recording the steady-state data for a particular case, the mass flow rate was adjusted to achieve the next desired Reynolds number.

***Heat loss measurements***

Two methodologies were adopted in the current investigation to calibrate the system for heat losses. The first method includes the measurements from the 'no-flow' experiments, and the second method involves only the conduction losses through insulation during the forced convection runs. These two procedures are described below.

*No-flow experiments:* Steady-state experiments were performed without flow at two different specified heat inputs ($Q_{nf}$) for each lattice sample and the corresponding wall temperatures were recorded. The power output of each heater was calculated from the known heater resistance and voltage measured through multimeter as following:

**Equation 2-3**

$$Q_{nf} = \frac{V_{nf}^2}{R_{htr}}$$

Under no flow conditions, a nearly constant wall temperature was achieved over the substrate. Finally, the heat flux ($Q_{nf}/A_w$) was obtained as a quadratic function of ($T_w - T_{in}$) where $T_w$ was the mean wall temperature defined as:

**Equation 2-4**

$$T_w = \frac{1}{n}\sum_{i=1}^{n} T_{w,i}$$

and $T_{in}$ was the temperature upstream of the lattices recorded during each no flow run. The relationship between applied heat and the difference of wall and local fluid temperature characterizes the overall system loss which may include the lattice material effects on buoyancy-driven convection and the conduction losses through the insulation at the backside of the heaters. The experimental heat transfer measurements were conducted under two distinct thermal boundary conditions: one with both channel walls actively heated and another with only the bottom wall subjected to heating. Throughout the flow experiments, the calculated thermal losses from these configurations were found to range from approximately 5% to 18% of the total heat input supplied to the system..

*With-flow experiments*: The losses from the system when the air was forced through the test samples were taken as the one conducted through the insulation and evaluated using the Fourier's law:

**Equation 2-5**

$$Q_{wf} = kA_{ins}\frac{(\Delta T)_{ins}}{t_{ins}}$$

where, $k$, $A_{ins}$, $(\Delta T)_{ins}$ and $t_{ins}$ were the thermal conductivity, area normal to the heat flow direction, temperature difference across the insulation and thickness of the insulation, respectively. These losses were 1% to 3.3% of the total heat supplied during the flow experiments.

***Data reduction for heat transfer coefficient***

In accordance with the heat loss measurement procedures outlined above, this study employs two distinct methodological approaches to quantify and report the experimental heat transfer coefficient values across the tested configurations.

*Total heat transfer coefficient (h)*: The local total heat transfer coefficient was defined as:

**Equation 2-6**

$$h_t = \frac{Q_t - Q_{wf}}{A_w(T_{w,l} - T_{b,l})}$$

where, the heat losses subtracted from the total heater power output corresponded to the conduction losses estimated using Eq. 2.5. This heat transfer coefficient included the effects of the flow conditions, lattice topology, working fluid, and buoyancy-induced convection, thereby it represented the true overall conjugate benefits of the lattice samples.

The obtained temperature data at the four thermocouple slots in each substrate wall was plotted against the axial position of holes to obtain the polynomial curve fit. This curve fit as a function of streamwise length was used to obtain the local wall temperature values. The wall temperature curve fit equation was used to find local wall temperatures corresponding to a unit cell in streamwise direction by using its distance from the lattice inlet as a parameter. Local bulk fluid temperature as a function of the axial location was obtained using the following energy balance method:

**Equation 2-7**

$$T_{b,x} = T_{in} + \frac{Q"_{net} W}{\dot{m} c_p} x$$

where $Q"_{net}$ was the net heat flux into the system, $W$ was the spanwise width of the sample and $x$ denoted the axial distance from the lattice entrance.

*Forced heat transfer coefficient* ($\tilde{h}$)*:* Local *'forced'* heat transfer coefficient was defined as following:

**Equation 2-8**

$$h_f = \frac{Q_t - Q_{nf}}{A_w(T_{w,l} - T_{b,l})}$$

where the '*no-flow'* losses have been subtracted from the total heater output. The *'forced'* heat transfer defined here did not include the effects of buoyancy-driven convection and the conduction losses through any possible venues of the test section.

The measurement uncertainty analysis was carried out through sequential perturbation method [2.26]. The typical uncertainty range for Nusselt number was between 2-5% and that for the Reynolds number was within 4%.

## Results and discussion

This section reports the results of validation test runs, local heat transfer coefficient trends, mean Nusselt number, flow losses, thermal-hydraulic performance and pumping power requirements of the investigated lattice topologies. These results provide a comprehensive understanding of the heat transfer and fluid flow characteristics of each lattice structure.

### *Benchmarking heat transfer data*

Validation in the current study was conducted by evaluating the Nusselt number distribution of smooth plate. Since the roughness profiles on the additively manufactured surfaces makes the comparison with the standard correlations challenging, the set-up was validated by performing the test runs on the smooth machined aluminum plate for a wide range of Reynolds numbers. **Figure 2.5** shows the streamwise distribution of the local Nusselt number enhancement ($Nu_{d_h}/Nu_0$) of the smooth plate with respect to the well-known Dittus-Boelter correlation. The streamwise length of the plate was ~ 10 $d_h$ which was sufficient for the flow to become thermally fully developed where the ratio $Nu_{d_h}/Nu_0$~ 1 was achieved for all the investigated Reynolds numbers. The data beyond ~ 0.7 was influenced by the exit effects and therefore is not represented here. The velocity profile near the exit region showed significant deviation from the fully developed flow conditions, introducing uncertainties in the measurements. The Nusselt number ($h_f d_h/k_f$) presented in **Figure 2.5** was calculated using Eq. 2.8 where the 'no-flow' effects were separated out from the total heater output. The experimental data demonstrated strong concordance with the well-established Dittus-Boelter correlation, providing substantial validation for the accuracy and reliability of the results presented in subsequent sections. The experimental apparatus and methodology were carefully designed and implemented with error minimization in mind incorporating multiple rounds of validation testing and calibration procedures to ensure maximum accuracy.

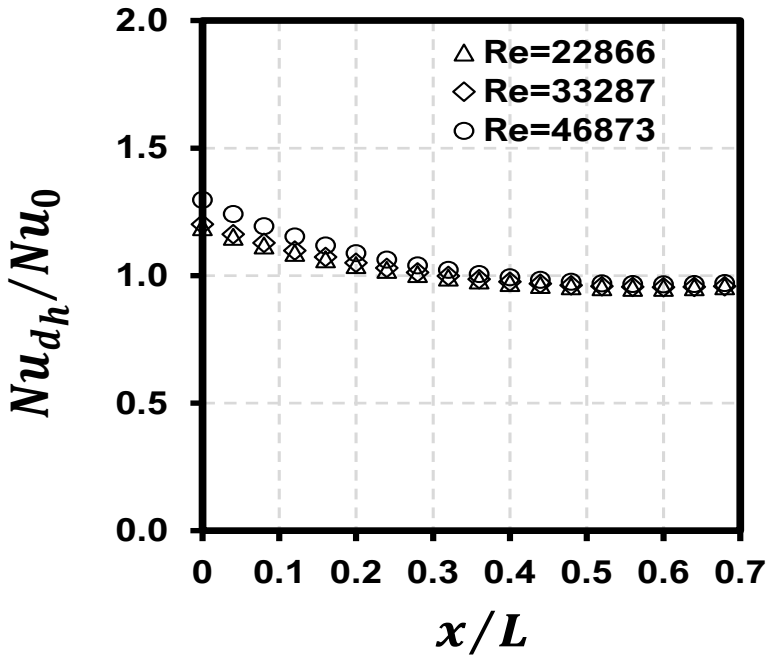



**Figure 2.5 Streamwise distribution of Nusselt number in the smooth channel**

**Figure 2.6** presents the local total transfer coefficient (Equation 2.6) for both-walls heated and only bottom-wall heated scenarios. The local heat transfer coefficient trends of top and bottom walls were close to each other, which indicated proper setup of heaters and flow uniformity through the lattice. Local heat transfer coefficient showed decreasing trend initially and finally converging to a near-constant value indicating that the periodic heat transfer behavior was achieved. Such zones are highlighted in each plot with dashed outline. When both walls were heated, the heat transfer for Octet and Cube became periodic at $x/L \geq 0.6$, whereas for FD-Cube and TKD this phenomenon was observed at the axial distance of $x/L \geq 0.5$. These conclusions were somewhat different for Octet and TKD in single wall heating conditions, where the heat transfer became fully periodic at $x/L \geq 0.7$ and $x/L \geq 0.6$, respectively. Since the total streamwise length ($L$) was 100 mm and unit cell size corresponded to 10 mm, the axial distance of $x/L = 0.5$ corresponded to the exit of the 5$^{th}$ row of cells from the entrance. It can be concluded that a minimum of 5 to 6 rows in the streamwise direction were required for the establishment of periodic heat transfer behavior in all the tested configurations. This observation suggests that a sufficient number of rows are necessary to allow for the development of consistent and repeating thermal patterns within the lattice structures.

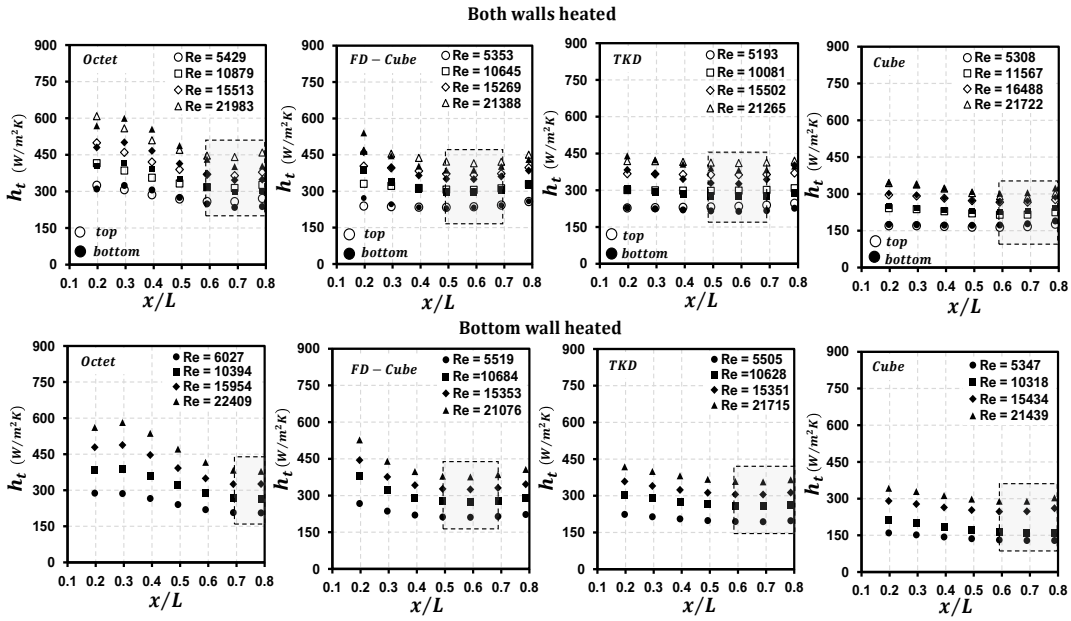



**Figure 2.6 Streamwise distribution of Nusselt number in the smooth channel**

Furthermore, it was observed that the heat transfer coefficient values of the Octet, FD-Cube, and TKD lattices tended to converge towards very similar values in the thermally developed zones, indicating that these different lattice types exhibit comparable heat transfer performance once the flow and temperature fields become fully established.

**Figure 2.7** shows the forced heat transfer coefficient (Eq.2.2) for both-walls heated and only bottom-wall heated scenarios, illustrating the thermal performance under different boundary conditions. The plots in **Figure 2.7** are qualitatively same as that presented in **Fig. 2.6** and demonstrate deviation only in the magnitude, which can be attributed to the different methodologies used in calculating the heat transfer coefficients. The relative difference in the magnitudes of the heat transfer coefficients in the fully developed zones (the areas of interest in the current investigation) in **Figure 2.6** and **Figure 2.7** is discussed in detail in the next subsection, where the implications of these variations on overall thermal performance are analyzed. Octet demonstrated slightly increasing trend for Nusselt number in thermally developing zones at the highest Reynolds number, indicating enhanced heat transfer characteristics in these regions due to complex flow interactions. This phenomenon was also observed numerically by Iasiello et al. [2.20] for interfacial heat transfer coefficient variation of Tetrakaidecahedron lattice where the authors refer to this zone as the impingement zone, highlighting the importance of local flow structures in heat transfer enhancement. Their numerical investigations provided valuable insights into the mechanisms driving this behavior, particularly in the entrance regions of the lattice structure. Kaur and Singh [2.24] analyzed the conjugate thermal performance of four Octet cells in a single cell thick configuration and reported the cell-based variation of conjugate heat transfer coefficient and found monotonically decreasing trend for laminar flow, which aligns with the theoretical predictions for developing flow in periodic structures. Their comprehensive analysis revealed the intricate relationships between cell geometry, flow characteristics, and thermal performance, providing crucial insights for optimizing lattice designs for specific applications. These findings collectively demonstrate the complex nature of heat transfer mechanisms in lattice structures and their dependence on various geometric and flow parameters.

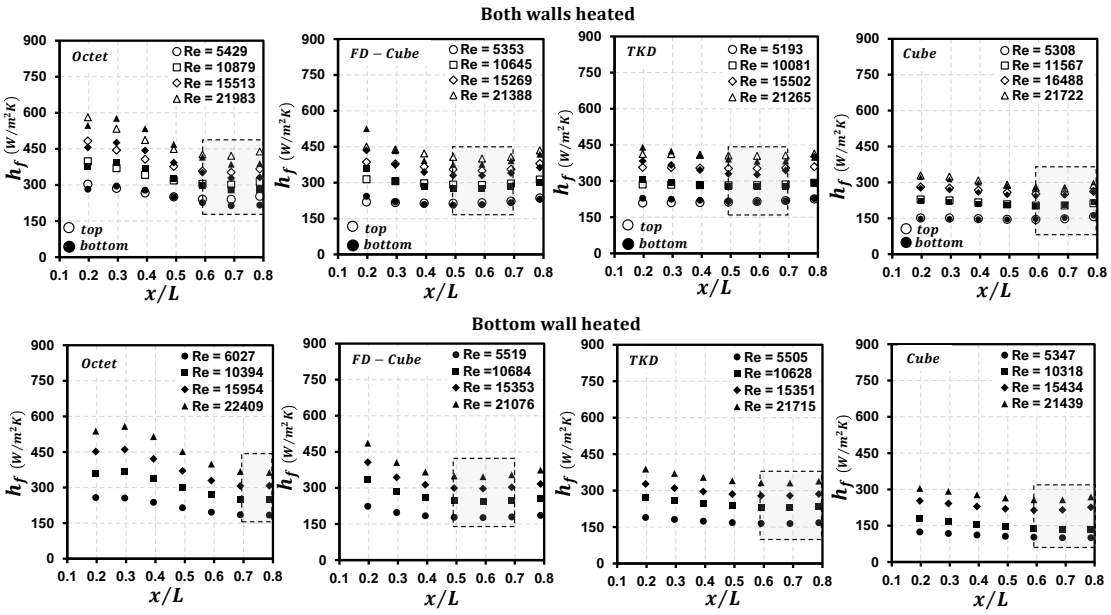



**Figure 2.7 Mean total and forced heat transfer coefficient under both wall and only bottom wall heated conditions**

In the current investigation, the increasing or decreasing trend of the Octet lattice at the instance of the highest Reynolds number is not highly consequential as the proposed correlations in the following section are based on the fully developed zones downstream.

***Mean heat transfer characteristics***

*Mean heat transfer coefficient*: The total and forced convective heat transfer coefficient values were systematically evaluated under two distinct thermal boundary conditions: both-walls heated and only bottom-wall heated configurations, with the comprehensive results presented in **Fig. 2.8**. The heat transfer coefficient values reported in this analysis represent carefully calculated averages obtained from the periodic heat transfer zones, which are clearly delineated within the dashed enclosures shown in **Figure 2.6** and **Figure 2.7**. These zones were specifically selected to capture the fully developed heat transfer behavior, ensuring that entrance and exit effects did not influence the reported results. As discussed above, the values of Octet, FD-Cube, and TKD converged to a similar value and therefore demonstrated same levels of mean heat transfer coefficient under all the heating conditions for the investigated range of Reynolds number. The total heat transfer for both-wall heating condition was in the range of ~ 216 $W/m^2K$ to 415 $W/m^2K$ for Octet, FD-Cube, and TKD, whereas for only-bottom-wall heating the heat transfer coefficient values were between ~ 188 $W/m^2K$ to 367 $W/m^2K$. The mean total heat transfer coefficient for both-wall heated condition was about ~4.4% - 8.8%, 3.3% - 11%, and 9.1% - 17.4% higher than the forced heat transfer coefficient of Octet, FD-Cube, and TKD, respectively. For bottom-wall heating condition, the total heat transfer coefficient was 4.4% - 12.3%, 8.9% - 20%, and 8.2%- 19% higher than the forced heat transfer coefficient for Octet, FD-Cube, and TKD, respectively. Cube was the simplest topology and demonstrated the weakest performance amongst the investigated RUC topologies. The addition of fiber complexity to the RUC architecture clearly did not provide any benefits from the thermal performance perspective if the periodicity of the heat transfer in the lattices was considered. The heat transfer characteristics in the periodic region became almost independent of the topology for relatively complex RUCs (Octet, FD-Cube, and TKD). This observation suggests that beyond a certain threshold of geometric complexity further structural modifications may not yield improvements.

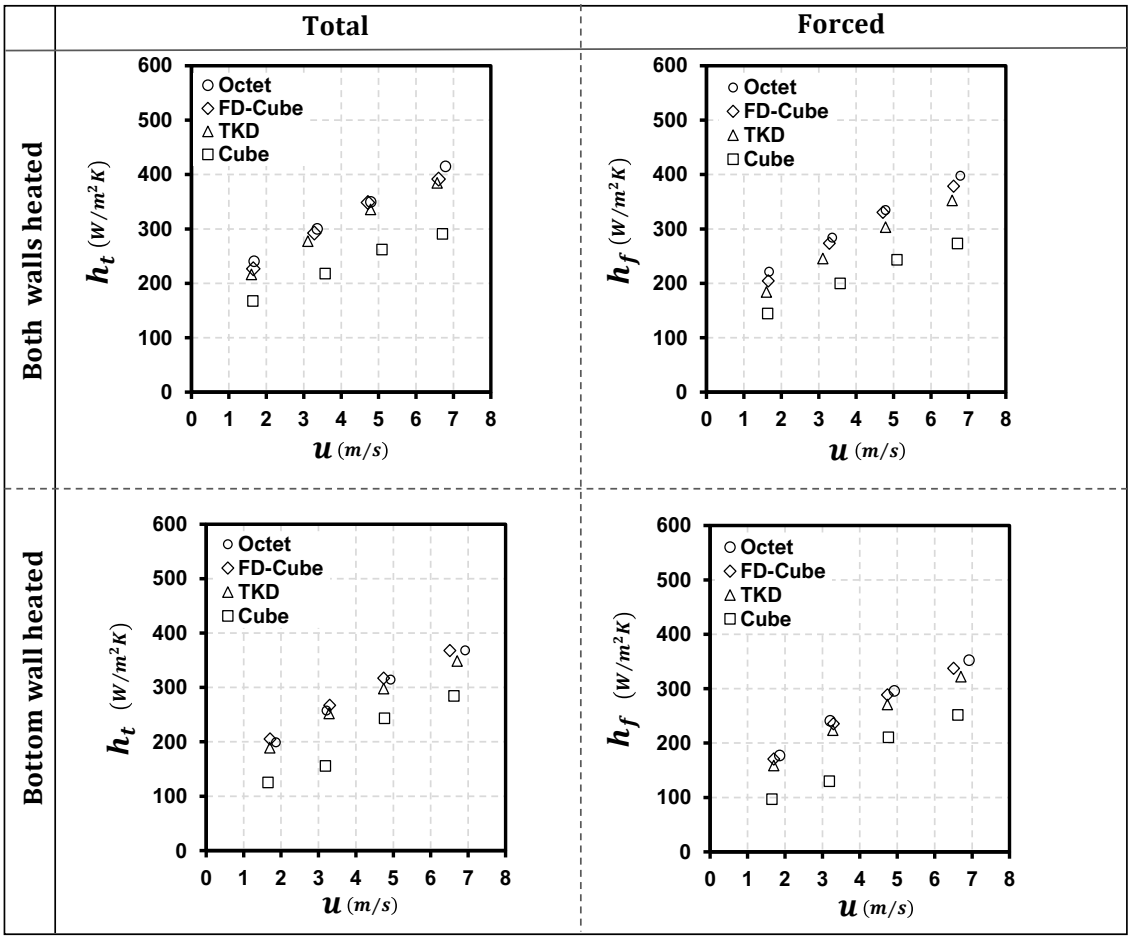



**Figure 2.8 Mean total and forced heat transfer coefficient under both wall and only bottom wall heated conditions**

Several factors such as interfacial heat transfer coefficient, surface area to volume ratio and lattice-endwall connection can dictate the overall thermal performance of the lattices in conjugate thermal exchange. Cube was the simplest investigated topology in the current investigation and demonstrated significantly lower specific surface area as compared to other topologies. This significantly undermined the overall thermal performance of the Cube topology. Octet exhibited the highest specific surface area but could not outperform the FD-Cube and TKD lattices. Each topology rendered different near-wall phenomenon as the fibers connected to the endwall in each lattice interrupted the development of flow and thermal boundary layer uniquely. Since the configurations are reticulated in three-dimensional space, the thermal transport phenomenon occurring in the core volume of the lattice blocks was significantly important. Also, it should be noted that the effective thermal conductivity of these lattices for the investigated porosity value of ~ 0.86-0.87 was independent of the unit cell topology as established by Wang et al. [2.25].

*Nusselt number based on channel hydraulic diameter:* The heat transfer coefficient (**Figure 2.8**) is presented in non-dimensional form of Nusselt number as a function of Reynolds number in **Figure 2.9**. The characteristic length chosen in these plots is the channel hydraulic diameter, therefore the definitions of total and forced Nusselt number were  and , respectively. The Reynolds number was defined as . The heat transfer behavior showed strong dependence on flow characteristics, with the relationship between Nusselt and Reynolds numbers following established scaling laws. Since the Nusselt number trends for Octet, FD-Cube, and TKD were similar to each other, a single trendline could be extracted to predict the performance of the lattices. The Nusselt number is typically presented as a power law function of Reynolds number $Nu = cRe^m$ **Tables 2.2-2.3**. Although the porosities of the investigated samples were different, the variation was small due to which the assumption that the Nusselt number depended only on the Reynolds number for the air as the working fluid in this investigation is justified. The similarity in heat transfer performance across different lattice geometries suggests underlying physical mechanisms that govern the thermal transport in these structures. These findings have important implications for thermal management applications.

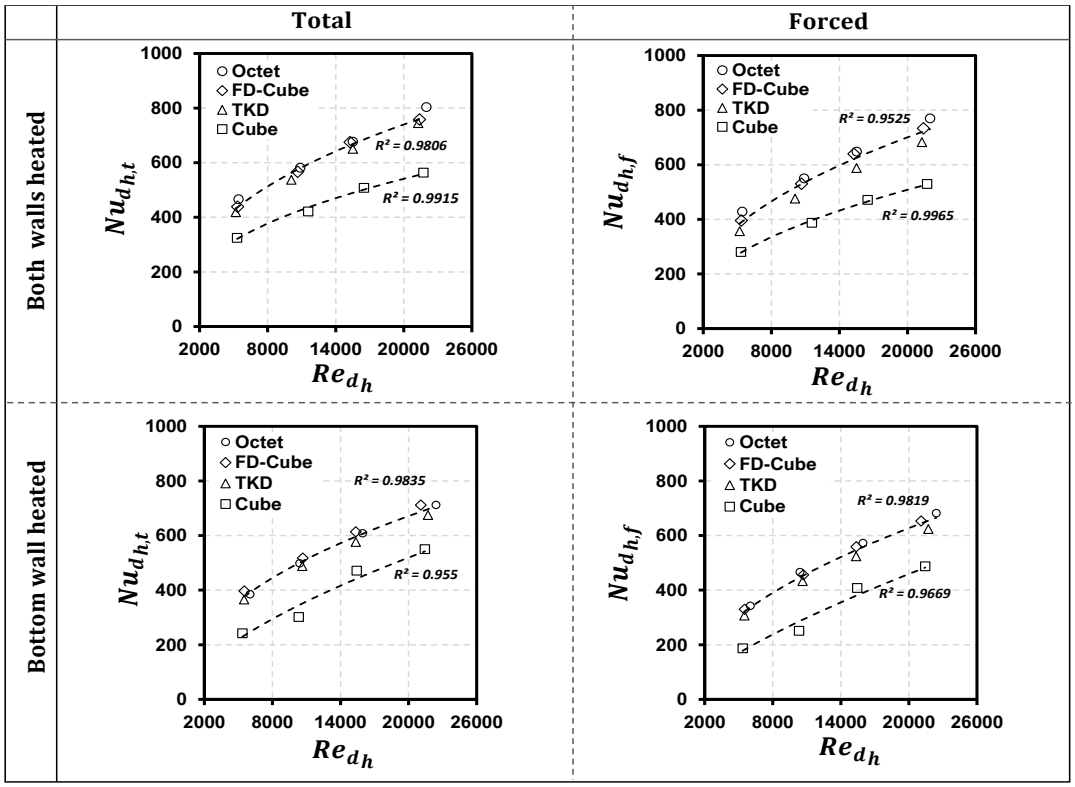



**Figure 2.9 Nusselt number as a function of Reynolds number based on channel hydraulic diameter**

**Table 2.2 Correlation $cRe_{d_h}^{m}$ for Octet, FD-Cube, and TKD under different heating conditions**

| | Total | Forced |
|---|---|---|
| **Both walls heated** | $14.14\ Re_{d_h}^{0.40}$ | $8.50\ Re_{d_h}^{0.45}$ |
| **Bottom wall heated** | $7.86\ Re_{d_h}^{0.45}$ | $3.70\ Re_{d_h}^{0.52}$ |

**Table 2.3 Correlation $cRe_{d_h}^{m}$ for Cube under different heating conditions**

| | Total | Forced |
|---|---|---|
| **Both walls heated** | $10.94\ Re_{d_h}^{0.39}$ | $5.59\ Re_{d_h}^{0.46}$ |
| **Bottom wall heated** | $1.12\ Re_{d_h}^{0.62}$ | $0.37 Re_{d_h}^{0.72}$ |

*Nusselt number based on pore diameter and fiber diameter:* Various characteristic length scales have been used by researchers in the past to define Nusselt number. While channel hydraulic diameter ($d_h$) is a macroscopic dimension of the channel, pore diameters and fiber diameters are better representative of the pore-level dimensional scales. These microscopic length scales provide more accurate insights into the local heat transfer phenomena occurring within the lattice structure. Hwang et al. [2.27] defined the pore Reynolds number as ($\rho u d_p/\varepsilon\mu$) and pore Nusselt number corresponding to volumetric heat transfer coefficient as ($h_v d_p^2/k_f$). Iasiello et al. [2.28] also adopted the same definitions as provided in [2.27] to present the pore-scale heat transfer parameters. Fiber diameter is not a very common characteristic length scale for defining Reynolds number and Nusselt number as compared to pore diameter. Calmidi and Mahajan [2.14] reported interfacial Nusselt number of high porosity metal foams based on fiber diameter ($Nu_{sf} = h_{sf} d_f/k_f$) as a function of Reynolds number ($Re_{d_f} = \rho u d_f/\varepsilon\mu$) and Prandtl number. This relationship framework was based upon the correlations for cylinders in crossflow configuration with an assumption that flow over metal fibers is similar to that of cylinders. The definition of pore diameter and the values of fiber diameter are not very consistent in the literature pertaining to open-cell metal foams. For periodic lattices like the ones investigated in the current study, defining the pore can be challenging as the voids of each topology can have multiple characteristic dimensions depending on the chosen reference direction and cross-section. A more systematic approach to defining these characteristics becomes necessary to enable meaningful comparisons across different lattice structures. For periodic lattices like the ones investigated in the current study, defining the pore can be challenging as the voids of each RUC is unique in shape and can exhibit complex geometrical features that vary significantly between different lattice topologies. Ketan et al. [2.29] performed numerical investigation on triply periodic minimal surfaces (TPMS) which are sheet-based category of structures involving channels of different shapes for the fluid flow. The authors defined the pore diameter as the maximum diameter of the sphere that could pass through the smallest channel in the heat sinks, providing a standardized method for characterizing these complex geometries.

Similar methodology was adopted by Kaur and Singh [2.30] to define pore diameters for TPMS and TKD structure, demonstrating the applicability of this approach across various lattice configurations. The pore diameters in this study were also defined as in [2.29,2.30], and the spheres corresponding to which the diameters were calculated are highlighted in **Fig. 2.10**.

TKD topology consisted of six smaller squares and eight larger hexagonal openings. Although, one can choose the smaller dimensional scale as the pore diameter, the value considered in the present investigation was the weighted average of both types of openings. Initial computational analysis suggested this weighted average approach better represented the effective flow characteristics through the structure. The values of pore diameters for different RUC topologies are provided in **Table 2.4** The pore Nusselt number ($Nu_{d_p} = hd_p/k_f$) of the four investigated samples is presented in **Fig. 2.11** as a function of pore Reynolds number ($Re_{d_p} = \rho u d_p/\varepsilon\mu$). The porosity value used in the Reynolds number definition was the actual measured bulk porosity of each lattice sample. This approach of using measured bulk porosity rather than theoretical values provided more accurate representation of the actual flow conditions in the manufactured samples. With the above definitions of pore-diameter, Nusselt number showed a very coherent data set for all the four lattices. The coherence in the data suggests that the chosen characteristic length scales effectively captured the underlying heat transfer mechanisms across different lattice geometries.

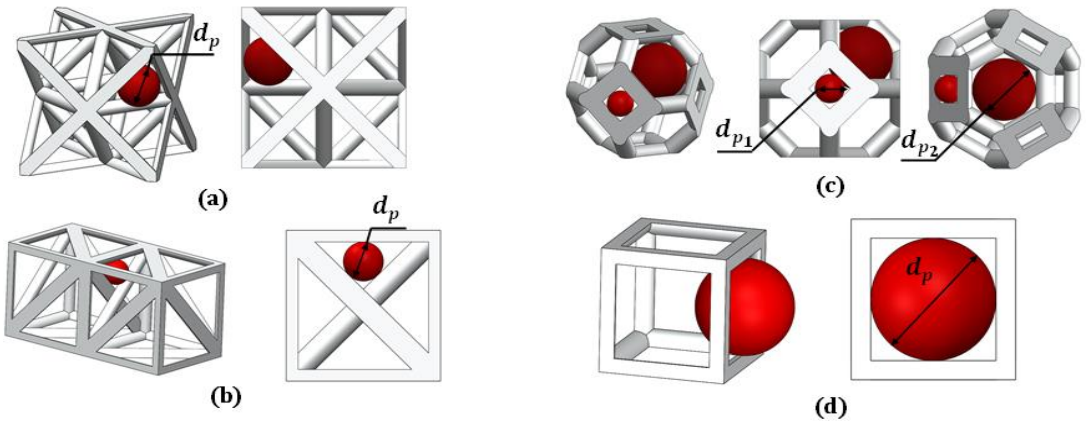



**Figure 2.10 Pore diameters ($d_p$) corresponding to the largest sphere that could pass through the voids of (a) Octet, (b FD-Cube, (c) Tetrakaidecahedron, and (d) Cube.**

**Table 2.4 Pore diameter of different RUC topologies**

| RUC Topology | Pore diameter |
|---|---|
| **Octet** | 3.082 mm |
| **DF-Cube** | 2.603 mm |
| **TKD** | $\frac{(6d_1+8d_2)}{14} = 3.608$ mm |
| **Cube** | 7.63 mm |

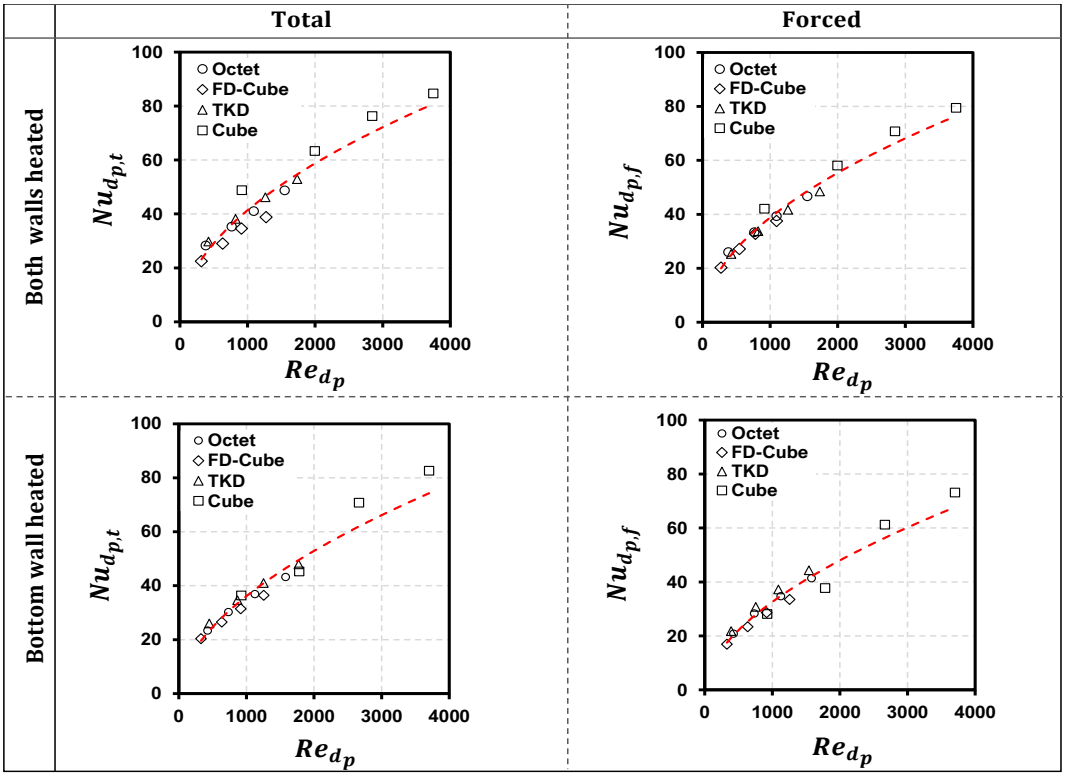



**Figure 2.11 Pore diameter based Nusselt number as a function of Reynolds number**

The methodology for defining pore diameters in periodic lattices serves as a robust and standardized tool for predicting heat transfer performance across different topologies. By utilizing fiber diameter as the characteristic length scale, this approach simplifies the calculation of Nusselt numbers while ensuring consistency. This is particularly valuable in scenarios where unit cell size and porosity remain fixed, as it facilitates direct comparison between varying lattice designs. The use of fiber diameter in defining the Nusselt number ($Nu_{d_f}$) as a function of the Reynolds number ($Re_{d_f}$), presented in **Fig. 2.12**, showcases its effectiveness in analyzing heat transfer characteristics.

The fiber diameter values employed for these calculations were derived from the CAD models of the representative unit cells (RUCs), as provided in **Table 2.1**. This systematic approach not only guarantees accuracy but also minimizes variability in the overall dataset. By adopting fiber diameter as the characteristic length scale, it becomes possible to establish a uniform basis for calculating both the Nusselt and Reynolds numbers, thereby reducing complexity. The results demonstrated that this methodology produces a narrow spread in the data, further emphasizing its reliability. Additionally, a unique trendline was derived to predict the heat transfer performance of the investigated topologies. This trendline correlates $Nu_{d_f}$ with $Re_{d_f}$ through a power-law relationship of the form $Nu_{d_f} = cRe_{d_f}^{m}$. The constants c and m were determined from the experimental data and are provided in **Tables 2.5** and **2.6** for different heating conditions and topologies. These coefficients form the foundation of predictive models that can estimate the Nusselt number with a high degree of accuracy.

A comparison of the predicted values using these correlations with the corresponding experimental data (as depicted in **Fig. 2.13**) revealed a deviation of less than ±15%. This narrow-spread underscores the robustness of the predictive models and their applicability across a variety of conditions. Furthermore, the consistency in the predicted results highlights the importance of employing a well-defined characteristic length scale, such as the fiber diameter, in thermal performance evaluations. **Table 2.7** Summarizes the coefficients (c and m) of correlations ($Nu_{d_f} = cRe_{d_f}^{m}$) for different heating conditions and characteristics length scales, based on the information provided in **table 2.5** and **2.6.**

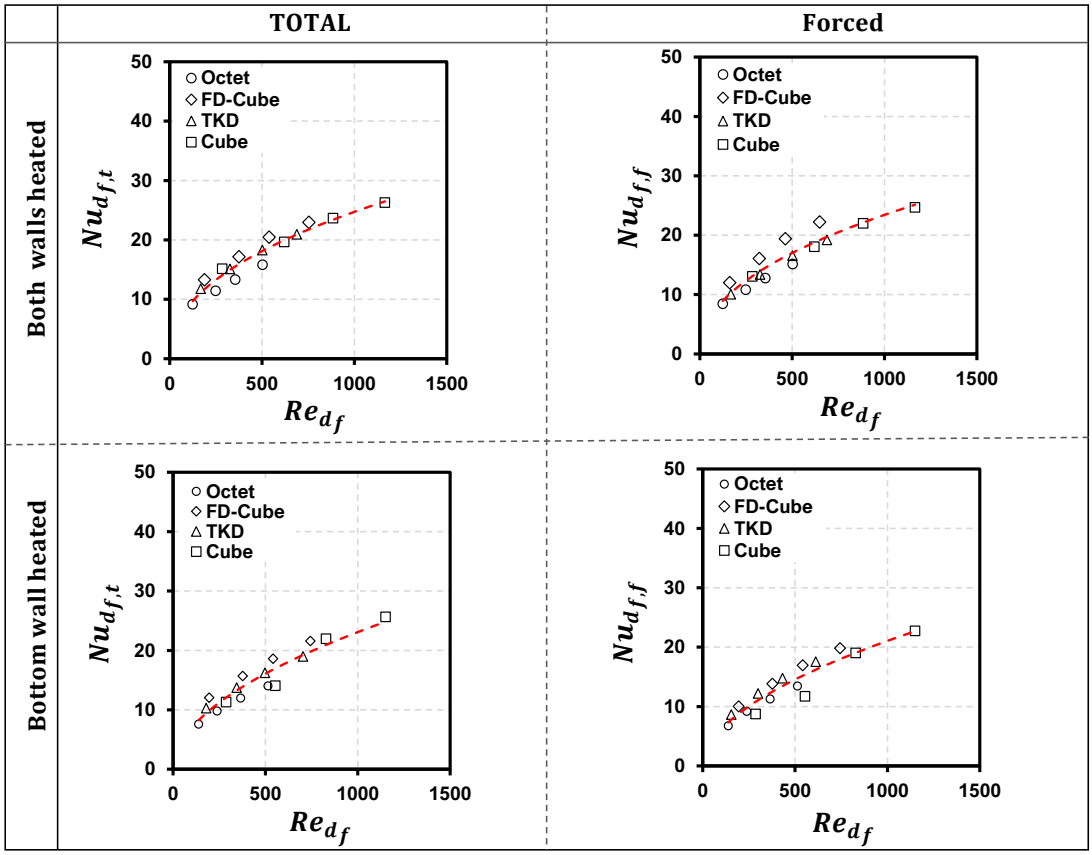



**Figure 2.12 Fiber diameter based Nusselt number as a function of Reynolds number**

**Table 2.5 Correlation $cRe_{d_p}^{m}$ for all investigated topologies under different heating conditions**

| | Total | Forced |
|---|---|---|
| **Both walls heated** | $1.25\ Re_{d_p}^{0.51}$ | $1.12\ Re_{d_p}^{0.51}$ |
| **Bottom wall heated** | $0.8\ Re_{d_p}^{0.55}$ | $0.69\ Re_{d_p}^{0.56}$ |

**Table 2.6 Correlation $cRe_{d_f}^{m}$ for all investigated topologies under different heating conditions**

| | Total | Forced |
|---|---|---|
| **Both walls heated** | $1.11\ Re_{d_f}^{0.45}$ | $0.97\ Re_{d_f}^{0.46}$ |
| **Bottom wall heated** | $0.63\ Re_{d_f}^{0.52}$ | $0.53\ Re_{d_f}^{0.53}$ |

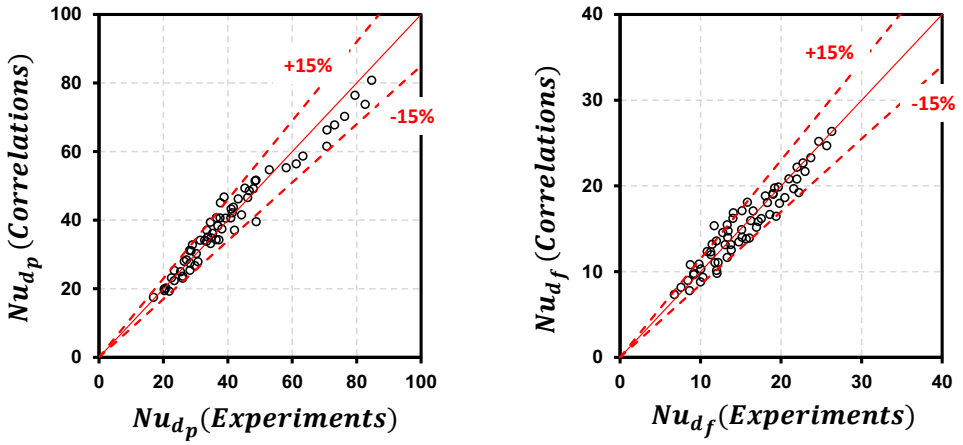



**Figure 2.13 Comparison of values predicted from correlations with the values obtained from experiments**

**Table 2.7 Values of coefficients in correlation $Nu = cRe^{m}$ for different characteristic length scales**

| Heating conditions | Characteristics length = $d_p$ | | | | Characteristics length = $d_f$ | | | |
|---|---|---|---|---|---|---|---|---|
| | Conjugate | | Non-Conjugate | | Conjugate | | Non-Conjugate | |
| | c | m | c | m | c | m | c | m |
| **Both walls heated** | 1.25 | 0.51 | 1.12 | 0.51 | 1.11 | 0.45 | 0.97 | 0.46 |
| **Bottom wall heated** | 0.8 | 0.55 | 0.69 | 0.56 | 0.8 | 0.52 | 0.53 | 0.53 |

***Heat transfer augmentation***

The augmentation in heat transfer provided by the lattices with respect to smooth channel is shown in **Fig 2.14**.

The baseline smooth channel Nusselt number was predicted using Dittus-Boelter correlation ($Nu_0 = 0.023Re_{d_h}^{0.8}Pr^{0.4}$) developed for turbulent and fully developed thermal flows in smooth channels. The Nusselt number of the lattices corresponding to only total heat transfer coefficient based on channel hydraulic diameter length scale ($Nu_{d_h} = hd_h/k_f$) presented in **Fig. 2.8** is used here to discuss the enhancement levels.

This seemed relevant as in practical applications the potential of lattices are fully realized due to their conjugate thermal exchange abilities including buoyancy-effects. When both the top and bottom walls were heated, Octet, FD-Cube, and TKD provided about 13 to 23 times higher heat transfer than the smooth channel, whereas Cube yielded about 9.5 to 17 times higher heat transfer. When only bottom wall was heated, the heat transfer enhancement relative to smooth channel provided by Octet, FD-Cube, and TKD was 11.3 to 20 times, but Cube provided augmentation of 9.4 to 12.5 times as compared to the smooth channel. Overall, the employment of lattices with varying topologies in a channel is capable of producing heat transfer as high as 10 to 20 times relative to the corresponding smooth channel configurations. It should be noted that the enhancement levels shown in **Fig. 14** reflect both the conjugate thermal exchange of each topology and the surface roughness effects present on the fibers and integrated endwalls.

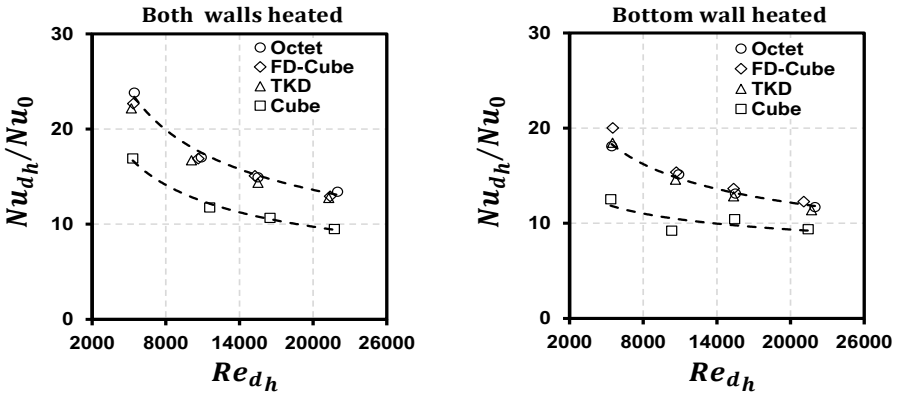



**Figure 2.14 Nusselt number enhancement with respect to smooth channel Dittus-Boelter correlation**

***Pressure drop characteristics***

Lattices yield high heat transfer levels through enhanced surface area and flow mixing, but at a significant cost of increased pumping power requirements due to friction losses. To compare the flow losses of various lattice topologies, the pressure gradient across the lattices is presented as a function of the mean flow velocity in **Fig.2.15a**, enabling direct performance comparisons. Pressure drop measurements were conducted under isothermal conditions where no heating was applied on the top and bottom substrate walls to isolate geometric effects. Pressure gradient ($\Delta P/L$) as a function of the mean flow velocity is used to represent the flow losses incurred by the lattices, where mean flow velocity was calculated from the volumetric flow rate and channel cross-section area.

The non-dimensional form of the pressure drop, i.e., Fanning friction-factor was also calculated according to the following definition:

**Equation 2-9**

$$f = \frac{\Delta P}{L}\frac{d_h}{2\rho u^2}$$

FD-Cube had the highest-pressure gradient, followed by Octet, TKD, and Cube. The intersection of diagonal fibers at the face of the unit cell as shown in **Fig. 2.10b** provided large resistance to the fluid flow. The least value of pore diameter was also exhibited by the FD-Cube topology (**Table. 2.4**)

Highest inertial losses are expected for FD-Cube lattice topology. Cube had the simplest fiber connection and large pores; therefore, it provided the lowest pressure drop values. Pressure gradient of ~ 717 to 8804 Pa/m, 604 to 7121 Pa/m, 378 to 4651 Pa/m, and 184 to 2298 Pa/m was obtained for FD-Cube, Octet, TKD and Cube, respectively.

Flow losses in non-dimensional form are presented in terms of friction factor (Equation 2-9). Enhancement in the friction factor values relative to the smooth channel is shown in **Fig. 15b**, where the baseline smooth channel friction factor was evaluated using the Blasius equation ($f_0 = 0.079Re_{d_h}^{-0.25}$). FD-Cube, Octet, TKD, and Cube provided 613 to 667, 487 to 514, 334 to 355, and 158 to 169 times enhancement, respectively, with respect to the smooth channel. The friction factor enhancement did not show very strong dependence on the Re for a particular topology investigated.

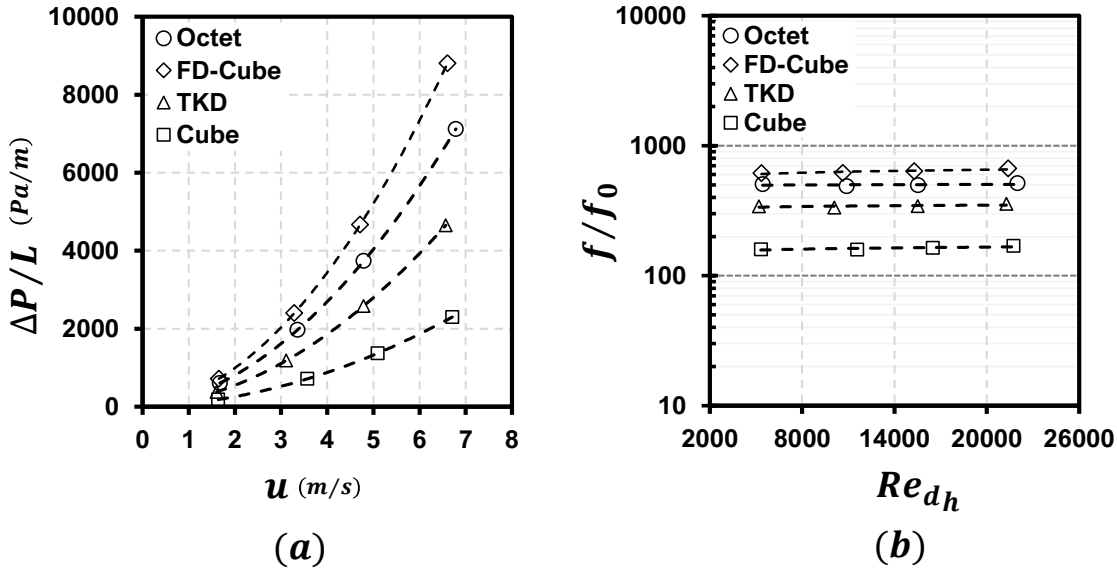



**Figure 2.15 Conjugate heat transfer coefficient as a function of pumping power requirement**

**Pumping power requirements**

The total heat transfer coefficient for investigated lattices is presented with respect to the pumping power requirement ($\Delta P\dot{m}/\rho$) in **Fig. 2.16**. Octet and TKD provided the best thermal performance over the studied range of pumping power when both walls were heated. The performance was closely followed by FD-Cube, which demonstrated consistently strong thermal characteristics across the tested range, whereas Cube exhibited the least heat transfer coefficient at any considered pumping power, indicating a clear hierarchical performance pattern among the lattice structures. When only bottom wall was heated, Octet, FD-Cube, and TKD provided similar characteristics of heat transfer coefficient with respect to the pumping power conditions, suggesting that these three topologies maintain comparable thermal performance effectiveness under single-wall heating scenarios despite their distinct structural differences. The heat transfer increased with increasing pumping power, with the Cube topology exhibiting the maximum slope among all structures. The heat transfer coefficient levels of Cube approached and eventually matched those provided by the other lattices at the higher pumping power conditions, demonstrating a unique performance characteristic at elevated power inputs. Therefore, Cube can outperform other lattices at high pumping power constraints, suggesting its potential advantage in applications where higher pumping power availability is not a limiting factor and maximum heat transfer performance is desired. The Cube topology showed approximately 15% higher heat transfer rates compared to other geometries at the maximum tested pumping power. Furthermore, these findings have significant implications for practical applications in thermal management systems. The observed behavior of the Cube topology at higher pumping powers suggests a potential design strategy where system operators could dynamically adjust power inputs based on cooling demands. This flexibility could be particularly valuable in applications with variable thermal loads, such as data centers or industrial processing equipment. This comprehensive investigation into the pressure drop behavior demonstrated that the distinct and intricate pore structure of the Cube topology facilitates superior mixing capabilities at elevated Reynolds numbers, ultimately leading to its improved performance.

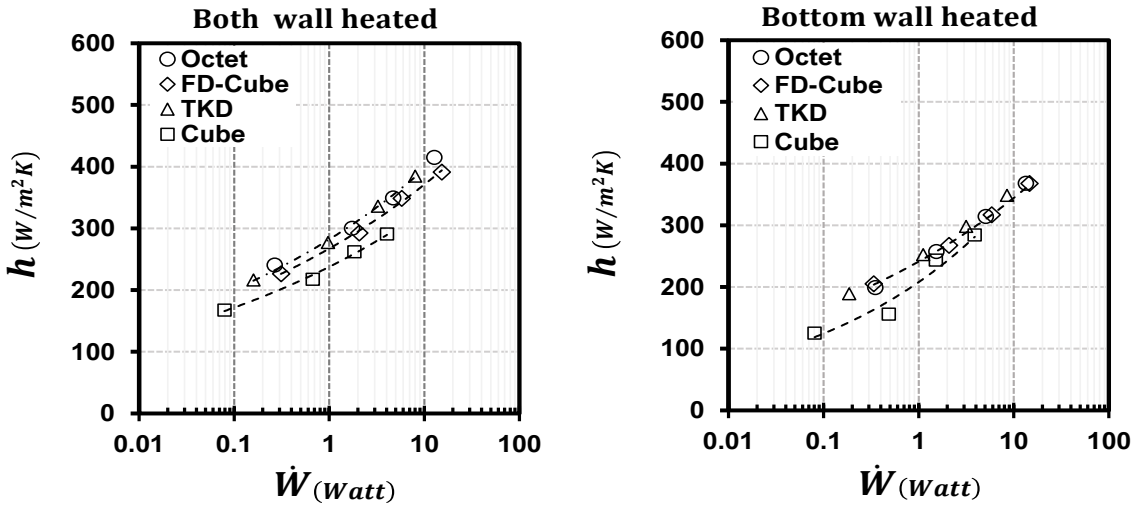



**Figure 2.16 Conjugate heat transfer coefficient as a function of pumping power requirement**

### Thermal-hydraulic performance (THP)

The augmentation in heat transfer through employment of lattices is accompanied by significant flow losses. To quantify the gain in thermal performance relative to the pressure drop penalty, thermal-hydraulic performance (THP) parameter is generally defined [2.31,2.32]. The THP is determined by the following equation:

**Equation 2-10**

$$THP = \frac{\left(Nu_{d_h}/Nu_0\right)}{(f/f_0)^{1/3}}$$

where, $Nu_0 = 0.023Re_{d_h}^{0.8}Pr^{0.4}$ is the Dittus-Boelter equation for the Nusselt number prediction in the smooth channel and $f_0 = 0.079Re_{d_h}^{-0.25}$ is the Blasius equation for estimating friction factor in the smooth channel. The augmentation in thermal performance relative to the gain in pressure drop of different lattices is presented in terms of THP (Equation 2-10) in **Fig. 2.17**. The THP of all the lattices was around ~ 3 at the lowest investigated Reynolds number when both the walls were heated. The THP of all the lattices was quite similar, therefore, for the engineering applications where pressure drop is not the constraint variable, Octet, FD-Cube and TKD could be employed as they generated higher heat transfer than the Cube topology. This finding aligns with previous studies that have demonstrated the superior thermal performance of these complex lattice structures in various heat exchanger applications.

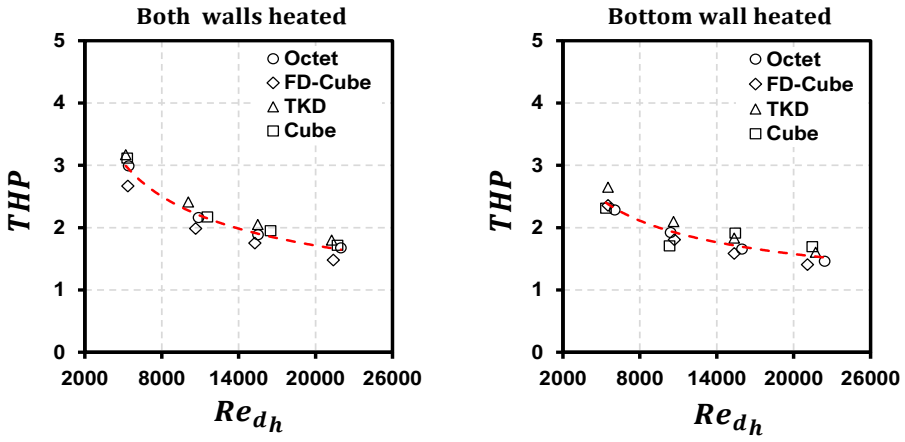



**Figure 2.17 Thermal-hydraulic performance based on conjugate Nusselt number in reference to the Reynolds number**

The higher heat transfer of complex topologies compensated for the higher pressure drop yielding the competing THP against the Cube topology. Since all the investigated topologies provided same THP levels irrespective of the fiber inter-connections, other factors such as cost of fabrication and lead time can be weighed in to choose a topology for heat exchanger when THP is the primary design constraint because it is clear that a topology as simple as Cube can provide THP comparable to other topologies. However, if one needs to design a heat exchanger oriented towards mechanical load bearing applications, then topologies with superior mechanical properties can be selected without compromising the overall THP. Based on the data provided in **Fig. 2.17**, dependence of the form $THP = cRe_{d_h}^{-m}$ can be obtained for the thermal-hydraulic performance of the investigated samples. The correlations for both walls heated, and only bottom wall heated configurations were $102.99Re_{d_h}^{-0.414}$ and $37.22Re_{d_h}^{-0.319}$, respectively.

## Conclusions

Experimental investigation on flow and heat transfer characteristics of additively manufactured lattice blocks composed of four different unit cell topologies, namely, Octet, FD-Cube, TKD, and Cube has been caried out. The porosity of lattice was ~0.88 and cell density of 2.5 cpi. Heat transfer and pressure drop experiments were conducted over Reynolds number 5,000 < $Re_{d_h}$< 22, 500, with air as working fluid. Heat transfer experiments were conducted for two types of heating conditions in which: (a) both the endwalls were heated, and (b) only bottom wall was heated. Following major conclusions were drawn from the current investigation:

1. The length of the samples in the mean flow direction was 100 mm which was sufficient for flow to reach thermally fully developed condition after travelling over five to six rows of unit cells in streamwise direction. Octet, FD-Cube, and TKD provided similar total heat transfer coefficient values of ~216 $\mathrm{W/m^2K}$ to 415 $\mathrm{W/m^2K}$ in thermally fully developed zones whereas Cube yielded the lowest heat transfer coefficient values between 167 $\mathrm{W/m^2K}$ and 290 $\mathrm{W/m^2K}$.

2. Introduction of pore diameter and fiber diameter as characteristic length scale to define Nusselt number yielded very coherent data set for all the topologies. Both the

characteristic length scales allowed the construction of a single trendline to predict the thermal performance of all the topologies with $\pm$15% spread for a particular heating condition.

3. Lattices could augment the Nusselt number by roughly 10 – 20 times with respect to the smooth channel.

4. From the flow losses perspective, the maximum pressure gradient was incurred by the FD-Cube and the least pressure drop penalty was provided by Cube topology. At any given pumping power condition, Octet, FD-Cube, and TKD were equally promising for the investigated range of mass flow rates, however, Cube could be useful at very high mass flow rates when only one wall is heated.

5. The thermal-hydraulic performance was quite similar for all the topologies which showed that Octet, FD-Cube, and TKD can be very useful in practical engineering applications where pressure drop is not a constraint variable because these topologies generated higher heat transfer than Cube. The investigated topologies provided THP of ~ 3 at the lowest investigated Reynolds number.

6. Overall, it can be concluded that increasing the complexity of the RUC topology is not a very effective method of improving the heat transfer from a surface especially when the dimensions of the samples are large enough to achieve fully developed thermal flows. In the current study, the heat transfer coefficient enhancement with respect to smooth channel for lattices with relatively higher degree of complexity showed negligible dependence on the RUC topology.

**Nomenclature**

| | |
|---|---|
| $A_{ins}$ | base area of insulation/endwall |
| CAD | computer aided design |
| $c, m$ | coefficients in correlation |
| $c_p$ | specific heat capacity |
| cpi | cells per inch |
| $d_f$ | fiber-diameter |
| $d_h$ | hydraulic diameter |

| | |
|---|---|
| $d_p$ | pore-diameter |
| $f$ | friction factor |
| H | height of the sample |
| $h_t$ | local total transfer coefficient |
| $h_f$ | local forced heat transfer coefficient |
| $k_f$ | fluid thermal conductivity |
| L | streamwise length of the sample |
| $\dot{m}$ | mass flow rate |
| $Nu$ | Nusselt number |
| ppi | pores per inch |
| $Pr$ | Prandtl number |
| $Q_{net}$ | net heat input into the lattice |
| $Q_{nf}$ | heater output under *no-flow* conditions |
| $Q_t$ | total heater output |
| $Q_{wf}$ | heat lost through backside insulation |
| $Q"_{net}$ | net heat flux |
| $R_{htr}$ | resistance of the heater |
| $Re$ | Reynolds number |
| RUC | representative unit cell |
| $t_{ins}$ | insulation thickness |
| $T$ | temperature |
| $THP$ | Thermal hydraulic performance |
| TPMS | triply periodic minimal surface |
| $u$ | mean flow velocity |
| $V$ | voltage |
| W | width of the sample |
| $\dot{W}$ | pumping power |
| $\Delta P$ | pressure drop |
| $\Delta$T | temperature difference |

**Greek symbols**

| | |
|---|---|
| $\mu$ | dynamic viscosity |
| $\rho$ | density |
| $\varepsilon$ | porosity |
| ins | insulation |

**Subscripts**

| | |
|---|---|
| $b$ | bulk fluid |
| $f$ | fiber |
| $l$ | local |
| $nf$ | *no-flow* |
| $p$ | pore |
| $sf$ | interfacial |
| $w$ | substrate endwall |
| $w,i$ | running index for the hole number in the endwalls |
| $wf$ | with-flow |
| 0 | standard correlation |

## References

[2.1] Younis_Viskanta_Experimental determination of the volumetric heat transfer coefficient between stream of air and ceramic foam.pdf, (n.d.).

[2.2] S. Mancin, C. Zilio, A. Diani, L. Rossetto, Air forced convection through metal foams: Experimental results and modeling, Int. J. Heat Mass Transf. (2013). https://doi.org/10.1016/j.ijheatmasstransfer.2013.02.050.

[2.3] A.J. Fuller, T. Kim, H.P. Hodson, T.J. Lu, Measurement and interpretation of the heat transfer coefficients of metal foams:, Http://Dx.Doi.Org/10.1243/095440605X8414. 219 (2016) 183–191. https://doi.org/10.1243/095440605X8414.

[2.4] P.J. Tan, S.R. Reid, J.J. Harrigan, On the dynamic mechanical properties of open-cell metal foams - A re-assessment of the “simple-shock theory,” in: Int. J. Solids Struct., 2012: pp. 2744–2753. https://doi.org/10.1016/j.ijsolstr.2012.03.026.

[2.5] C.Y. Zhao, Review on thermal transport in high porosity cellular metal foams with open cells, Int. J. Heat Mass Transf. (2012). https://doi.org/10.1016/j.ijheatmasstransfer.2012.03.017.

[2.6] P. Ranut, On the effective thermal conductivity of aluminum metal foams: Review and improvement of the available empirical and analytical models, Appl. Therm. Eng. (2016). https://doi.org/10.1016/j.applthermaleng.2015.09.094.

[2.7] I. Kaur, P. Singh, Critical evaluation of additively manufactured metal lattices for viability in advanced heat exchangers, Int. J. Heat Mass Transf. 168 (2021) 120858. https://doi.org/10.1016/j.ijheatmasstransfer.2020.120858.

[2.8] H. Yan, X. Yang, T. Lu, G. Xie, Convective heat transfer in a lightweight multifunctional sandwich panel with X-type metallic lattice core, Appl. Therm. Eng. (2017). https://doi.org/10.1016/j.applthermaleng.2017.08.081.

[2.9] X. Jin, B. Shen, H. Yan, B. Sunden, G. Xie, Comparative evaluations of thermofluidic characteristics of sandwich panels with X-lattice and Pyramidal-lattice cores, Int. J. Heat Mass Transf. (2018). https://doi.org/10.1016/j.ijheatmasstransfer.2018.07.087.

[2.10] L. Dong, V. Deshpande, H. Wadley, Mechanical response of Ti-6Al-4V octet-truss lattice structures, Int. J. Solids Struct. (2015). https://doi.org/10.1016/j.ijsolstr.2015.02.020.

[2.11] I. Kaur, P. Singh, State-of-the-art in heat exchanger additive manufacturing, Int. J. Heat Mass Transf. 178 (2021) 121600. https://doi.org/10.1016/j.ijheatmasstransfer.2021.121600.

[2.12] K. Hazeli, B.B. Babamiri, J. Indeck, A. Minor, H. Askari, Microstructure-topology relationship effects on the quasi-static and dynamic behavior of additively manufactured lattice structures, Mater. Des. 176 (2019). https://doi.org/10.1016/j.matdes.2019.107826.

[2.13] X. Cao, D. Xiao, Y. Li, W. Wen, T. Zhao, Z. Chen, Y. Jiang, D. Fang, Dynamic compressive behavior of a modified additively manufactured rhombic dodecahedron 316L stainless steel lattice structure, Thin-Walled Struct. 148 (2020). https://doi.org/10.1016/j.tws.2019.106586.

[2.14] V. V Calmidi, R.L. Mahajan, Forced convection in high porosity metal foams, J. Heat Transfer. (2000). https://doi.org/10.1115/1.1287793.

[2.15] N. Dukhan, Ö. Bałci, M. Özdemir, Thermal development in open-cell metal foam: An experiment with constant wall heat flux, Int. J. Heat Mass Transf. 85 (2015) 852–859. https://doi.org/10.1016/j.ijheatmasstransfer.2015.02.047.

[2.16] A. Arbak, N. Dukhan, Ö. Bağcı, M. Özdemir, Influence of pore density on thermal development in open-cell metal foam, Exp. Therm. Fluid Sci. 86 (2017) 180–188. https://doi.org/10.1016/j.expthermflusci.2017.04.012.

[2.17] J.S. Noh, K.B. Lee, C.G. Lee, Pressure loss and forced convective heat transfer in an annulus filled with aluminum foam, Int. Commun. Heat Mass Transf. 33 (2006) 434–444. https://doi.org/10.1016/j.icheatmasstransfer.2005.11.003.

[2.18] K. Hooman, A. Haji-Sheikh, D.A. Nield, Thermally developing Brinkman-Brinkman forced convection in rectangular ducts with isothermal walls, Int. J. Heat Mass Transf. 50 (2007) 3521–3533. https://doi.org/10.1016/j.ijheatmasstransfer.2007.01.011.

[2.19] A. Haji-Sheikh, D.A. Nield, K. Hooman, Heat transfer in the thermal entrance region for flow through rectangular porous passages, Int. J. Heat Mass Transf. 49 (2006) 3004–3015. https://doi.org/10.1016/j.ijheatmasstransfer.2006.01.040.

[2.20] M. Iasiello, S. Cunsolo, N. Bianco, W.K.S. Chiu, V. Naso, Developing thermal flow in open-cell foams, Int. J. Therm. Sci. 111 (2017) 129–137. https://doi.org/10.1016/j.ijthermalsci.2016.08.013.

[2.21] Z. Wu, C. Caliot, G. Flamant, Z. Wang, Numerical simulation of convective heat transfer between air flow and ceramic foams to optimise volumetric solar air receiver performances, Int. J. Heat Mass Transf. 54 (2011) 1527–1537. https://doi.org/10.1016/j.ijheatmasstransfer.2010.11.037.

[2.22] A.S. Suleiman, N. Dukhan, Forced convection inside metal foam: Simulation over a long domain and analytical validation, Int. J. Therm. Sci. 86 (2014) 104–114. https://doi.org/10.1016/j.ijthermalsci.2014.06.022.

[2.23] I. Kaur, P. Singh, Flow and Thermal Transport Through Unit Cell Topologies of Cubic and Octahedron Families, Int. J. Heat Mass Transf. 158 (2020). https://doi.org/10.1016/j.ijheatmasstransfer.2020.119784.

[2.24] I. Kaur, P. Singh, Numerical investigation on conjugate heat transfer in octet-shape-based single unit cell thick metal foam, Int. Commun. Heat Mass Transf. 121 (2021) 105090. https://doi.org/10.1016/j.icheatmasstransfer.2020.105090.

[2.25] N. Wang, I. Kaur, P. Singh, L. Li, Prediction of Effective Thermal Conductivity of Porous Lattice Structures and Validation with Additively Manufactured Metal Foams, Appl. Therm. Eng. (2021) accepted. https://doi.org/10.1016/j.applthermaleng.2021.116558.

[2.26] R.J. Moffat, Describing the uncertainties in experimental results, Exp. Therm. Fluid Sci. 1 (1988) 3–17. https://doi.org/10.1016/0894-1777(88)90043-X.

[2.27] J.J. Hwang, G.J. Hwang, R.H. Yeh, C.H. Chao, Measurement of interstitial convective heat transfer and frictional drag for flow across metal foams, J. Heat Transfer. (2002). https://doi.org/10.1115/1.1416690.

[2.28] M. Iasiello, S. Cunsolo, M. Oliviero, W.M. Harris, N. Bianco, W.K.S. Chiu, V. Naso, Numerical analysis of heat transfer and pressure drop in metal foams for different morphological models, J. Heat Transfer. (2014). https://doi.org/10.1115/1.4028113.

[2.29] O. Al-Ketan, M. Ali, M. Khalil, R. Rowshan, K.A. Khan, R.K. Abu Al-Rub, Forced Convection Computational Fluid Dynamics Analysis of Architected and Three-Dimensional Prin**table** Heat Sinks Based on Triply Periodic Minimal Surfaces, J. Therm. Sci. Eng. Appl. (2021). https://doi.org/10.1115/1.4047385.

[2.30] I. Kaur, P. Singh, Flow and thermal transport characteristics of Triply-Periodic Minimal Surface (TPMS)-based gyroid and Schwarz-P cellular materials, Numer. Heat Transf. Part A Appl. 79 (2021) 553–569. https://doi.org/10.1080/10407782.2021.1872260.

[2.31] M. Iasiello, N. Bianco, W.K.S. Chiu, V. Naso, The effects of variable porosity and cell size on the thermal performance of functionally-graded foams, Int. J. Therm. Sci. 160 (2021) 106696. https://doi.org/10.1016/J.IJTHERMALSCI.2020.106696.

[2.32] M. Siavashi, H.R. Talesh Bahrami, E. Aminian, Optimization of heat transfer enhancement and pumping power of a heat exchanger tube using nanofluid with gradient and multi-layered porous foams, Appl. Therm. Eng. 138 (2018) 465–474. https://doi.org/10.1016/J.APPLTHERMALENG.2018.04.066.

# CHAPTER THREE :
# EXPERIMENTAL STUDY ON FLOW AND THERMAL TRANSPORT IN ADDITIVELY MANUFACTURED LATTICES BASED ON CUBE-SHAPED UNIT CELL

## Abstract

This paper presents the convective heat transfer coefficient of cubic lattices under both buoyancy-induced and forced convection. Additionally, it examines the effective thermal conductivity, permeability, and inertial coefficient of a cubic unit cell of porosity ~0.87. The test specimens were additively manufactured using stainless steel 420 (with 40% bronze infiltration) using the binder jetting technique. In the buoyancy-driven convection experiments, three different aspect ratios (width/height) varying from 0.5 to 2 were tested across three different heating orientations, viz. bottom wall (0°), side wall (90°), and top wall (180°). The lattice with the lowest aspect ratio had the highest convective heat transfer coefficient in all three heating orientations.

The forced convection heat transfer coefficient was determined for an AM part comprising 10 x 10 cubic unit cell array in the plane perpendicular to the flow and 20 unit cells in the streamwise direction. Additionally, the flow characteristics of the cubic lattice were characterized through permeability (K) and inertial coefficient ($C_f$), determined by conducting separate pressure drop experiments over a wide range of flow velocities. The thermal hydraulic performance of the cubic lattice was assessed by combining the periodic regime convective heat transfer coefficient with the pressure drop data obtained from the experimentally determined values of K and $C_f$. The comprehensive characterization of flow and thermal transport, including K and $C_f$, along with $h_{sf}$, $k_{eff}$, presented in this paper, provides a robust foundation for their application in volume-averaged computations for detailed parametric study.



Keywords: Cubic lattice; enhanced heat transfer; additive manufacturing; convection.


## Introduction

High porosity metal foams have superior capabilities to dissipate large heat flux levels under both buoyancy- and forced-convection scenarios. Typically, the unit cell of metal foams produced by foaming process can be approximated as a tetrakaidecahedron (TKD) shape. These metallic foams offer high specific surface area ($m^2/m^3$), highly tortuous flow paths, and complex interconnections of struts, resulting in enhanced flow mixing and thermal dispersion. Metal foams significantly enhance the effective thermal conductivity of the medium as well as the interstitial heat transfer coefficient at the strut-

level, leading to an overall high rate of heat dissipation. The metal foams obtained with this manufacturing process have porosities greater than 0.9, with pore densities ranging from 5-40 pores per inch. These metallic foams are typically manufactured in aluminum, copper, and nickel. The flow and thermal transport properties of such metal foams (aluminum) have been experimentally characterized by Mahajan and co-workers under different conditions [3.1–3.6]. A comprehensive review on the thermal transport of such metal foams can be found in [3.7,3.8].

Despite the superior thermal transport characteristics of metal foams, their widespread adoption has been limited due to several challenges, including geometrical constraints (pore density, porosity), limited material options, limitations on unit cell topology and metal foam block's form factor, machining difficulties, and the need for additional bonding with the substrate/plate subjected to heat loads. These challenges, however, present an opportunity to innovate and retain the benefits of metal foams while eliminating these limitations.

To this end, metal additive manufacturing presents an exciting opportunity by enabling the production of desired unit cell topology at different length-scales, porosities, materials, and form factors, which significantly expands the application domain of metal foams. Further, AM parts can be integrally manufactured where the plate subjected to the heat load and the lattice structures are built as a single solid body, thereby eliminating the thermal contact resistance issue, which is prominent in the foaming process enabled metal foam and its assembly with heated plates. Additionally, as pointed out earlier, metal foams produced via the traditional foaming processes are available only in high porosities, and uniform porosity distribution throughout the volume, limiting their functional versatility. In contrast, metal additive manufacturing enables the creation of porous media with moderately low porosities, along with functionalized grading, to achieve a desired local porosity distribution within the metal foam volume. Given these advantages, there has been a growing number of investigations to develop advanced concepts pertaining to lattice topology concepts for a variety of applications including, forced and buoyancy-induced convection with different working fluids, phase change material integration with lattices, flow and pool boiling, heat pipes etc. In this study, our

focus is on forced, and buoyancy-induced convection. A brief review of the literature in these two convective heat transfer categories is presented below.

***Lattice structures for forced convection***

In forced convection research, the primary objective is to enhance the heat dissipation rate while balancing this against the associated cost of increase in pressure drop or pumping power. Enhanced heat transfer performance is typically quantified by comparing it to a similar geometry without enhancements (baseline configuration). Thermal-hydraulic performance, on the other hand, considers both, the enhanced heat transfer and the increased pressure drop in reference to the baseline configuration.

As discussed above, incorporating metal foams enhances effective thermal conductivity and local interstitial heat transfer coefficient. In addition, metal foams provide a high specific surface area, leading to increased heat dissipation rates. However, the complex strut interconnections and high flow blockage also cause a significant increase in pressure drop. Hence, the motivation behind the development of advanced porous media concepts is to retain and further improve on the benefits offered by metal foams while addressing the above-mentioned challenges and striking a balance between the enhanced heat transfer and increased pressure drop. One promising approach to achieving these objectives is the use of lattice structures with tunable unit cells. With recent advancements in metal additive manufacturing, complex and ordered unit cell topologies can be realized with high precision. Some of the recent studies related to forced convection on additively manufactured lattice structures are discussed below.

Liang et al. [3.9] carried out an experimental study to characterize different lattice topologies including, body centered cubic (BCC), face centered cubic (FCC), Kagome, and X-type in a lattice frame configuration with a single unit cell in the thickness of the porous volume. Selective laser sintering (SLS) method was employed to additively manufacture the test articles. The authors concluded that the X-type lattice provided the highest heat transfer enhancement for air forced convection. Takarazawa et al. [3.10] conducted an experimental study on lattice blocks based on BCC, FCC, and their variants with a higher number of struts, where the samples were additively manufactured using selective laser melting (SLM) technique. The results showed that FCC lattice and its

variants had higher effective thermal conductivity compared to their BCC counterparts, whereas BCC and its variants were more effective in forced convection scenarios.

As discussed earlier, the unit cell of the metal foams produced via foaming process can be approximated to a TKD shape. Typically, the struts of the TKD unit cell are of tricuspid shape [3.11], which is a result of the minimal free surface energy principle on which this manufacturing process is based on. With metal AM, the strut shape can also be controlled to achieve the desired flow and thermal transport characteristics. Lorenzon et al. [3.12] recently evaluated BCC type unit cells in a lattice frame configuration, where the strut shapes were varied. The authors investigated cam-like, drop-like, and elliptical cross-section struts for the BCC unit cell configuration where Laser Powder Bed Fusion (LPBF) technique was used to 3D print the samples in AlSi10Mg. They found that the strut shape had a significant effect on the pressure drop, and elliptical shape struts had heat transfer performance similar to that of circular struts while exhibiting low pressure drop penalty. Chaudhari et al. [3.13] carried out an experimental study on lattice frame configuration based on Octet-shaped unit cell, where the parts were printed in AlSi10Mg for porosities between 0.7 and 0.9. The authors characterized the permeability, inertial coefficient, effective thermal conductivity, and interstitial heat transfer for the three samples within the above porosity range.

Recently, a series of experimental studies investigated four different unit cell topologies— cubic, face diagonal cube (FD-Cube), TKD, and octet— in different configurations using air as the working fluid. In the lattice frame configuration [3.14], it was experimentally found that at a porosity of ~0.87, the FD-Cube exhibited the highest heat transfer coefficient for a given flow velocity, while the simple cubic lattice showed the highest heat transfer coefficient at a given pumping power for the same porosity. However, as porosity decreased, thermal hydraulic performance improved as the gain in heat transfer compensated for the increase in pressure drop. It is important to note that in lattice frame configuration, where only one unit cell is present in the thickness of the porous media volume, the endwall also plays a significant role in flow and thermal transport. The endwall characteristics for three different unit cell topologies— octet, octa and V-octet— were determined experimentally by Kaur and Singh [3.15], using liquid

crystal thermography to determine the local convective heat transfer coefficient. For the three unit cell topologies tested, the configuration featured a single column of five interconnected unit cells in the streamwise direction. The presence of X-shaped half struts at the endwall in the octet and V-octet topologies had a distinct effect on local heat transfer, as the flow separated and reattached in the immediate downstream vicinity of the half struts. Additionally, the lattice topology affected the flow mixing.

Aider et al. [3.16] carried out an experimental study to characterize the convective heat transfer coefficients of large lattice structures composed of unit cells similar to those described in [3.14]. The foam volume consisted of 5 x 5 unit cells in the plane perpendicular to bulk flow and 10 unit cells in the streamwise direction, in contrast to the lattice frame configuration of 5 x 1 x 5 unit cells in [3.14]. The selection of the foam volume with several repeated unit cells by Aider and co-authors [3.16] was deliberate, aiming to minimize endwall effects and focus solely on the effects of individual unit cell topology. The authors reported heat transfer coefficient values for four unit cell topologies in the periodic heat transfer regime, where convective heat transfer coefficients at the unit cell level remained nearly constant, implying that the temperature rise of the working fluid across a unit cell (along the flow direction) in the periodic regime was similar. It was found that heat transfer coefficients in the periodic regime for the octet, FD-Cube, and TKD unit cells were comparable, while the cubic unit cell exhibited distinctly lower heat transfer coefficients compared to the other topologies. However, when analyzing thermal hydraulic performance (THP) versus channel hydraulic diameter, it was observed that all structures had nearly similar THP values across the investigated range of Reynolds number. This observation suggests that while complex topologies can potentially yield higher convective heat dissipation, they may also incur a fairly large concomitant pressure drop. Further research is needed to explore the thermal-hydraulic performance of lattice topologies with varying degrees of complexity. The unique benefits offered by additively manufactured lattice structures are comprehensively discussed in Kaur and Singh [3.17,3.18]. These findings underscore the importance of considering both geometric complexity and manufacturing constraints when designing lattice structures for specific thermal management applications.

***Lattice structures for buoyancy-induced convection***

Buoyancy-driven convection is a passive cooling technology known for its reliability, ease in maintenance, and no requirement of pumping power for coolant flow. The convective heat transfer rates for a typical heated plate can be enhanced by installing high porosity metal foams, which provide high specific area per unit volume and high local interstitial heat transfer as the fluid moves through the pores and interacts with the struts. Phanikumar and Mahajan [3.2] conducted a numerical study on aluminum foams under buoyancy-driven convection, where the pore density was varied between 5-40 PPI. The authors demonstrated that metal foams significantly enhanced heat transfer, and low pore density foam was superior to the higher pore density foam, as it allowed easier escape of the spent fluid to the ambient. This observation was confirmed experimentally by Bhattacharya and Mahajan [3.4] where the 5 PPI foam significantly outperformed the 40 PPI foams for Rayleigh numbers varying between $10^5$ to $10^6$. Note that despite the high surface area offered by 40 PPI foams relative to 5 PPI, the higher permeability of 5 PPI foams dominated the resultant buoyancy-driven convection heat transfer. The authors extended this concept to longitudinal finned heat sink where the passage between the adjacent fins (solid) was packed with high porosity metal foams. The permeability of metal foams was found to be an important parameter which affected the convective heat transfer under buoyancy-driven convection involving metal foams. Zhao et al. [3.19] studied the natural convection in FeCrAlY metal foams and demonstrated that the local thermal non-equilibrium effects must be considered for accurate prediction of the thermal performance- a finding similar to the one reported in [3.2]. In contrast with [3.4], Feng et al. [3.20] studied the thermal performance of metal foam strips made from copper, where the space occupied by solid longitudinal fins as in [3.4] was kept empty to allow the movement of air. The number of metal foam strips were varied along with the individual strip height. It was found that an intermediate configuration with 7 foam strips performed better than 4 or 10 foam strip configurations for the different heights studied. The hypothesis behind such a configuration was to increase the effective permeability of the volume occupied by the heat sink by allowing free motion of air between adjacent strips. An experimental study was conducted by Qu et al. [3.21] where copper metal foams'

orientation with respect to the gravity vector was studied under buoyancy-driven convection. It was shown that 60-75° orientation resulted in optimum thermal performance for different metal foam configurations, where the inclination was varied between 0° (horizontal) and 90° (vertical).

High porosity metal foams investigated in the aforementioned buoyancy-driven convection studies were manufactured via *foaming* process, resulting in a randomized arrangement of struts and pores, where a typical pore can be closely represented by a TKD shaped unit cell topology. From the above studies, it can be concluded that an easy escape passage of spent fluid may result in enhanced thermal performance, a characteristic feature of low pore density foams. This advantage compensates for the reduced surface area available for heat dissipation in buoyancy-driven convection transport. A more structured arrangement of unit cell topologies has the potential to yield higher heat transfer rates compared to a randomized arrangement.

To this end, recently Aider et al. [3.22] carried out an experimental study on buoyancy-driven convection transport in  configurations involving two parallel plates with structured lattice unit cells packed between them. They investigated five unit cell topologies— cube, FD-cube (two patterns of adjacent unit cell attachment), TKD, and Octet—under two different heating configurations (one and both side walls heated). The samples were manufactured via binder jetting in SS420 (40% bronze infiltration). The results indicated that the cubic lattice (the simplest topology) exhibited the highest heat transfer among the five-unit cell topologies, which was ~6 times that of the baseline configuration of two vertically heated parallel plates. This was attributed to its remarkably high permeability, which allowed easy departure of heated air, while the Octet topology, despite its high surface area to volume ratio, resulted in the weakest thermal transport due to its low permeability.

From the literature review, simpler unit cell topologies can outperform complex structures in thermal hydraulic performance during forced convection and overall heat dissipation in buoyancy-driven convection, primarily due to higher permeability. This study presents a comprehensive experimental investigation of flow and thermal transport

in lattice configurations based on simple cubic unit cells. The research uniquely demonstrates the effectiveness of simple unit cell topology in both forced and buoyancy-driven convection scenarios, while highlighting their potential for fabrication via conventional manufacturing processes including subtractive manufacturing, wire-woven techniques, and brazing.

The experimental investigation characterized forced and buoyancy-induced convection transport coefficients, along with effective thermal conductivity, permeability, and inertial coefficient. Test sections and specimens were 3D printed using Binder jet technology with Stainless Steel 420 (40% bronze infiltration). The following sections detail the experimental setups, test articles, procedures, data reduction methods, and discuss the results.

## Experimental setups

This section provides details of the test setups used for effective thermal conductivity, buoyancy-induced convection, and forced convection experiments.

### *Effective thermal conductivity experimental setup*

The effective thermal conductivity of the cubic unit cell was determined through steady state experiments, as illustrated in **Figure 3.1**. This measurement is critical for understanding the thermal transport properties of the cubic lattice sample by virtue of its topology, while the air occupying the void space is mostly stagnant. The sample was positioned on an aluminum slab partially submerged in an ice-water slurry, which resulted in the slab temperature of ~ 0°C in steady state conditions.

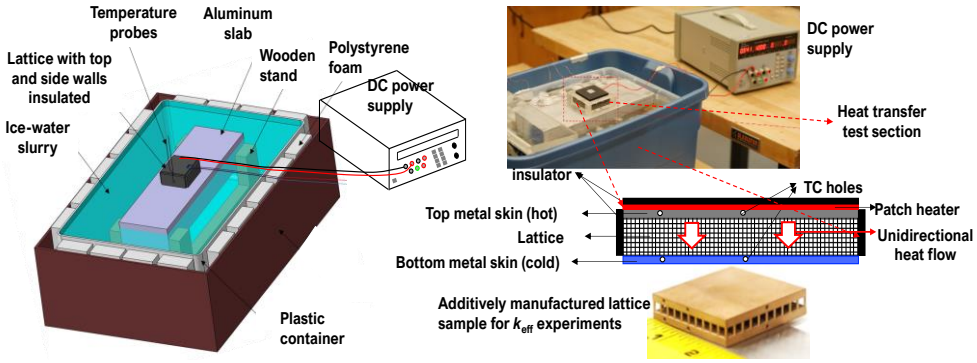



**Figure 3.1 Thermal conductivity test setup, and additively manufactured sample**

A patch heater attached to the top plate of the lattice sample ensured a uniform heat flux input to the lattice frame. The patch heater was powered by a DC source, which also displayed the current in the circuit.

By knowing the patch heater's resistance and the current in the circuit, the total heat input was determined. The stray heat losses were minimized by attaching a rubber foam insulation (k ~ 0.037 W/mK) of 3.2 mm thickness.

The heat flow through the insulator was also determined by measuring the temperature drop across it and applying Fourier's law of heat conduction. The bottom plate of the lattice sample was glued onto the aluminum slab, maintained at a steady temperature of ~0°C. The large thermal mass of the aluminum slab effectively served as a cold reservoir, and the heat input to the top plate did not result in noticeable temperature rise in the cold reservoir. This experimental design ensured unidirectional heat flow through the thickness of the lattice frame, which was essentially one unit cell thick. With the known value of heat conducted through the thickness of the lattice sample, the effective thermal conductivity was calculated by measuring the temperature drop across the thickness of the lattice. The heat flux used in the effective thermal conductivity experiments was chosen to keep the temperature difference between the top and bottom plate temperature small. This ensured low Rayleigh numbers for the air trapped in the void spaces, thereby minimizing the buoyancy-driven convection. Note that since the solid-phase thermal conductivity was much larger than that of the fluid phase, the effective thermal conductivity determined via the above procedure depends on the lattice topology, its porosity, and the solid material used.

In addition to determining $k_{eff}$ of the lattice frame configuration cubic unit cell sample, the thermal conductivity of the solid sample made in SS420 (with 40% bronze infiltration) via the same AM process used to manufacture the lattice samples, was also measured. This solid block was 25.4 x 25.4 mm in cross-section and 100 mm in height. Four slots for thermocouple-based measurements were incorporated in the AM process itself. These samples were also tested on the same test bench as the lattice frame materials, as shown in **Fig. 3.1**. The thermal conductivity of the solid ($k_s$) was found to be 20.8 W/mK.

***Buoyancy-driven convection experimental setup***

The experimental setup for conducting buoyancy-driven convection experiments is shown in **Fig. 3.2**. The setup comprised of four wooden supports and two plastic wires, which suspended the additively manufactured cubic lattices in various heating orientations. This setup ensured minimal heat loss from the lattice to the supporting accessories, allowing free air flow through the lattice for all three heating orientations. The careful design of the suspension system was essential to maintain the structural integrity of the setup while minimizing any potential interference with the natural convection phenomena being studied.

The positioning of the supports was strategically determined to provide optimal stability while maximizing the exposure of the lattice surfaces to air flow. It was crucial to maintain constant laboratory ambient conditions throughout the course of steady-state experiments to prevent their influence on the convective heat transport within the lattice. The additively manufactured samples used in the buoyancy-driven convection experiments are shown in **Fig. 3.3**. Three aspect ratios were tested across bottom wall (BW), top wall (TW), and side wall (SW) heating orientations (**Fig. 3.2**). The samples were manufactured via binder jetting using stainless steel 420 with 40% bronze infiltration, with 5.08 mm cubic unit cells and cylindrical struts. A constant heat flux was maintained on the substrate using a firmly adhered flexible polyamide patch heater, backed by polystyrene insulation. Heat loss was monitored via two thermocouples placed inside and outside the insulation. The experiments covered Rayleigh numbers corresponding to substrate-ambient temperature differences of 10-60°C. The 3 mm thick substrate included a pre-designed hole (incorporated in the AM CAD model) for thermocouple placement, terminating at the center of the 50 mm x 50 mm substrate, 1 mm below the solid-fluid interface. Due to the material's high thermal diffusivity and the substrate's compact size, temperature measurements at this location effectively represented the wall temperature ($T_w$). The additively manufactured test sample was a single, integrated piece, eliminating contact resistance between the cubic lattices and the substrate. **Figure 3.3** shows CAD models of three lattice configurations with different aspect ratios.

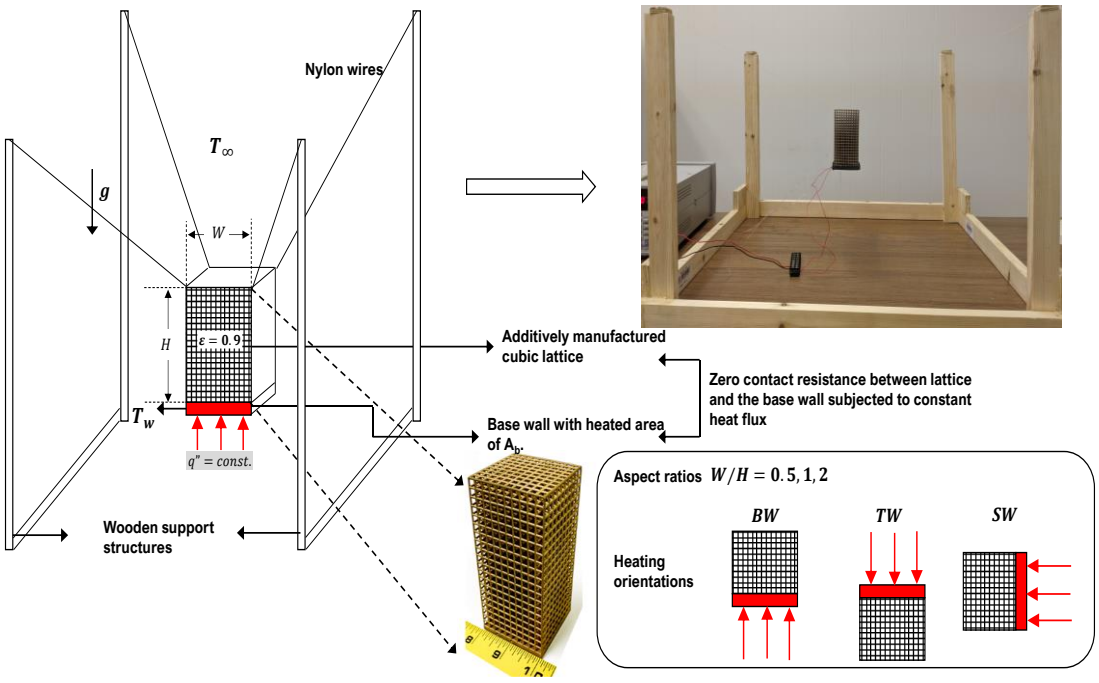



**Figure 3.2 Schematic representation of test setup for buoyancy-driven convection experiments, sample cubic lattice, and three different heating orientations**

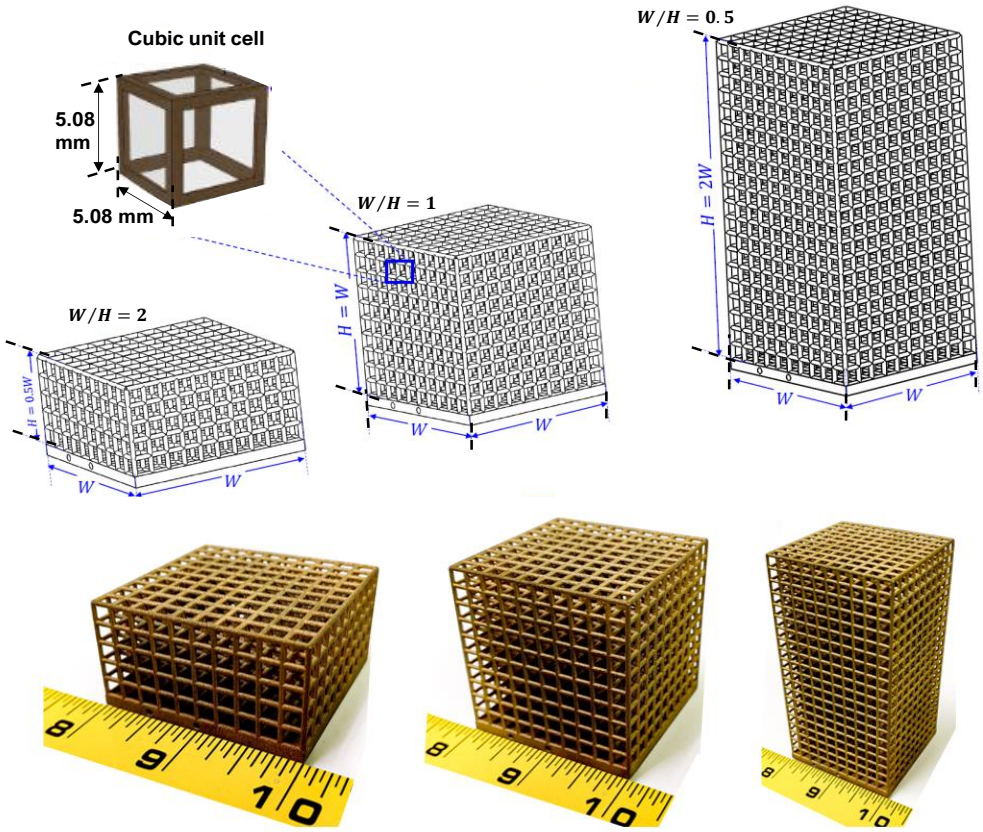



**Figure 3.3Three different aspect ratios (width-to-height ratio) for buoyancy-driven convection experiments (sample images are not representative of their true size, the scale shown at the bottom of each sample's image should be used for the intercomparisons of the size of samples)**

The lattices were designed with a porosity (ε) of 0.9 with cylindrical struts of ~1 mm diameter ($d_f$). Dimensions chosen to ensure accurate manufacturability via Binder jetting. The final 3D printed parts used in buoyancy-driven convection experiments achieved a porosity of ~0.87. This integrated manufacturing approach represents an advancement in thermal management design by eliminating thermal bottlenecks at contact interfaces while maintaining structural integrity. The minor difference between designed (0.9) and achieved (0.87) porosity falls within acceptable tolerances for binder jetting processes, validating this fabrication method for complex lattice structures. The 1 mm strut diameter selection optimizes both structural requirements and manufacturing constraints.

***Forced convection experimental setup***

The experimental setup for the forced convection experiments is shown in **Fig. 3.4**. These experiments were conducted using air drawn from a compressed air tank maintained at 100 psi pressure. The supply pressure was regulated down to a lower value based on the required air flow rate corresponding to the desired Reynolds number at the test section. This regulated flow system ensured precise control over experimental conditions while maintaining steady-state operation throughout the testing period.

Following pressure regulation, the air flow rate was metered using an orifice plate. Pressure, temperature, and differential pressure across the orifice plate were measured using Dwyer DPG-002, T-type thermocouple and Dwyer 477 AV-2 devices.

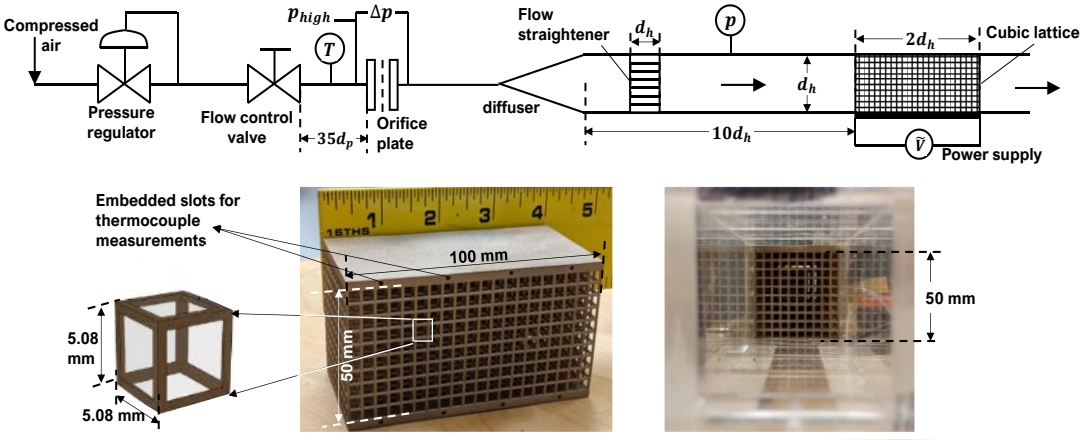



**Figure 3.4 Schematic of the forced convection experimental setup, test sample and its placement in the duct as seen by the flow entering the test section**

These measurements were used in the in-house computer program to iteratively determine the mass flow rate through the determination of flow coefficient and discharge coefficient of the orifice plate.

The air flow was then routed to a diffuser section connected to the test section. The diffuser was designed such that a uniform supply pressure could be obtained in the plane perpendicular to the bulk flow. The test section comprised of a straight channel ($10d_h$ in length) leading to the test article, allowing hydrodynamic flow development. The pressure drop at the test section was measured slightly upstream of the test section via a static pressure transducer. An exit length was also provided to avoid any back pressure effects resulting from sudden discharge of spent air into the laboratory ambience.

**Figure 3.4** also shows the test article used in the forced convection experiments. The heat transfer test article was manufactured in the same way as the test articles used in the buoyancy-driven convection experiments described above. In forced convection, the aim was to determine the convective heat transfer coefficient in the regime where net convective heat transport across one unit cell in streamwise direction does not change with streamwise location. The test article contained 10x10 cubic unit cells in the plane perpendicular to the bulk flow direction, while 20 unit cells were present in the streamwise direction. This arrangement resulted in unit aspect ratio of the channel. The unit aspect ratio is common in different heat exchanger applications, such as a typical circular duct in a shell-and-tube heat exchanger, square cross-section channels in crossflow heat exchanger with alternate hot and cold streams, mid-chord region of gas turbine airfoil internal which typically features angled rib turbulator on its two opposite walls. In several heat exchanger configurations, heat exchange from one channel typically occurs through the two opposite walls, while the other two confining walls are attached with adjacent channels carrying the same working fluid. Hence, the heating orientation in this study featured constant heat flux applied to the opposite walls, while the other two confining walls were adiabatic.

Forced convection experiments were conducted under steady-state conditions, with the two opposite walls (endwalls) subjected to constant heat flux via patch heaters. Stray heat losses from the thermal system were minimized by installing rubber foam insulation (k ~

0.037 W/mK) of 3.2 mm thickness on the backsides of the two opposite base plates subjected to heat flux. The remainder of the test section was made from clear acrylic which has low thermal conductivity, to further minimize stray heat loss. Although the heat loss was minimal due to the above-mentioned measures, the loss was still determined by measuring temperature drop across the insulator on both ends. The wall temperatures were measured at pre-existing slots for thermocouples distributed along the length of the test article. The patch heaters were connected to a DC power supply. The power supplied to individual patch heaters was determined by measuring the patch heaters' resistance and the current in the circuit as displayed in the DC power source. The forced convection experiments were conducted for Reynolds numbers between 5,000 – 20,000, which is lies in the turbulent flow regime, and finds its application in wide range of heat exchanger and thermal energy dissipation applications.

## Data reduction procedures

### *Effective thermal conductivity*

The effective thermal conductivity ($k_{eff}$) of the lattice was determined under steady-state conditions with one wall subjected to constant heat flux and the opposite wall maintained at a constant temperature (see **Fig. 3.1**). With known heat flux input and quantification of stray heat loss from the five faces of the cubic lattice sample (**Fig. 3.1**), the effective thermal conductivity was calculated as,

**Equation 3-1**

$$k_{eff} = \frac{(q_{total} - \sum q_{loss})H}{A_b(\tilde{T}_{w,top} - \tilde{T}_{w,bot})}$$

The total heat input ($q_{total}$) supplied to the system was determined using the fundamental relationship $i^2R_{htr}$, where $i$ represents the electrical current, and $R_{htr}$ is the resistance of the patch heater. The heat loss ($q_{loss}$) was determined by measuring temperature drop across the rubber foam thermal insulator (used to minimize the heat loss). It was found that the heat loss was less than 3% of the total heat input via the patch heater. In Eq. 3.1, $A_b$ is the area through which the unidirectional heat was being diffused, $\tilde{T}_w$ is the spatially averaged wall temperature, measured at both, the top and bottom walls, and $H$ is the height of the cubic unit cell (~5.08 mm).

***Buoyancy-driven convection experiment***

For each test condition, the DC power source was first set at a fixed voltage before switching on the power. Measurements were taken once the test section reached a steady state. The total heat supplied was determined by the current ($i$) flowing through the circuit and known resistance ($R_{htr}$) of the patch heater ($q_{total} = i^2 R_{htr}$). Further, the wall temperature ($T_w$) was measured by a thick thermocouple properly secured and flushed into the slot in the thickness of the substrate. Ambient temperature ($T_f$) was measured in the vicinity of the heated test section, although not exactly above the lattice sample to avoid the contribution from the plume. The convective heat transfer coefficient for buoyancy-driven convection was calculated from,

**Equation 3-2**

$$h = \frac{(q_{total} - q_{loss})}{A_b(T_w - T_f)} = \frac{q_{conv}}{A_b(T_w - T_f)}$$

where, $q_{conv}$ is the convective heat transfer determined by subtracting the heat loss ($q_{loss}$) from the backside of the patch heater from the total heat supplied ($q_{total}$), and $A_b$ is the base area. Heat transfer coefficient is also presented in normalized form of Nusselt number ($Nu$), where $Nu = hL_c/k_f$, $L_c$ is the characteristic length scale and $k_f$ is fluid thermal conductivity evaluated at the film temperature ($T_{film}$). For calculation of Rayleigh numbers ($Ra$), the required thermophysical properties were evaluated at the film temperature ($T_{film}$).

***Forced convection experiment***

The convective heat transfer coefficients for forced convection were determined based on the thermal measurements when the system had reached the steady state. It is calculated as:

**Equation 3-3**

$$h(x) = \frac{q_{total} - q_{loss}}{(A_b)\{T_w(x) - T_b(x)\}} = \frac{q"_{conv}}{\{T_w(x) - T_b(x)\}}$$

where the convective heat flux ($q"_{conv}$) was determined by calculating the total heat provided ($q_{total}$) to one patch heater and the heat loss ($q_{loss}$). Heat loss during forced convection experiments accounted for less than 3% of the total applied heat load. The

total heat provided during the steady-state experiments ($i^2 R_{htr}$) was determined by measuring the current ($i$) in the circuit for each of the patch heaters and the resistance of the patch heater ($R_{htr}$). Heat loss ($kA_b\ (\Delta T)_{ins}/t_{ins}$) was calculated using Fourier's law of conduction, with the temperature drop across the insulation measured as $(\Delta T)_{ins} = T_{ins,in} - T_{ins,out}$. Wall temperatures ($T_w$) were measured at four discrete locations on both top and bottom plates. The thermocouple slots are shown in **Fig. 3.4**. To determine the unit cell-based local heat transfer coefficient, the wall temperatures measured at four discrete locations were used to carry out interpolation between the four discrete locations to estimate temperatures at intermediate points and extrapolation to reach entrance and exit locations. The local bulk fluid temperature (Eq. 3.4) was determined by measuring the inlet temperature of air and performing a control volume-based analysis to determine the net heat added to the moving fluid via convection.

**Equation 3-4**

$$T_b(x) = T_{b,in} + \frac{2q"_{conv}W}{\dot{m}c_p}x$$

In Eq. 3.4, $T_{b,in}$ is the fluid temperature at the inlet, $\dot{m}$ is the mass flow rate of air, $c_p$ is the specific heat capacity of air, $W$ is the width of the channel, and "$x$" is the local position in the streamwise direction at which the local bulk fluid temperature was determined.

## Results and discussion

In this section, the flow and thermal characteristics of lattice structures constructed from a cubic unit cell are presented. The section is divided in three parts, (i) effective thermal conductivity, (ii) buoyancy-induced convection, and (iii) forced convection. The forced convection section also includes results for permeability and inertial coefficient results, followed by thermal hydraulic performance analysis.

### *Effective thermal conductivity*

Thermal transport in cellular materials depends on both the material's effective thermal conductivity and the interstitial heat transfer coefficient at its surfaces. Accurate determination of $k_{eff}$ is crucial for designing high heat dissipation systems and for volume-averaged computations using empirical correlations for $k_{eff}$.

**Figure 3.5** shows the $k_{eff}$ results for a cubic unit cell, determined from a lattice frame configuration featuring a single unit cell. This configuration functions as an inline array of cylindrical pin fins connecting the two endwalls that enclose the cubic unit cell. To ensure that the reported $k_{eff}$ is independent of the thermal boundary conditions, the $k_{eff}$ experiments were conducted by subjecting the top plate to three different heat flux levels. The normalized $k_{eff}/k_s$ was found to be independent of the applied heat flux level. The $k_{eff}$ results were normalized with $k_s$ (solid intrinsic thermal conductivity), which was determined through separate experiments on a solid block printed using the exact same procedure as for the lattices. Detailed results are presented in [3.23], with the average value of $k_s$ found to be 20.8 W/mK. Thus, samples for $k_{eff}$ experiments were designed to have a porosity of 0.87 to ensure that flow and heat transfer results could be presented for the cubic unit cell at a fixed porosity (0.87). However, the actual porosity of the 3D printed part turned out to be 0.85. Although the difference between the designed and actual porosity was not significant, the obtained $k_{eff}$ values were still modified to reflect the intended 0.87 porosity. This calculation was carried out using the *generalized* $k_{eff}$ correlations prescribed by Kaur et al. [3.24] and the cubic unit cell *specific* correlation prescribed by Wang et al. [3.23]. Both these approaches yielded similar $k_{eff}$ values of the cubic unit cell for lattice porosity of 0.87, as shown in **Fig. 3.5**.

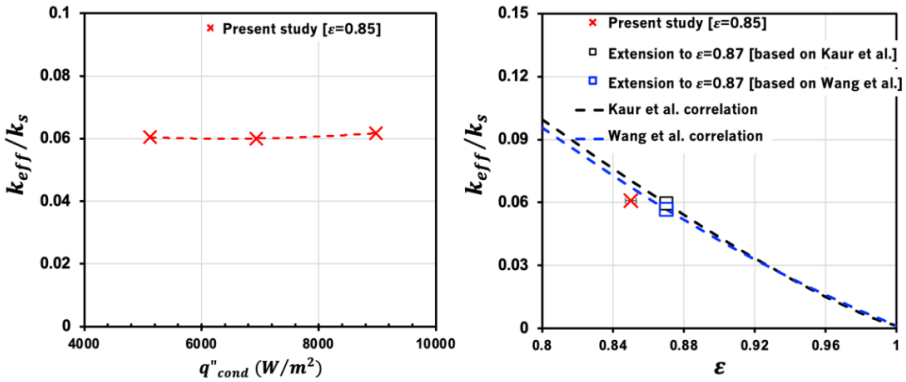



**Figure 3.5 Normalized results for effective thermal conductivity in the form keff/ks with respect to different levels of heat flux (left), comparison of the keff/ks results with correlations prescribed by Kaur et al. [3.24] and Wang et al. [3.23], along with the extension of obtained keff results to lattice porosity of 0.87**

***Buoyancy-induced convection***

Buoyancy-driven convection over a small plate with a cubic lattice structure integrally manufactured on top of it was investigated for three different cubic lattice configurations, each for three different heating orientations. For all three configurations, the heated area was 50 x 50 $mm^2$, essentially a small plate where edge effects are expected to influence local heat transfer. For further insight, see, for example, references [3.25] and [3.26] . The authors presented a qualitative sketch (**Fig. 3.6**) of typical flow over a small hot plate subjected to buoyancy-driven convection, with the hot side facing upwards [3.26]. The sketch reveals that in this particular configuration, boundary layer flows interact with each other, resulting in a complex flow with plume rising upwards from the center of the plate, which significantly impacts the overall heat transfer.

**Figure 3.7** illustrates the variation in the convective heat transfer coefficient for the three configurations shown in **Fig. 3.3** tested under three different heating orientations. Across all heating orientations, it was observed that the lower aspect ratio lattice configuration (taller samples) exhibited higher heat transfer compared to the shorter, higher aspect ratio lattice (**Fig. 3.3**). The lower aspect ratio lattice provided a higher wetted surface area but imposed greater blockage to the rising flow. While the larger wetted surface area aids in heat dissipation, the increased blockage diverts the flow to the path of least resistance, often sideways. For taller samples, smaller plate dimensions facilitated spent air escape along the open faces. Between competing factors—high wetted surface area and increased flow resistance—greater surface area appears dominant for low aspect ratio samples, yielding highest heat transfer. Among heating orientations, sideways heating (90°) yielded highest heat transfer, followed by bottom wall (0°) and top wall heating (180°), where bottom and top wall heating correspond to classic buoyancy-induced convection adjacent to heated plates facing upward and downward respectively. Since the purge through the side planes is common in all configurations, the overall trends were driven by the plate heating orientation [3.25]. Huang et al. [3.27] investigated three heating orientations for a flat plate featuring an array of pin fins and found that the heat transfer rates for sideways and bottom wall heating were comparable to each other and higher than the values for the top wall heating configuration.

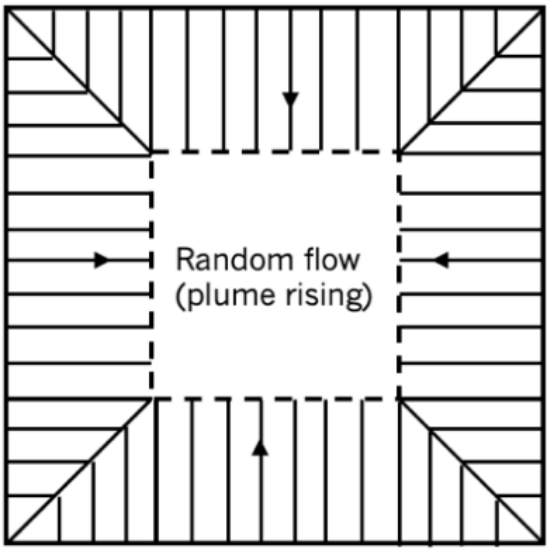



**Figure 3.6 A qualitative description of convection over a flat plate (small) with hot surface facing upwards, based on [3.26]**

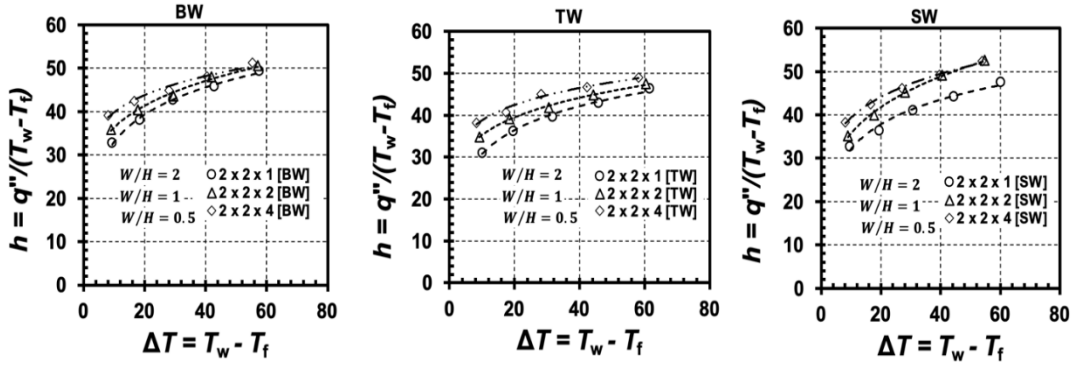



**Figure 3.7 Convective heat transfer coefficient versus wall to fluid temperature difference**

The authors' experiments on a flat plate (100 x 100 mm$^2$) showed that sideways heating produced slightly higher heat transfer rates than bottom wall heating, with both configurations significantly outperforming top heating orientations, as validated against Al-Arabi and El-Riedy [3.26].

**Figure 3.8** shows the normalized form of **Fig. 3.7**, where the Nusselt number is presented as a function of the Rayleigh number, and the characteristic length scale was based on the side length (W) of the heated plate. The overall trends discussed for **Fig. 3.7** are the same for **Fig. 3.8** as well. For the BW heating orientation, a comparison has been presented with respect to a baseline flat plate correlation [3.26] to show the enhancement in heat transfer due to the presence of the cubic lattice structures. The buoyancy-induced convection mode does not require additional pumping power to facilitate air flow through these lattice structures, making them highly reliable for cooling. This concept can be effectively applied in data center cooling, where the volume between adjacent racks can be packed with cube-shaped unit cells to enhance heat dissipation. Such an arrangement would result in a sideways heating configuration, as reported above. Additionally, while the cubic lattice samples studied here were additively manufactured, such geometries can also be manufactured via other techniques such as wire-based methods, which are considerably more cost-effective and are scalable. Such a manufacturing approach would require bonding of the lattice structure with the base plate from where the heat must be dissipated.

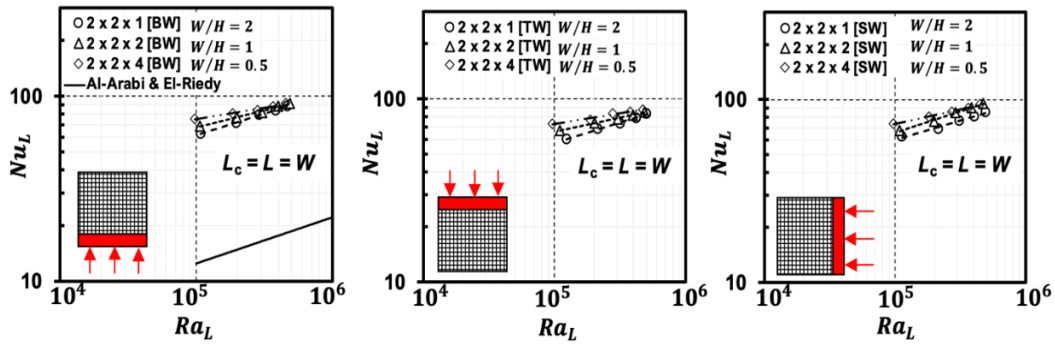



**Figure 3.8 Nusselt number versus Rayleigh number based on characteristic length scale of length or width of heated plate, also shown Al-Arabi & El-Riedy [3.26] correlation for flat heated plate facing upwards ($Nu_L = 0.7Ra_L^{1/4}$)**

***Forced convection***

Forced convection experiments were conducted using the cubic unit cell tested for effective thermal conductivity and buoyancy-driven convection. The sample featured 10 x 10 cubic unit cells in the plane perpendicular to bulk flow, with 20 unit cells arranged in the streamwise direction. This configuration was chosen to achieve periodic heat transfer at the unit cell level. **Figure 3.9** shows the unit cell level convective heat transfer coefficient variation with streamwise direction for four different flow conditions. Wall temperatures were measured at both top and bottom plates, as depicted in the sample image in **Fig. 3.4**. These measurements at the four discrete locations were used to extrapolate the measured temperature to the entrance and exit edges of the top and bottom plates and interpolate to obtain the wall temperatures at the unit cell level. The wall temperatures corresponding to each unit cell location in the streamwise direction were then used in Eq. 3.3 to derive the local convective heat transfer coefficient.

The experimental data presented in **Fig. 3.9** can be systematically divided into three distinct domains, each characterized by unique heat transfer behavior. The first domain, designated as the entry region (i), encompasses approximately the initial 40% of the streamwise length. This region exhibited both hydrodynamically and thermally developing flow characteristics as the fluid entered and adjusted to the porous medium environment.

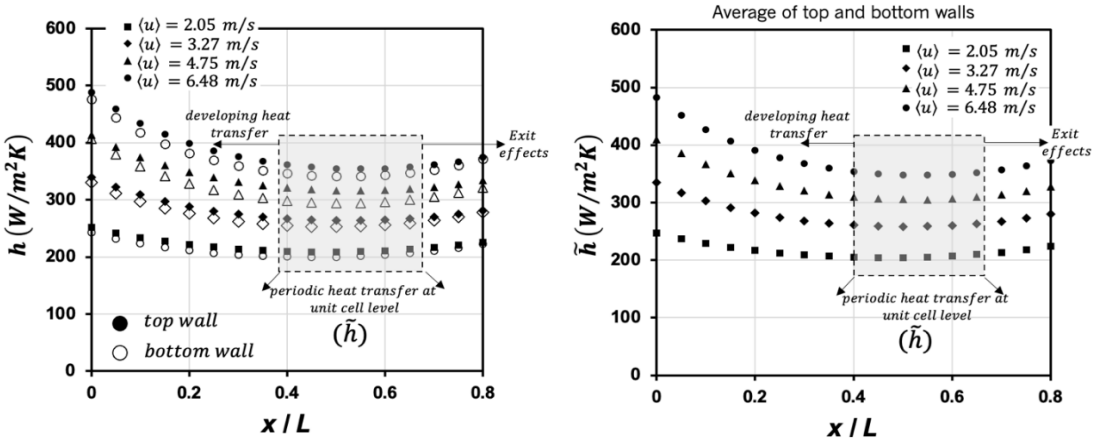



**Figure 3.9 Streamwise variation of local convective heat transfer coefficient determined at the top and bottom walls, also shown is the averaged heat transfer coefficient ($\tilde{h}$) by taking the local mean of the top and bottom plate *h*.**

The presence of an unheated entry length in this region significantly contributed to the enhanced heat transfer performance observed. This enhancement in the entrance region highlights the critical role of developing flow conditions in heat transfer systems. Moving downstream, the second region (ii), which comprises approximately 35% of the total streamwise length, is characterized by a nearly uniform heat transfer coefficient distribution. The convective heat transfer measurements obtained in this regime demonstrated values approximately 20% lower than those recorded in the entrance region when operating at the lowest flow velocity of 2.05 m/s.. Notably, comparable percentage reductions in heat transfer coefficients were consistently observed across all investigated flow velocities, as clearly illustrated in **Figure 3.9**.The convective heat transfer values corresponding to region (ii) represent a "periodic" nature, where the values are nearly similar at the unit cell level. Here, the periodicity in heat transfer refers to the case when the temperature rise of the working fluid when it passes through one unit cell in the streamwise direction is nearly the same. The convective heat transfer coefficient in the periodic regime can be used in the volume-averaged computations, as it is free from the entrance and exit effects and is representative of the sole effect of the unit cell topology on heat dissipation. Finally, in the last ~25% of the streamwise length (region iii), exit effects came into play.

**Figure 3.9** shows the average convective heat transfer coefficient between top and bottom walls at each unit cell, revealing distinct regional variations.. The heat transfer ($\bar{\bar{h}}$) reported in **Fig. 3.10** was taken to be the average of top and bottom wall heat transfer coefficient in the periodic regime as highlighted in **Fig. 3.9**. As expected, a power law dependence between $\bar{\bar{h}}$ and $\langle u \rangle$ was observed. Note that $\langle u \rangle$ is the average flow velocity at the entrance of the lattice sample and is determined by the total mass flow rate and total flow area in the supply duct leading to the test section (**Fig. 3.4**). The average flow velocity inside the lattice sample will be higher than $\langle u \rangle$, and is dependent on the lattice porosity ($\langle u \rangle_{lattice} \sim \langle u \rangle / \varepsilon$), where $\varepsilon$ is the porosity of the lattice sample (in this case, $\varepsilon$=0.87). For volume-averaged simulations, the flow velocity selected based on the respective formulations and appropriately apply the correlation, $\bar{\bar{h}} = 148.72 \langle u \rangle^{0.46}$.

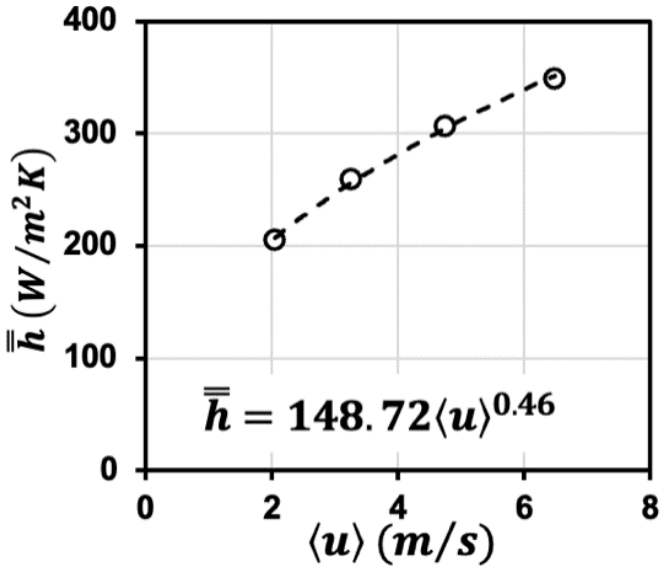



**Figure 3.10 Convective heat transfer coefficient in the periodic regime versus average inlet flow velocity**

In experimental investigations focused on enhanced heat transfer studies, the convective heat transfer coefficient arising from forced convection conditions is carefully evaluated against the pumping power requirements necessary to achieve desired cooling rates. This pumping power consumption fundamentally depends on both the properties of the working fluid and the geometric characteristics of the fluid flow path. When analyzing lattice structures or porous media, the flow resistance is typically characterized through the determination of two key parameters: the permeability (K) and the inertial coefficient ($C_f$). These parameters are essential for understanding the pressure losses within the system. The pressure gradient developing in the streamwise direction, can be mathematically expressed through the following relationship:

**Equation 3-5**

$$-\frac{dP}{dx} = \frac{\mu\langle u\rangle}{K} + \frac{\rho C_f}{\sqrt{K}}\langle u\rangle^2$$

In this study, the permeability and inertial coefficient of the lattice sample used in the forced convection study were determined by conducting pressure drop experiments for a wide range of flow velocities, as shown in **Figure 3.11**. The experimental data allowed us to accurately characterize both the low and high velocity effects. The relationship between the pressure gradient and the flow velocity was then used to perform regression

analysis to determine the values of K and $C_f$. The flow experiments were conducted separately to obtain the pressure drop data for multiple flow velocities over a wide range.

The K and $C_f$ values shown in **Fig. 3.11** were determined by carrying out regression analysis for different $\langle u \rangle_{max}$ values, where $\langle u \rangle_{max}$ represents the velocity up to which the pressure gradient dependence on flow velocity was considered.

Although theoretically, the $K$ and $C_f$ values should be independent of the choice of $\langle u \rangle_{max}$, our study showed otherwise. It was found that the knowledge of pressure drop for a broad range of flow velocities is essential to accurately capture $K$ and $C_f$ of the lattice structure. Such a behavior was also observed by Boomsma and Poulikakos [3.28] in an experimental study on compressed metal foams, where $K$ and $C_f$ values were found to be sensitive towards the choice of $\langle u \rangle_{max}$.

Interestingly, it was observed that $K$ and $C_f$ values became less sensitive to the choice of $\langle u \rangle_{max}$, for values $> 2\ m/s$. For the cubic lattice sample, these values were determined to be 3.7x10$^{-7}$ m$^2$ and ~0.047, respectively. These values characterize the net pressure drop across the cubic lattice samples for a given inlet flow velocity and can be used as inputs in volume-averaged computations. Note that these values of permeability and inertial coefficient are inclusive of the inherent roughness in the additively manufactured cubic lattice structure used in the experiments. The average roughness length scales for the employed AM technique are expected to be in the range of 20-30 $\mu m$, with localized roughness as large as 100 $\mu m$ [3.29]. The heat transfer coefficient results in the periodic heat transfer regime (region II), **Fig.3.10**, are presented in terms of Nusselt number ($Nu = \bar{\bar{h}} d_h / k_f$) vs Reynolds number ($\langle u \rangle d_h / \vartheta$), using the channel hydraulic diameter, $d_h$, as the length scale for normalization (**Fig. 3.12**).
Further, the enhancement in heat transfer is compared to a geometrically similar configuration without of the lattice structure, using the Dittus-Boelter correlation (Eq. 3.6) which provides a well-established relationship for predicting the Nusselt number in developed turbulent flow within tubes.

**Equation 3-6**

$$Nu_0 = 0.023 Re^{0.8} Pr^{0.4}$$

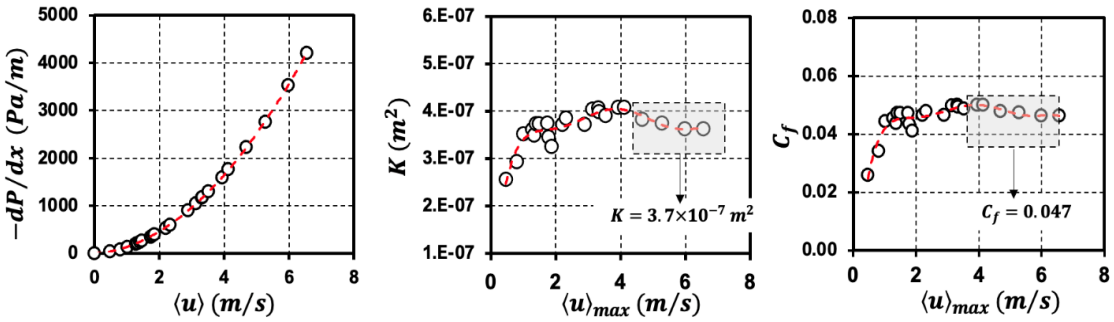



**Figure 3.11 Variation of pressure gradient with flow velocity, dependence of determined values of $K, C_f$ on the choice of $\langle u \rangle_{max}$ for regression analysis**

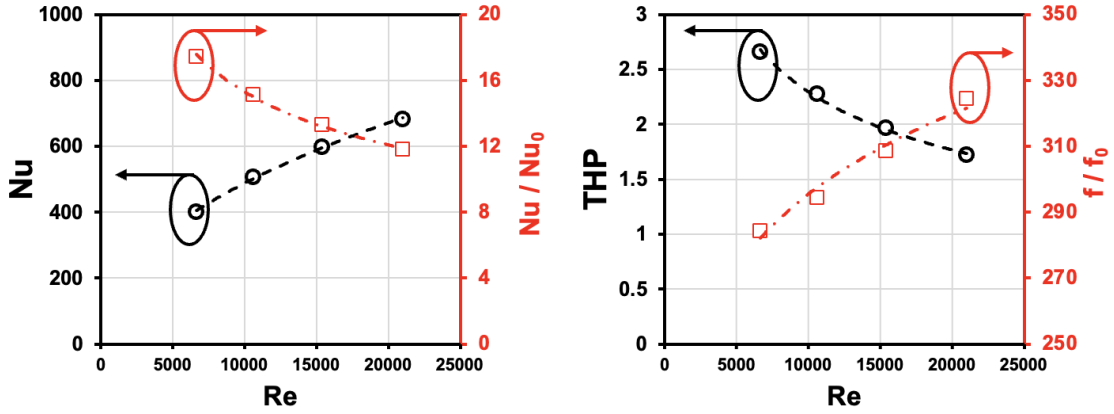



**Figure 3.12 Variation of $Nu$ and $Nu/Nu_0$ with Reynolds number (left), variation of THP and $f/f_0$ with Reynolds number (right)**

**Figure 3.12** shows the variation of Nusselt number and enhancement in Nusselt number with Reynolds number, where a power law dependence was observed for the Nu variation with Re.

The ratio $Nu/Nu_0$ showed a monotonically decreasing trend with increasing Reynolds number, which is also an expected trend in enhanced heat transfer studies in turbulent flow regime [3.14,3.16,3.30,3.31]. The heat transfer enhancement ranged between 12-18 times that of the smooth channel configuration across the investigated range of Reynolds number. Compared to smooth channel, lattice structures integrated with the smooth walls, offer superior heat transfer due to increase in wetted surface area augmenting the conjugate heat transfer, and endwall- and strut-based convective heat transfer coefficient enhancement due to strut-endwall interfaces and strut interconnections.

Although the enhancement is large compared to other enhanced heat transfer concepts such as rib turbulators, it is important to recognize that the concept employed in the present study occupied the entire channel flow cross section area and flow volume, unlike enhanced heat transfer features such as rib turbulators, which are near-wall placements. Consequently, the pressure drop for porous media concepts is expected to be large, despite the high porosity of the employed lattice structures. Thus, it is critical to evaluate the enhancement in heat transfer in conjunction with the concomitant increase in pressure drop. The normalized pressure drop is given as,

**Equation 3-7**

$$\frac{f}{f_0} = \frac{(\Delta p)_L}{2\rho(\langle u \rangle)^2}\frac{d_h}{L}\left[\frac{1}{0.079Re^{-0.25}}\right]$$

The thermal hydraulic performance (THP) metric, which combines the enhancement in heat transfer ($Nu/Nu_0$) with the penalty on pressure drop ($f/f_0$) is given as,

**Equation 3-8**

$$THP = \frac{(Nu/Nu_0)}{(f/f_0)^{(1/3)}}$$

**Figure 3.12** also shows the variation of the THP and $f/f_0$ versus Reynolds number. Although the pressure drop penalty was large, the significant enhancement in heat

transfer compensates for this loss, resulting in an overall higher thermal hydraulic performance was observed for the cubic lattice structure. Across the range of Reynolds number, the THP was found to vary between 1.5 and 2.5.

## Conclusions

A comprehensive experimental study was conducted to characterize the flow and thermal transport in lattice structures made from cubic unit cells in buoyancy-induced and forced convection. These structures were made using binder jet additive manufacturing technique in stainless steel 420 (with 40% bronze infiltration). The experiments revealed crucial insights into the effective thermal conductivity, permeability, inertial coefficient, and convective heat transfer coefficients of these structures, as follows.

(a) The effective thermal conductivity closely followed the correlation proposed by Kaur et al. [3.24], with $k_{eff}/k_s$ ~ 0.06 for porosity between 0.85-0.87, where $k_s$ ~ 20.8 W/mK. The $k_{eff}$ results were minimally affected by roughness since the air trapped in the void spaces was mostly stagnant, and local roughness was accounted for in the reported measured porosity values.

(b) Permeability and inertial coefficient for cubic lattice structure with 0.87 porosity were ~ $3.7\text{x}10^{-7}$ $m^2$ and 0.047, respectively.

(c) The buoyancy-driven convection data taken for three cubic lattice configurations with aspect ratios of 0.5, 1.0 and 2.0, using three different heating orientations—sideways heating (90°), bottom wall heating (0°) and top wall heating (180°)— revealed that sideways heating and bottom wall heating exhibit similar heat transfer performances, with both being superior to top wall heating.

(d) The steady state forced convection data with cubic unit cells placed in a channel with top and bottom walls subjected to constant heat flux indicated that the presence of cubic lattice structures enhanced heat transfer by 12-18 times compared to a smooth channel, across the investigated range of Reynolds number. The thermal hydraulic performance (THP) varied between 1.5 and 2.5. Furthermore, the unit cell heat transfer coefficient in the periodic heat transfer regime correlated with the average flow velocity at the inlet, by $\bar{\bar{h}} = 148.72\langle u \rangle^{0.46}$.

In conclusion, cubic lattice structures offer promising cooling solutions, achievable through additive manufacturing or more cost-effective wire-based and subtractive techniques with potentially lower surface roughness.

## Nomenclature

| | |
|---|---|
| $A_b$ | plate surface area |
| $C_f$ | inertial coefficient |
| $d_h$ | channel hydraulic diameter |
| $f$ | friction factor |
| $h$ | *convective* heat transfer coefficient |
| $k_{eff}$ | effective thermal conductivity |
| $k_f$ | air thermal conductivity |
| K | permeability |
| L | length of sample used in forced convection |
| $L_c$ | characteristic length scale |
| $Nu$ | Nusselt number |
| p | pressure |
| $Q_{total}$ | total heat supplied |
| $Ra$ | Rayleigh number |
| Re | Reynolds number |
| $R_{htr}$ | heater resistance |
| $T_{film}$ | film temperature |
| $T_w$ | wall temperature |
| $T_f$ | ambient temperature |
| THP | thermal hydraulic performance |
| $\langle u \rangle$ | inlet velocity in forced convection experiments |

## Greek symbols

| | |
|---|---|
| $\rho$ | density of air |
| $\vartheta$ | kinematic viscosity of air |

## References

[3.1] V.V. Calmidi, R.L. Mahajan, Forced Convection in High Porosity Metal Foams, Journal of Heat Transfer 122 (2000) 557–565. https://doi.org/10.1115/1.1287793.

[3.2] M.S. Phanikumar, R.L. Mahajan, Non-Darcy natural convection in high porosity metal foams, International Journal of Heat and Mass Transfer 45 (2002) 3781–3793. https://doi.org/10.1016/S0017-9310(02)00089-3.

[3.3] A. Bhattacharya, R.L. Mahajan, Finned Metal Foam Heat Sinks for Electronics Cooling in Forced Convection, J. Electron. Packag 124 (2002) 155–163. https://doi.org/10.1115/1.1464877.

[3.4] A. Bhattacharya, R.L. Mahajan, Metal Foam and Finned Metal Foam Heat Sinks for Electronics Cooling in Buoyancy-Induced Convection, Journal of Electronic Packaging 128 (2005) 259–266. https://doi.org/10.1115/1.2229225.

[3.5] A. Bhattacharya, V.V. Calmidi, R.L. Mahajan, Thermophysical properties of high porosity metal foams, International Journal of Heat and Mass Transfer 45 (2002) 1017–1031. https://doi.org/10.1016/S0017-9310(01)00220-4.

[3.6] V.V. Calmidi, R.L. Mahajan, The Effective Thermal Conductivity of High Porosity Fibrous Metal Foams, Journal of Heat Transfer 121 (1999) 466–471. https://doi.org/10.1115/1.2826001.

[3.7] C.Y. Zhao, Review on thermal transport in high porosity cellular metal foams with open cells, Int. J. Heat Mass Transf 55 (2012) 3618–3632. https://doi.org/10.1016/j.ijheatmasstransfer.2012.03.017.

[3.8] Y. Li, L. Gong, M. Xu, Y. Joshi, A Review of Thermo-Hydraulic Performance of Metal Foam and Its Application as Heat Sinks for Electronics Cooling, Journal of Electronic Packaging 143 (2021). https://doi.org/10.1115/1.4048861.

[3.9] D. Liang, G. He, W. Chen, Y. Chen, M.K. Chyu, Fluid flow and heat transfer performance for micro-lattice structures fabricated by Selective Laser Melting, International Journal of Thermal Sciences 172 (2022) 107312. https://doi.org/10.1016/j.ijthermalsci.2021.107312.

[3.10] S. Takarazawa, K. Ushijima, R. Fleischhauer, J. Kato, K. Terada, W.J. Cantwell, M. Kaliske, S. Kagaya, S. Hasumoto, Heat-transfer and pressure drop characteristics of micro-lattice materials fabricated by selective laser metal melting technology, Heat Mass Transfer 58 (2022) 125–141. https://doi.org/10.1007/s00231-021-03083-0.

[3.11] I. Kaur, P. Singh, Flow and Thermal Transport Through Unit Cell Topologies of Cubic and Octahedron Families, International Journal of Heat and Mass Transfer 158 (2020) 119784. https://doi.org/10.1016/j.ijheatmasstransfer.2020.119784.

[3.12] A. Lorenzon, E. Vaglio, L. Casarsa, G. Totis, Effects of different cross-sections of Body Centered Cubic cells on pressure drop and heat transfer of additively manufactured heat sinks, International Journal of Heat and Mass Transfer 222 (2024) 125170. https://doi.org/10.1016/j.ijheatmasstransfer.2024.125170.

[3.13] A. Chaudhari, P. Ekade, S. Krishnan, Experimental investigation of heat transfer and fluid flow in octet-truss lattice geometry, International Journal of Thermal Sciences 143 (2019) 64–75. https://doi.org/10.1016/j.ijthermalsci.2019.05.003.

[3.14] I. Kaur, Y. Aider, K. Nithyanandam, P. Singh, Thermal-hydraulic performance of additively manufactured lattices for gas turbine blade trailing edge cooling, Applied Thermal Engineering 211 (2022) 118461. https://doi.org/10.1016/j.applthermaleng.2022.118461.

[3.15] I. Kaur, P. Singh, Endwall heat transfer characteristics of octahedron family lattice-frame materials, International Communications in Heat and Mass Transfer 127 (2021) 105522. https://doi.org/10.1016/j.icheatmasstransfer.2021.105522.

[3.16] Y. Aider, I. Kaur, H. Cho, P. Singh, Periodic heat transfer characteristics of additively manufactured lattices, International Journal of Heat and Mass Transfer 189 (2022) 122692. https://doi.org/10.1016/j.ijheatmasstransfer.2022.122692.

[3.17] I. Kaur, P. Singh, State-of-the-art in heat exchanger additive manufacturing, International Journal of Heat and Mass Transfer 178 (2021) 121600. https://doi.org/10.1016/j.ijheatmasstransfer.2021.121600.

[3.18] I. Kaur, P. Singh, Critical evaluation of additively manufactured metal lattices for viability in advanced heat exchangers, International Journal of Heat and Mass Transfer 168 (2021) 120858. https://doi.org/10.1016/j.ijheatmasstransfer.2020.120858.

[3.19] C.Y. Zhao, T.J. Lu, H.P. Hodson, Natural convection in metal foams with open cells, Int. J. Heat Mass Transf 48 (2005) 2452–2463. https://doi.org/10.1016/j.ijheatmasstransfer.2005.01.002.

[3.20] S. Feng, F. Li, F. Zhang, T.J. Lu, Natural convection in metal foam heat sinks with open slots, Exp, Therm. Fluid Sci 91 (2018) 354–362. https://doi.org/10.1016/j.expthermflusci.2017.07.010.

[3.21] Z. Qu, T. Wang, W. Tao, T. Lu, Experimental study of air natural convection on metallic foam-sintered plate, International Journal of Heat and Fluid Flow 38 (2012) 126–132. https://doi.org/10.1016/j.ijheatfluidflow.2012.08.005.

[3.22] Y. Aider, I. Kaur, R.L. Mahajan, P. Singh, Enhancing buoyancy-driven convection transport between two vertical parallel plates with symmetric and asymmetric heating using additively manufactured lattice structures, International Journal of Heat and Mass Transfer 222 (2024) 125141. https://doi.org/10.1016/j.ijheatmasstransfer.2023.125141.

[3.23] N. Wang, I. Kaur, P. Singh, L. Li, Prediction of effective thermal conductivity of porous lattice structures and validation with additively manufactured metal foams, Appl. Therm. Eng 187 (2021) 116558,. https://doi.org/10.1016/j.applthermaleng.2021.116558.

[3.24] I. Kaur, R.L. Mahajan, P. Singh, Generalized correlation for effective thermal conductivity of high porosity architectured materials and metal foams, International Journal of Heat and Mass Transfer 200 (2023) 123512. https://doi.org/10.1016/j.ijheatmasstransfer.2022.123512.

[3.25] B. Gebhart, Y. Jaluria, R. Mahajan, B. Sammakia, Buoyancy-induced Flows and Transport, Hemisphere Publishing Corporation, 1988.

[3.26] M. Al-Arabi, M.K. El-Riedy, Natural convection heat transfer from isothermal horizontal plates of different shapes, International Journal of Heat and Mass Transfer 19 (1976) 1399–1404. https://doi.org/10.1016/0017-9310(76)90069-7.

[3.27] R.-T. Huang, W.-J. Sheu, C.-C. Wang, Orientation effect on natural convective performance of square pin fin heat sinks, International Journal of Heat and Mass Transfer 51 (2008) 2368–2376. https://doi.org/10.1016/j.ijheatmasstransfer.2007.08.014.

[3.28] K. Boomsma, D. Poulikakos, The Effects of Compression and Pore Size Variations on the Liquid Flow Characteristics in Metal Foams, Journal of Fluids Engineering 124 (2001) 263–272. https://doi.org/10.1115/1.1429637.

[3.29] I. Kaur, P. Singh, Effects of inherent surface roughness of additively manufactured lattice frame material on flow and thermal transport, International Journal of Heat and Mass Transfer 209 (2023) 124077. https://doi.org/10.1016/j.ijheatmasstransfer.2023.124077.

[3.30] P. Singh, Y. Ji, S.V. Ekkad, Multipass Serpentine Cooling Designs for Negating Coriolis Force Effect on Heat Transfer: 45-deg Angled Rib Turbulated Channels, J. Turbomach 141 (2019). https://doi.org/10.1115/1.4042648.

[3.31] P. Singh, Y. Ji, S.V. Ekkad, Experimental and numerical investigation of heat and fluid flow in a square duct featuring criss-cross rib patterns, Appl. Therm. Eng 128 (2018) 415–425. https://doi.org/10.1016/j.applthermaleng.2017.09.036.

# CHAPTER FOUR :

# EXPERIMENTAL STUDY ON FLOW AND THERMAL TRANSPORT CHARACTERISTICS OF MOVING PACKED BED THROUGH A CHANNEL FEATURING SINGLE COLUMN OF INLINE CYLINDRICAL PINS

## Abstract

An experimental study is conducted to understand the fundamental flow and thermal transport characteristics of moving packed bed (MPB) through closely spaced parallel plates. An enhanced heat transfer concept based on cylindrical pins is experimentally investigated in this study. A simplified geometry involving two parallel plates as baseline configuration is considered, where the pin fin configuration involved a series of pin fins arranged in a single column, joining the two parallel plates. Steady-state heat transfer experiments have been conducted with particles of diameter ~400 μm and for three parallel plate spacings (3-7 mm) as well as three pin heights (3-7 mm). The heat transfer experiments involved parallel plates subjected to uniform heat flux with particles supplied at room temperature. The optical flow experiments were conducted to determine high spatio-temporal resolution near-wall flow-field of moving packed bed of particles. The experiments reveal that the separation between the parallel plates have a dominant effect on convective heat transfer, with lowest plate spacing yielding the highest heat transfer. Further, addition of pin fins results in local enhancement in flow velocities around the pin, while also resulting in a dead zone of stagnant or very slowly moving packed bed in the region upstream of the pins, and a void zone just downstream of the pin which does not feature particles. Pin fins also provide increased wetted surface area along with facilitating the conjugate heat transfer by transferring energy between the walls and the moving heat transfer media (HTM: particles). As a result of these complex mechanisms at play, the pin fin configurations had superior heat transfer performance compared to the baseline configurations.

Keywords: moving packed bed; concentrating solar power; enhanced heat transfer.

## Introduction

We have carried out a comprehensive experimental study to understand the fundamental flow and thermal transport of MPB of particles through an inline arrangement of cylindrical obstructions, where the plate spacing was varied between 3 to 7 mm, which represents the state-of-the-art shell-and-plate heat exchangers. The particles' flow-field near the wall is captured through a novel optical flow method, and the local heat transfer coefficient is determined by carrying out quasi steady state

experiments. Following sections provide details on the different experimental setups employed for the study of flow and thermal transport of MPB of particles, test section details, flow, and heat transfer measurement technique, followed by uncertainty analysis, results and their discussion, and concluding remarks.

## Test section details

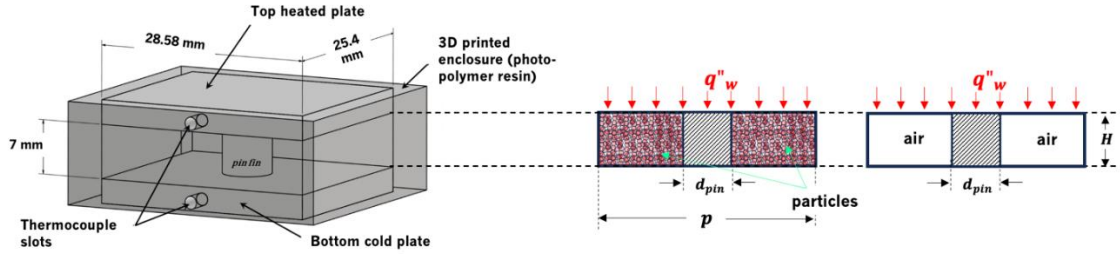
In this comprehensive study, three distinct types of experiments were conducted to thoroughly characterize both the flow behavior and thermal transport phenomena in a Moving Packed Bed (MPB) of particles flowing through an inline arrangement of cylindrical pin fins. These experiments were designed to investigate multiple critical aspects of the system's performance and validate key hypotheses. To test the hypothesis, that adding solid metallic obstruction joining the two parallel plates enhances the effective thermal conductivity ($k_{eff}$) of the packed bed of particles even at a cost of lower mass of particles: dedicated experiments to quantify the $k_{eff}$ of a periodic test section featuring a cylindrical pin, with and without the packed bed of particles. Further, to test the second hypothesis that the addition of pin fins modifies the particle flow field and facilitate conjugate heat transfer through enhanced surface area and joining the heated walls together through the flow domain. To quantify the effects of pin fins on convective heat transfer coefficient, MPB experiments were conducted at the University of Tennessee, Knoxville Particle Elevator and Heat Exchanger Test Facility, in a quasi-steady state through continuous supply of particles to the heated test section. In the end, to understand the obtained heat transfer results of MPB of particles, optical flow experiments were conducted in the same test facility, but with optically clear test section.

### *Effective thermal conductivity experiments*

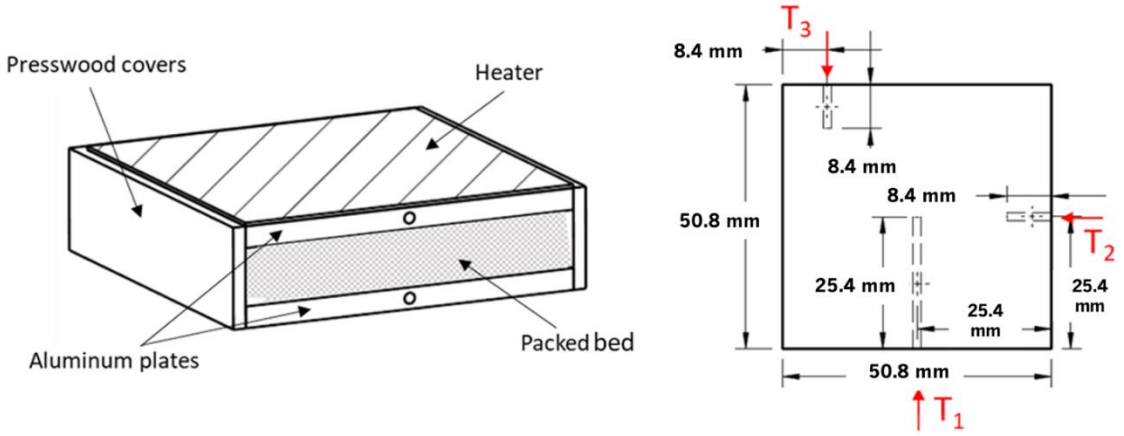
Figure 4.1 provides a detailed illustration of the test section designed and implemented for quantifying the thermal performance of a sample featuring a cylindrical pin, both in isolation and in combination with a packed bed of particles. The central component of this experimental setup consisted of an isolated cylindrical pin, precisely positioned at the geometric centers of two parallel plates measuring 25.4 mm x 28.58 mm. This critical component was manufactured through computerized numerical controlled (CNC) machining techniques, resulting in exceptionally smooth surface profiles. The surface

quality was rigorously monitored throughout the manufacturing process using high-precision profilometry to ensure consistency across all test specimens. The achieved average surface roughness was approximately 3 micrometers, a value that proves negligibly small when compared to the other significant length scales that define the fundamental parameters of this experimental investigation. It's important to note that the dimensional specifications were carefully chosen: the 25.4 mm measurement represents the characteristic channel width, while the 28.58 mm dimension corresponds to the precise pitch spacing between two consecutive pins in the flow and heat transfer experiments. This precise dimensional control was essential for maintaining experimental repeatability and ensuring accurate comparison with computational fluid dynamics simulations. For comparative purposes, a secondary baseline case investigating the thermal behavior of a packed bed of particles without the presence of a cylindrical pin was previously examined and thoroughly documented in our earlier research publication [4.1].

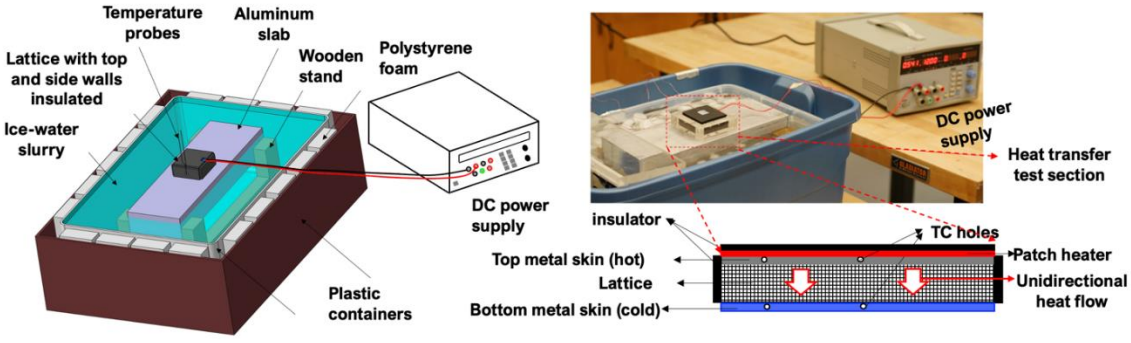
In the context of the present experimental investigation, CARBOBEAD particles, specifically the CP 30/60 grade, were selected as the primary thermal energy storage medium and heat transfer material (HTM). The mean particle diameter was approximately 400 micrometers, determined using an Anton Paar PSA 1190 LD particle size analyzer, as detailed in our previous work [4.1]. The experimental methodology involved the particles within the test section depicted in **Fig. 4.1**, employing a systematic approach that included periodic vibration of the test section combined with controlled particle addition to maximize the occupancy of available void space. The packing density was carefully monitored throughout the filling process using real-time mass measurements to ensure uniform distribution and optimal void space utilization. Thermocouple slots were imbedded into both the top and bottom walls of the samples. CNC machining was implemented for creating thermocouple slots of diameter 1.65 mm. This was necessary to ensure a tight fit between the thermocouple sheath and wall material that we are measuring. For this series of thermal performance investigations, the experiments were specifically conducted using a test section configuration incorporating a single pin fin with a precisely maintained height of 7 millimeters.




**(a)**




**(b)**




**(c)**

**Figure 4.1 (a) single-pin test coupon for $k_{eff}$ characterization, (b) heater assembly and thermocouple slot arrangement, (c) test section for $k_{eff}$ experiments**

***Convective heat transfer and optical flow experiments***

The convective heat transfer and optical flow experiments were conducted on a single column of inline arrangement of cylindrical pin fins where the test section was designed such that both, developing and periodic heat transfer regimes could be obtained. To this end, **Fig. 4.2** shows the test section details for the heat transfer, which comprised of an integrated part with nine cylindrical pin fins along with the bottom plate, a top plate, sidewalls with through-holes to allow the insertion of thermocouples in the CNC machined top and bottom plates, through-holes allowing press fit of the top and bottom plate-assembly, to avoid any thermal contact resistance. The test section was joined with 3D printed diffusers which allowed uniform distribution of particles at the inlet and allowed fine control of mass flow rate by selecting constriction at the bottom diffuser to facilitate a MPB arrangement. The assembled test section shown in **Fig. 4.2b** was installed in the particle elevator and heat exchanger test facility (discussed later). A total of 9 cylindrical pins of diameter 6.35 mm were arranged in line with each other, where the MPB flow of particles was confined in a narrow channel with a width (W) of ~ 25 mm, with channel heights varied as 3, 5 and 7 mm. These channel heights were selected as they represent the design domain of the falling particle side of the state-of-the-art shell-and-plate heat exchanger for particle-to-s$CO_2$ heat transfer [4.2]. Further, typical particle sizes explored for this application range from 200-1000 μm [4.1,4.2], where it has been shown that smaller particle diameters yield in superior thermal transport. However, smaller particle diameters also present a challenge in maintaining their morphology and properties with prolonged operations. Hence, to strike a balance between the ability to yield high convective transport and maintaining the morphology, we chose a particle diameter of ~400 μm for the current investigation. The centers of adjacent pins in the streamwise direction were separated by 28.58 mm (**Fig. 4.3** The top and bottom plates featured nine thermocouple slots drilled to mid-channel span beneath each pin fin center, with the first and last pin fins positioned 19.05 mm from the channel entrance and exit, respectively. Additional temperature measurements were carried out in the vicinity of the $7^{th}$ and $8^{th}$ pin from the inlet by drilling holes in the thickness of the top and bottom plate (shown in zoomed view)

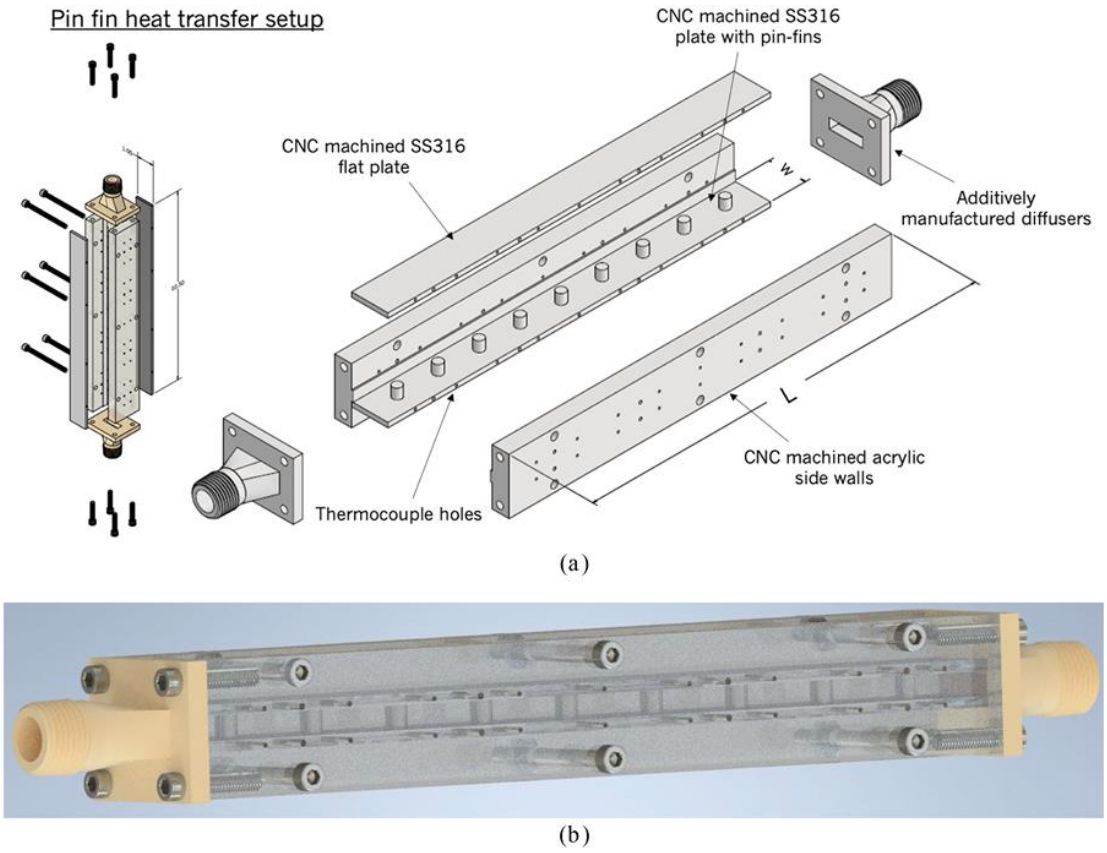



**Figure 4.2 (a) exploded view of the convective heat transfer test section, (b) assembled view of the same test section.**

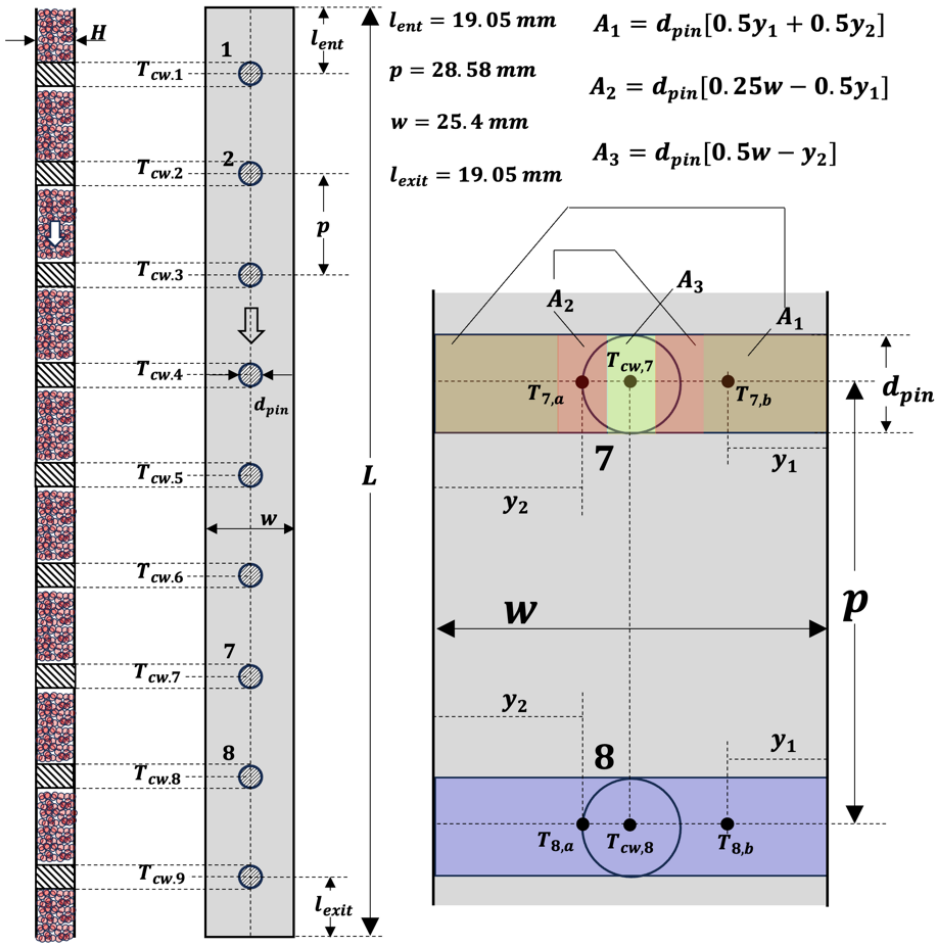



**Figure 4.3 Details of nomenclature used for convective heat transfer experiments**

The detailed local temperature measurements around a pin allowed the calculation of convective heat transfer coefficient which is appropriate for the local pin. More details on the selection of $7^{th}$ and $8^{th}$ pin for local temperature measurements are provided in the subsequent test sections.

For the convective heat transfer experiments, the test section was CNC machined with Stainless Steel 316L (SS316L) material to capture the conjugate heat transfer characteristics of concept involving extended surfaces, such as pin fins in this case. The SS316L material was chosen as the state-of-the-art particle-to-s$CO_2$ heat exchangers are manufactured in this material. In order to capture the near-wall particle flow dynamics, separate test sections were constructed which could allow optical access for high-speed imaging. **Figure 4.4** shows the optical flow experimental setup in reference to the particle elevator and heat exchanger test facility, which comprised of a series of interconnected buckets by a chain, where the chain's motion was powered by an electric motor and its speed was controlled via a variable frequency drive (VFD). The elevator facility was constructed to allow a continuous-mode particle-based experiments which are critical for both heat transfer and flow characterization.

In context to heat transfer, a quasi-steady state condition must be maintained to determine the convective heat transfer coefficient due to MPB of particles between parallel plates subjected to spatially uniform and temporally invariant heat flux. The elevator facility featured a large hopper which stored a large mass of particles. The hopper had a small opening at its bottom to allow a desired flow rate of particles into the test section. This facility was used for both heat transfer and optical flow experiments. In the case of optical flow experiments, a high-speed camera and high-intensity light were installed in front of the test section to illuminate the particles and capture the frames as the packed bed moves through the pin fin test section. For the optical flow experiments, separate test sections were made which could allow optical access inside the moving packed bed (**Fig. 4.4c**). To this end, pin fins of diameter 6.35 mm and of different heights (varying between 3-7 mm) were additively manufactured using stereolithography technique with high layer resolution. The layer thickness was maintained at 50 micrometers accuracy.

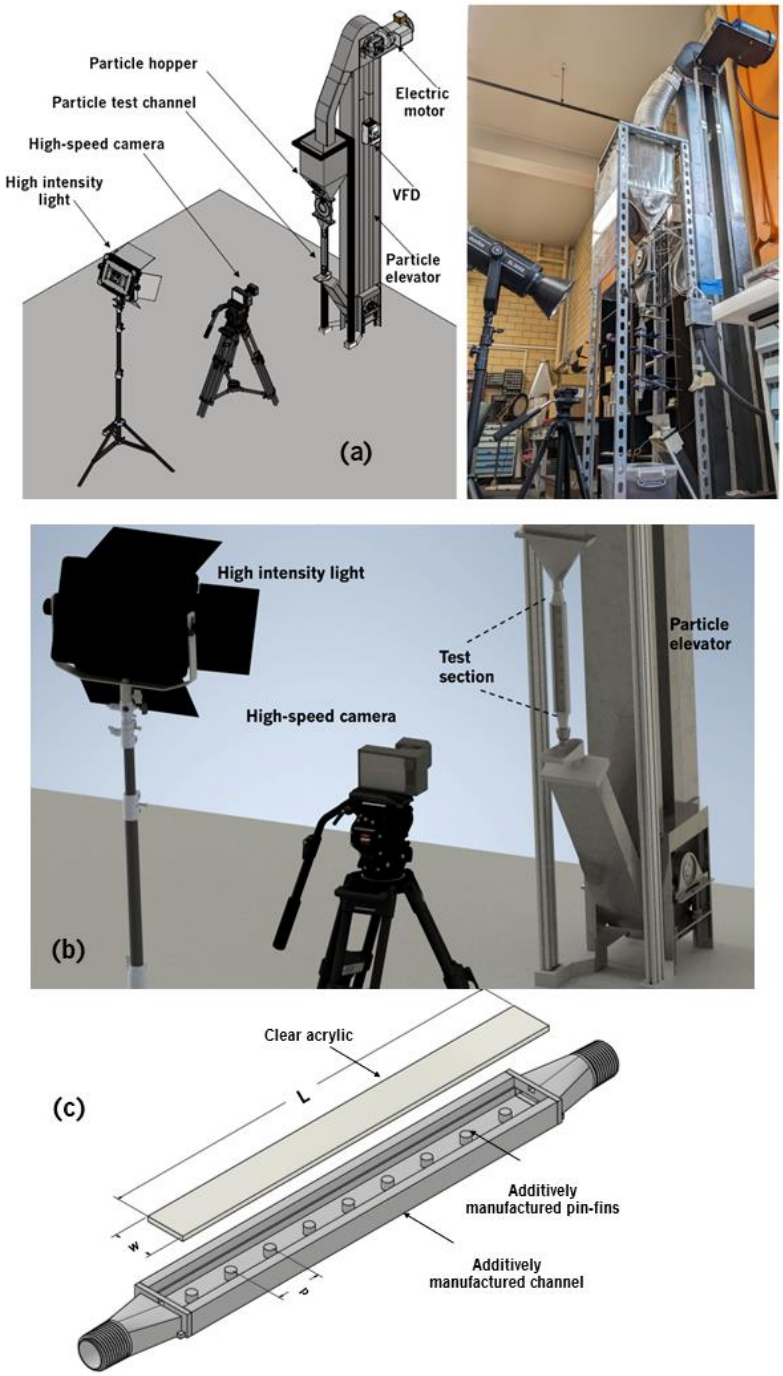



**Figure 4.4(a) CAD model of the optical flow test setup including the particle elevator and heat exchanger test facility, (b) zoomed-in view of optical flow experimental test setup, (c) details of the test section employed for optical flow experiments**

The pins were then joined with two parallel plates made in clear acrylic and machined through water jet technique to achieve precise dimensions. Note that in flow experiments, the contact resistance between the pin fins and the top and bottom plates is not relevant since the experiments do not include heat transfer, and MPB of particles were maintained at the room temperature.

## Experimental procedures and measurement techniques

In this section, the experimental procedure and measurement techniques employed to process the heat transfer and optical flow experiments, to obtain effective thermal conductivity, convective heat transfer coefficient, and local velocity magnitude of particles, are presented.

### *Effective thermal conductivity experiments*

The test setup employed for $k_{eff}$ determination is shown in **Fig. 4.1c**. The test sample comprised of two plates with a single cylindrical pin sandwiched between them. The bottom plate was attached to a thick aluminum slab which was partially submerged in an ice-water slurry maintained at ~ 0℃. The large thermal mass of the aluminum slab served as the chilled reservoir for the heat transfer experiments. The top plate was subjected to a spatially uniform and time-independent heat flux. This arrangement of cold bottom plate and heated top plate separated by a pin of 7 mm height, allowed a unidirectional heat flow from the top to the bottom plate, through the volume comprising of pin, air, or particles/air. The steady-state experiments were conducted at three different heat flux levels applied to the top plate, ensuring that the reported $k_{eff}$ values were independent of the thermal boundary conditions. Further, the top plate and particles/pin's temperature was only 10-20℃ greater than the bottom plate's temperature, hence the effects of radiation was neglected. The sole purpose of $k_{eff}$ experiments was to establish the efficacy of introducing pin fins as a means of increasing the effective thermal conductivity in reference to simple packed bed of particles, as tested in [4.1]. Once the steady state was reached, the conductive heat flux, and the top and bottom plate temperatures were measured, to determine $k_{eff}$ based on Fourier's law of conduction

(Eqns. 4.1, 4.2). The measurements were recorded after ensuring temperature a steady state condition.

**Equation 4-1**

$$k_{eff} = \frac{(q_{cond}/A)H}{\Delta T} = \frac{[\{q_{total} - \sum q_{loss}\}/A]H}{\tilde{T}_{top} - \tilde{T}_{bottom}}$$

**Equation 4-2**

$$\sum q_{loss} = \frac{k_{ins}}{t_{ins}}\left[A\left(T_{top,in} - T_{top,out}\right) + 2(p + W)H(T_{side,in} - T_{side,out})\right]$$

In the above Eqns. 4.1 and 4.2, "A" is the heated area, $q_{cond}$ is the conducted heat from top to bottom plate, "H" is the height of pin, $\tilde{T}_{top}$, $\tilde{T}_{bottom}$ are the area-weighted averaged top and bottom plate temperature. The insulation helped in minimizing the heat loss, however, the reported $k_{eff}$ accounts for the small heat loss through the insulators applied at the back of the patch heater at the top plate and the four side edges. The temperature drop across the insulators was measured by thin thermocouples, to determine the net heat loss through them. In the experiments, it was noticed that the heat loss was <3% of the total heat supplied. The patch heater was powered by a DC voltage power supply, and the total heat provided by the patch heater to the top plate was determined by measuring the current in the circuit and the resistance of the patch heater $(q_{total} = i^2 R_{htr})$.

***Convective heat transfer experiments***

The convective heat transfer experiments were conducted by releasing a desired mass flux of particles stored in the hopper at room temperature, into the test section. The test section as described in **Fig. 4.2**, comprised of two parallel plates with inline arrangement of pins sandwiched between them. These two plates were subjected to constant heat flux. Initially, the plates were heated up by setting a particular heat flux, and once the wall temperatures stabilized, the particles were released from the hopper into the test section. As a result, the wall temperatures started to reduce and reached a steady state after an hour or so, depending upon the particle mass flux. As the particles moved through the test section, they picked by heat by virtue of convection through their interactions with the endwalls and the pin walls. These particles were collected at the bottom of the test section

and transported back to the hopper via a series of buckets. As a result of this transport, heated particles loose some of their thermal energy to the buckets, and the laboratory ambient. The mass of particles stored in the hopper was several times greater than the mass of heated particles added over a significant period of time.

Hence, the hopper filled with particles essentially served as a reservoir which could provide particles to the test section at near room temperature over the entire test duration.

During the above experimental procedure, the temperature of particles was measured at the inlet and the outlet of the test section, along with the discrete wall temperature measurements. These temperature measurements were displayed in real time in a LabVIEW console and were monitored during the course of experiments to establish the steady state. Once the steady state was established, the temperature data was recorded at 10 Hz for an extended period, typically 0.5 hours. The time-dependent temperature data on particles, walls, and the space and time independent heat flux data was used to determine the convective heat transfer coefficient using the following relationship.

**Equation 4-3**

$$h(x,t) = \frac{q"_{conv}(t)}{T_w(x,t) - T_f(x,t)} = \frac{[q_{total} - \sum \tilde{q}_{loss}(t)]/(2A_b)}{T_w(x,t) - T_f(x,t)}$$

Note that the test sections were insulated in convective heat transfer experiments as well. The stray heat loss through the insulation was also accounted for by subtracting it from the total heat provided. Note that although a space/time-independent heat flux was supplied, the heat loss was space/time-dependent as the temperature drop across the insulator varied. The total heat loss, although significantly lower than the total heat supplied (3%), was determined by averaging over space. The temporally varying heat loss was then reduced from the total heat supplied to determine the time-dependent convective heat flux. Note that the total heat supplied is inclusive of both the parallel plates and $A_b$ was the surface area of one of the parallel plates. The local wall temperatures ($T_w(x,t)$) were measured at the locations shown in **Fig. 4.3**. The local HTM temperature ($T_f(x,t)$) was determined based on the two measurements conducted at the entrance and exit of the test section, and linearly interpolating between these two locations, which is allowed due to the constant heat flux boundary condition imposed at

the walls. The local time-dependent convective heat transfer coefficient ($h(x,t)$) was then determined. In the subsequent sections, the reported local convective heat transfer coefficients were obtained when the values became independent of time.

***Optical flow experiments***

The optical flow experimental setup involved a high-speed camera and high-intensity lighting, along with a test section with the exact same arrangement of pin fins as in the convective heat transfer experiments, however, allowing optical access. In these experiments, the stored particles in the hopper were released into the test section, where the particles were kept at room temperature and the walls of the test section were unheated. The bottom portion of the test section featured a converging nozzle which was further connected to a custom-built opening to allow only a certain mass flux of particles through the test section, while maintaining a packed bed configuration. Once a steady flow of particles through the test section was achieved, the flow measurement experiments were conducted.

The high-speed camera (KRONICA Chronos 1.4) captured 24-bit images with a spatial resolution of 1280×1024 at a rate of 500 Hz. The raw images acquired from the high-speed camera were first enhanced using MATLAB image processing code which converts them to gray scale and enhances the clarity and contrast using histogram equalization technique CLAHE (**Fig. 4.5**). The CLAHE filter is an important step in the post-processing of images prior to the implementation of the optical flow algorithm to enhance the contrast of images without the amplification of noise. The images were then saved as a 10-bit .TIFF files, which were later read for optical flow measurement. The contrast enhancement was essential for optical flow algorithm since these algorithms work by tracking the change in light intensity for a given point in the image. Increasing the contrast improves the accuracy of the tracking algorithm. The images are analyzed using a python code based on OpenCV library [4.3]. The image processing algorithm involves the sequential import and careful analysis of two consecutive images from the experimental dataset using the Farnebäck algorithm. This algorithm computes flow by approximating neighborhoods in consecutive frames with quadratic polynomials, enabling fast and robust motion tracking.

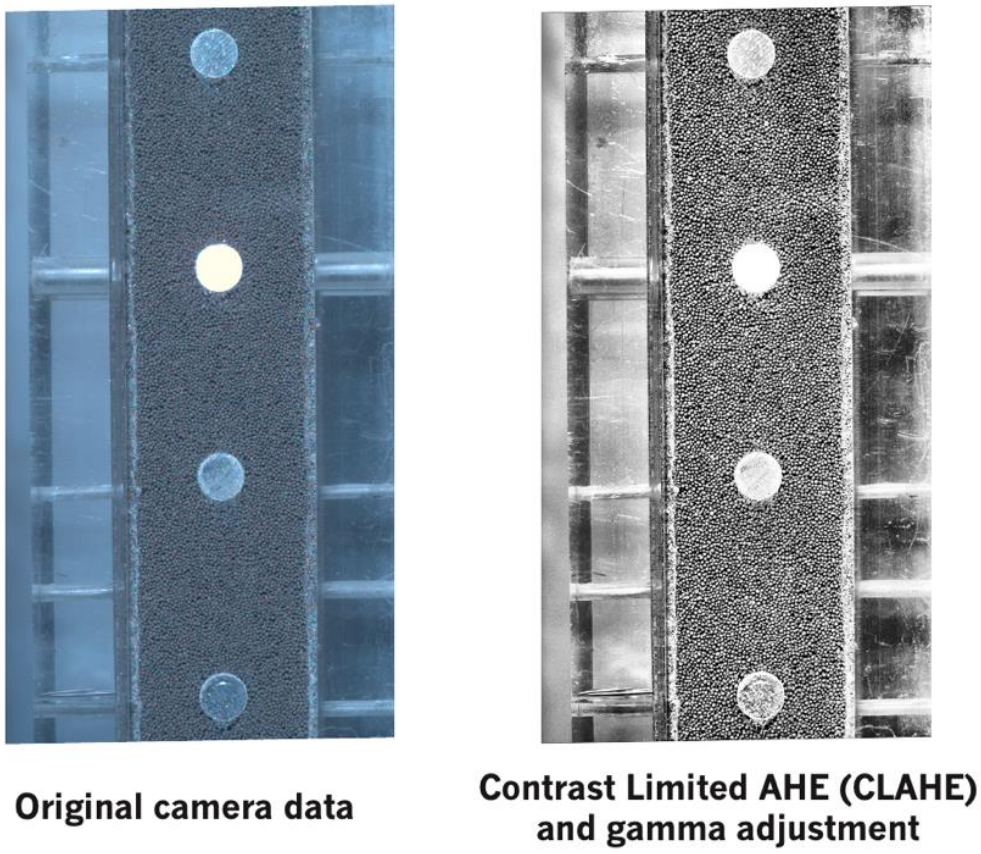



**Figure 4.5 Image enhancement to facilitate post-processing of images acquired in optical flow experiments**

Using this displacement, the time between each 2 frames (1/500 s), and a scale that converts from pixel size to physical length, the local flow velocity magnitude and velocity vector was calculated. A vector field quiver plot as well as the velocity magnitude contour plots were exported for each image sequence. The optimal settings for capturing the local flow in the MPB were, a pyramid scale of 0.5, level number of 3, window size of 15 pixels, gave the best results. To capture the fine details in the complex bubbling flows, a polynomial expansion was used to approximate the flow at the neighboring 7 pixels for each window. In the Farnebäck algorithm, a gaussian smoothing function was used to smooth the image data for noise reduction, in which a standard deviation of 1.5 was used to strike a balance between noise reduction and edge preservation for proper optical flow tracking. After running the optical flow code on all the image sequences, a MAT file of the flow-field consisting of x-velocity component (u) and y-velocity component (v) was created. The file was then used to create the contour, and vector field plots of the moving packed bed.

**Uncertainty analysis**

The uncertainty analysis was carried out based on the sequential perturbation method demonstrated by Moffat [4.4]. The heat transfer experiments were designed such that the theoretical uncertainty levels are low. In the $k_{eff}$ experiments, the sources of uncertainty were resistance and current through the patch heater, temperatures at the top and bottom plates, as well as the temperature drop across the insulation. The temperatures were measured by T-type thermocouples with error contributions of 0.5℃ each. The contribution of temperature errors on the overall uncertainty in $k_{eff}$ was reduced by maintaining a reasonable difference between the top and bottom plates. The reported $k_{eff}$ values had uncertainty <3%.

The sources of uncertainty in the reported values of convective heat transfer coefficient were resistance and current through the patch heaters, temperature measurements at the walls and across the insulator. In these experiments as well, the prime contributor of uncertainty was the temperature measurements. This effect was minimized by maintaining a reasonable difference between the local wall and particle

temperatures. The reported values of convective heat transfer coefficient had uncertainty less than 4%.

For the optical flow experiments, the source of uncertainty in the reported values of local particle flow velocities, were the scale in the field of view and the time interval between two successive frames. Due to high spatio-temporal of the camera, both these errors were extremely low. The error in the length scales was 0.07 mm and the error in time was 4 ms. The reported particle flow velocities had uncertainty <1%.

## Results and discussion

In this section, the experimental results on effective thermal conductivity and convective heat transfer coefficient are presented, along with the particle flow-field results. **Figure 4.6** shows the effective thermal conductivity of three configurations, (a) packed bed, (b) pin-fin with void space occupied by air, (c) pin-fin with void space occupied by particles/air. The addition of extended surface area which also joins the top and bottom plates in the $k_{eff}$ experimental configuration, or parallel plates between which the particles would move, is expected to enhance the heat transfer due to conjugate heat transfer effects. This effect is quantified for stationary packed bed of particles to elucidate the true contribution of the pin in the enhancement of $k_{eff}$. The experiments were conducted at three different heat flux levels to demonstrate that the reported averaged $k_{eff}$ values are independent of the applied thermal boundary condition and is a true representation of the test article and its constituents. The baseline configuration of packed bed of particles had an effective thermal conductivity of ~ 0.41 W/mK. The secondary baseline configuration involved one pin fin where the void space was occupied by air, which yielded an averaged $k_{eff}$ ~ 0.56 W/mK. The final configuration involved packed particles in the pin fin configuration which resulted in averaged $k_{eff}$ of ~ 0.7 W/mK. Hence, addition of pin-fin to the packed bed of particles resulted in ~70% enhancement in $k_{eff}$ of the packed bed of particles. The pin fin configuration, where void spaces are filled with particles, establishes two distinct parallel pathways for heat conduction. The first pathway is through the pin fin itself, while the second is through the packed bed of particles (as illustrated in **Fig. 4.6**).

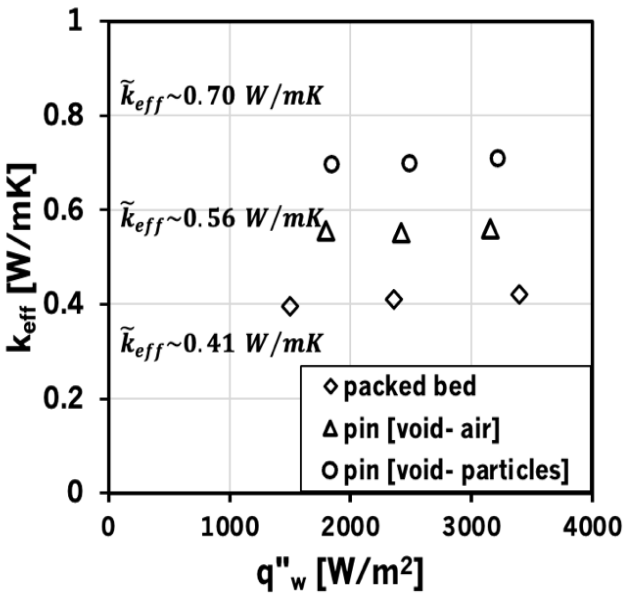



**Figure 4.6 Effective thermal conductivity versus conduction heat flux for three configurations**

Although the pin fin occupies only a small cross-sectional area in the direction of heat flow compared to the substantially larger area occupied by the packed particle bed, its contribution to the overall heat transfer performance is remarkably significant due to its enhanced surface area and flow disruption characteristics. This is because the pin fin material possesses an intrinsic thermal conductivity approximately 30 times greater than that of the packed bed of particles. This substantial difference in thermal conductivity means that despite its smaller area, the pin fin provides an efficient channel for heat conduction, complementing the heat transfer through the packed particle bed. The combination of these two parallel pathways - the highly conductive pin fin and the more broadly distributed packed bed - creates a synergistic heat transfer system that leverages the advantages of both components. This dual-pathway configuration ultimately results in enhanced overall thermal performance compared to traditional single-pathway heat transfer systems The above two aspects of the pin fin-packed bed configuration results in superior effective thermal conductivity.

Note that convective transport is an added mechanism for thermal transport and the above enhancement is only a result of the addition of a single pin-fin to a configuration where the particles were stationary.

***Heat transfer and flow dynamics of MPB [baseline configuration]***

The efficacy of moving packed bed of particles through an inline column of pin fins is now demonstrated through the convective heat transfer results. To this end, a baseline configuration (plane channel) was first tested, which did not involve the pin fins, where the particles moved in a packed bed configuration between two parallel plates. **Figure 4.7** shows the convective heat transfer coefficient variation with streamwise location for the plane channel configuration, where the experiments were carried out for different mass flow rates of particles. The systematic variation of mass flow rates enabled comprehensive characterization of heat transfer behavior across a wide range of operating conditions, providing crucial baseline data for comparison with pin fin configurations. The convective heat transfer coefficients presented in **Fig. 4.7** were based on Eq. 4.3 where local wall temperature measurements corresponding to the center of each pin was taken ($T_{cw,i}$, **Fig. 4.3**), to determine the local $h$ values. For the parallel plate configurations, the wall temperatures were only measured at the slots present at $T_{cw,i}$ locations shown in **Fig. 4.3**. The local particle temperatures corresponding to the center location of each pin was determined by linearly interpolating the inlet and outlet particle temperature values. Also, these reported values correspond to the quasi-steady state where both wall and particle temperatures reach a steady state condition. The data is presented till 80% of the channel length, since for all values, the exit effects led to increase in heat transfer. This effect is not a universal phenomenon and is dependent on the exit conditions, on the method of collecting particles at the bottom of the test section, and the diffuser interface, which determines the extent to which ambient air (cool) gets entrained or interact with the last leg of the test section (~10% of total channel height).

A developing heat transfer trend was observed for all three configurations with 3, 5, and 7 mm spacings between the parallel plates. Specifically, it was found that the convective heat transfer coefficient exhibited an increasing trend as the mass flow rate increased, while the inter-plate spacing demonstrated a significant influence on both the developing heat transfer characteristics and the periodic regime heat transfer performance across all experimental conditions. The observed variations in heat transfer behavior can be attributed to the reduction in conductivity paths between bulk center and walls.

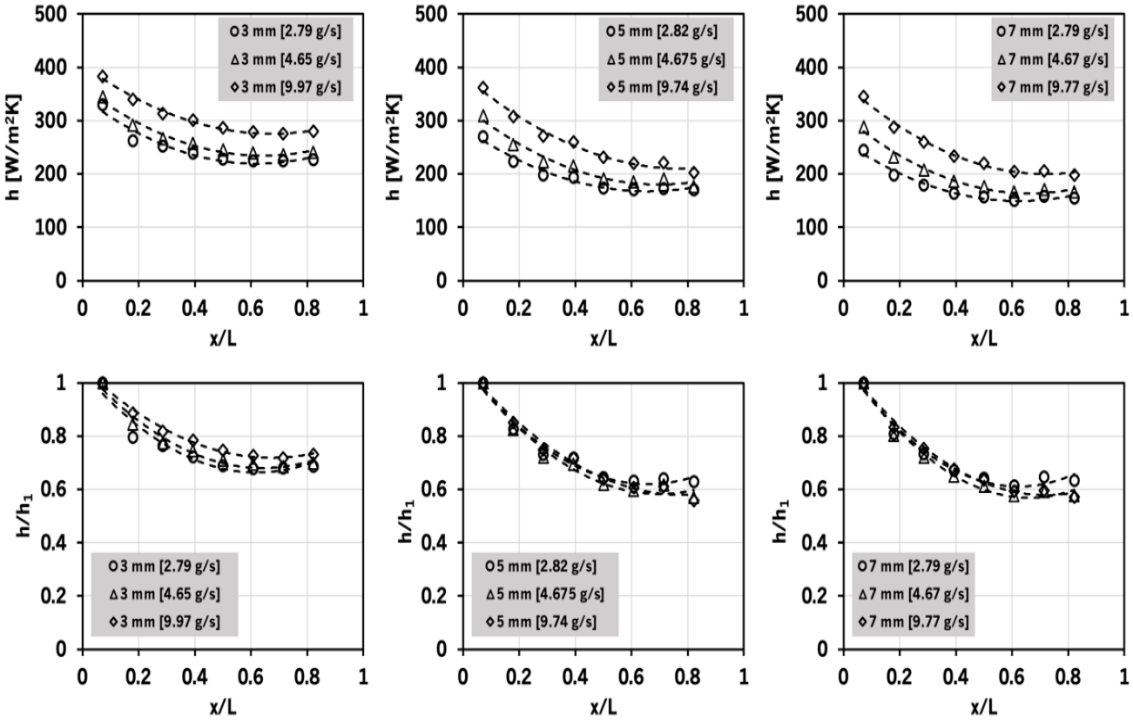



**Figure 4.7 Variation of local convective heat transfer coefficient with streamwise distance for different plate spacings of baseline configuration (parallel plates with no pin fins). $h_1$ is the convective heat transfer coefficient obtained from the wall temperature measurement at $T_{cw,1}$ (Fig. 4.3)**

The smallest spacing of 3 mm yielded the highest heat transfer rate, following by 5- and 7-mm configurations, which had nearly similar heat transfer levels. For a given mass flow rate of particles, the local flow velocities in the 3 mm channel are expected to be highest, followed by 5- and 7-mm plate spacings, under the assumption that particles' flowability is not affected by reducing the channel width. Higher flow velocity has a first order effect on the convective heat transfer. From the thermal perspective, low plate spacings would yield larger thermal gradients, which also promotes local convection heat transfer, in comparison to larger inter-plate spacings.

Further, for the 3 mm plate spacing, a less gradual decline in the heat transfer was observed, compared to the 5- and 7-mm configurations. The bottom row of plots shows the heat transfer coefficient values normalized with the heat transfer levels obtained for the region corresponding to the first pin for the respective mass flow rates, to show the streamwise length traversed by MPB before the heat transfer levels became periodic. Here, the periodic heat transfer is defined as the scenario when heat transfer values repeat themselves with increasing streamwise location (or pin row number).

For all three plate spacings, the heat transfer became periodic at 50% of the channel's total streamwise length (L). For 5- and 7-mm plate spacings, the periodic heat transfer values settled at 60% of the maximum heat transfer (in the entrance region) value for a given mass flow rate of particles. For the lowest plate spacing of 3 mm, the heat transfer values settled at a relatively higher value (~70% of entrance region heat transfer), compared to the other two larger plate spacings. Compared to the reduced order modeling (ROM) work on MPB flow between parallel plates, the experimentally obtained developing heat transfer length from the entrance was significantly larger than the ones obtained through ROM, e.g. [4.2]. Effective particle velocities vary with plate spacing at constant mass flow. To compare heat transfer trends, we evaluate them using mass flux values ($\dot{m}_{p,total}/A_{channel}$), where $A_{channel}$ is the flow cross-sectional area ($wH$). **Figure 4.8** shows the convective heat transfer coefficient values in the periodic heat transfer regime (post 50% of the total plate length) with respect to mass flux and mass flow rate of MPB.

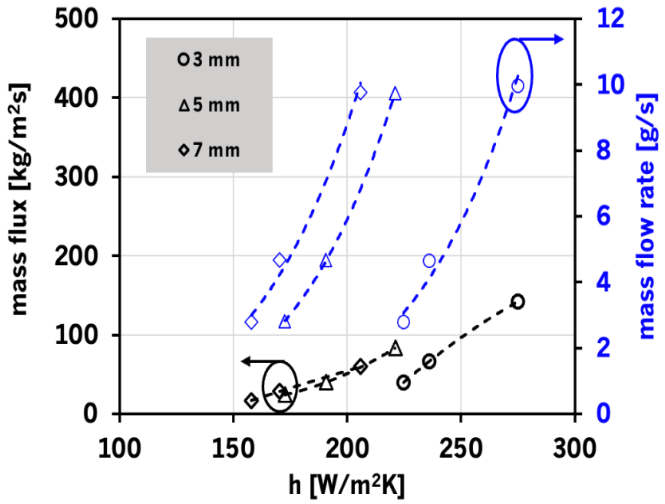



**Figure 4.8 Periodic regime convective heat transfer coefficient variation with MPB mass flux and flow rate**

As expected from **Fig. 4.7**, a strong dependence of convective heat transfer coefficient can be observed on the mass flow rate parameter. However, when mass flow rate was normalized by flow cross-sectional area to obtain mass flux, the 5- and 7-mm plate spacings result in similar heat transfer levels, while the 3-mm plate spacing had a distinctively higher heat transfer. The analysis based on mass flux normalized the 1$^{st}$ order contribution of flow velocities on the resultant heat transfer. Hence, the observed enhancement at 3-mm plate spacing in terms of mass flux, reveals that the strong temperature gradient in the lowest plate spacing had a prominent effect on the resultant heat transfer. In summary, a thorough analysis of the baseline configuration of parallel plates (absence of pin fins) separated by 3-mm, 5-mm, and 7-mm distance, reveals that the plate spacing has a dominant effect on convective heat transfer. Further, increase in MPB flow velocity and higher temperature gradients in the MPB are desired attributes for enhanced heat transfer, which were fulfilled by the 3 mm plate spacing.

To further enhance the fundamental understanding of the thermal transport due to MPB of particles between closely spaced parallel plates, optical flow experiments were conducted, which provided high spatio-temporal resolution of particles' velocity magnitude and direction. **Figure 4.9** shows the velocity magnitude contour for the three plate spacings. The velocity vectors were aligned completely with the gravitational vector

and are not presented in the interest of brevity. As discussed above, velocity magnitude for 3-mm plate spacing was largest and that for 7-mm was lowest. Further, the particles near the side walls also moved in nearly similar velocities in 3-mm configuration, as those in the channel core. For 5-mm and 7-mm configurations, effect of side walls can be seen, where flow velocities were lower than that in the channel core.

The averaged velocity magnitude values provide important information on the net flow and thermal transport. From the processing of raw output images from the high-speed camera, we observed some interesting transient dynamics. A portion of transient dynamics of the MPB of particles is presented in video format in the supplementary information section. As can be observed from the video, the largest plate spacing of 7 mm exhibited a smoothly moving packed bed of particles throughout the test section domain. For the 5 mm plate spacing, the packed of particles still moved smoothly, but now with intermittent pause. This phenomenon became more pronounced for the lowest plate spacing of 3 mm and can be clearly seen in the video of MPB flow of particles, that packed bed of particles does not traverse the streamwise length smoothly and exhibit a more frequently occurring intermittent pause and release of a portion of the packed bed. The frequency of these pause-release cycles was found to increase exponentially as the plate spacing decreased from 5 mm to 3 mm, suggesting a non-linear relationship between plate spacing and flow interruption. For the smallest inter-plate spacing of 3 mm, the intermittent pause and release of a batch of particles is due to the pronounced effect of the two parallel plates on the MPB bulk flow. Wall-induced flow obstruction propagated in the MPB core, causing brief pause and release. This phenomenon gradually diminished with increasing inter-plate spacing. Note that the particle flow characterization experiments were conducted at room temperatures. At the elevated temperatures, the properties of the particles change, which result in change in local velocity magnitude. It is expected that with increase in temperature, the flow velocities will reduce under the same flow potential, due to increase in friction coefficients. The temperature dependence of particle-wall interactions was particularly evident in preliminary high-temperature tests, where surface modifications of the particles were observed to further complicate the flow dynamics.

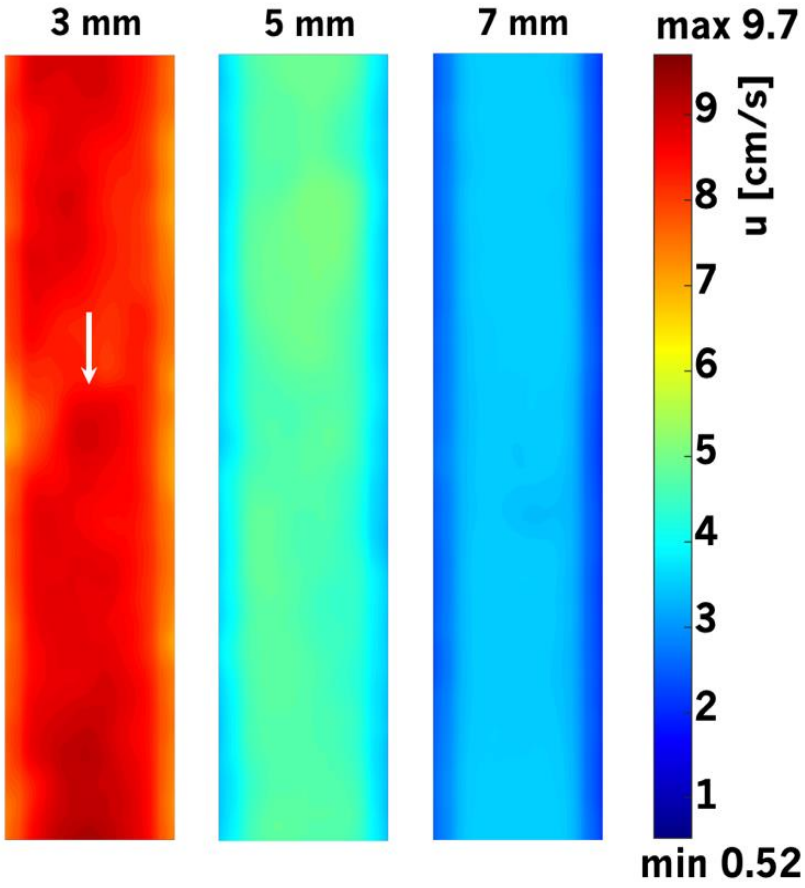



**Figure 4.9 Near-wall time-averaged flow velocity magnitude of MPB in cm/s, total mass flow rate of particles for each configuration: ~ 9.95 g/s.**

***Heat transfer and flow dynamics of MPB [pin-fin configuration]***

Convective heat transfer and optical flow experiments were conducted on the three configurations involving pin-fins between two parallel plates. The pin heights were varied as 3, 5, and 7 mm, where the pins connected the two parallel plates. The convective heat transfer results have been presented for the periodic heat transfer regime. The 7$^{th}$ pin from the inlet was considered for the detailed convective heat transfer coefficient calculation based on the thermocouple measurement locations shown in **Fig. 4.3.** The presence of pin fins significantly modified the local temperature distribution in the endwall. To this end, additional temperature measurements were carried out for the 7$^{th}$ pin, capturing the span of the channel corresponding to the pin cross-section, as shown in **Fig. 4.3.** The area-weighted wall temperature representative of the pin region is given as,

**Equation 4-4**

$$\tilde{T}_w = \frac{T_{cw}A_3 + T_a(2A_2) + T_b(2A_1)}{W d_{pin}}$$

The convective heat transfer coefficient was then determined by using the area-averaged wall temperature in Eq. 4.3. **Figure 4.10** shows the convective heat transfer coefficient variation with MPB mass flow rate and mass flux for the pin fin configuration, along with the corresponding local convective heat transfer coefficient for the baseline configuration. All pin configurations resulted in higher heat transfer in reference to their respective baseline configurations of parallel plates with absence of pin fins. Further, a power-law dependence of *h* on mass flow rate was observed for each configuration. The consistency of this power-law relationship across different pin heights suggests a fundamental scaling behavior that could be valuable for system design and optimization. To normalize the MPB flow velocity effects, the *h* values are plotted with respect to mass flux. In this comparison as well, pin fins demonstrated clear heat transfer enhancement benefits over parallel plate configurations. Note that the addition of pin fins imposes no penalty in the operational costs as the packed bed of particles is driven by gravity. These experimental findings were further validated through repeated trials, showing excellent reproducibility with variations less than 5% across all test conditions. The experiments were highly reproducible confirming the robustness of the enhancement.

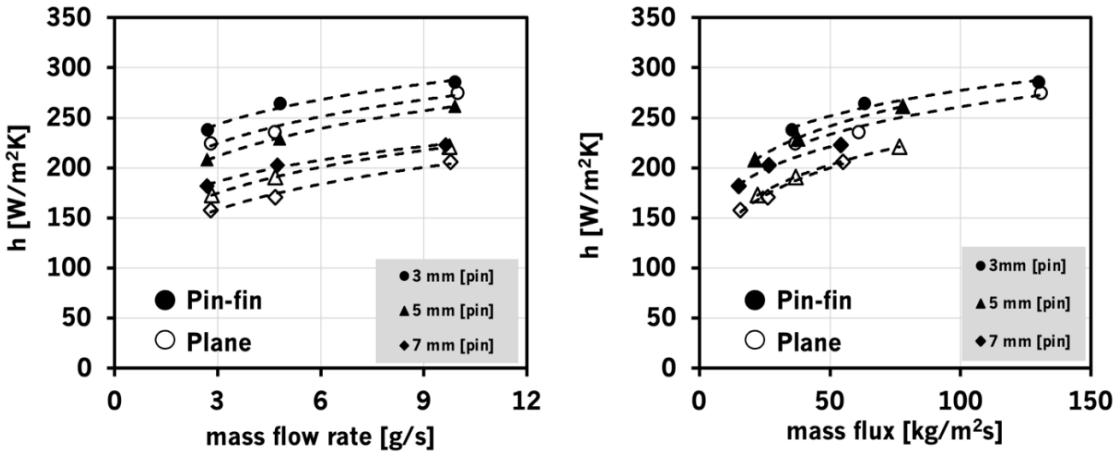



**Figure 4.10 Variation of convective heat transfer coefficient with mass flow rate and mass flux, for pin-fin and plane channel configurations. The pin-fin *h* data is taken for the 7$^{th}$ pin from the entrance (periodic heat transfer regime). The corresponding location for plane channel (also periodic heat transfer regime) is plotted for direct comparison.**

The time-averaged near-wall MPB velocity magnitude for the three pin fin configurations is presented in **Fig. 4.11**. The local enhancement or reduction in MPB velocity directly impacted the resultant convective heat transfer. To this end, three distinct flow properties of MPB was revealed by the optical flow experiments, (a) enhanced flow velocity of particles around the pins, (b) a dead zone above the pin where particles mostly did not move- this zone also extended to the adjacent upstream pin, (c) a void zone right underneath the pin which did not contain particles.

Each of the above identified zones affected the local convective heat transport. The enhanced flow velocities directly resulted in increased local convective heat transfer coefficient. The dead zone above each pin exhibited near-zero particle flow velocities. Through image analysis, we identified that in this zone, a batch of particles agglomerate above the pin, and this agglomeration was slowly disturbed by the incoming fresh batch of particles. These zones known as “Stagnation” and “Void” regions in literature occur in packed bed flow around pipes in shell and tube MPBHX designs. This phenomenon does not necessarily result in reduced heat transfer. On some occasions, higher particle residence time allows heat exchange between the particles and neighboring solid body or interacting particles.

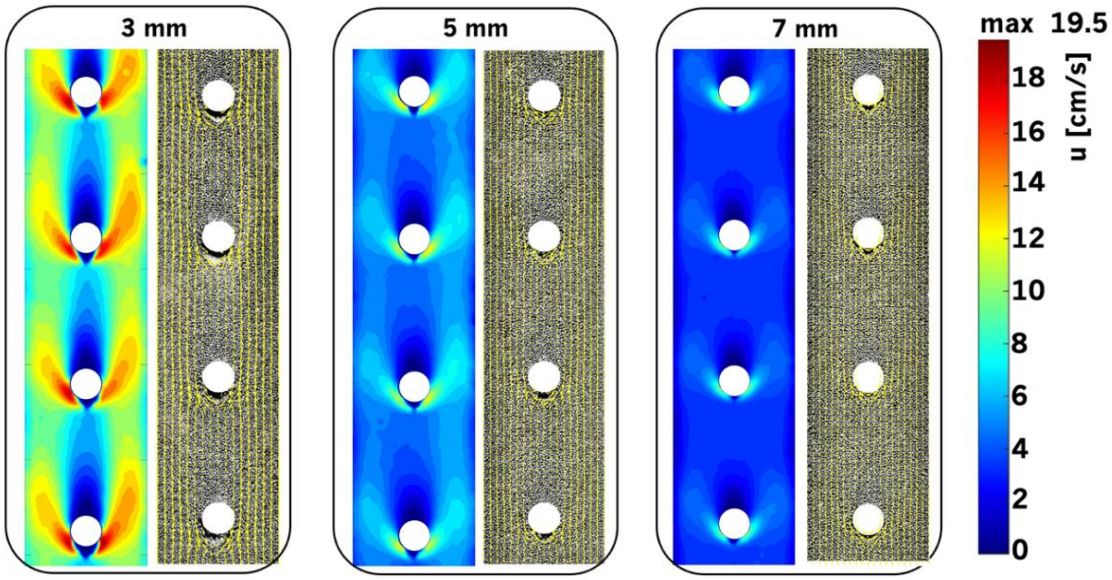



**Figure 4.11 Time-averaged near-wall moving packed bed velocity magnitude for 3-, 5-, 7-mm pin fin heights. The contours are shown for domain corresponding to periodic heat transfer. Total mass flow rate of particles for each configuration: ~ 9.95 g/s. The packed bed movement is vertically downwards.**

However, if the residence time is too large, then the heat transfer will be negatively affected, as the particle (source) temperature will approach that of the sink temperature. Further, higher residence time in localized zones also means lower flow velocities, which adversely affects heat transfer. Hence, there are competing mechanisms which affect the local heat transfer characteristics. The third distinct zone was observed right underneath the pin fin and is a result of the separation of particles from the pin fin as it moves around it. This results in a three-dimensional zone which is devoid of particles and this volume is essentially occupied by stagnant air, which has an order of magnitude lower thermal conductivity compared to that of the particles. Further, since the air occupying this zone is stagnant, the only path for heat exchange is via conduction, which is very low due to the low thermal conductivity of air in reference to particles.

In summary, the flow and thermal transport in MPB of particles are dependent on several factors, and these factors increase in number, when the parallel plate configuration is modified through the inclusion of obstructions. Note that the above discussion is based on the near-wall flow imaging. The MPB flow in the channel core is expected to be slightly different. A detailed probe into that aspect can be facilitated with high-fidelity discrete element modeling (DEM), which is validated by the experimentally obtained near-wall MPB flow-field.

The local flow velocities have been further quantified via line plots to represent the azimuthal variation around a pin and the streamwise variation at three spanwise locations. **Figure 4.12** shows the nomenclature used for this presentation, along with the azimuthal variation of u (cm/s) for three pin configurations. As observed from the contours (**Fig. 4.11**), the 3 mm configuration had the highest flow velocity overall, and this trend was found for the azimuthal ($\phi$) around a pin as well. The peak velocity magnitude was observed at $\phi$ =120° for the 3 mm configuration, while a ~10° shift in the peak velocity was observed for 5- and 7-mm pin configurations. The uni-directional nature of the gravitational force results in the locations correspond to the dead and the void zones, respectively, as identified in **Fig. 4.11**. The lowest flow velocities were observed for $\phi = 0°, 180°$, where these azimuthal. The streamwise variation of time-averaged local velocity are shown in **Fig. 4.13**.

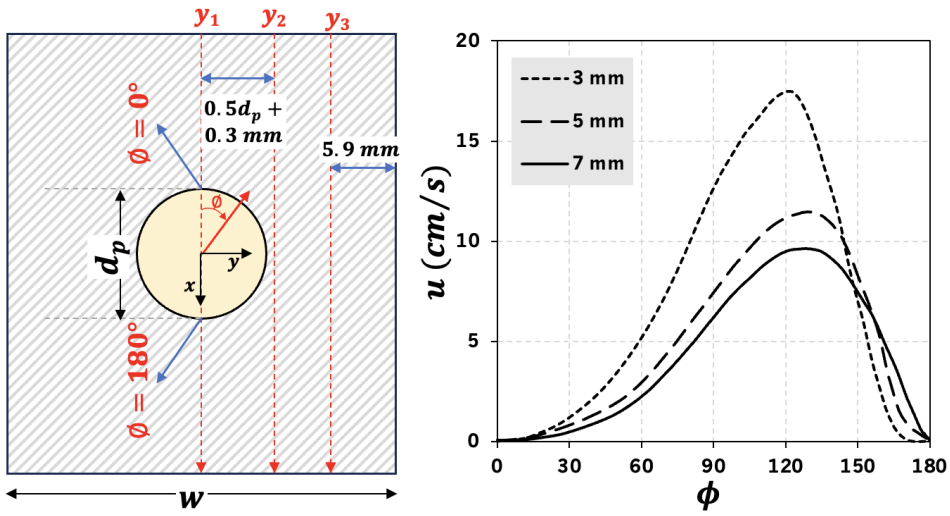



**Figure 4.12 The nomenclature used for azimuthal and streamwise variation of flow velocities, azimuthal variation of u (cm/s) for the three pin configurations**

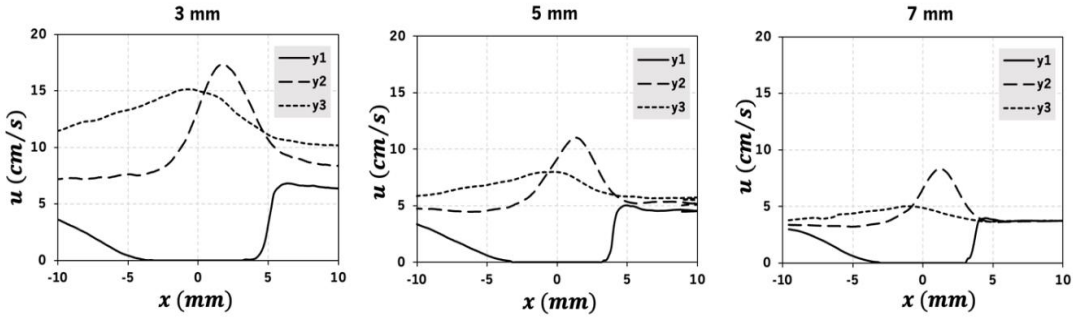



**Figure 4.13 Streamwise variation of u (cm/s) for three pin configurations. x=0 corresponds to pin fin center (Fig. 4.13).**

Along the streamwise line passing through the pin centerline, the upstream of the pin exhibited sharply decreasing velocity which corresponds to the strengthening of the dead zone, followed by a sharp rise in the immediate vicinity of the downstream region of the pin (post the void zone). This trend for $y_1$ was also observed for the 5- and 7-mm configurations. The line $y_2$ passed very closely in reference to the pin periphery, where this line largely avoids the upstream dead zone as well as the downstream void zone. It also captured the peak velocity zone which corresponds to azimuthal locations of 125°±5° for the three configurations. The particles moving between the pin periphery and the sidewall (line $y_3$) also exhibited higher velocities as the MPB approached the pin periphery, with the maximum velocity observed in correspondence to the pin center (x=0) for all three pin configurations. As indicated above, for the baseline configuration (parallel plates), that with the reduction in plate separation distance, an intermittent pause and release of MPB was observed.

This phenomenon was not observed for the pin configurations, even at the lowest pin height of 3 mm. The presence of pin modified the spanwise uniform movement of particles by creating high and low velocity zones, which essentially facilitated enhanced flowability of packed bed.

## Conclusions

An experimental study was conducted to understand the flow and thermal transport of moving packed bed of particles between two parallel plates as a baseline configuration, and with inline arrangements of pin fins joining the two parallel plates as the enhanced heat transfer configuration. The heat transfer medium (HTM) responsible for convective heat transfer was CARBOBEAD particles with mean diameter of 400 μm. Steady state heat transfer experiments were conducted to determine the effective thermal conductivity for stagnant packed bed of particles, and local convective heat transfer coefficient for moving packed bed of particles between the parallel plate configurations. Further, to understand the enhanced heat transfer mechanisms due to closely spaced parallel plates and the presence of pin fins, optical flow experiments were conducted to obtain high spatio-temporal measurements of near-wall flow-field of the moving packed bed of particles. Following major conclusions are drawn from this study:

(a) The presence of a pin fin in a stagnant packed bed of particles enhanced the effective thermal conductivity by 70% compared to the baseline configuration of stagnant packed bed of particles in the absence of pin fin.

(b) For the baseline configuration, a slow developing heat transfer trend was observed for all three inter-plate spacings, where the periodic heat transfer regime was obtained after 50% of the channel height. Further, the 5- and 7-mm configurations' convective heat transfer settled at 60% of their respective entrance regions' heat transfer levels, while for the smallest plate spacing configuration of 3 mm, the periodic heat transfer regime exhibited 70% of the entrance region heat transfer.

(c) For the baseline configuration, a monotonic increase in convective heat transfer was observed with decrease in the inter-plate spacing. Through detailed probe of raw transient flow data, it was observed that for 3 mm configuration, the moving packed bed exhibited intermittent pause and release.

(d) The addition of pin fins resulted in heat transfer enhancement for all three configurations in terms of both, mass flow rate and mass flux of MPB of particles.

(e) The presence of pin fins modified the MPB flow-field, with peak local velocities observed at an azimuthal location of 125°±5° for the three configurations. Further, a dead zone of stagnant or slowly moving particles was observed upstream of the pins, while a void zone (absence of particles) was observed right downstream of the pin fins.

(f) The dead and void zones were also affected by the pin fin heights, with the 3 mm configuration having the largest of both the zones, compared to the 5- and 7-mm configurations.

The research findings from this study will be used for further development of extended surface concepts which could be integrated with the parallel plates which facilitate MPB flow of particles. Topologies with high specific surface area, which also result in minimized dead and void zones, are expected to advance the particle-based thermal transport technology for concentrating solar thermal application.

## References

[4.1] Y. Aider, I. Kaur, A. Mishra, L. Li, H. Cho, J. Martinek, Z. Ma, P. Singh, Heat Transfer Characteristics of Particle and Air Flow Through Additively Manufactured Lattice Frame Material Based on Octet-Shape Topology, Journal of Solar Energy Engineering 145 (2023). https://doi.org/10.1115/1.4062196.

[4.2] K.J. Albrecht, C.K. Ho, Design and operating considerations for a shell-and-plate, moving packed-bed, particle-to-sCO2 heat exchanger, Solar Energy 178 (2019) 331–340. https://doi.org/10.1016/j.solener.2018.11.065.

[4.3] The OpenCV library - ProQuest, (n.d.). https://www.proquest.com/docview/202684726?parentSessionId=4vEcdLBL3QCfBC2kY%2FY6e6Avq5Am8we3zZqb87nhtqw%3D&sourcetype=Trade%20Journals (accessed April 1, 2024).

[4.4] R.J. Moffat, Describing the uncertainties in experimental results, Experimental Thermal and Fluid Science 1 (1988) 3–17. https://doi.org/10.1016/0894-1777(88)90043-X.

# CHAPTER FIVE :
# GRANULAR FLOW IN NOVEL OCTET SHAPE-BASED LATTICE FRAME MATERIAL

## Abstract

Moving packed-bed heat exchanger in concentrated solar power (CSP) plants involves heat transfer between heated falling particles and supercritical carbon dioxide. The overall effective thermal conductivity of the moving packed bed and particle-side channel contact resistances are still the bottlenecks in achieving the desirable thermal transport levels. To this end, a novel moving packed bed heat exchanger consisting of Octet lattice packed between the walls of the particle-side channel is proposed in this study. Granular flow analysis in Octet lattice moving-packed bed heat exchanger (OLHX) was conducted through experiments and DEM-based numerical simulations. The experimental images clearly demonstrated stagnation regions upstream of lattice fibers, void regions downstream of the fiber junctions and wavy type unobstructed flow on lateral sides of the fibers. DEM simulations were successful in capturing all these critical flow phenomena. Larger flow velocities were observed on the lateral sides of the fibers in the simulations. Also, when the particles in the silo were emptied, the final images showed accumulation of particles on the inter-fiber as well as fiber-channel wall junctions. Moreover, the fiber connections resulted in some regions devoid of the particle contact on the channel endwall which means that these regions would suffer from poor thermal exchange. The overall mass flow rate increased with increasing porosity for a fixed particle diameter.


## Introduction

Supercritical carbon-dioxide ($sCO_2$) based Brayton cycle is a promising alternative to the traditional steam-powered Rankine cycle because of its potential for achieving high thermal-to-electric conversion efficiency of ~50% [5.1]. The overall conversion efficiency of power cycle can be improved by increasing the working fluid temperature at the turbine inlet (typically $\geq$ 700℃). To this end, the power cycles are coupled with the solar energy field in concentrating solar power plants (CSPs) as shown in **Fig. 5.1** [5.2]. The CSPs are an attractive technology as they feed on solar energy, a renewable source, and there has been continuous effort to ensure their commercial scalability. In CSPs, the heat transfer fluid (HTF) flowing in a closed loop gets heated by the concentrated solar energy in the receiver section, and this thermal energy is eventually transferred to the working fluid ($sCO_2$) of power cycle via particle-to-sCO$_2$ heat exchanger.

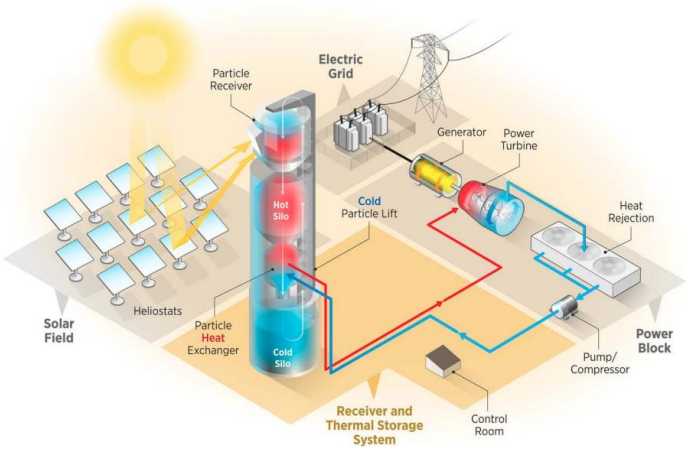



**Figure 5.1 Schematic of the falling-particle receiver system coupled with power cycle [5.2]**

These HTFs also act as thermal energy storage (TES) systems which store the heat energy so that it can be dispatched as and when required, such as, at instances when solar energy is not readily available.

Molten salt and granular media are the most widely known HTFs for CSP application and several heat exchanger (HX) designs such as shell-and-tube, shell-and-plate, and printed circuits have been investigated in the past based on these HTFs. Du et al. [5.3] investigated heat transfer characteristics of HITEC ($NaNO_3$ – $KNO_3$ – $NaNO_2$ eutectic) salt-oil pair in a shell-and-tube HX and provided empirical correlations to predict the thermal performance. He et al. [5.4] analyzed the turbulent heat transfer characteristics of molten HITEC salt and YD-350 synthetic oil pair in a shell-and-tube HX and reported that no significant heat transfer augmentation occurred when salt was replaced by water as HTF. Qian et al. [5.5] compared the thermal performance of molten salt and conductive 320- oil in baffled shell-and-tube HX, where molten salt provided higher heat transfer performance. Shell-and-tube HX design is one of the most primitive designs which suffers from fluid leakage, large volume, and inability to sustain high pressures [5.6]. Printed circuit HXs have considerable advantage over these traditional HXs in terms of specific area for heat transfer, sustainability of high pressure drops (up to 60 MPa), and relatively compact sizes [5.6].

Printed circuit heat exchangers (HXs) represent an advanced thermal management solution, where robust contact between the adjacent plates is ensured through diffusion

bonding process. These plates contain minichannels fabricated in various geometric configurations such as straight, trapezoidal, serpentine, zig-zag, and other optimized shapes [5.6]. The diffusion bonding process creates a metallurgical bond at the molecular level, resulting in exceptional mechanical strength and thermal performance characteristics that surpass traditional brazed or welded joints. Wang et al. [5.7] experimentally evaluated a printed circuit heat exchanger with airfoil fins, using molten salt (HITEC) and synthetic oil (YD-325) as hot and cold fluids, respectively. The compact nature of these heat exchangers, combined with their high pressure tolerance and excellent heat transfer capabilities, makes them particularly suitable for applications in nuclear power plants, petrochemical processing, and advanced energy systems.

The heat transfer of airfoil channel was ~ 7 times higher than straight channel due to disruptions of fluid flow by the fins. Nikitin et al. [5.8] experimentally determined the heat transfer and pressure drop characteristics of $sCO_2$ in a printed circuit HX having zig-zag channels with semi-circular cross-section profile. The overall heat transfer coefficient for zig-zag channel was obtained in the range of 300 to 650 $W/m^2K$. Despite hosting several advantages over traditional shell-and-tube HXs, minichannels of printed circuit HXs have drawback of potential plugging by the salt. Montes et al. [5.1] suggested a compact honeycomb HX where the molten salt flowed through central tube and the $sCO_2$ was present on the outer trapezoidal ducts surrounding the tube. The proposed design prohibited the clogging of channels and avoided large mechanical stresses due to high pressures of $sCO_2$. Molten salts inherit some other limitations such as thermal instability, high melting points and corrosive behavior [5.9]. Popular molten metals such as Nitrates have maximum operating temperature limit of 560℃, which prohibits the realization of turbine inlet temperatures $\geq$ 700℃. On the other hand, solid particles as heat transfer media can have very high working temperatures (> 1000 °C), high heat capacity, low-cost, and non-corrosive behavior [10]. Particle-to-$sCO_2$ heat exchangers have been actively investigated recently due to these advantages and two of the most widely researched concepts are – (a) fluidized bed, and (b) gravity-driven moving packed-bed.

Fluidized bed technology provides higher overall particle-to-wall heat transfer coefficient values, but the cost associated with the machinery required to supply fluidized

gas and with the recuperative heat exchange devices to minimize convective heat transfer losses from the gas poses challenges in their commercial applications [5.11]. Gravity-driven moving packed-bed heat exchangers have become a viable alternative due to their simpler set-up and lower operational costs [5.12]. However, the heat transfer coefficient values of the moving packed-bed HXs are lower than the fluidized-beds, which is being countered by developing innovative HX designs by several researchers. Albrecht and Ho [5.12] investigated a counter-flow multi-bank shell-and-plate HX where $sCO_2$ flowed in serpentine fashion via parallel plates and the particles moved in between the stacked plates under the influence of gravitational force. It was found that the thermal exchange in such configurations is limited by the low thermal conductivity of the particle bed. The authors in [5.12] proposed reduced order modeling methodology to predict the heat transfer in HX and reported that an overall heat transfer coefficient of 400 $W/m^2K$ could be achieved for particle channel width of 4 mm and particle diameter of 200 μm at CSP plant operating temperatures (500°C - 800°C). Baumann and Zunft [5.13] investigated crossflow shell-and-tube HX where the dense granular medium moved downwards in a shell enclosing the tubes through which the working fluid of power cycle passed. In such configurations, the heat transfer performance can be deteriorated due to stagnation zone on the upper vertex and the void zone in the wake of the tubes. The narrowing down of the horizontal tube pitch in [5.13] provided increment in the overall heat transfer due to shorter particle-wall-contact time.

The formation of the stagnation and void zones around the tubes in a shell-and-tube HX can be reduced by adopting more sophisticated tube designs as compared to the traditional circular ones. Tian et al. [5.14] proposed elliptical-like combined tube shape constructed from the arrangement of three circular tubes. The stagnation and cavity zones in the novel elliptical-like tube was significantly lower than that in the conventional circular tubes resulting in the outside tube heat transfer performance due to particles similar to pure-elliptical configuration. The inside tube heat transfer of the elliptical-like configuration was compared with the corresponding elliptical- and circular-only configurations using the standard Gnielinski equation. For the same mass flow rate, the heat transfer coefficient was the highest for the elliptical-like configuration. In a recent

study, Tian et al. [5.15] proposed a trapezoidal corrugated modification to the standard plates in a shell-to-plate HX where the trapezoidal bulge was reported to significantly improve the heat transfer between the particles and plate. The trapezoidal bulge enhanced particle-particle mixing and destroyed the thermal boundary layer development resulting in improved heat transfer in the downstream regions. The base angle of the trapezoidal bulge was reported to have significant influence on the particle-to-wall heat transfer. Guo et al. [5.16] investigated the influence of the tube inclination on the particle-to-tube heat transfer. The contact resistance first increased and then decreased with the increment in the inclination angle. An optimum inclination angle of 15° to 37.5° was suggested by the authors to slow down the development of penetration resistance.

As discussed above, several novel HX designs have been explored in the past to improve the efficiency of the CSP plants. The granular flow and thermal exchange characteristics are being actively investigated through experimental and numerical means. Owing to the large capital investment required to conduct experiments, computational procedures have become a relatively more economical tool for testing and optimizing the new HX configurations and understating the intrinsic fundamental granular flow behavior. The discrete element method has become a very reliable and robust model in the recent years to predict the macroscopic behavior of any granular system by resolving the particle-scale interactions. The concept of DEM was first proposed by Cundall and Strack [5.17]. This method uses Lagrangian framework to explicitly solve the trajectories of particles by evaluating the inter-particle forces resulting from contact. The DEM theory is being currently employed by several researchers to model granular interactions and discussion on some relevant studies is presented below.

Bartsch and Zunft [5.18] used DEM to model the dense granular flow-field around the circular tubes in a moving packed-bed HX. The simulated results were in good agreement with the velocity profiles obtained from the PIV experiments. Yarrington et al. [5.19] measured the granular properties required as input in DEM simulations at elevated temperatures and consequently investigated its impact on the particles flowing down on an inclined plane. The free surface velocity magnitudes, flow volume fraction, average velocity magnitude, and mass flux contours were analyzed. Besides the simulation of

moving packed-bed HXs in regards to the CSP plant applications, DEM is being extensively used to model the mixing and blending of particles in a rotating drum for chemical, pharmaceutical, ceramic, and fertilizer industries [5.20–5.22]. DEM in used in combination with computational fluid dynamics (CFD) to model the particle flow behavior in fluidized beds as well [5.23–5.25]. Guo et al. [5.26] employed DEM to investigate heat transfer in moving packed-bed tube HX, where the tubes were subjected to oscillations to improve the heat transfer. Tube oscillations improved thermal exchange by accelerating the particle update and improving the solid fraction in local zones. However, stronger oscillations led to separation of particles from the tube, thereby deteriorating the heat transfer. Tian et al. [5.27] also investigated the effect of pin-fin and its oscillation on the gravity-driven granular flow. Several other researchers in the past have developed DEM codes to model the complex particle-particle heat transfer phenomenon [5.28–5.30].

The particle-to-s$CO_2$ heat transfer is influenced by several factors such as particle side bulk thermal conductivity, particle-wall contact resistance, particle size, channel width, interstitial gas, particle velocity, and particle residence time [5.31–5.33]. As discussed above, several types of HX concepts have been reported which can potentially augment the thermal exchange from the particle-side channel. In this study, the authors propose a novel gravity-driven moving packed-bed HX with Octet lattice framework packed between the plates of the channel on the falling-particle side. Octet has been investigated extensively in the past for its superior mechanical properties [5.34,5.35]. The past work by our group focused on experimentally and numerically analyzing the convective heat transfer augmentation capabilities of fiber-based lattices from both Cubic and Octahedron family in forced convection channel configurations with both air and water as the working fluid [5.36–5.40]. A thorough flow and heat transfer investigation has been conducted to characterize the flow patterns and thermal exchange dynamics rendered by four different topologies, viz Octet, Tetrakaidecahedron, Cube, and FD-Cube, subjected to both laminar and turbulent flow conditions. Extensive experimental and numerical investigation was conducted recently to establish the stagnant thermal conductivities of the aforementioned lattices with water and air filled in their void volume [5.41,5.42].

Amongst these four investigated topologies, Octet provided the highest interfacial heat transfer coefficient values on the fibers whereas effective thermal conductivity was found to be independent of lattice topology for porosity $\geq 0.8$. From prior investigations, it has been well established that Octet exhibits superior interfacial heat transfer and mechanical properties [5.43]. These previous findings are a motivation to extend the utilization of unique fiber-based Octet topology to granular flow systems employed in CSP plants. Recently, Aider et al. [5.44] experimentally evaluated the convective heat transfer coefficient of Octet lattice moving packed-bed heat exchanger (OLHX) additively manufactured in 420 stainless steel and found that the particle flow through OLHX channel provided heat transfer coefficient of 400 $W/m^2K$ at lattice porosity of 0.88. Moreover, the effective thermal conductivity of Octet-particles combination configurations was about 4-8 times higher than the corresponding particles-*only* configurations. OLHX therefore has the potential to reduce the particle-side thermal resistance and provide enhanced heat transfer owing to large wetted specific-area. The current study aims at experimentally visualizing the flow of particles and eventually develop DEM framework to simulate the granular flow through OLHX. The mass flow rates of the particles under free-fall through OLHX were measured through experiments. The results from DEM simulations were compared to the experimental data in terms of the mass flow rate as well as local flow features. The particle-side heat transfer coefficient is critical in determining the viability of granular-based heat exchange technology in CSP plants as dictated by the $/kWh metrics and the proposed OLHX can be optimized to meet these cost and power requirements of power plants.

**Experimental setup and computational domain**

**Figure 5.2** shows the schematic of experimental setup used for granular flow visualization in OLHX and **Fig. 5.3** provides the details of the corresponding computational domain used in the DEM simulations. The OLHX consisted of single-cell thick Octet lattice packed in an enclosure made of 12.7 mm thick acrylic sheets, which provided transparent access to record the granular flow motion using a Sony A-7RII camera at 30 Hz and included a large hopper formed by riveted mild steel sheets for particle storage to flow through the lattice under the influence of gravity.

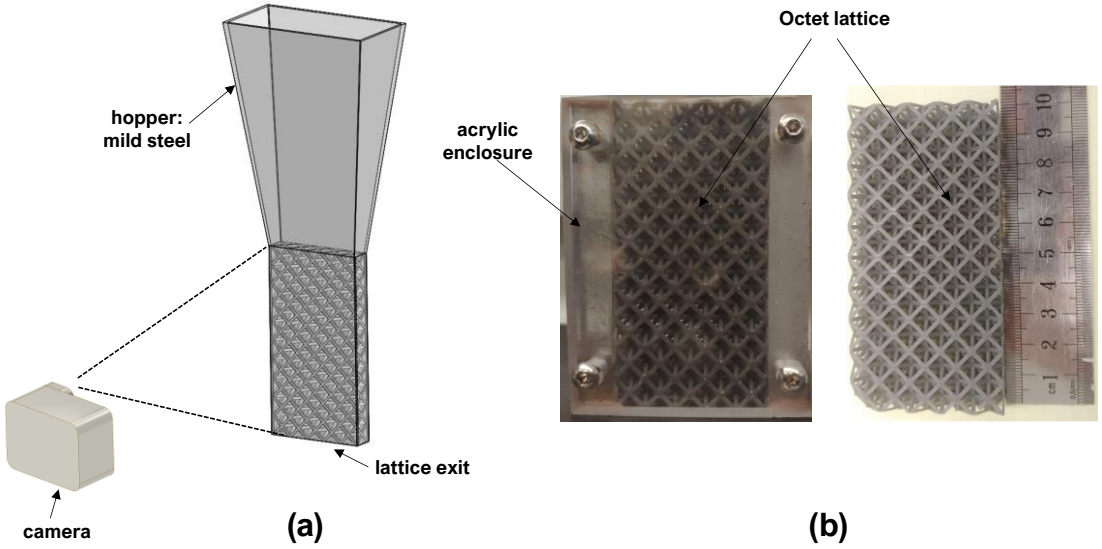



**Figure 5.2 (a) Schematic of experimental set-up used for granular flow visualization (not drawn to scale), (b) additively manufactured Octet lattice packed between enclosure of acrylic glass**

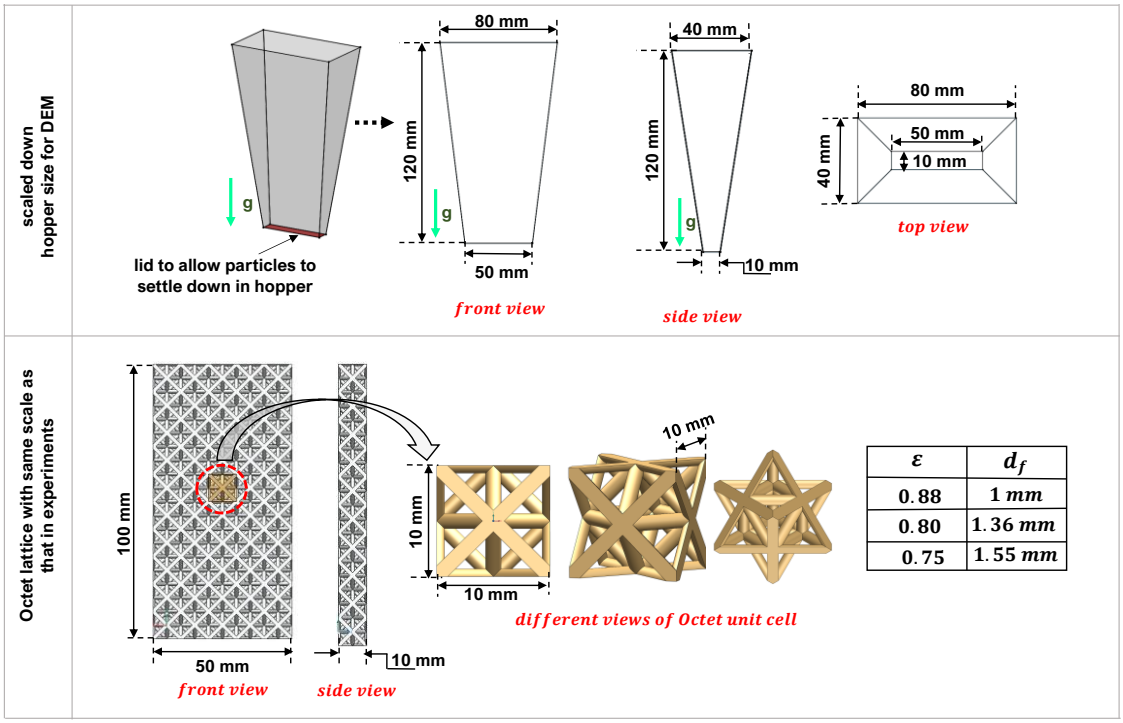



**Figure 5.3 Geometrical dimensions of the hopper and lattice section in the computational domain**

At the beginning of every test-run (t = 0) the lattice exit (shown in **Fig. 5.2**) was sealed with cardboard sheet and the particles were poured from the top into the hopper such that the whole Octet lattice section and a certain known height of the hopper were charged with stagnant particles. The cardboard sheet at the lattice exit was then instantly removed to allow the particles to fall into a container underneath the exit. A stopwatch was used to monitor the time during the free-fall and the time when all the particles had drained out of the OLHX was recorded. The particles collected underneath the OLHX exit were then measured on a high-precision weighing scale to evaluate the mass of the particles. The measured mass of the particles and the recorded time were finally used to evaluate the time-averaged mass flow rate of particles. Each run was repeated several times to ensure the repeatability of results and accuracy of the procedure adopted.

The Octet lattices used in the experiments were additively manufactured in resin using an in-house Form 3 SLA printer (from Formlabs). The total length of each lattice in the mean-flow direction was 100 mm and the width of the lattice was 50 mm (shown in **Fig. 5.3**). The lattice was single-cell thick where each repeating unit cell had dimensions of 10 mm x 10 mm x 10 mm resulting in total ten cells along the streamwise direction and five along the channel span. Different views of the Octet topology are also shown in **Fig. 5.3**. Three porosities of the Octet lattice were investigated experimentally and numerically, viz 0.75, 0.80, and 0.88. The corresponding fiber diameters were 1.55 mm, 1.36 mm, and 1 mm, respectively. The dimensional scales of the lattice section in the computational domain were exactly the same as that of the experiments. However, the large computational time and memory requirements prohibited the simulation of exact same mass of particles as filled during experiments. A relatively lower mass of particles was simulated (due to computational cost of DEM) due to which a scaled down version of hopper was modeled as shown in **Fig. 5.3**. The hopper in the computational domain resembled a frustrum with a rectangular base. The width and depth of the base where it connected with the lattice section was 50 mm and 10 mm, respectively, in order to completely conform to the lattice entrance. The total height of the hopper was 120 mm which opened to a rectangular cross-section of 80 mm x 40 mm on the top.

Unlike experiments, the covering lid was placed at the junction of the frustrum base and the lattice entrance (shown in red color in **Fig.5.3**) in computations. The lattice was bounded by walls of zero-thickness on the four sides in simulations. In the first step, the particles were injected from the top of the hopper and allowed to accumulate down on the lid under the influence of gravity. When the required amount of particle mass was injected into the hopper, the particles were allowed to settle down for some time to ensure that the mass flow rate during free-fall was calculated from the initial resting state of the particle just like experiments. **Figure 5.4** shows the resting particles filled in hopper before the free-fall. Once the particles were settled, the lid below them was removed and they were allowed to fall through the Octet lattice under the gravitational force.

**Particle characteristics**

Three different batches of sintered bauxite CARBOBEAD particles were experimentally investigated. **Figure 5.5** shows the distribution profiles from the particle size analysis performed using Anton Paar PSA 1190 LD. The investigated particles and the corresponding mean diameters are provided in **Table 5.1**. The flow of particles (3 different diameters) was experimentally investigated for three different Octet lattice porosities; however, the simulations were performed using only CARBOBEAD-CP 30/60 particles for all three porosities of the lattice. This selective focus on CARBOBEAD-CP 30/60 particles for simulations enabled a detailed comparative analysis while maintaining computational efficiency. Each experimental trial was conducted under carefully controlled ambient conditions with temperature and humidity monitoring to ensure consistency and reproducibility of results.

**Table 5.1 Mean diameter values of three different particle types experimentally investigated**

| Particle type | Mean diameter |
|---|---|
| CARBOBEAD-CP 40/100 | ~ 266 µm |
| CARBOBEAD-CP 30/60 | ~ 397 µm |
| CARBOBEAD-HSP 20/40 | ~ 966 µm |

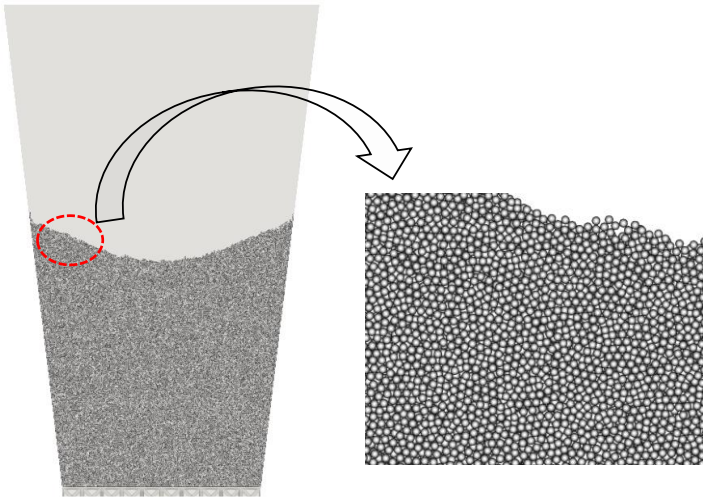


**Figure 5.4 Particles settled in the hopper before being discharged through the Octet lattice**

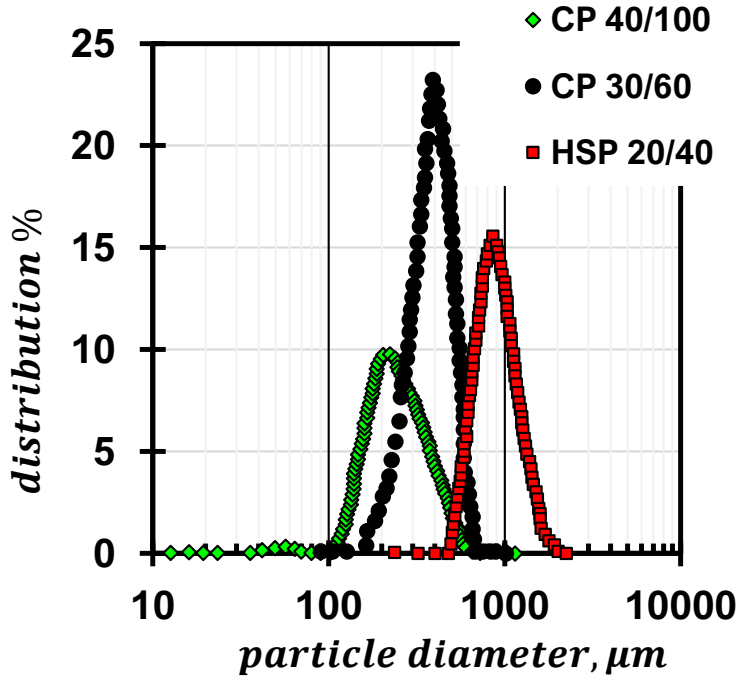



**Figure 5.5 Particle-size distribution profiles**

## Discrete element method (dem) procedure

In the present study, the DEM simulations were performed using the open-source code LIGGGHTS (LAMMPS Improved for General Granular and Granular Heat Transfer Simulations) [5.45] which predicts the motion of a particle using the Newtons' law of motion as given below [5.46].

For translational motion:

**Equation 5-1**

$$\dot{\boldsymbol{v}} = \frac{\sum \boldsymbol{F}}{m} + \boldsymbol{g}$$

For angular motion:

**Equation 5-2**

$$\dot{\boldsymbol{\omega}} = \frac{\sum \boldsymbol{T}}{\boldsymbol{I}}$$

where $\boldsymbol{v}$ is the velocity vector, $\boldsymbol{F}$ is the net contact force acting on the particle, $\boldsymbol{\omega}$ is the angular velocity vector, $\boldsymbol{T}$ is the net torque and $\boldsymbol{I}$ is the moment of inertia.

The particle-particle collision was modelled using 'soft sphere' scheme where the deformation was approximated through normal and tangential inter-particle overlaps. These overlaps were then used to evaluate the normal and tangential forces acting on the particle.

**Figure 5.6** represents the interactive-forces schematic between contacting particles through a spring-dashpot model [5.19,5.47]. Energy dissipation in the system is represented through the dashpot connected in parallel to the elastic springs. The sliding element placed in series with the spring in the tangential direction allows to account for the sliding of particles with each other while limiting the magnitude of tangential force. The spring-dashpot model effectively captures both the elastic and dissipative aspects of particle interactions, making it particularly suitable for granular flow simulations. The normal and tangential force components are calculated independently, with the normal force primarily responsible for preventing particle interpenetration while the tangential force accounts for friction and rotational effects. This comprehensive modeling approach enables accurate prediction of both static and dynamic particle behavior.

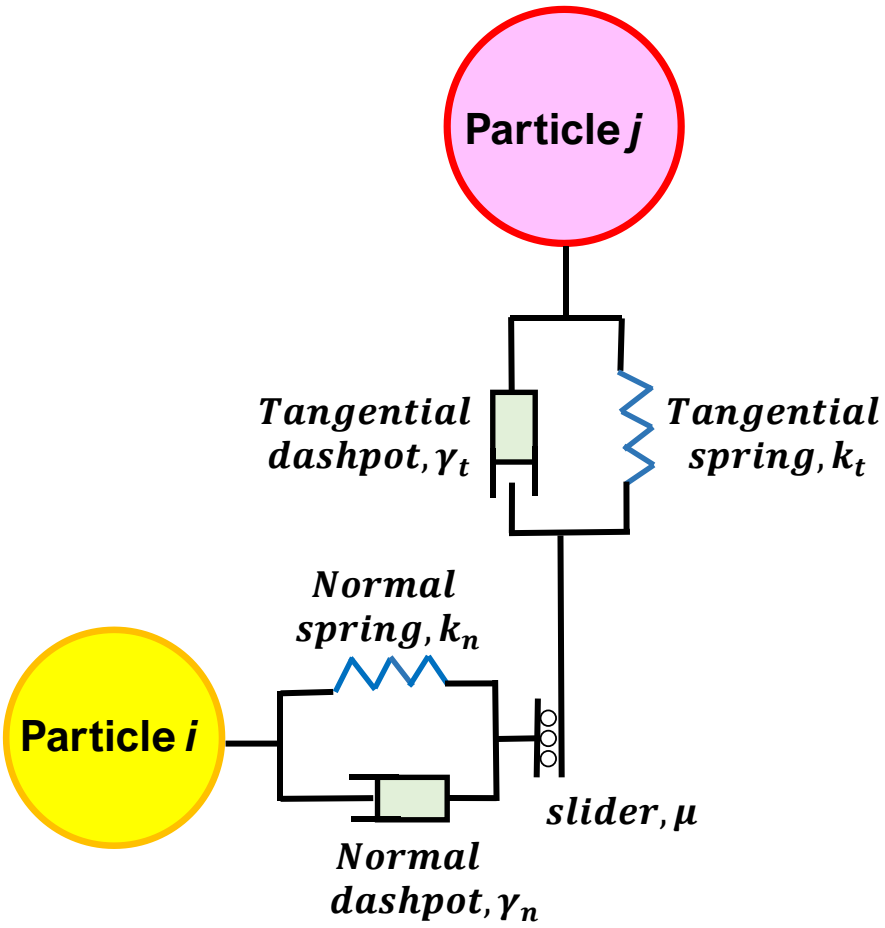



**Figure 5.6 Spring-dashpot model for interaction in the normal and tangential directions**

The Hertz-Mindlin contact model was specified during the simulations which calculates the inter-particle forces as following, provided the distance (D) between the two interacting particles of radii ($R_i$ and $R_j$) is less than the contact distance d = ($R_i$ + $R_j$):

**Equation 5-3**

$$F = \underbrace{\left(k_n \delta_{n_{ij}} - \gamma_n v_{n_{ij}}\right)}_{normal\ force} + \underbrace{\left(k_t \delta_{t_{ij}} - \gamma_t v_{t_{ij}}\right)}_{tangential\ force}$$

The normal force had the contribution from spring and damping forces whereas the tangential forces were formulated using shear and damping forces. The values of elastic constants ($k_n$ and $k_t$) and viscoelastic damping constants ($\gamma_n$ and $\gamma_t$) were evaluated using the material properties and particle overlaps ($\delta_n$ and $\delta_t$) as following:

**Equation 5-4**

$$k_n = \frac{4}{3} Y^* \sqrt{R^* \delta_n}$$

**Equation 5-5**

$$\gamma_n = -2\sqrt{\frac{5}{6}}\beta\sqrt{S_n m^*} \geq 0$$

**Equation 5-6**

$$k_t = 8G^*\sqrt{R^* \delta_n}$$

**Equation 5-7**

$$\gamma_t = -2\sqrt{\frac{5}{6}}\beta\sqrt{S_t m^*} \geq 0$$

where

**Equation 5-8**

$$S_n = 2Y^*\sqrt{R^* \delta_n}$$

**Equation 5-9**

$$S_t = 8G^*\sqrt{R^* \delta_n}$$

**Equation 5-10**

$$\beta = \frac{\ln(e)}{\sqrt{\ln^2(e) + \pi^2}}$$

**Equation 5-11**

$$\frac{1}{Y^*} = \frac{(1-\nu_i^2)}{Y_i} + \frac{(1-\nu_j^2)}{Y_j}$$

**Equation 5-12**

$$\frac{1}{G^*} = \frac{2(2-\nu_i)(1+\nu_i)}{Y_i} + \frac{2(2-\nu_j)(1+\nu_j)}{Y_j}$$

**Equation 5-13**

$$\frac{1}{R^*} = \frac{1}{R_i} + \frac{1}{R_j}$$

**Equation 5-14**

$$\frac{1}{m^*} = \frac{1}{m_i} + \frac{1}{m_j}$$

In the above formulae, $Y$ is the Young's modulus, G is the shear modulus, $\nu$ is the Poisson's ratio, and $e$ represents the coefficient of restitution. The superscript asterisk (*) refers to the effective properties. The shear force accounting for the tangential displacement between two interacting particles for the duration of contact time is a "history effect". The tangential overlap was truncated to fulfil the criteria $F_t \leq \mu_s F_n$, where $\mu_s$ is the coefficient of static sliding friction and $F_n$ is the normal force.

For the angular motion, the net torque is contributed by the torque from the tangential force and the rolling friction. Two rolling friction models from the current code library, namely, constant directional torque (CDT), and elastic-plastic spring-dashpot (EPSD2) were used in the current study.

The CDT model adds rolling friction torque as following:

**Equation 5-15**

$$T_{CDT} = \mu_r k_n \delta_n R^* \frac{\omega_{s,ij}}{|\omega_{s,ij}|}$$

where, $\omega_{s,ij}$ is the projection of relative angular velocity ($\omega_i$ - $\omega_j$) into the shear plane. For CDT model, the coefficient of rolling friction ($\mu_r$) must be specified. The EPSD2

model is determined as following over multiple time steps without using the viscous damping contribution:

**Equation 5-16**

$$T_{EPSD2,t+\Delta t} = T_{EPSD2,t} - k_t R^{*2} \Delta\theta_r$$

where, $\Delta\theta_r$ is the incremental relative rotation between the interacting particles. The maximum magnitude of spring torque is limited by the full mobilization torque determined using normal force and coefficient of rolling friction:

**Equation 5-17**

$$\left|T_{EPSD2,t+\Delta t}\right| \leq \mu_r R^* F_n$$

The correct evaluation of forces as per the equations presented in this section require accurate a priori determination of several input properties such as Young's modulus, Poisson's ratio, and coefficients of sliding friction, rolling friction, and restitution. The properties and other numerical inputs adopted in the simulations of the current study are discussed in the next section.

## Numerical setup

The parameters provided as input to evaluate particle-particle, particle-fiber, and particle-channel wall interactions are provided in **Table 5.2**. Both the fiber-surfaces and channel-walls were provided with the same material properties. The variables particle-particle sliding friction, rolling friction, and restitution coefficients were adopted from a recent study by Bagepalli et al. [5.48], where the authors experimentally measured the mechanical properties of CARBOBEAD-CP 30/60 proppants. The authors also reported the contact properties of particles against alumina- and resin-walls. The coefficient of sliding friction and rolling friction between particle-alumina wall was 1.0 and 0.41, respectively, whereas the coefficient values for particle-resin wall were 0.80 and 0.40, respectively. The particle-wall sliding friction values of 0.25 and 0.30 were used in DEM simulations by Gallego et al. [5.49] when the walls were considered to be made of steel and methacrylate, respectively, while the glass beads were the falling granular medium.

In the current study, alumina particles interacted with steel surface in the hopper, resin-wall in the lattice volume, and acrylic glass on the bounding walls in the experimental setup. However, all the surfaces in a simulation were attributed the same

sliding friction coefficient value for particle interaction. Three different cases of particle-wall sliding friction (0.3, 0.5, and 1.0) covering a wide range of values as reported in the literature discussed above were simulated in order to calibrate it against the current experimental data.

Time step size ($\delta t$) for Hertzian contact model in DEM simulations is based on the Rayleigh time as provided by the following theoretical expression [5.50,5.51]:

**Equation 5-18**

$$t_{Ray} = \frac{\pi R}{0.8766 + 0.163\nu}\sqrt{\frac{\rho}{G}}$$

The considered time step ($\delta t$) should be smaller than the particle's contact duration [5.52]. A common guideline is to adopt $\delta t$ of about 20% of $t_{Ray}$ for stable solution, however, larger time steps can be adopted if the achieved particle velocities in the computational domain are not expected to be very large. In the current study, $\delta t$ = 5x10$^{-6}$ was specified in all the simulations. The value of Young's modulus significantly influences the time step size because larger the Young's modulus smaller is the time step required to resolve particle-scale interactions. Researchers generally use a reduced elastic modulus magnitude as compared to the actual Young's modulus of particles [5.46,5.52] to reduce the computational time. Zhou et al. [5.53] investigated the sensitivity of angle of repose of monosized spheres to various factors such as particle characteristics, material properties, and geometrical constraints. Young's modulus range of $10^5$ – $10^8$ N/m$^2$ was investigated which showed no obvious effect on the angle of repose. The major controlling factors for translational and rotational motion of particles were found to be sliding and rolling frictions. Yan et al. [5.54] performed a parametric multi-level sensitivity analysis to understand the effect of DEM input particle properties on the bulk response for system involving discharge of particles from a flat bottom cylindrical container onto a plate. With all other parameter fixed, change in Young's modulus from 0.02 GPa to 200 GPa demonstrated small influence on the final shape of pile of material and average velocity of particles near the orifice. However, computational time increased from 0.4 hours for Young's modulus value of 0.02 GPa with time step size of 5 x 10$^{-6}$ s to 240 hours for Young's modulus value of 200 GPa at time step size of 5 x 10$^{-8}$ s. Xu et al.

[5.55] investigated the effects of material properties on granular flow in a silo. The authors found that material modulus with artificial value of 1/1000 of the actual value yielded no significant difference in flow pattern and discharge rate suggesting that soft-sphere approach (lower modulus values) can be used to predict of behavior of hard particles to save computational time.

Yarrington et al. [5.19] and Bagepalli et al. [5.48] reported the Young's modulus value of alumina particles to be ~ 209 GPa which would require a very small time step. Instead, Young's modulus of $1x10^7$ Pa was used in the current study to reduce the overall computational cost.

In DEM simulations, the neighbor list of potential contacts is built periodically which is checked at every time step and the pairs of particles that are too far away from each other to be in contact are excluded. The pair of interacting particles can be included in the list based on a certain range as given by the following formula [5.45]:

**Equation 5-19**

$$||\boldsymbol{x}_i - \boldsymbol{x}_j|| < r_i + r_j + s$$

where "s" is the skin parameter that is specified by the user. All interacting pairs within the cut-off distance provided by Eq. 3.19 are stored in the list which is periodically updated to account for the relocation of particles in a domain upon interaction. The larger the skin parameter, less often the neighbor list requires rebuilding, however, a greater number of pairs must be checked every time step for any possible interactions. The skin parameter used in the current study was 800 $\mu$m, i.e., twice of the particle diameter. A 100g of total particle mass was injected into the hopper before the free-fall. The mass flow rate profiles were obtained from simulations at the exit plane of the Octet lattice.

## Results and discussion

### *Calibration of sliding friction coefficient for DEM simulations*

As discussed in detail within the previous section, three distinct values (0.3, 0.5, and 1.0) of particle-wall sliding friction coefficient were systematically investigated through numerical simulations. The characteristic mass flow rate behavior of CP 30/60 particles utilizing these three coefficient values in an OLHX configuration having porosity of 0.88 is comprehensively presented in **Fig. 5.7**, where all simulation results correspond to the

EPSD2 rolling friction model implementation. The time designation t=0 in these plots corresponded to the precise moment of particle injection initiation into the hopper system. To ensure consistency across all simulations, identical time durations were allocated for both particle filling and resting phases before their subsequent release for free-fall conditions. The experimentally measured mass flow rate for the considered lattice porosity was determined to be 38.98 g/s. The simulated mass of particles falling through the OLHX demonstrated a steady-state mass flow rate for a considerable duration, confirming that the selected 100g sample mass was sufficient to thoroughly analyze the flow behavior while avoiding both start-up and end-effects. Notably significant deviations in mass-flow rates were observed across the three different particle-wall sliding friction coefficients investigated. A clear trend emerged showing that as the coefficient of sliding friction decreased, the predicted mass flow rate value increased proportionally. For the current experimental setup and configuration, the closest agreement with the experimental data was achieved using a friction coefficient value of 0.5. This optimized value, adopted for all simulations, ensured consistent and reliable numerical predictions across all simulation cases.

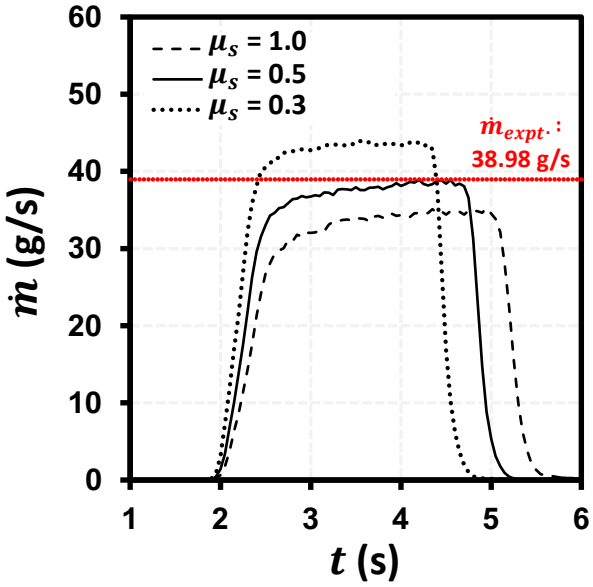



**Figure 5.7 Comparison of mass flow rates obtained from DEM simulations for three different particle-wall sliding friction coefficients against the experimental data**

***Rolling friction models***

Once the coefficient of sliding friction was fixed at 0.5, we conducted a detailed analysis to examine how different rolling friction models affected the mass flow rate behavior. **Figure 5.8** presents the temporal evolution of mass-flow rates for CP 30/60 particles within the OLHX system, which maintained a porosity of 0.88. The investigation compared two distinct rolling friction models: the Elasto-Plastic Spring-Dashpot (EPSD2) model and the Continuous Deformation Theory (CDT) model. Our analysis revealed that the choice between these models had minimal impact on the overall mass-flow rate characteristics. During the steady-state period (3-5.5 seconds), the EPSD2 model predicted marginally lower flow rates while the CDT model showed slightly higher values compared to the mean experimental value. The consistency between both models' predictions suggests that the particle flow dynamics in this system are primarily governed by sliding friction rather than rolling effects. Given that the selection of rolling friction model did not significantly influence the final mass-flow rate predictions, we chose the EPSD2 model for conducting subsequent simulations. This robustness across models increases confidence in the numerical predictions and indicates accurate capture of the underlying physics.

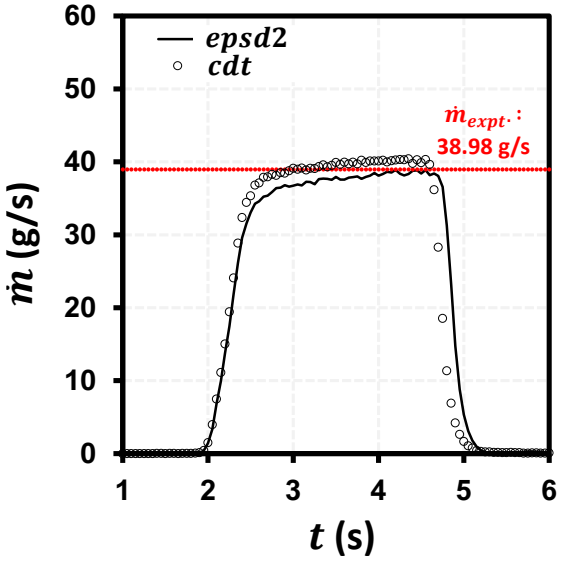



**Figure 5.8 Comparison of mass flow rates obtained from DEM simulations for two different rolling friction models**

***Instantaneous flow characteristics***

**Figure 5.9** shows the image of particles taken during experiments at instants when the particles were in steady-fall condition. Also presented is the zoomed-in image of the front side of the acrylic panel of OLHX having 0.88 porosity with CP 30/60 particles to better understand the granular motion.

From the front view, three distinct flow characteristics were observed, i.e., (a) stagnant-zone upstream of the fiber junctions, (b) cone-shaped void zone in the wake of the fibers, and (c) unobstructed wavy-type motion of particles on lateral sides of the fibers. The upstream stagnation of particles and downstream void due to particle separation is a common characteristic of granular flow around tubes in a shell-and-tube type heat exchanger.

The downstream regions of fibers typically remain devoid of the contact with the heated particles leading to weaker heat transfer. The overall conjugate heat transfer coefficient of OLHX depends on the effective thermal conductivity of the system and interfacial heat transfer coefficient values. The interfacial heat transfer coefficient depends on the flow fields rendered by the moving media in the lattice. The local heat transfer coefficient distribution around discrete arrangement of circular tubes arranged normally and inclined to the mean flow direction is reported in literature. However, the current OLHX represents a relatively complex scenario where all the cylindrical fibers of the repeating unit cell are placed at a different angle to the encountering particles. The solid fibers attached to the bounding walls, when fabricated in thermally conductive metallic materials, will inherently develop complex internal thermal gradients, leading to interesting thermal exchange dynamics with the flowing particles.

**Figure 5.10** shows the images of OLHX ($\varepsilon = 0.88$) during discharge of particles CP 30/60 colored by the local flow velocities obtained from the simulations. The particles along fiber sides exhibited higher velocities, corresponding to the wavy motion in **Fig. 5.9**. Fig. 5.10b reveals void regions beneath fiber junctions, while **Fig. 5.10c** shows poor particle contact at front- and side-acrylic walls. These contact variations would result in non-uniform heat transfer coefficients on sCO2-side channel walls, creating regions of locally high and low heat transfer.

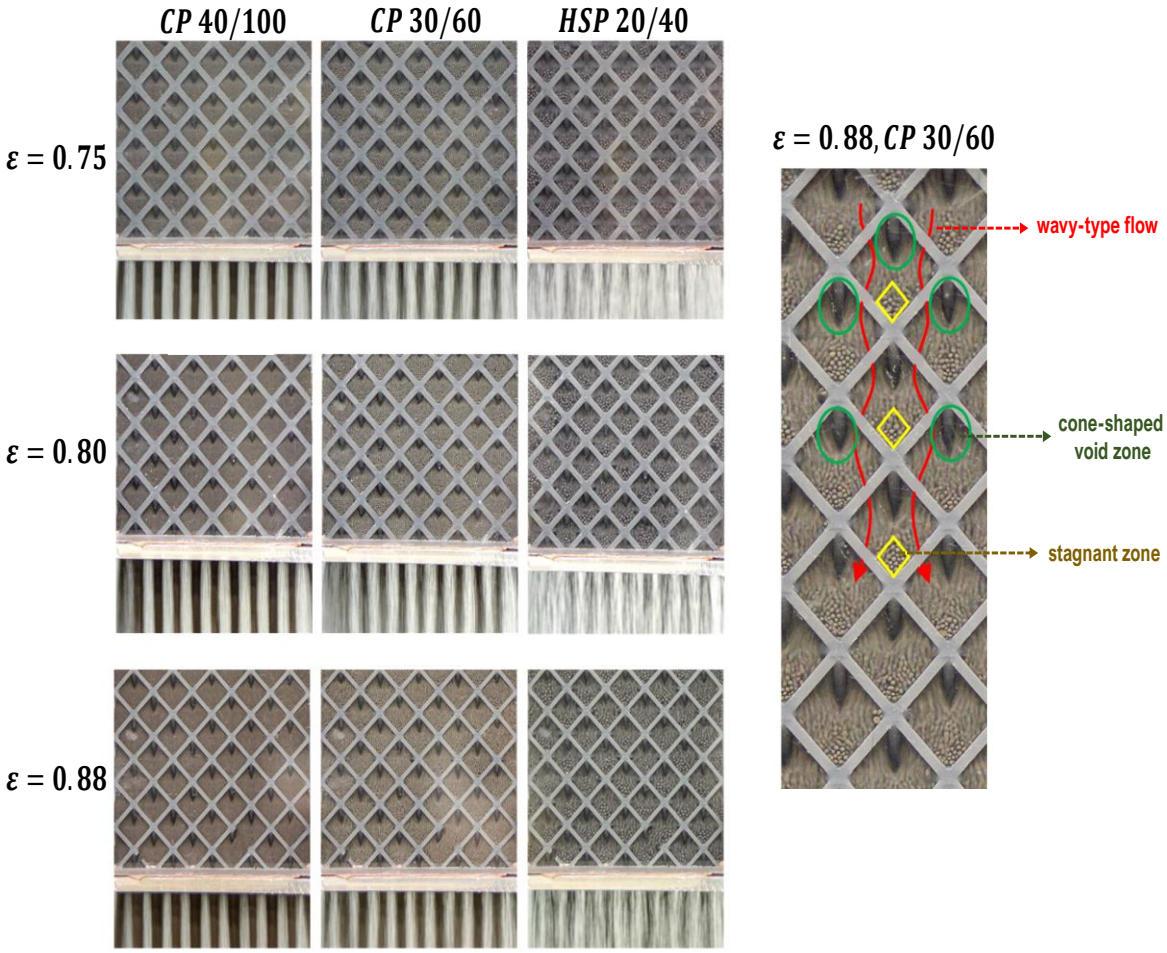



**Figure 5.9 Instantaneous images of the free-fall of particles in three different lattices taken during experiments**

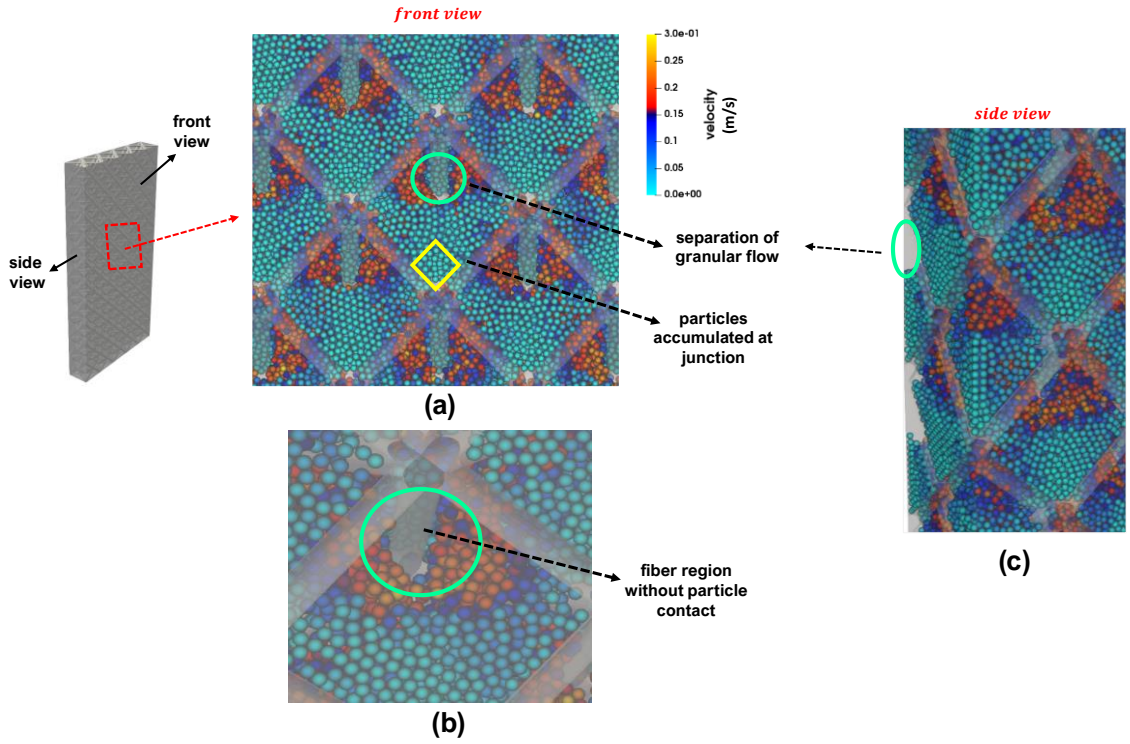



**Figure 5.10 (a) Instantaneous image of the free-fall of particles from DEM simulations with particles colored with their local flow velocities, (b) zoomed-in view of the front side of the channel, and (c) zoomed-in side view of the channel**

Moreover, the fiber-fiber junctions and fiber-channel wall junctions provided accommodation to the particles for accumulation as demonstrated in the post free-fall image in **Fig. 5.11**.

Stagnant particles in the junctions reduce heat transfer by blocking the flow of fresh heated particles.

***Effect of porosity on the mass flow rate***

The temporal evolution of mass flow rate profiles for CP 30/60 particles at three different lattice porosities is provided in **Fig. 5.12.** For the same total mass of particles, the mass flow rate was maximum for the highest porosity value of 0.88. Therefore, the particles drained out of 88% porous OLHX in the least time span. The lowest porosity value of 0.75 provided the maximum hinderance to the free flow of the particles resulting in the maximum discharge time.

**Figure 5.13a** shows mass flow rates obtained from the experimental runs of three different particle batches as a function of lattice porosity. The trends with respect to the porosity variation were similar for particles of different diameters, where the mass flow rate increased with increasing porosity. The difference in mass flow rates of CP 40/100 and 30/60 particles remained almost same across the entire porosity range. The gap between mass-flow rates for HSP 20/40 particles with respect to the other batches decreased as the lattice porosity increased. Larger porosity of the lattices ensures greater voidage volume for the particles to fall freely resulting in increased flow velocities in the domain resulting in relatively larger mass-flow rates. However, it should be noted that the stagnant effective thermal conductivity would decrease with increasing porosity too. **Figure 5.13b** shows the comparison of experimental mean mass flow rate data with the numerically predicted values as a function of porosity for CP 30/60 particles. Overall, the predicted values were in good agreement with the corresponding experimental data, especially for the higher porosities. The simulated mass had spherical particles of uniform diameter as opposed to the distribution profile provided in **Fig. 5.5.** This is expected to influence the mass-flow rate values predicted via simulations. The discrepancy between experimental and simulated results stems from differences in particles sizes in nature.

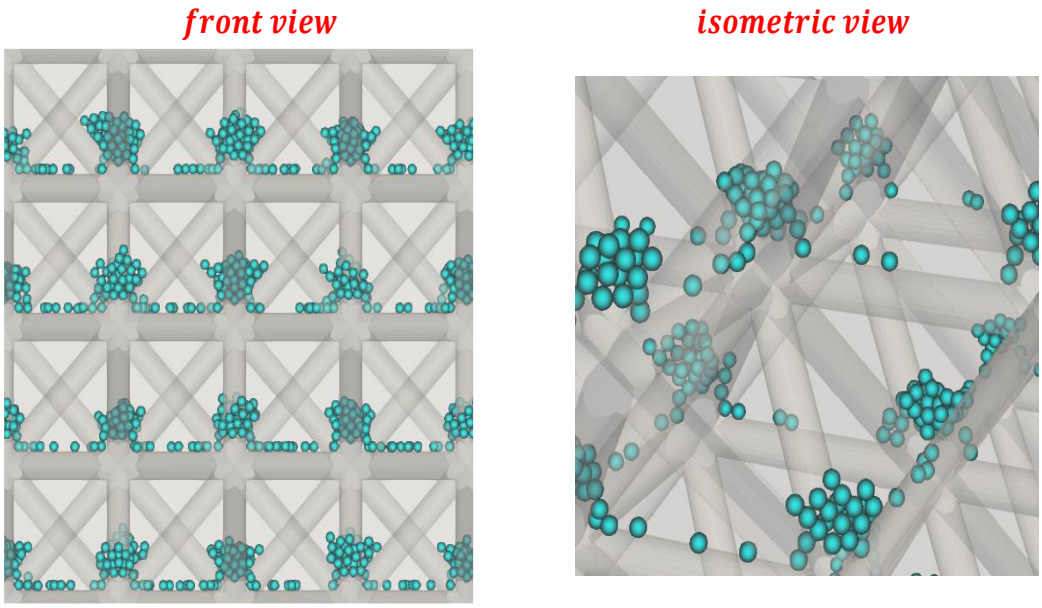



**Figure 5.11 Image of the particles taken after the completion of the DEM simulation showing accumulation in the junction regions**

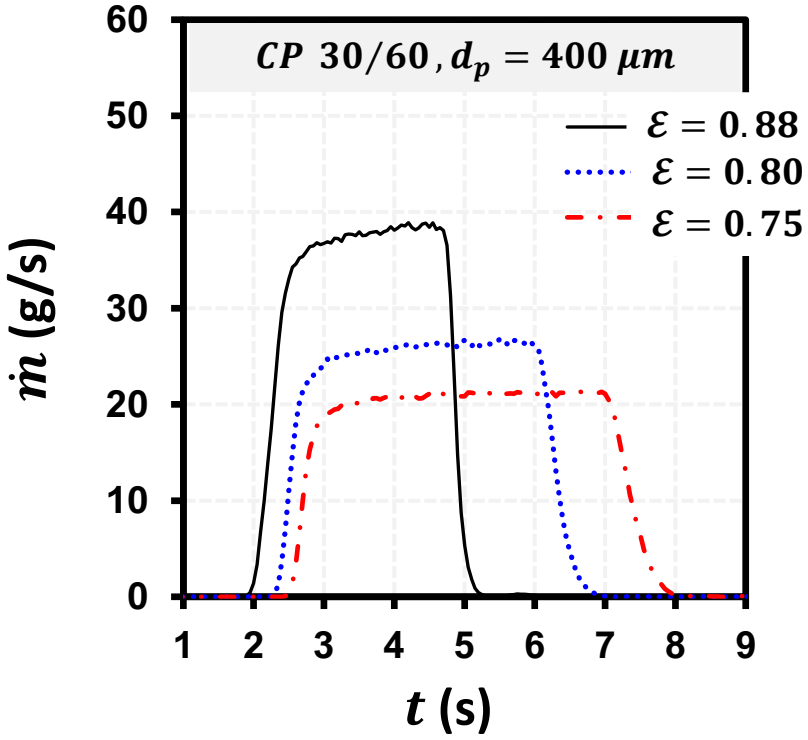



**Figure 5.12 Temporal evolution of mass flow rate profiles for three lattice porosities obtained from DEM simulations**

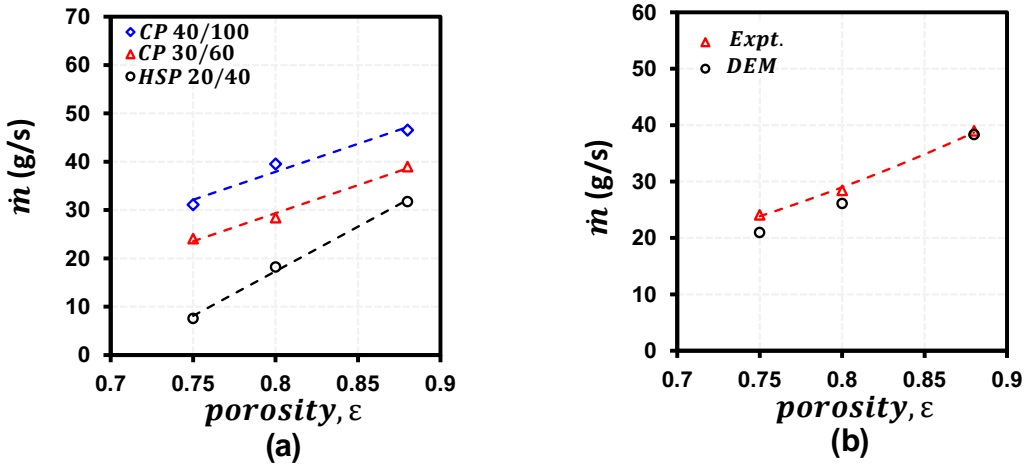



**Figure 5.13 (a) Experimentally obtained mass flow rates for three different particle batches as a function of lattice porosity, (b) comparison of mean mass flow rates obtained from the experiments and DEM simulations for CP 30/60 particles as a function of lattice porosity**

***Effect of particle diameter on the mass flow rate***

**Figure 5.14** shows the experimentally obtained mass flow rates for three different porosities of Octet lattice as a function of particle diameter. At a fixed porosity, the mass flow rate diminished with increasing particle diameter. The smaller diameter particles at any fixed porosity will have tendency of moving faster in the porous volume and subsequently have more frequent interactions with the fibers of the lattice oriented at different angles. In the case of OLHX where the fiber-network can be very dense for lower porosities, the scale of particles with respect to the fiber dimensions can be a very critical parameter of investigation. The previous study by the authors [5.44] showed that the particles with smaller diameter provided higher overall heat transfer coefficient for OLHX at a fixed porosity. This correlation between particle size, flow rate, and heat transfer efficiency suggests an optimal design window where both flow and thermal performance can be maximized simultaneously. The findings also indicate that the selection of particle diameter must be carefully balanced against manufacturing constraints and system pressure drop considerations to achieve optimal system performance. These experimental observations were further validated through extensive repeatability tests, which demonstrated consistent trends across multiple trials with variations less than 3%. The relationship between particle diameter and mass flow rate exhibited a non-linear behavior, particularly pronounced at lower porosities, suggesting complex interactions between particle dynamics and lattice geometry. This non-linear behavior can be attributed to the increasing significance of particle-wall interactions as the ratio of particle diameter to fiber spacing approaches unity. Additional parametric studies revealed that the effect of particle diameter on mass flow rate became more prominent at lower porosities, where the confined geometry created more complex flow patterns and increased particle-structure interactions. Understanding these intricate relationships is crucial for optimizing the design of OLHX systems for specific applications, as the choice of particle size can significantly impact both the thermal and hydraulic performance of the system. Mass flow rate was most sensitive to particle diameter variations at intermediate porosity, a critical design region where careful particle size selection can optimize performance.

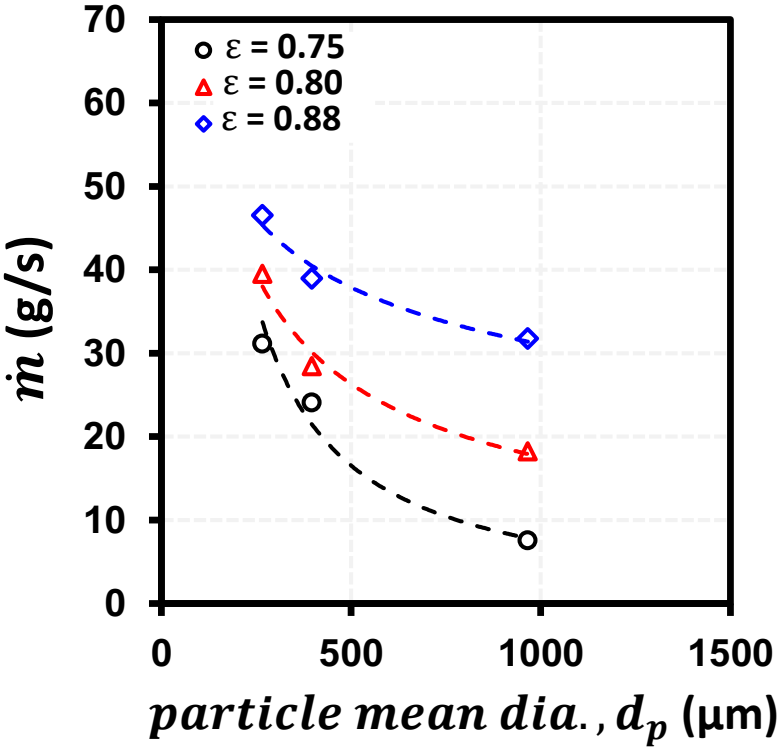



**Figure 5.14 Experimentally obtained mass flow rates for three different lattice porosities as a function of particle diameter**

## Conclusions

The experimental and DEM-based numerical investigation is conducted for flow in novel Octet lattice moving packed-bed heat exchanger (OLHX) in this study with potential applications in CSP-based power generation. The OLHX packed beds demonstrate high effective thermal conductivity and overall heat transfer coefficients, therefore, it is imperative to gain in-depth knowledge of how it modifies the granular flow field. In the present study, experimental flow visualization was conducted on three different porosities, viz 0.75, 0.80, and 0.88, of OLHX for three different CARBOBEAD particle batches – (a) CP 40/100, (b) CP 30/60, and (c) HSP 20/40. The DEM framework to simulate the granular flow through the OLHX was then developed in the open source LIGGGTHS software, the results from which provided good agreement with the corresponding experimental data. This framework will be further developed to investigate the heat transfer in complex OLHX configurations. Major conclusions from this flow analysis study are highlighted below:

(a) For a fixed particle diameter, the mass flow rate increased with increasing OLHX porosity. For a fixed porosity of the OLHX, mass flow rate decreased with increasing particle diameter. The enhanced particle flow velocities coupled with frequent interactions with the fiber network is expected to provide high overall heat transfer coefficient values.

(b) The experimental images showed cone-shaped void zones downstream of fibers, stagnation areas upstream of junctions, and wavy type unobstructed motion around fibers. The DEM simulations were able to capture all these important flow features of the experimental results.

(c) DEM images clearly demonstrated regions of the fiber network as well as channel walls which were completely devoid of the particle contact. These regions will provide very low thermal exchange opportunity leading to non-uniform heat transfer coefficient distribution on the fibers as well as channel walls in contact with the working fluid of the power cycle.

(d) The images of OLHX domain post completion of simulations showed the accumulation of the particles on the junctions of fibers with other fibers as well as with

the channel walls. These regions did not have very frequent update of the fresh incoming particles which can prove to be the hot-spots for poor thermal exchange over time.

(e) The DEM simulations were conducted with the assumption of particles being spherical and having uniform fixed diameter which was different from the measured morphological characteristics of the particles used in experiments. Modeling of real-like particle distribution can further improve the accuracy of the DEM simulations.

## Acknowledgments

This material is based upon work supported by the U.S. Department of Energy's Office of Energy Efficiency and Renewable Energy (EERE) under the Solar Energy Technologies Office Award Number DE-EE0009377. This report was prepared as an account of work sponsored by an agency of the United States Government. Neither the United States Government nor any agency thereof, nor any of their employees, makes any warranty, express or implied, or assumes any legal liability or responsibility for the accuracy, completeness, or usefulness of any information, apparatus, product, or process disclosed, or represents that its use would not infringe privately owned rights. Reference herein to any specific commercial product, process, or service by trade name, trademark, manufacturer, or otherwise does not necessarily constitute or imply its endorsement, recommendation, or favoring by the United States Government or any agency thereof. The views and opinions of authors expressed herein do not necessarily state or reflect those of the United States Government or any agency thereof.

## Nomenclature

| | |
|---|---|
| $d_f$ | fiber diameter |
| $d_p$ | mean particle diameter |
| e | coefficient of restitution |
| $F$ | force acting on the particle |
| G | shear modulus |
| $g$ | gravitational force |
| $I$ | moment of inertia |

| | |
|---|---|
| $k_n$ | elastic constant for normal contact |
| $k_t$ | elastic constant for tangential contact |
| $m$ | mass of the particle |
| R | radius of the particle |
| $s$ | skin parameter |
| $S_n$ | material constant in normal direction |
| $S_t$ | material constant in tangential direction |
| $T$ | torque acting on the particle |
| $t_{Ray}$ | Rayleigh time step criteria |
| $v$ | velocity |
| $v_n$ | normal component of the relative velocity |
| $v_t$ | tangential component of the relative velocity |
| $Y$ | Young's modulus |
| $x$ | particle position |

**Greek symbols**

| | |
|---|---|
| ε | porosity |
| $\delta_n$ | normal overlap distance between two particles |
| $\delta_t$ | tangential displacement between two particles |
| $\gamma_n$ | viscoelastic damping constant for normal contact |
| $\gamma_t$ | viscoelastic damping constant for tangential contact |
| $\nu$ | Poisson's ratio |
| $\mu_s$ | sliding friction coefficient |
| $\mu_r$ | rolling friction coefficient |
| $\omega$ | angular velocity |
| $\rho$ | density of the particle |
| $\beta$ | material constant used to calculate interacting forces in LIGGGHTS |

**Abbreviations**

| | |
|---|---|
| CDT | constant direction torque |
| CSP | concentrated solar power plant |

| | |
|---|---|
| DEM | discrete element method |
| EPSD | elastic-plastic spring dashpot |
| HTF | heat transfer fluid |
| HX | heat exchanger |
| OLHX | Octet lattice moving packed-bed heat exchanger |
| $sCO_2$ | supercritical carbon-dioxide |
| TES | thermal energy storage |

**Superscript**

| | |
|---|---|
| * | effective properties |

## References

[5.1] Montes, M.J., Linares, J.I., Barbero, R., and Moratilla, B.Y., 2020, "Optimization of a New Design of Molten Salt-to-CO2 Heat Exchanger Using Exergy Destruction Minimization," *Entropy,* 22, p. 883. https://doi.org/10.3390/e22080883.

[5.2] Mehos, M., Turch, C., Vidal, J., Wagner, M., Ma, Z., Ho, C., Kolb, W., Andraka, C., and Kruizenga, A., 2017, "Concentrating Solar Power Gen3 Demonstration Roadmap,". https://doi.org/10.2172/1338899.

[5.3] Du¸ B.C, He, Y.L., Qiu, Y., Liang, Q., and Zhou, Y.P., 2018, "Investigation on heat transfer characteristics of molten salt in a shell-and-tube heat exchanger," *International Communications in Heat and Mass Transfer,* 96, pp. 61-68. https://doi.org/10.1016/j.icheatmasstransfer.2018.05.020.

[5.4] He, Y.L., Zheng, Z.J., Du, B.C., Wang, K., and Qiu, Y., 2016, "Experimental investigation on turbulent heat transfer characteristics of molten salt in a shell-and-tube heat exchanger," *Applied Thermal Engineering,* 108, pp. 1206-1213. https://doi.org/10.1016/j.applthermaleng.2016.08.023.

[5.5] Qian, J., Kong, Q.L., Zhang, H.W., Zhu, Z.H, Huang, W.G., and Li, W.H, 2017, "Experimental study for shell-and-tube molten salt heat exchangers," *Applied Thermal Engineering,* 124, pp. 616-623. https://doi.org/10.1016/j.applthermaleng.2017.06.005.

[5.6] Huang, C, Cai, W., Wang, Y., Liu, Y., Li, Q., and Li. B, 2019, "Review on the characteristics of flow and heat transfer in printed circuit heat exchangers," *Applied Thermal Engineering,* 153, pp.190-205. https://doi.org/10.1016/j.applthermaleng.2019.02.131.

[5.7] Wang, W.Q., Qiu, Y., He, Y.L., and Shi, H.Y., 2019, "Experimental study on the heat transfer performance of a molten-salt printed circuit heat exchanger with airfoil fins for concentrating solar power," *International Journal of Heat and Mass Transfer,* 135, pp. 837-846. https://doi.org/10.1016/j.ijheatmasstransfer.2019.02.012.

[5.8] Nikitin, K., Kato, Y. and Ngo, L., 2006, “Printed circuit heat exchanger thermal–hydraulic performance in supercritical CO2 experimental loop,” *International Journal of refrigeration*, *29*(5), pp.807-814. https://doi.org/10.1016/j.ijrefrig.2005.11.005.

[5.9] Encinas-Sánchez, V., Lasanta, M.I., De Miguel, M.T., García-Martín, G. and Pérez, F.J., 2021, “Corrosion monitoring of 321H in contact with a quaternary molten salt for parabolic trough CSP plants,” *Corrosion Science*, *178*, p.109070. https://doi.org/10.1016/j.corsci.2020.109070.

[5.10] Tian, X., Yang, J., Guo, Z., Wang, Q. and Sunden, B., 2020, “Numerical study of heat transfer in gravity-driven dense particle flow around a hexagonal tube,” *Powder technology*, *367*, pp.285-295. https://doi.org/10.1016/j.powtec.2020.04.001.

[5.11] Albrecht, K.J. and Ho, C.K., 2019, “Heat transfer models of moving packed-bed particle-to-sCO2 heat exchangers,” *J Sol Energy Eng*, *141*(3), p.031006. https://doi.org/10.1115/1.4041546.

[5.12] Albrecht, K.J. and Ho, C.K., 2019, “Design and operating considerations for a shell-and-plate, moving packed-bed, particle-to-sCO2 heat exchanger,” *Solar Energy*, *178*, pp.331-340. https://doi.org/10.1016/j.solener.2018.11.065.

[5.13] Baumann, T. and Zunft, S., 2015, “Development and performance assessment of a moving bed heat exchanger for solar central receiver power plants,” *Energy Procedia*, *69*, pp.748-757. https://doi.org/10.1016/j.egypro.2015.03.085.

[5.14] Tian, X., Guo, Z., Jia, H., Yang, J. and Wang, Q., 2021, “Numerical investigation of a new type tube for shell-and-tube moving packed bed heat exchanger,” *Powder Technology*, *394*, pp.584-596. https://doi.org/10.1016/j.powtec.2021.08.080.

[5.15] Tian, X., Zhu, F., Guo, Z., Zhang, J., Yang, J. and Wang, Q., 2022, “Numerical investigation of gravity-driven particle flow along the trapezoidal corrugated plate for a moving packed bed heat exchanger,” *Powder Technology*, *405*, p.117526. https://doi.org/10.1016/j.powtec.2022.117526.

[5.16] Guo, Z., Yang, J., Tan, Z., Tian, X. and Wang, Q., 2021, " Numerical study on gravity-driven granular flow around tube out-wall: Effect of tube inclination on the heat transfer," *International Journal of Heat and Mass Transfer*, *174*, p.121296. https://doi.org/10.1016/j.ijheatmasstransfer.2021.121296

[5.17] Cundall, P.A. and Strack, O.D., 1979, "A discrete numerical model for granular assemblies," *geotechnique*, *29*(1), pp.47-65. https://doi.org/10.1680/geot.1979.29.1.47.

[5.18] Bartsch, P. and Zunft, S., 2019, "Granular flow around the horizontal tubes of a particle heat exchanger: DEM-simulation and experimental validation," *Solar Energy*, *182*, pp.48-56. https://doi.org/10.1016/j.solener.2019.01.086.

[5.19] Yarrington, J.D., Bagepalli, M.V., Pathikonda, G., Schrader, A.J., Zhang, Z.M., Ranjan, D. and Loutzenhiser, P.G., 2021, " Numerical analyses of high temperature dense, granular flows coupled to high temperature flow property measurements for solar thermal energy storage," *Solar Energy*, *213*, pp.350-360. https://doi.org/10.1016/j.solener.2020.10.085.

[5.20] Soni, R.K., Mohanty, R., Mohanty, S. and Mishra, B.K., 2016, "Numerical analysis of mixing of particles in drum mixers using DEM," *Advanced Powder Technology*, *27*(2), pp.531-540. https://doi.org/10.1016/j.apt.2016.01.016.

[5.21] Liu, P.Y., Yang, R.Y. and Yu, A.B., 2013, "DEM study of the transverse mixing of wet particles in rotating drums," *Chemical Engineering Science*, *86*, pp.99-107. https://doi.org/10.1016/j.ces.2012.06.015.

[5.22] Xiao, X., Tan, Y., Zhang, H., Deng, R. and Jiang, S., 2017, "Experimental and DEM studies on the particle mixing performance in rotating drums: Effect of area ratio," *Powder technology*, *314*, pp.182-194. https://doi.org/10.1016/j.powtec.2017.01.044.

[5.23] Deb, S. and Tafti, D.K., 2014, "Two and three dimensional modeling of fluidized bed with multiple jets in a DEM–CFD framework," *Particuology*, *16*, pp.19-28. https://doi.org/10.1016/j.partic.2014.04.005.

[5.24] Li, T. and Guenther, C., 2012, “MFIX-DEM simulations of change of volumetric flow in fluidized beds due to chemical reactions,” *Powder technology*, *220*, pp.70-78. https://doi.org/10.1016/j.powtec.2011.09.025.

[5.25] Xu, Y., Li, T., Musser, J., Liu, X., Xu, G. and Rogers, W.A., 2017, “CFD-DEM modeling the effect of column size and bed height on minimum fluidization velocity in micro fluidized beds with Geldart B particles,” *Powder technology*, *318*, pp.321-328. https://doi.org/10.1016/j.powtec.2017.06.020.

[5.26] Guo, Z., Zhang, S., Tian, X., Yang, J. and Wang, Q., 2020, “Numerical investigation of tube oscillation in gravity-driven granular flow with heat transfer by discrete element method,” *Energy*, *207*, p.118203. https://doi.org/10.1016/j.energy.2020.118203.

[5.27] Tian, X., Yang, J., Guo, Z. and Wang, Q., 2021, “Numerical Investigation of Gravity-Driven Granular Flow around the Vertical Plate: Effect of Pin-Fin and Oscillation on the Heat Transfer,” *Energies*, *14*(8), p.2187. https://doi.org/10.3390/en14082187.

[5.28] Peng, Z., Doroodchi, E. and Moghtaderi, B., 2020, “Heat transfer modelling in Discrete Element Method (DEM)-based simulations of thermal processes: Theory and model development,” *Progress in Energy and Combustion Science*, *79*, p.100847. https://doi.org/10.1016/j.pecs.2020.100847.

[5.29] Batchelor, G.K. and O'brien, R.W., 1977, “Thermal or electrical conduction through a granular material,” *Proceedings of the Royal Society of London. A. Mathematical and Physical Sciences*, *355*(1682), pp.313-333. https://doi.org/10.1098/rspa.1977.0100

[5.30] Wang, S., Luo, K., Hu, C., Lin, J. and Fan, J., 2019, “CFD-DEM simulation of heat transfer in fluidized beds: Model verification, validation, and application,” *Chemical Engineering Science*, *197*, pp.280-295. https://doi.org/10.1016/j.ces.2018.12.031.

[5.31] Denloye, A.O.O. and Botterill, J.S.M., 1977, “Heat transfer in flowing packed beds,” *Chemical Engineering Science*, *32*(5), pp.461-465. https://doi.org/10.1016/0009-2509(77)87001-2

[5.32] Sullivan, W.N. and Sabersky, R.H., 1975, “Heat transfer to flowing granular media,” *International Journal of Heat and Mass Transfer, 18*(1), pp.97-107. https://doi.org/10.1016/0017-9310(75)90012-5.

[5.33] Spelt, J.K., Brennen, C.E. and Sabersky, R.H., 1982, “Heat transfer to flowing granular material,” *International Journal of Heat and Mass Transfer, 25*(6), pp.791-796. https://doi.org/10.1016/0017-9310(82)90091-6.

[5.34] Lv, W., Li, D. and Dong, L., 2020, “Study on mechanical properties of a hierarchical octet-truss structure,” *Composite Structures, 249,* p.112640. https://doi.org/10.1016/j.compstruct.2020.112640.

[5.35] Deshpande, V.S., Fleck, N.A. and Ashby, M.F., 2001, “Effective properties of the octet-truss lattice material,” *Journal of the Mechanics and Physics of Solids, 49*(8), pp.1747-1769. https://doi.org/10.1016/S0022-5096(01)00010-2.

[5.36] Kaur, I. and Singh, P., 2020, “Flow and thermal transport through unit cell topologies of cubic and octahedron families,” *International Journal of Heat and Mass Transfer, 158,* p.119784. https://doi.org/10.1016/j.ijheatmasstransfer.2020.119784.

[5.37] Kaur, I. and Singh, P., 2021, “Numerical investigation on conjugate heat transfer in octet-shape-based single unit cell thick metal foam,” *International Communications in Heat and Mass Transfer, 121,* p.105090. https://doi.org/10.1016/j.icheatmasstransfer.2020.105090.

[5.38] Kaur, I. and Singh, P., 2022, “Direct pore-scale simulations of fully periodic unit cells of different regular lattices,” *Journal of Heat Transfer, 144*(2), p.022702. https://doi.org/10.1115/1.4053204.

[5.39] Aider, Y., Kaur, I., Cho, H. and Singh, P., 2022, “Periodic heat transfer characteristics of additively manufactured lattices,” *International Journal of Heat and Mass Transfer, 189,* p.122692. https://doi.org/10.1115/1.4053204.

[5.40] Kaur, I., Aider, Y., Nithyanandam, K. and Singh, P., 2022, “Thermal-hydraulic performance of additively manufactured lattices for gas turbine blade trailing edge cooling,” *Applied Thermal Engineering, 211,* p.118461. https://doi.org/10.1016/j.applthermaleng.2022.118461.

[5.41] Kaur, I., Mahajan, R.L. and Singh, P., 2023, “Generalized correlation for effective thermal conductivity of high porosity architectured materials and metal foams,” *International Journal of Heat and Mass Transfer*, *200,* p.123512. https://doi.org/10.1016/j.ijheatmasstransfer.2022.123512.

[5.42] Wang, N., Kaur, I., Singh, P. and Li, L., 2021, “Prediction of effective thermal conductivity of porous lattice structures and validation with additively manufactured metal foams,” *Applied Thermal Engineering, 187,* p.116558. https://doi.org/10.1016/j.applthermaleng.2021.116558.

[5.43] Dong, L. and Wadley, H., 2015, “Mechanical properties of carbon fiber composite octet-truss lattice structures,” *Composites Science and Technology*, *119,* pp.26-33. https://doi.org/10.1016/j.compscitech.2015.09.022.

[5.44] Aider, Y., Cho, H. and Singh, P., 2022, “Convective Heat Transfer Potential of Particles/Airflow Through Single Cell Thick Additively Manufactured Octet-Shaped Lattice Frame Material,” *Heat Transfer Summer Conference,* 85796, p. V001T06A004. https://doi.org/10.1115/HT2022-81856

[5.45] Kloss, C., Goniva, C., Hager, A., Amberger, S. and Pirker, S., 2012, “Models, algorithms and validation for opensource DEM and CFD–DEM,” *Progress in Computational Fluid Dynamics, an International Journal*, *12*(2-3), pp.140-152. https://doi.org/10.1504/PCFD.2012.047457.

[5.46] Jahani, M., Farzanegan, A. and Noaparast, M., 2015, “Investigation of screening performance of banana screens using LIGGGHTS DEM solver,” *Powder Technology*, *283,* pp.32-47. https://doi.org/10.1016/j.powtec.2015.05.016.

[5.47] Deb, S. and Tafti, D., 2014, “Investigation of flat bottomed spouted bed with multiple jets using DEM–CFD framework,” *Powder technology*, *254*, pp.387-402. https://doi.org/10.1016/j.powtec.2014.01.045.

[5.48] Bagepalli, M.V., Yarrington, J.D., Schrader, A.J., Zhang, Z.M., Ranjan, D. and Loutzenhiser, P.G., 2020, “Measurement of flow properties coupled to experimental and numerical analyses of dense, granular flows for solar thermal energy storage,” *Solar Energy*, *207*, pp.77-90. https://doi.org/10.1016/j.solener.2020.06.062.

[5.49] Gallego, E., Fuentes, J.M., Wiącek, J., Villar, J.R. and Ayuga, F., 2019, "DEM analysis of the flow and friction of spherical particles in steel silos with corrugated walls," *Powder Technology*, *355*, pp.425-437. https://doi.org/10.1016/j.powtec.2019.07.072.

[5.50] Washino, K., Chan, E.L., Miyazaki, K., Tsuji, T. and Tanaka, T., 2016, "Time step criteria in DEM simulation of wet particles in viscosity dominant systems," *Powder Technology*, *302*, pp.100-107. https://doi.org/10.1016/j.powtec.2016.08.018.

[5.51] Burns, S.J., Piiroinen, P.T. and Hanley, K.J., 2019, "Critical time step for DEM simulations of dynamic systems using a Hertzian contact model," *International Journal for Numerical Methods in Engineering*, *119*(5), pp.432-451. https://doi.org/10.1002/nme.6056.

[5.52] Paulick, M., Morgeneyer, M. and Kwade, A., 2015, "Review on the influence of elastic particle properties on DEM simulation results," *Powder Technology*, *283*, pp.66-76. https://doi.org/10.1016/j.powtec.2015.03.040.

[5.53] Zhou, Y.C., Xu, B.H., Yu, A.B. and Zulli, P., 2001, "Numerical investigation of the angle of repose of monosized spheres," *Physical Review E*, 64(2), p.021301. https://doi.org/10.1103/PhysRevE.64.021301.

[5.54] Yan, Z., Wilkinson, S.K., Stitt, E.H. and Marigo, M.J.C.P.M., 2015, "Discrete element modelling (DEM) input parameters: understanding their impact on model predictions using statistical analysis," *Computational Particle Mechanics*, *2*, pp.283-299. https://doi.org/10.1007/s40571-015-0056-5.

[5.55] Xu, Y., Kafui, K.D., Thornton, C. and Lian, G., 2002. Effects of material properties on granular flow in a silo using DEM simulation. *Particulate Science and Technology*, *20*(2), pp.109-124. https://doi.org/10.1080/02726350215338.

# CHAPTER SIX :
# HEAT TRANSFER CHARACTERISTICS OF PARTICLE AND AIR FLOW THROUGH ADDITIVELY MANUFACTURED LATTICE FRAME MATERIAL BASED ON OCTET-SHAPE TOPOLOGY

## Abstract

Particle-to-supercritical carbon dioxide (sCO2) heat exchanger is a critical component in next-generation concentrating solar power (CSP) plants. The inherently low heat transfer between falling particles and sCO2 imposes a challenge towards economic justification of levelized cost of electricity produced through solar energy. Introduction of integrated porous media with the walls bounding particle flow has the potential to enhance the overall particle-to-sCO2 heat exchanger performance. This paper presents an experimental study on heat transfer characterization of additively manufactured lattice frame material based on Octet-shaped unit cell with particles and air as working fluids. The lattice structures were additively manufactured in Stainless Steel (SS) 316L and SS420 (with 40% bronze infiltration) via Binder jetting process, where the lattice porosities were varied between 0.75 and 0.9. The mean particle diameters were varied from 266-966 μm. The effective thermal conductivity and averaged heat transfer coefficient were determined through steady-state experiments. It was found that the presence of lattice enhances the effective thermal conductivity by 2-4 times when compared to packed bed of particles alone. Furthermore, for gravity-assisted particle flow through lattice panel, significantly high convective heat transfer coefficients ranging from 200-400 W/m2K were obtained for the range of particle diameters tested. The superior thermal transport properties of Octet-shape-based lattice frame for particle flow makes it a very promising candidate for particle-to-sCO2 heat exchanger for CSP application.

## Introduction

Supercritical carbon dioxide ($sCO_2$)-based Brayton cycle has the potential for higher efficiency (>50%) compared to steam-based Rankine cycles at concentrated solar power (CSP) relevant temperatures [6.1] because of its high temperature operability. The $sCO_2$ process has relatively simpler turbomachinery and offers lower installment, maintenance, and operational costs [6.2]. CSP Gen3 technology identifies three pathways, viz. molten salt, gas-phase and falling particles [6.2] to develop $sCO_2$-based heat exchangers that can operate efficiently at CSP relevant temperatures while being both reliable and cost effective. Liquified nitrate salts can be operated at temperatures up to 565ºC [6.3] while chloride salts can go up to 700ºC under practical considerations [6.2], however, corrosion

to stainless steel medium is of major concern in the case of chloride salts [6.4]. In context with the above drawbacks of molten salt, particles are considered an attractive solution. Particles such as bauxite and silica sand can be directly heated up to 1000ºC and above, in the receiver section through a heliostat field [6.5]. There have been several investigations on particle-based receiver designs [6.5-6.12]. Heated particles can then be driven with the help of gravity from the central receiver to a particle storage container or directly to a heat exchanger.

Particle-to-s$CO_2$ heat exchangers have been identified as one of the most crucial components demanding innovation to achieve the CSP Levelized Cost of Electricity (LCoE) targets of $0.05/kWh by 2030 [6.2]. The simplest particle heat exchangers can be in the form of tube bundles, where the fluid such as air or water passes inside the tubes and a heated packed bed of particles is driven around the tubes, thus heating the fluid. This type of heat exchanger is known to have a highly localized heat transfer coefficient in which only the sides of the tubes benefit from the movement of the packed bed while the top and bottom of each tube get lower heat transfer [6.13]. More efficient heat exchangers such as shell-and-plate and shell-and-tube have also been considered for particle-to-fluid applications. Tian et al. [6.14] suggested a novel tube shape for implementation in shell-and-tube particle heat exchanger, where the elliptical shaped tube enhanced heat transfer at the top and bottom of the tube (compared to circular shape) by 42% and 53%, respectively. Experimental study done by Maskalunas et al. [6.15] showed that the heat transfer coefficient between silica particles and the surface of a parallel plate heat exchanger can vary between 200-250 $W/m^2K$. Parallel plate heat exchangers can be easily manufactured from high performance materials such as stainless steel and zirconium carbide composite for high temperature and pressure applications. These materials can be diffusion bonded to create very compact heat exchangers known as printed circuit heat exchangers (PCHEs) [6.4]. In an evaluation study, based on factors such as thermal transport capabilities, heat exchanger's structural integrity and its manufacturability, as well as scalability and erosion characteristics, shell-and-plate design was demonstrated to be the best [6.16].

**Figure 6.1** shows a typical CSP plant for power generation, where the present study is focused on the particle-to-$sCO_2$ heat exchanger. The overall heat transfer coefficient of this heat exchanger is given as,

**Equation 6-1**

$$U_{HX} = \left( \frac{1}{h_{sCO_2}} + \frac{t_{HX}}{k_{HX}} + R_C + \frac{1}{h_p} \right)^{-1}$$

where, the thermal resistances are comprised of convection due to $sCO_2$ $(1/h_{sCO_2})$, conduction in the wall separating hot and cold sides $(t_{HX}/k_{HX})$, particle contact resistance $(R_c)$ and convection on the hot side due to falling particles $(1/h_p)$. The $sCO_2$ flows through mini- or micro-channels offering superior convective transport, hence yielding significantly lower thermal resistance than that on the hot side due to falling particles. The present study is focused on improving the particle side thermal resistance through incorporation of porous media on the hot side.

To this end, a novel enhanced heat transfer concept is developed for the falling particle channel side of the particle-to-sCO2 heat exchanger for potential employment in a shell-and-plate type heat exchanger (**Fig. 6.1**). The convective heat transfer coefficient on the falling particle side is enhanced by packing the parallel plates with Octet-shaped lattices. The Octet unit cells, and the enclosing plates were additively manufactured in Stainless Steel 316L and SS420 (with 40% bronze infiltration) via Binder jetting technology. The Octet lattice has been chosen after carrying out direct simulations which quantified its superior heat transfer enhancement characteristics compared to other common unit cell topologies [6.17-6.19]. The unique geometry of the Octet lattice creates optimal flow patterns that maximize particle-surface contact while minimizing pressure drop penalties. The computational analysis also revealed that this lattice configuration provides exceptional structural stability under thermal cycling conditions, a critical factor for long-term operation. The goal of this paper is to: (a) determine the effective thermal conductivity of lattice structures with void space occupied by particles of different sizes, (b) determine the convective heat transfer coefficient for air and particles flow in large panel of Octet lattice manufactured additively via Binder jetting. The following sections present details of different experimental setups employed to measure effective thermal conductivity of

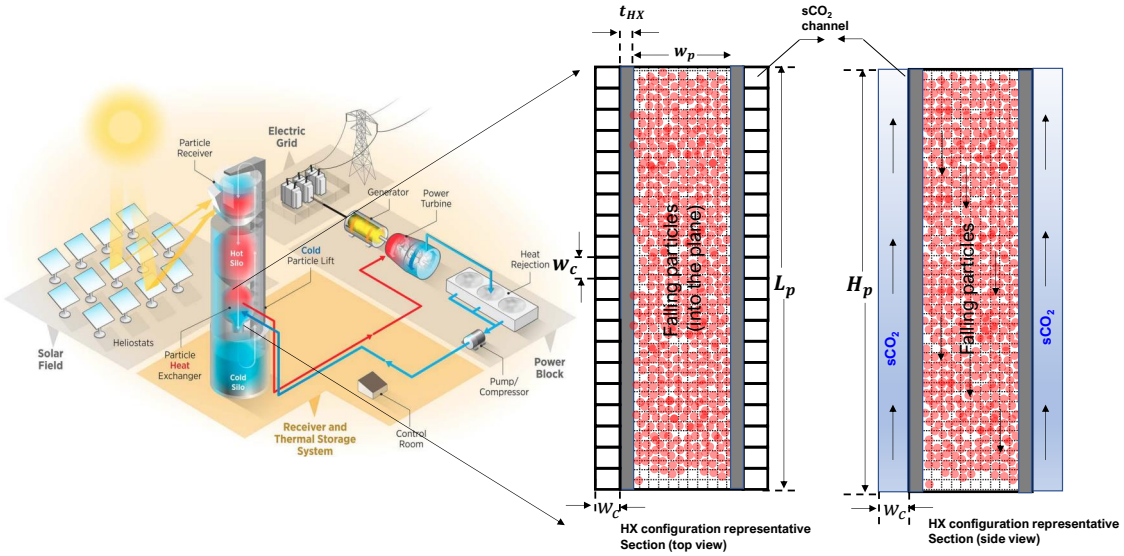



**Figure 6.1 Concentrating solar power plant [6.2] and representation of particle-to-sCO2 heat exchanger; present study focused on particle-side heat transfer enhancement**

lattices made from Octet unit cells where void space is packed with particles of varying diameter. A forced convection setup to quantify the overall convective heat transfer coefficient of sandwich-type Octet panel with air as the working fluid is discussed. Finally, a unique test facility was built to carry out particle-based heat transfer experiments. After this section, the results are presented and analyzed. The paper concludes with major findings from this comprehensive experimental program and path forward based on these findings.

## Experimental setups and measurement techniques

Effective thermal conductivity experiments were carried out on the additively manufactured lattice frames for two different cases: a) void space was occupied by air, b) void space was occupied by particles. Further, convective heat transfer capabilities of single cell thick lattice for air and particle flows have been investigated experimentally. Three different experimental setups were built to measure the above-mentioned quantities. Each setup was carefully calibrated to ensure precise thermal measurements and consistent boundary conditions across all tests.

### *Effective thermal conductivity test samples, experimental setup and $k_{eff}$ measurement procedure*

The lattice samples for $k_{\text{eff}}$ experiments were made from a 5 x 5 array of Octet-shaped unit cells in the span and single unit cell in the thickness as shown in **Fig. 6.2**. The Octet unit cell could be contained in a cube of edge length $\Delta z$ =10 mm. The overall dimensions of each sample were 50 mm x 50 mm x 10 mm. Three samples having as-designed lattice porosities ($\varepsilon$) of 0.75, 0.8 and 0.886 were tested for effective thermal conductivity evaluation. However, the actual measured porosities of the additively manufactured lattices were 0.733, 0.798, 0.884, respectively. Porosity of lattice structures has a dominant effect on the $k_{\text{eff}}$ for a given solid-fluid pair, hence it is imperative that accurate measurement of porosity be carried out in such studies since deviations from as-designed and AM-assisted samples are frequent. As mentioned above, the actual porosities differed from the intended ones, and the deviation is attributed to the AM process – a trend observed in many prior research efforts [6.20,6.21]. It is noted that the AM samples have inherent roughness and defects at both the fibers and endwalls.

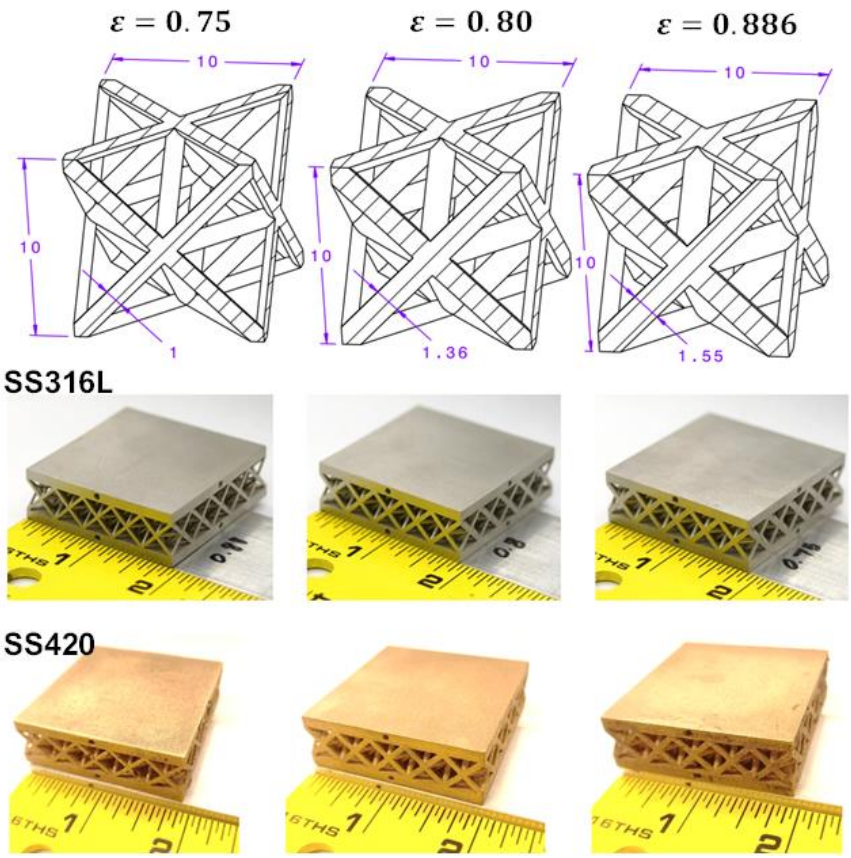



**Figure 6.2 Three samples of different porosities tested for effective thermal conductivity (dimensions in top figure in mm, scale in sample images in inches)**

However, the measurement of porosity of such structure accounts for all the defects [6.22]. For $k_{eff}$ experiments in particular, the void space is occupied by stagnant air/particles, hence the AM induced defects are not expected to have an added contribution on $k_{eff}$, other than the porosity itself. Hence $k_{eff}$ results are reported as a function of measured porosities of the AM parts.

The effective thermal conductivity ($k_{eff}$) setup is shown in **Fig. 6.3.** A steady-state heat transfer experiment was developed to obtain the $k_{eff}$ of additively manufactured samples. A unidirectional heat flow was achieved from top plate to bottom plate of the sample, where Octet-shaped unit cells were sandwiched between the two plates. A cold thermal reservoir was created with the help of an ice-water slurry which was periodically stirred to avoid thermal stratification. An aluminum slab (10 x 10 x 2.5 $cm^3$) was then partially submerged into the chilled reservoir which acted as a near-constant cold reservoir, owing to its large thermal mass.

The effective thermal conductivity ($k_{eff}$) was determined using Fourier's law of conduction (Eq. 6.2). The sample was tested under steady-state conditions with a constant heat flux maintained at the top wall, while the bottom wall was firmly bonded to an aluminum slab serving as a cold reservoir. Tests conducted at three different heat flux values confirmed that the determined $k_{eff}$ was independent of the applied heat flux. The net heat conduction across the one-unit cell thick sample was calculated by subtracting stray heat losses from the total heat supplied.

**Equation 6-2**

$$k_{eff} = \frac{(q_{cond}/A)\Delta z}{\Delta T} = \frac{(\{q_{total} - \sum q_{loss}\}/A)\Delta z}{\tilde{T}_{top} - \tilde{T}_{bot}}$$

**Equation 6-3**

$$\sum q_{loss} = \frac{k_{ins}}{t_{ins}}\left[A\left(T_{Top,in} - T_{Top,out}\right) + 4b\Delta z\left(T_{side,in} - T_{side,out}\right)\right]$$

where, "$A$" is the lattice base area, "$\Delta z$" is the thickness of single unit cell of lattice and "$b$" is the edge length of square cross-sectioned lattice (**Fig. 6.2**). The stray heat loss venues involved the top wall insulation and the four side wall insulations. Thin thermocouples were secured at the inner and outer skins of the insulation.

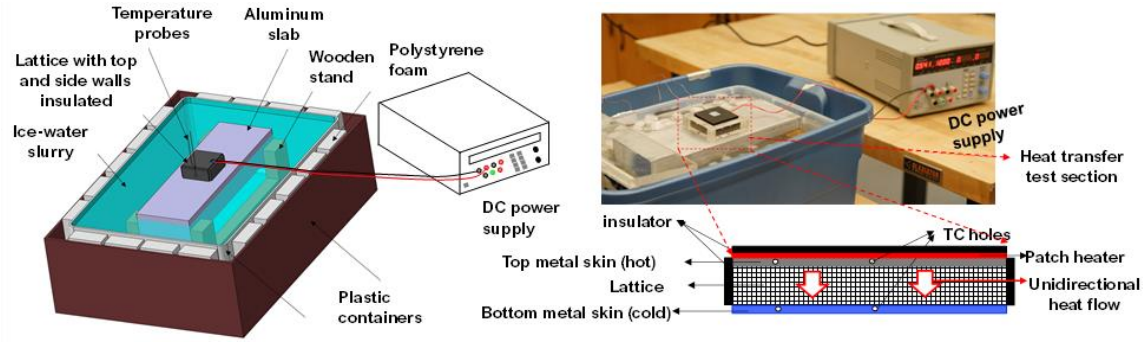



**Figure 6.3 (a) Experimental setup for keff determination, (b) unidirectional heat flow obtained via patch heater and cold sink (bottom)**

This is done to calculate the stray heat loss, with the knowledge of the thermal conductivity of the insulation material (Eq. 6.3). This accounting of the heat loss ensured that the reported effective thermal conductivity is only a contribution of the unit cell topology, solid- and fluid-phase thermal conductivities, and lattices' effective porosity.

***Forced convection setup with air as working fluid, and heat transfer coefficient calculation procedure***

**Figure 6.4** shows the schematic of the experimental facility used in the present study where air was the working fluid under forced convection scenario. Air was drawn from a compressed air tank maintained at ~ 1MPa. A pressure regulator was installed downstream of the compressor to adjust the mass flow rate to a desired value. Air was then directed to an orifice plate for flow metering. Differential pressure across the orifice plate static air pressure upstream of the orifice plate and air temperature were measured using Dwyer 477AV-2 (0-10 kPa), Dwyer DPG-002 (0-100 kPa) and fast response T-type thermocouple, respectively. These pressure and temperature measurements were then fed into an in-house MATLAB code to determine the mass flow rate. The metered flow was then passed through a control valve regulating the flow into the test section. The transition of the flow from circular pipe to square duct was executed with the help of a trapezoidal shaped diffuser. **Figure 6.4** also shows the schematic of the heat transfer test section. The sandwich panel was heated with patch heaters attached to both the top and bottom walls using thermally conductive silicone compound (CHEMPLEX ® 1381 DE). Rubber foam thermal insulation with thermal conductivity of 0.037 (W/mK) and thickness of 3.2 mm was pasted on the surface of the heaters. T-type thermocouples were used to measure the temperature inside each thermocouple slot which was very close to the solid-fluid interface and this temperature was treated as the representative wall temperature in the convective heat transfer coefficient calculations. A constant heat flux type thermal boundary condition was created with the help of the patch heaters mentioned above, where the heating power was controlled with variable transformers having voltage indicators. The sandwich panel featuring an array of Octet unit cells had top and bottom walls of 15 cm x 25 cm dimension and thickness was 1 cm. Hence, the flow channel had high aspect ratio (width/height) of 15.

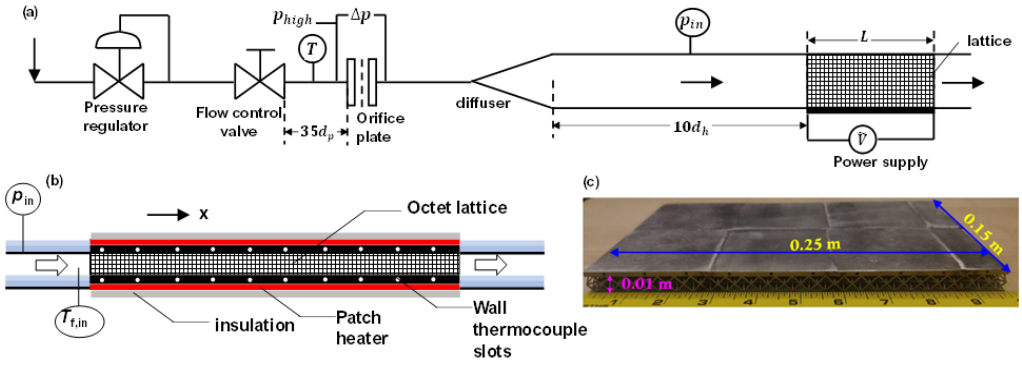



**Figure 6.4 (a) Schematic of the experimental setup (not drawn to scale), (b) zoom-in view of heat transfer section, (c) additively manufactured sandwich-type Octet panel in SS316L**

It is generally challenging to achieve a uniform hydrodynamically developed flow at the entrance of the test section with such a high aspect ratio. To address this, a ~ 33 cm long plexiglass duct was installed between the heat transfer test section and the trapezoidal diffuser. The samples used in this part were made by reticulating Octet unit cell in span where the sample was one unit cell thick. The sample was additively manufactured from Stainless Steel 316L and SS420 using binder jetting technology. The bed size of the 3D printer limited the maximum size of the lattice which can be printed in one run. Therefore, the sandwich panel shown in **Fig. 6.4** was obtained by 3D printing different smaller sections and then joining them together. For the SS316 panel, all the parts were joined together using tungsten inert gas (TIG) welding. TIG welding works by creating a very high-temperature plasma that melts and joins the panel parts together creating a seamless SS316 panel. The additively manufactured SS420 lattice panel parts were joined together by soldering. Since SS420 material is infiltrated with bronze, tin metal can easily bond to the SS420 panel parts.

The steady-state heat transfer experimental procedure included heating both top and bottom panels via the glued patch heaters. The experimental procedure included firstly heating the top and bottom plates and allowing them to reach a primary steady-state in absence of air flow. This step was followed by allowing desired airflow through the test section and allowing the setup to reach a second steady-state. At this stage, the measurements of flow inlet temperature, wall temperature at discrete locations, and temperature drop across the insulation were carried out. Note that the panel was 15 cm wide and 25 cm long, and a representative wall temperature would only be found by measuring local wall temperatures at several discrete locations on both the top and bottom walls.

An array of 10 equi-spaced thermocouple slots were incorporated (in the AM phase itself) along the streamwise length of the samples with a depth of W/2 and W/6 into the span of both endwalls sandwiching the lattice section, where W is the width of the panel obtained after joining the smaller AM parts as described above. Under the assumption that the temperature distribution would be symmetric about the channel centerline in the streamwise direction, the representative wall temperature at a particular streamwise

location was then obtained by calculating the area-averaged temperature based on the two measurements carried at the span of W/2 (centerline) and W/6. A trendline for streamwise variation of wall temperature was obtained for both top and bottom walls, to get a continuous variation $T_w(x)$ from the discrete measurements. Convective heat transfer coefficient at these discrete locations along the streamwise direction is given as,

**Equation 6-4**

$$h(x) = \frac{q"_{conv}}{T_w(x) - T_f(x)}$$

The local fluid temperature $T_f(x)$ was determined by linear interpolation between inlet and outlet air temperature measurements. The linear interpolation is justified due to the constant heat flux boundary condition on the two opposite walls of the channel. The local convective heat transfer coefficient ($h(x)$) obtained from above procedure was then used to calculate a representative heat transfer coefficient for each row of unit cells in the streamwise direction. In this paper, we have presented convective heat transfer coefficient for air-based experiments in the periodic heat transfer regime.

***Particle heat transfer test facility and heat transfer coefficient calculation procedure***

The heat transfer test section described in **Fig. 6.4** above was used in the experiments for determination of convective heat transfer coefficient with particles as working fluid. Unlike air-based convection experiments, the particles which carry heat from the test section had to be transported back into the system. To this end, a bucket elevator-system was designed, developed, and built for these experiments. Bucket elevator works by rotating a set of buckets attached to a chain or a belt, and by doing so, the buckets scoop the particles from the bottom of the elevator casing and discharge them at the top.

The actual assembled test facility, assembly CAD model, instrumented heat transfer test section, and schematic representation of heat transfer scenario involving falling particles are shown in **Fig. 6.5.** Particles are first stored at room temperature in the top hopper while the top and bottom walls of the sandwich panel were being electrically heated with a set of patch heaters. This method enables a more precise measurement of the supplied heat to the system enabling a more accurate heat transfer coefficient predition.

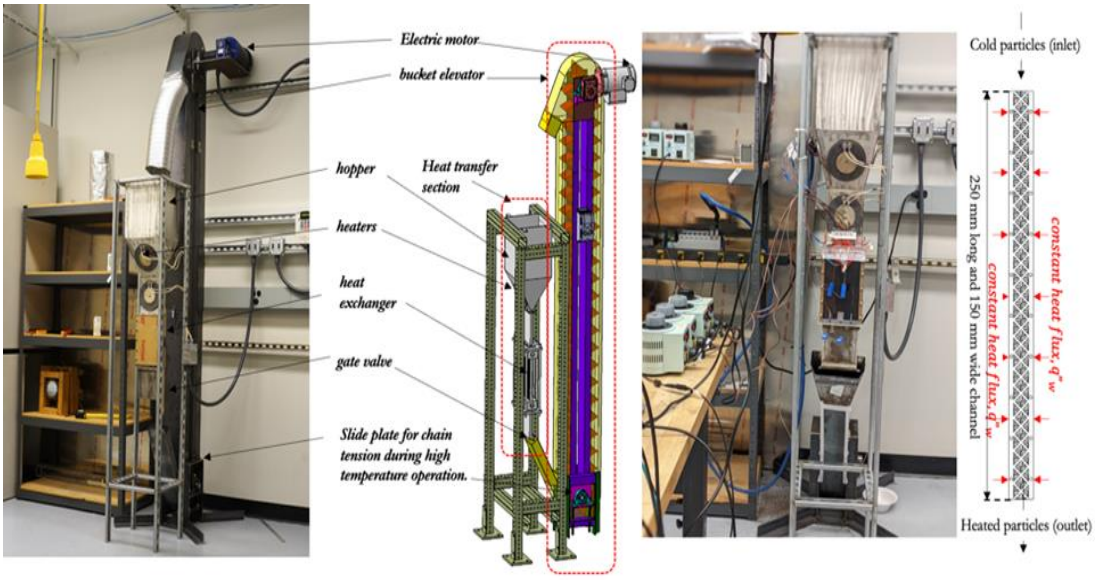



**Figure 6.5 Particle heat transfer test facility**

The particles were held until the panel walls reached a temperature of ~100ºC. A gate valve was installed right downstream of the heat transfer section, which facilitated the on/off type flow of particles across the heat transfer test section. Once the desired panel wall temperatures were achieved, the gate valve was flipped and the elevator was started at the same time, to allow the transport of the spent particles back into the top hopper via a series of equi-spaced buckets. It should be noted that particle heat transfer experiments are different from the air-based experiments in the sense that the working fluid was recirculated and fed back into the heat transfer section. Due to convection, particles carry away some heat from the heated walls and the same batch of particles is transported back into the hopper above the test section via the bucket elevator. During the transport in the buckets, the particles loose some heat to the laboratory ambient, however, in our initial testing and the design of heat transfer experiments, we observed that the particle temperatures continue to keep increasing as they are recirculated for a prolonged duration. Further, it was decided that bucket-elevator-based experiments should not be allowed to run for very long periods of time, as particles can get destroyed/crushed during the transport, which may inherently change the particle size distribution with time, and a satisfactory steady state could never be achieved, both in the sense of heat transfer and the working fluid rhealogical properties. Furthermore, for each set of experiments,

fresh batch of particles were used to ensure that the rheological properties of the particles are same, and that the morphed or destroyed particles are not used.

To address the above aspect, a novel quasi-steady state heat transfer methodology was devised exclusively for this part of the investigation, which could effectively provide local convective heat transfer coefficient where heat transfer was facilitated through falling particles. In this approach, firstly the hopper is filled with desired type of particles where the total mass of particles was decided such that a packed bed flow could be achieved at the heat transfer test section. Once the hopper was charged with particles, the heating process was started where all the eight patch heaters occupying the entire 150 x 250 $mm^2$ panel on both left and right sides of sandwiched panel were heated. Once the steady-state heat transfer condition was achieved, the particle flow through the Octet panel was initiated by opening the gate valve installed at the bottom of the heat exchanger to 100%. Note that this facility also allows a fine control over the particle flow rate through the gate valve while still maintaining a packed moving bed through the Octet panel. In this study, the maximum possible particle mass flow rate was studied, hence 100% opening of the gate valve was set. Prior to the particle flow start, the data acquisition system was initiated which involved over 20 thermocouple measurements across the heat transfer test section, including a pair of temperature measurements for particle inlet and outlet. Once the particles started to flow through the Octet panel, the walls of the panel started to cool down rapidly to a local minima. At that point onwards, the particle and the wall temperatures continued to slowly increase for the remainder of the transient experiment. The reason behind this phenomena is explained above. In the heat transfer coefficient calculation, the wall and particle temperatures during this slow heat ramp up period were taken into consideration and the local instantaneous convective heat transfer coefficient was determined through the following eqation:

**Equation 6-5**

$$h(x,t) = \frac{q"_{conv}(t)}{T_w(x,t) - T_f(x,t)}$$

where, $q"_{conv}(t)$ is the heat convected away from the walls via the particles in motion and this was obtained by subtracting the local heat losses from the backside of the eight

patch heaters occupying and supplying constant heat flux on the left and right sides of the panel. The instantaneous local particle temperature $T_f(x,t)$ was determined by linear interpolation between inlet and outlet particle temperature measurements, a procedure similar to the one followed for air-based experiments described above. Note that the temperature drop across the insulation material was measured at multiple locations along the streamwise length and also recorded along with the wall temperature at the same fequency throughout the transient operation. The heat loss however was minimal compared to the total heat supplied.

**Particle size distribution and particle packing in AM lattice parts**

The particles used in the experiment were made from sintered bauxite. Three different particle batches were tested: CARBOBEAD-CP 40/100 with a mean particle diameter of 266 µm, CARBOBEAD-CP 30/60 with a mean particle diameter of 397 µm, and CARBOBEAD HSP 20/40 with a mean particle diameter of 966 µm. Particle size analysis was performed using Anton Paar PSA 1190 LD particle size analyzer.

The particle size distribution is shown in **Fig. 6.6**. For other thermo-physical and spectral properties of these particles, the readers are reffered to [6.8,6.23,6.24].

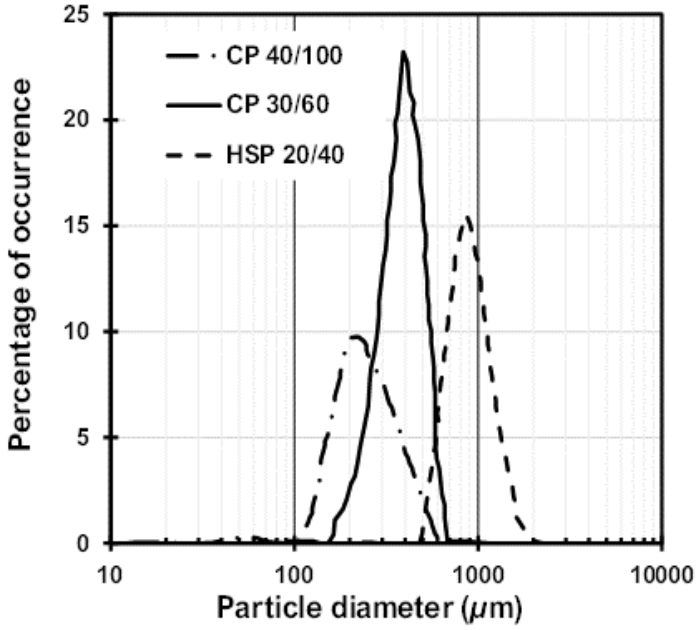



**Figure 6.6 Particle Size Distribution (PSD) measured using laser diffraction method**

## Uncertainty analysis

The uncertainty analysis for each of the reported quantities was carried our using the sequential perturbation method prescribed by Moffat [6.25]. The uncertainty in the reported fiber diameters was ~3% which is a direct contribution of the device used for the measurement. The uncertainty for a typically value of reported values of effective thermal conductivity was ~3%. The uncertainty in typical values of Nusselt number and air flow Reynolds number is ~3% and ~4%, respectively.

## Results and discussion

In this section, we are presenting experimental results on effective thermal conductivity and convective heat transfer coefficient for air and particles as working fluids.

### *Effective thermal conductivity ($k_{eff}$)*

Effective thermal conductivity experiments were carried out for three cases, a) packed bed of particles (without lattice), b) lattice with void space occupied by air, c) lattice with void space occupied by particles. Each configuration was tested at three different heat flux levels to ensure that the reported $k_{eff}$ values were independent of the heating conditions. Note that the wall temperatures at these three different heat flux levels was ranging between 20-50℃, hence radiation effects and other solid-phase thermo-physical property changes can be ignored. The packed bed $k_{eff}$ was similar for all particles with diameters varying between 266-966 $\mu$m with an averaged value of ~ 0.4 W/mK.

The second set of experiments were conducted on Octet lattice with void space occupied by air. **Figure 6.7** shows the $k_{eff}$ values for the samples printed in SS316L and SS420 as shown in **Fig. 6.2**. The thermal conductivity of solid-phase was measured to be ~13 W/mK and ~20.8 W/mK for SS316L and SS420 materials, respectively. It was found that $k_{eff}$ was a strong function of solid-phase intrinsic thermal conductivity and the lattice porosity. A suitable normalization of $k_{eff}/k_s$ collapses different $k_s$ samples onto one curve. A comparison is shown for $k_{eff}/k_s$ versus $\varepsilon$ with the generalized correlation prescribed recently by Kaur et al. [6.22] for porous media with porosities greater than 0.8. The comparison was found acceptable for this porosity range, with deviations typically remaining within 10% of the predicted values.

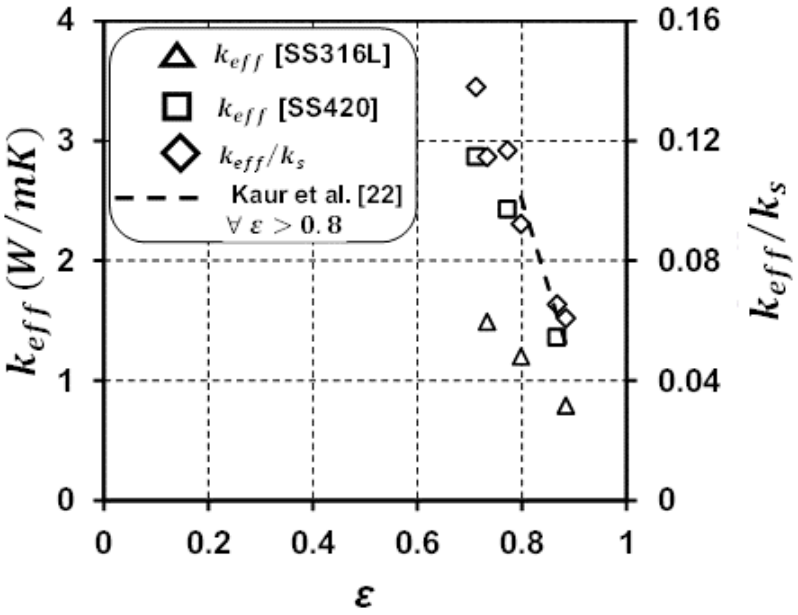



**Figure 6.7 Effective thermal conductivity of Octet lattice (void space occupied by air)**

The third set of $k_{eff}$ experiments were conducted on lattices with void space being occupied by the particles with diameters varying from 266 – 966 $\mu$m (**Fig. 6.8**). There was a clear decreasing trend in the $k_{eff}$ value with increasing lattice porosity, which is again consistent for the case when void space was occupied by air, indicating that particles do not alter the dominant impact of fibers and their intrinsic thermal conductivity values, even though particles are nearly 16 times more thermally conductive than air.

**Figure 6.8** also presents the relative enhancement in $k_{eff}$ values ($\eta = \left(k_{eff}\right)_{void \rightarrow particles} / \left(k_{eff}\right)_{packed\ bed}$) for the lattice when particles were packed in void space in reference to a packed bed of particles. This enhancement in $k_{eff}$ is one mode which implicitly affects the overall thermal transport between the hot and cold sides. Further, a rapid decline in $\eta$ was observed with increasing lattice porosity.

The enhancement levels were similar for different particle sizes for the three lattice porosities and varied from 2-4 times compared to the particle packed bed configurations (absence of lattice) for SS316L, while $\eta$ for SS420 was found to vary between 4-8 for three different particle sizes occupying the void space.

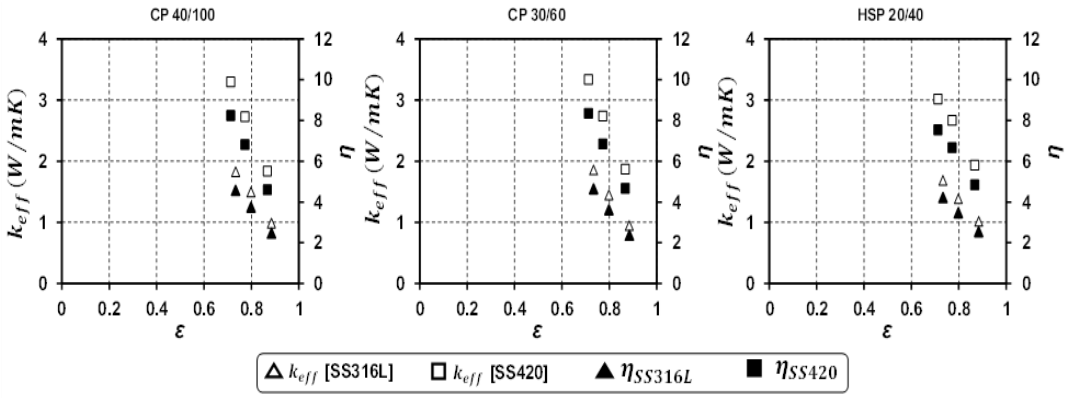



**Figure 6.8 Effective thermal conductivity of Octet lattice (void space occupied by particles) and $k_{eff}$ enhancement factor ($\eta$) with respect to packed bed of particles**

***Forced convection with air as working fluid***

This sub-section presents steady-state experimental results on local convective heat transfer coefficient offered by Octet unit cells when packed between two parallel plates (integrally manufactured) with air as the convective agent (**Fig. 6.9**). The panel is shown in **Fig. 6.4** and was formed by joining smaller pieces together as the maximum printable size was limited by the manufacturing method. The heat transfer development with increasing streamwise distance from the inlet section was presented by the authors in [6.26], where a periodic heat transfer (when unit cell-based *h* does not change with increasing distance) was observed after 40% of the channel length. **Figure 6.9** shows the *h* values for the two panels made from SS316L and SS420 in this perioidic heat transfer regime. Note that these values are conservative in nature and are presented to allow a direct comparison between two different plates and for heat exchangers made from Octet unit cells which are sufficiently larger in size. In practical scenarios, designers should leverage the high heat transfer values obtained in the developing flow regime as shown by Aider et al. [6.26]. Similar to prior heat transfer quantity ($k_{eff}$), SS420 sample had higher heat transfer compared to SS316L sample, due to the conjugate heat transfer effects which depend on the solid-phase intrinsic thermal conductivity. Both the *h* trends demonstrated a power law dependence on the working fluid flow velocity. Cooling designers can use these trends in the design of heat exchangers which are based on air, allowing them to optimize system performance across different operating regimes and flow conditions.

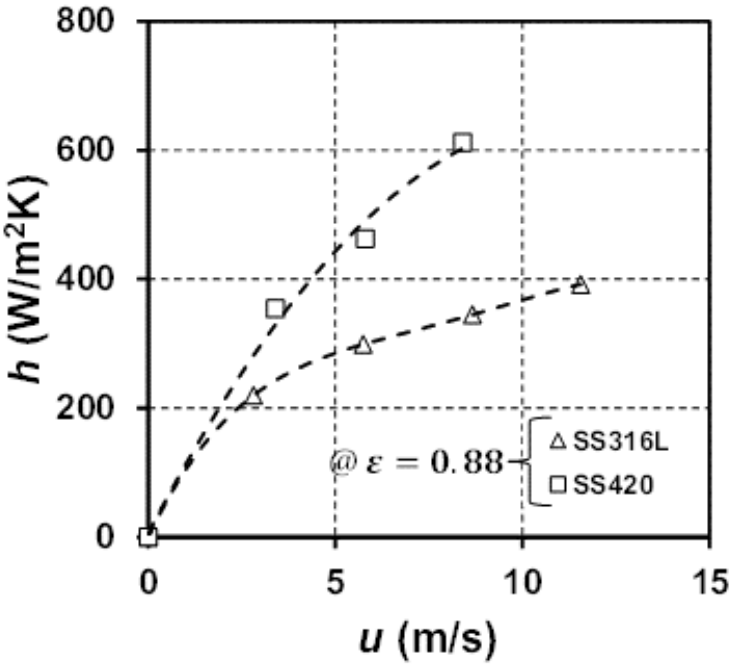



**Figure 6.9 Heat transfer coefficient in the periodic regime, variation presented with respect to average air flow velocity (measured at the inlet of the porous section) [channel diameter-based Reynolds numbers varied between 3,000 and 13,000 for SS316L and SS420 samples]**

***Forced convection with particle as working fluid***

Our preliminary flow visualization experiments carried out on particles flowing through Octet lattice revealed that the particle flow behviour around the fiber and endwall was similar to that of airflow. Similar flow stagnation and separation characteristics were observed for particles flowing through Octet unit cell, which was found to be similar to that of airflow, as shown in our prior publications [6.17–6.19,6.27].

However, it should be noted that particles moving through porous media, despite having similar flow characteristics as that of air or water flow through them, will not necessarily impart similar heat dissipation qualititatively. The stagnation zone observed in particle flow results in particle trapping resulting in lower particle refresh rate, which contributes to reduced heat transfer. Particle flow around the circular fibers in turn enhances heat transfer due to higher local particle speeds.

To characterize the heat transfer for particles, a novel quasi-steady state heat transfer technique was used to determine time-dependent local convective heat transfer

coefficient by carrying out measurements for over 30 minutes during the slow heat ramp-up phase of the experiment as described in **Figure 6.10** shows the transient heat transfer coefficient calculated at different streamwise locations for the three particle diameters flowing through Octet panel made with SS316L. Similar transient behavior was observed for SS420 panel as well and was presented in [6.26]. The results in **Fig. 6.10** are presented over a time-period in which the system was considered to be in quasi-steady state, and it should be noted that both the wall temperatures at different streamwise locations as well as the particle inlet and outlet temperatures were steadily increasing with time. However, their cummulative effect resulted in a time-independent behavior in *h* which is both expected and desired behavior in heat transfer experiments. The time-averaging of the presented *h* values in **Fig. 6.11** was carried out for the phase in which time-independent behavior in *h* was observed. **Figure 6.11** presents the time-averaged *h* values in the periodic heat transfer regime for both Octet panels made from SS316L and SS420 [6.26], as a function of particle diameter. The particle flow rates for CARBOBEAD-CP 40/100 ($d_p$- 266 $\mu$m), CARBOBEAD-CP 30/60 ($d_p$- 397 $\mu$m), and CARBOBEAD HSP 20/40 ($d_p$- 966 $\mu$m) were 95.25 g/s, 116.94 g/s, 139.65 g/s, respectively. Note that the flow rates of particles were similar for both SS316L and SS420 panels since they were of similar porosities. The convective heat transfer coefficient was found to be decreasing with increasing particle size. The difference between SS316L and SS420 was minimal for particle-based heat transfer, unlike air-based transfer. This is attributed to high heat carrying capacity of particles in comparison with air – this is an interesting finding, since material choice in CSP heat exchangers is critical due to the necessity of bonding hot and cold sides together. Diffusion bonding method is a popular method for bonding hot and cold sides together and this technology is demonstrated for SS316L material. Given these findings and considering the immediate objectives in CSP development, we recommend focusing future research efforts on exploring enhanced heat transfer concepts based on SS316L materials. Note that the particle heat transfer results presented in **Fig. 6.11** are for channels with distance between parallel plates equal to 10 mm. To demonstrate the Octet-Lattice's efficacy compared to parallel-plates, separate experiments were conducted (**Fig. 6.5**).

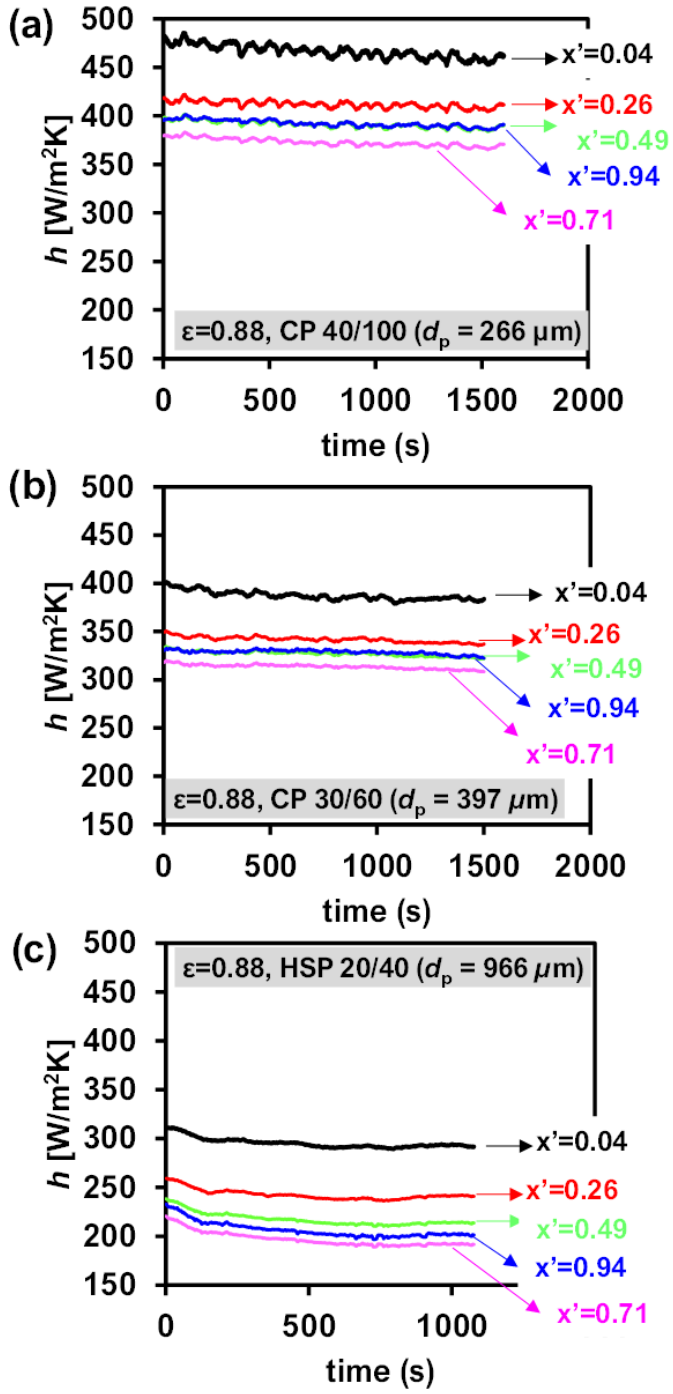



**Figure 6.10 Transient convective heat transfer coefficient at five different locations in the streamwise direction for three particle types (Octet panel porosity of 0.88, SS316L), (a) CP 40/100, (b) CP 30/60, (c) HSP 20/40**

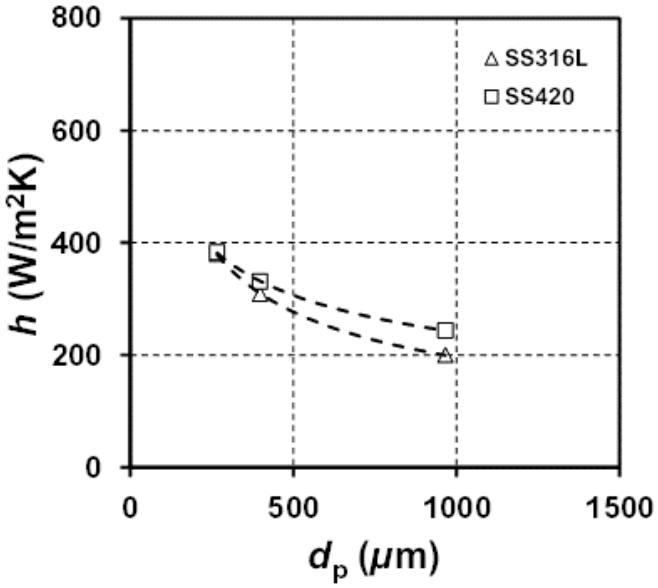



**Figure 6.11 Time-averaged heat transfer coefficient in the periodic heat transfer regime, variation presented with respect to particle diameter**

The distance between the two parallel plates was kept the same as 10 mm. For brevity, comparison plots are presented for SS316L case only, where parallel plates were also built from SS316L. **Figure 6.12** presents a developing heat transfer behavior for lattice and parallel plate configurations for the flow of three particles through them. The particle heat transfer experiments carried out for parallel plates covered a wide range of particle flow rates. For each streamwise location, a relationship was established for *h* and the average flow velocity of particles (*u*). The parallel plate heat transfer data presented in **Fig. 6.12** was obtained for the mass flow rates that were observed for the Octet panel particle experiments. Hence, a fair comparison between Octet panel versus parallel plate could be carried out where the distance between parallel plates in the two configurations as well as the mass flow rate were the same. A clear effect of particle diameter was observed on heat transfer for both lattice and parallel plate configurations. For the largest particle size, both Octet and plane channel configurations showed similar heat transfer, while smaller particle sizes demonstrated 30-40% higher convective heat transfer in the Octet panel, though parallel plates performed better in the entrance region. These findings highlight the importance of carefully selecting particle sizes based on the specific geometry and flow requirements of the system.

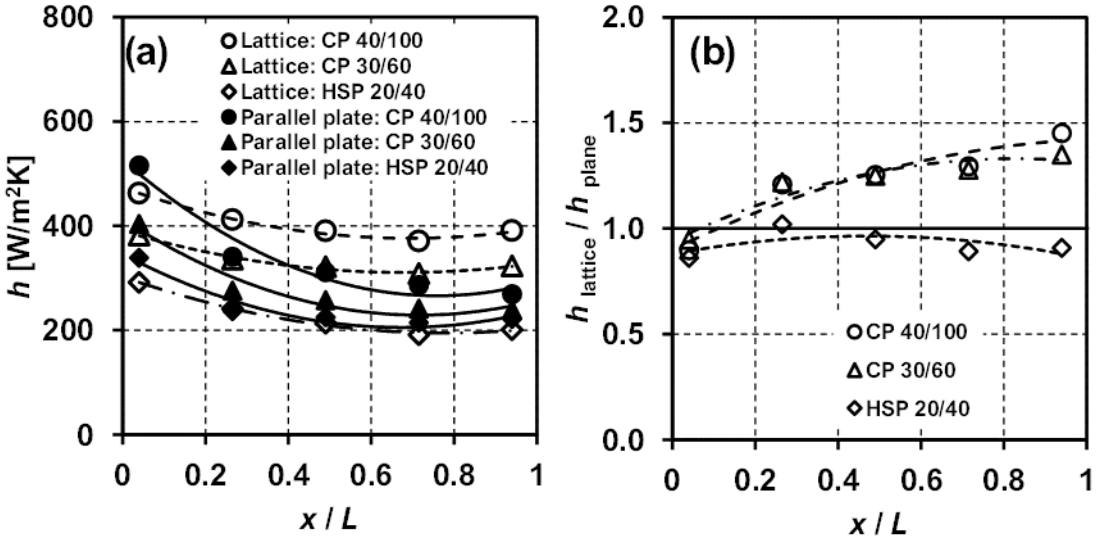



**Figure 6.12 (a) Time-averaged convective heat transfer coefficient variation with streamwise location, (b) enhancement factor of heat transfer coefficient with respect to streamwise location**

## Conclusions

An experimental investigation was carried out to evaluate the heat transfer performance of Octet-shaped unit cells for their capabiltiies to provide convective heat transfer enhancement with air and particles as the working fluids. Octet panels were manufactured via Binder jetting method using Stainless Steel 316L and SS420 materials. The effective thermal conductivity and averaged heat transfer coefficient was obtained experimentally for the cases where the void space was occupied by air and particles. The following major conclusions have been drawn from this work:

(a) Packing the void space of Octet lattice with particles results in thermal conductivity enhancements ranging from 2 to 4 and 4 to 8 times that of the packed bed of particles, for SS316L and SS420 materials. Maximum benefits were observed for the lowest lattice porosity.

(b) For airflow velocities ranging from 3-12 m/s, the convective heat transfer coefficients in the periodic heat transfer region varied between 200-600 $W/m^2K$ for the two materials.

(c) For particle flow through Octet lattice of porosity 0.88, the convective heat transfer coefficient was ~400 $W/m^2K$ for CP 40/100 for both the solid-phase materials.

(d) When compared to parallel plate configuration, the SS316L Octet panel resulted in heat transfer coefficient enhancement of 40-50% for CP 40/100 and CP 30/60 particles, however, no enhancement was observed for the largest particle size (HSP 20/40).

The enhancement levels obtained for the thermal transport quantities through incorporating lattice structures when compared to empty channel, is significant. Additive manufacturing or other manufacturing methods will have a promising role to play to increase the particle-to-s$CO_2$ heat exchanger effectiveness, through inclusion of enhanced heat transfer concepts, such as porous media or pin fins. Future work will include a demonstration of enhanced overall heat transfer coefficeint of porous media enabled particle-to-s$CO_2$ heat exchanger tested at CSP relevant conditions.

## Nomenclature

| | |
|---|---|
| $A$ | base area of the lattice [$m^2$] |
| $b$ | width of the lattice [m] |
| $h$ | heat transfer coefficient [$W/m^2K$] |
| $h_p$ | heat transfer coefficient due to convection by particles [$W/m^2K$] |
| $h_{sCO_2}$ | heat transfer coefficient due to convection by $sCO_2$ [$W/m^2K$] |
| $k_{\text{eff}}$ | effective thermal conductivity [W/mK] |
| $k_{HX}$ | thermal conductivity of the contacting channel wall [W/mK] |
| $k_{ins}$ | thermal conductivity of the insulation [W/mK] |
| $k_s$ | solid-phase intrinsic thermal conductivity [W/mK] |
| $q_{cond}$ | net heat conducted across the sample [W] |
| $q"_{conv}$ | net convected heat flux [W] |
| $q_{loss}$ | stray heat losses [W] |
| $q_{total}$ | net heat supplied to the lattice [W] |
| $R_C$ | particle contact resistance [$m^2K/W$] |
| $\tilde{T}_{bot}$ | mean temperature at the bottom wall of the lattice [ºC] |
| $T_f$ | working fluid temperature [ºC] |
| $t_{HX}$ | thickness of the contacting channel wall [m] |
| $t_{ins}$ | thickness of the insulation [m] |
| $T_{side,in}$ | inner-side temperature of the insulation covering the side of lattice [ºC] |
| $T_{side,out}$ | outer-side temperature of the insulation covering the side of lattice [ºC] |
| $\tilde{T}_{top}$ | mean temperature at the top wall of the lattice [ºC] |
| $T_{Top,in}$ | inner-side temperature of the insulation covering the top of lattice [ºC] |
| $T_{Top,out}$ | outer-side temperature of the insulation covering the top of lattice [ºC] |
| $T_w$ | wall temperature [ºC] |
| $U_{HX}$ | overall heat transfer coefficient of heat exchanger [$W/m^2K$] |
| W | total width of the samples used in convective experiments [m] |
| x’ | non-dimensional streamwise location (x/L) |
| $\Delta T$ | temperature difference [ºC] |

$\Delta z$ thickness of the lattice-section [m]

**Greek letters**

$\varepsilon$ porosity

$\eta$ relative $k_{eff}$ enhancement of particle-lattice combination configuration with respect to particles-*only* packed bed

**Abbreviations**

AM additive manufacturing

CSP concentrated solar power plant

PCHE printed circuit heat exchanger

$sCO_2$ supercritical carbon dioxide

SS stainless steel

TIG tungsten inert gas

**Acknowledgments**

This material is based upon work supported by the U.S. Department of Energy's Office of Energy Efficiency and Renewable Energy (EERE) under the Solar Energy Technologies Office Award Number DE-EE0009377. This report was prepared as an account of work sponsored by an agency of the United States Government. Neither the United States Government nor any agency thereof, nor any of their employees, makes any warranty, express or implied, or assumes any legal liability or responsibility for the accuracy, completeness, or usefulness of any information, apparatus, product, or process disclosed, or represents that its use would not infringe privately owned rights. Reference herein to any specific commercial product, process, or service by trade name, trademark, manufacturer, or otherwise does not necessarily constitute or imply its endorsement, recommendation, or favoring by the United States Government or any agency thereof. The views and opinions of authors expressed herein do not necessarily state or reflect those of the United States Government or any agency thereof.

## References

[6.1] Turchi, C. S., Ma, Z., Neises, T. W., and Wagner, M. J., 2013, "Thermodynamic Study of Advanced Supercritical Carbon Dioxide Power Cycles for Concentrating Solar Power Systems." ASME. *J. Sol. Energy Eng*. Vol. 135(4), pp. 041007.

https://doi.org/10.1115/1.4024030

[6.2] Mehos, M., Turchi, C., Vidal, J., Wagner, M., Ma, Z., Ho, C., Kolb, W., Andraka, C. and Kruizenga, A., 2017. *Concentrating solar power Gen3 demonstration roadmap* (No. NREL/TP-5500-67464). National Renewable Energy Lab.(NREL), Golden, CO (United States).

https://doi.org/10.2172/1338899

[6.3] G. Wilson, S. Sahoo, P. Sabharwal, H. Bindra, 2019, “Chapter Seven - Packed Bed Thermal Storage for LWRs”, H. Bindra, S. Revankar (Eds.), Storage Hybrid. Nucl. Energy, Academic Press, Cambridge, MA, pp. 229–248.

https://doi.org/10.1016/B978-0-12-813975-2.00007-7

[6.4] Zhu, Q., Tan, X., Barari, B., Caccia, M., Strayer, A.R., Pishahang, M., Sandhage, K.H. and Henry, A., 2021. Design of a 2 MW ZrC/W-based molten-salt-to-sCO2 PCHE for concentrated solar power. *Applied Energy*, Vol. *300*, p.117313.

https://doi.org/10.1016/j.apenergy.2021.117313

[6.5] Ho, C.K., 2016. A review of high-temperature particle receivers for concentrating solar power. *Applied Thermal Engineering*, Vol. *109*, pp.958-969.

https://doi.org/10.1016/j.applthermaleng.2016.04.103

[6.6] Martinek, J., and Ma, Z., 2015, "Granular Flow and Heat-Transfer Study in a Near-Blackbody Enclosed Particle Receiver." ASME. *J. Sol. Energy Eng*., Vol. 137(5), pp. 051008.

https://doi.org/10.1115/1.4030970

[6.7] Besarati, S. M., Yogi Goswami, D., and Stefanakos, E. K., 2015, "Development of a Solar Receiver Based on Compact Heat Exchanger Technology for Supercritical Carbon Dioxide Power Cycles." ASME. *J. Sol. Energy Eng*., Vol. 137(3), pp. 031018.

https://doi.org/10.1115/1.4029861

[6.8] Siegel, N. P., Gross, M. D., and Coury, R., 2015, "The Development of Direct Absorption and Storage Media for Falling Particle Solar Central Receivers." ASME. *J. Sol. Energy Eng.*, Vol. 137(4), pp. 041003.

https://doi.org/10.1115/1.4030069

[6.9] Wu, W., Trebing, D., Amsbeck, L., Buck, R., and Pitz-Paal, R., 2015, "Prototype Testing of a Centrifugal Particle Receiver for High-Temperature Concentrating Solar Applications." ASME. *J. Sol. Energy Eng.*, Vol. 137(4), pp. 041011.

https://doi.org/10.1115/1.4030657

[6.10] Siegel, N. P., Ho, C. K., Khalsa, S. S., and Kolb, G. J., 2010, "Development and Evaluation of a Prototype Solid Particle Receiver: On-Sun Testing and Model Validation." ASME. *J. Sol. Energy Eng.*, Vol. 132(2), pp. 021008.

https://doi.org/10.1115/1.4001146

[6.11] Pouransari, H., and Mani, A., 2016, "Effects of Preferential Concentration on Heat Transfer in Particle-Based Solar Receivers." ASME. *J. Sol. Energy Eng.*, Vol. 139(2), pp. 021008.

https://doi.org/10.1115/1.4035163

[6.12] Ho, C. K., Christian, J. M., Romano, D., Yellowhair, J., Siegel, N., Savoldi, L., and Zanino, R., 2016, "Characterization of Particle Flow in a Free-Falling Solar Particle Receiver." ASME. *J. Sol. Energy Eng.*, Vol. 139(2), pp. 021011.

https://doi.org/10.1115/1.4035258

[6.13] Hertel, J.D. and Zunft, S., 2022. Experimental validation of a continuum model for local heat transfer in shell-and-tube moving-bed heat exchangers. *Applied Thermal Engineering*, *206*, p.118092.

https://doi.org/10.1016/j.applthermaleng.2022.118092

[6.14] Tian, X., Guo, Z., Jia, H., Yang, J. and Wang, Q., 2021. Numerical investigation of a new type tube for shell-and-tube moving packed bed heat exchanger. *Powder Technology*, *394*, pp.584-596.

https://doi.org/10.1016/j.powtec.2021.08.080

[6.15] Maskalunas, J., Nellis, G. and Anderson, M., 2022. The heat transfer coefficient associated with a moving packed bed of silica particles flowing through parallel plates. *Solar Energy*, *234*, pp.294-303.

https://doi.org/10.1016/j.solener.2022.01.052

[6.16] Ho, C. K., Carlson, M., Albrecht, K. J., Ma, Z., Jeter, S., and Nguyen, C. M., 2019, "Evaluation of Alternative Designs for a High Temperature Particle-to-s$CO_2$ Heat Exchanger." ASME. *J. Sol. Energy Eng*., Vol. 141(2), pp. 021001.

https://doi.org/10.1115/1.4042225

[6.17] Kaur, I. and Singh, P., 2020. Flow and thermal transport through unit cell topologies of cubic and octahedron families. *International Journal of Heat and Mass Transfer*, *158*, p.119784.

https://doi.org/10.1016/j.ijheatmasstransfer.2020.119784

[6.18] Kaur, I. and Singh, P., 2021. Endwall heat transfer characteristics of octahedron family lattice-frame materials. *International Communications in Heat and Mass Transfer*, *127*, p.105522.

https://doi.org/10.1016/j.icheatmasstransfer.2021.105522

[6.19] Kaur, I. and Singh, P., 2021. Numerical investigation on conjugate heat transfer in octet-shape-based single unit cell thick metal foam. *International Communications in Heat and Mass Transfer*, *121*, p.105090.

https://doi.org/10.1016/j.icheatmasstransfer.2020.105090

[6.20] Kaur, I., Aider, Y., Nithyanandam, K. and Singh, P., 2022. Thermal-hydraulic performance of additively manufactured lattices for gas turbine blade trailing edge cooling. *Applied Thermal Engineering*, *211*, p.118461.

https://doi.org/10.1016/j.applthermaleng.2022.118461

[6.21] Aider, Y., Kaur, I., Cho, H. and Singh, P., 2022. Periodic heat transfer characteristics of additively manufactured lattices. *International Journal of Heat and Mass Transfer*, *189*, p.122692.

https://doi.org/10.1016/j.ijheatmasstransfer.2022.122692

[6.22] Kaur, I., Mahajan, R.L. and Singh, P., 2023. Generalized correlation for effective thermal conductivity of high porosity architectured materials and metal foams. *International Journal of Heat and Mass Transfer*, *200*, p.123512.

https://doi.org/10.1016/j.ijheatmasstransfer.2022.123512

[6.23] Chung, K.M., Zeng, J., Adapa, S.R., Feng, T., Bagepalli, M.V., Loutzenhiser, P.G., Albrecht, K.J., Ho, C.K. and Chen, R., 2021. Measurement and analysis of thermal conductivity of ceramic particle beds for solar thermal energy storage. *Solar Energy Materials and Solar Cells*, *230*, p.111271.

https://doi.org/10.1016/j.solmat.2021.111271

[6.24] Chen, C., Yang, C., Ranjan, D., Loutzenhiser, P.G. and Zhang, Z.M., 2020. Spectral radiative properties of ceramic particles for concentrated solar thermal energy storage applications. *International Journal of Thermophysics*, *41*, pp.1-25.

https://doi.org/10.1007/s10765-020-02733-5

[6.25] Moffat, R.J., 1988. Describing the uncertainties in experimental results. *Experimental thermal and fluid science*, *1*(1), pp.3-17.

https://doi.org/10.1016/0894-1777(88)90043-X

[6.26] Aider, Y, Cho, H, & Singh, P. "Convective Heat Transfer Potential of Particles/Airflow Through Single Cell Thick Additively Manufactured Octet-Shaped Lattice Frame Material." *Proceedings of the ASME 2022 Heat Transfer Summer Conference collocated with the ASME 2022 16th International Conference on Energy Sustainability*. *ASME 2022 Heat Transfer Summer Conference*. Philadelphia, Pennsylvania, USA. July 11–13, 2022. V001T06A004. ASME.

https://doi.org/10.1115/HT2022-81856

[6.27] Kaur, I., and Singh, P., 2022, "Direct Pore-Scale Simulations of Fully Periodic Unit Cells of Different Regular Lattices." ASME. *J. Heat Transfer*, Vol. 144(2), pp. 022702.

https://doi.org/10.1115/1.4053204

# CHAPTER SEVEN :
# CONCLUSIONS AND RECOMMENDATIONS FOR FUTURE WORK

This research investigated the feasibility of using stainless steel lattice structures, fabricated via binder jetting additive manufacturing, to enhance the heat transfer performance of moving packed bed heat exchangers for third-generation concentrating solar power (CSP) systems. The study began by evaluating the heat transfer coefficient and thermal-hydraulic performance of Octet, FD-Cube, TKD, and Cube lattice structures using air as the working fluid. Experiments were conducted for Reynolds numbers ranging from 5,000 to 22,500 under two heating conditions: both endwalls heated and only the bottom wall heated. The results showed that Octet, FD-Cube, and TKD provided similar heat transfer coefficients, while Cube yielded the lowest values. However, FD-Cube incurred the highest pressure drop, followed by Octet, TKD, and Cube. At a given pumping power, Cube exhibited the best overall thermal-hydraulic performance, especially at high airflow rates.

The investigation then focused on the Octet topology, assessing its flowability with particles using experiments and discrete element method (DEM) simulations. Three Octet lattice porosities (0.75, 0.80, and 0.88) and three particle size distributions (CP 40/100, CP 30/60, and HSP 20/40) were studied. The results demonstrated that particle mass flow rate increased with lattice porosity and decreased with particle size. DEM simulations successfully captured key experimental flow features, including void zones downstream of fibers, stagnation areas upstream of junctions, and wavy particle motion around fibers. The simulations also revealed particle accumulation zones on fiber-fiber and fiber-wall junctions, which could lead to non-uniform heat transfer. Based on these findings, the Octet lattice was selected for further study due to its potential for high heat transfer with gravity-driven particle flow.

The final phase of the research measured the heat transfer performance of Octet lattice panels with a porosity of 0.88, manufactured from SS316L and SS420 via binder jetting. Experiments were conducted with falling packed beds of various particle sizes. Packing the Octet void space with particles enhanced the effective thermal conductivity by factors of 2-4 and 4-8 compared to particle packed beds alone for SS316L and SS420, respectively. For airflow velocities of 3-12 m/s, the convective heat transfer coefficients in the periodic heat transfer region ranged from 200-600 W/m2K. With CP 40/100

particles flowing through the 0.88 porosity Octet lattice, the convective coefficient was approximately 400 W/m2K for both materials. Compared to parallel plate configurations, the SS316L Octet panel enhanced the heat transfer coefficient by 40-50% for smaller particles (CP 40/100 and CP 30/60), although no enhancement was observed for the largest particles (HSP 20/40).

This research demonstrated the significant potential of additively manufactured Octet lattice structures with a porosity of 0.88 to enhance heat transfer in moving packed bed heat exchangers for CSP applications. The lattice structures increased thermal conductivity, convective heat transfer coefficients, and overall heat exchanger effectiveness compared to traditional designs. The findings suggest that additive manufacturing can play a crucial role in integrating advanced heat transfer enhancement features, such as lattice structures, into next-generation CSP systems. Future work will focus on demonstrating these enhancements in a full-scale particle-to-supercritical CO2 heat exchanger tested under CSP-relevant conditions.

# VITA

Youssef Aider was born in Chefchaouen, Morocco on August 7, 1994. Before attending the University of Tennessee, Knoxville, he attended the International University of Rabat, where he earned a Bachelor's degree in Aerospace Engineering in June 2018. From there, he attended Mississippi State University, where he received a Master of Science in Aerospace Engineering in June 2019. He entered the University of Tennessee, Knoxville in August 2022, where he is pursuing his Ph.D. in Mechanical Engineering with an expected graduation date of December 2024.